

UNIVERSITÀ DEGLI STUDI DI ROMA
“TOR VERGATA”

FACOLTÀ DI SCIENZE MATEMATICHE, FISICHE E NATURALI
Dipartimento di Fisica



PhD thesis in Astronomy
XX Ciclo

**The Vela Molecular Ridge Young Population:
from pre-stellar condensations to young clusters**

Massimo De Luca

Supervisors

Dr. Teresa Giannini

Prof. Dario Lorenzetti

Coordinator

Prof. Roberto Buonanno

Abstract

The aim of this thesis is the characterization of the proto-stellar population of a star forming region (about one square degree) of the Vela Giant Molecular Cloud Complex, paying particular attention on the correlation between young objects and physical and morphological characteristics of the cloud interstellar medium. As a by-product, observational targets for new generation instrumentation have been also identified.

Giant Molecular Clouds contain over 80% of the molecular hydrogen content of the Galaxy and are now considered responsible for most of the star birth. They thus represent the most promising sites for the research activity on star formation.

By analysing the large-scale cloud structure we describe the gas-dust condensations inside which collapse into new stars begins. It follows a detailed inspection of both the infrared emission arising from such condensations and of the mass-loss phenomena (jets and outflows) associated with the youngest objects. This allows us to draw interesting conclusions regarding the star-forming modalities, both within each condensation and, more in general, within the cloud, enabling a comparison with other Galactic clouds.

The large analysed database covers the range from Near-Infrared to millimeter wavelengths and has been obtained by means of both ground based and space-born facilities (we present also the first results of the on-going study of maps acquired by the Spitzer Space Telescope).

The contribution given by this study to the present-day research activity on star formation mostly concerns the debates regarding: *(i)* the spatial relation between sites of star birth and interstellar material distribution, *(ii)* the link between the mass distribution of the cloud condensations and the Initial Mass Function, *(iii)* the statistics of different evolutionary stages of young objects within dust and molecular cores, *(iv)* the identification of interesting sources for a future investigation by means of more powerful instrumentation (*e.g.* ALMA and Herschel).

This work has been carried out within the Infrared group of the Astronomical Observatory of Rome (INAF-OAR) under the supervision of Dr. Teresa Giannini, Prof. Dario Lorenzetti (INAF-OAR), and on the behalf of the University “Tor Vergata” of Rome (supervisor Prof. Roberto Buonanno).

Abstract (Italiano)

Scopo di questa tesi è la caratterizzazione della popolazione proto-stellare di una regione di formazione stellare (circa un grado quadro) nel complesso di nubi molecolari giganti denominato Vela Molecular Ridge, con particolare riguardo per la correlazione tra oggetti giovani e caratteristiche fisiche e morfologiche del mezzo interstellare.

Le nubi molecolari giganti contengono più dell'80% del contenuto di idrogeno della Galassia e sono considerate responsabili della maggior parte della formazione stellare. Esse rappresentano quindi i siti maggiormente promettenti nell'ambito della ricerca sulla nascita delle stelle.

Analizzando la struttura su larga scala della nube, vengono descritte le condensazioni di gas e polvere dentro le quali si originano le stelle. Segue uno studio dettagliato, sia dell'emissione infrarossa proveniente da tali condensazioni, che dei fenomeni di perdita di massa (jet e outflow) associati agli oggetti più giovani. Ciò permette di trarre interessanti conclusioni riguardo le modalità della formazione stellare, tanto all'interno di ciascuna condensazione, quanto, più in generale, nella nube, consentendo altresì un raffronto con altre nubi Galattiche.

I dati analizzati spaziano dal vicino infrarosso alle lunghezze d'onda millimetriche e sono stati ottenuti per mezzo di osservazioni da Terra e dallo spazio (vengono presentati anche i primi risultati dello studio tutt'ora in corso di mappe acquisite dal telescopio spaziale Spitzer).

Il contributo fornito dal presente lavoro all'attuale attività di ricerca in formazione stellare riguarda principalmente: *(i)* la relazione spaziale tra siti dove le stelle hanno origine e distribuzione del mezzo interstellare, *(ii)* il legame tra distribuzione in massa delle condensazioni e funzione iniziale di massa, *(iii)* la statistica dei differenti stadi evolutivi delle proto-stelle in connessione con dette condensazioni, *(iv)* l'identificazione di sorgenti che meritano di essere osservate mediante strumentazione di nuova generazione in via di completamento (*e.g.* ALMA ed Herschel).

Questo lavoro è stato svolto nell'ambito del gruppo di astronomia infrarossa presso l'Osservatorio Astronomico di Roma, sotto la guida della Dott. Teresa Giannini, del Prof. Dario Lorenzetti, e presso l'Università di Roma "Tor Vergata", sotto la supervisione del prof. Roberto Buonanno.

List of keywords

Stars: formation

Stars: luminosity function, mass function

Stars: pre-main sequence

ISM: clouds

ISM: dust, extinction

ISM: HII regions

ISM: individual objects: Vela Molecular Ridge

ISM: jets and outflows

Infrared: stars

Young embedded clusters.

To my parents and my wife.

Acknowledgments

The fulfilment of this work has been possible thanks to the effort of many people.

First of all, I'm very grateful to my supervisors Teresa Giannini and Dario Lorenzetti, who spent a lot of time in teaching and encouraging me, thus making my research activity more meaningful and productive. I've also highly appreciated their friendship and personal support.

A fundamental part of this thesis arises from the fruitful collaboration with Davide Elia, Francesco Strafella and, especially, with Fabrizio Massi (good companion of a nice Christmas holiday in Patagonia).

I'd like also to thank Odysseas Dionatos, for the interesting discussions and his helpful suggestions, and Simone Antoniucci, Brunella Nisini, Gianluca Li Causi and Roberto Buonanno, for their constant support.

Finally, I thank my parents and, above all, my wife, for instilling me confidence and incentives for pursuing my PhD.

Contents

Introduction	17
1 Star Formation in the Vela-D Cloud: some questions	25
1.1 Which are the main modalities of star formation?	27
1.1.1 Where does star formation preferentially occur? .	27
1.1.2 Mainly in clusters or diffuse?	29
1.1.3 Are there any clues of evolution of these modal- ities?	34
1.1.4 Can be the star formation triggered by the nearby Supernova Remnant?	36
1.2 Which is the mass distribution of the young population?	38
1.2.1 Is it possible to derive a unique Initial Mass Function for the whole cloud?	38
1.2.2 How the Initial Mass Function is linked to the dust core mass distribution?	41
1.3 What is the current stage of star formation?	42
1.3.1 What are the youngest objects?	43
1.3.2 And what about the oldest ones?	46
1.3.3 Is the star formation still in progress?	49
1.3.4 What is the rôle played by mass-loss phenomena?	52
2 Gas and Dust large-scale emission	57
2.1 Molecular emission	58
2.1.1 CO data	58
2.1.2 CO maps and velocity structures	62
2.1.3 Searching for expanding shells and outflows . . .	71
2.1.4 Cloud mass evaluation	77
2.1.5 Molecular clump decomposition	78
2.1.6 Clump mass spectrum and mass-size relationship	82

2.2	Dust emission	86
2.2.1	Dust data	86
2.2.2	Dust emission regions	87
2.2.3	Dust core decomposition	88
2.2.4	Core properties	98
2.2.5	Core mass-size relationship	99
2.2.6	Core mass spectrum	102
3	Vela-D in the Infrared	107
3.1	Near-Infrared observations	108
3.1.1	2MASS (J, H, K bands)	108
3.1.2	IRAC2 (J, H, K bands)	109
3.1.3	SofI (J, H, K bands)	109
3.2	Mid- and Far-Infrared observations	110
3.2.1	IRAS (12, 25, 60, 100 μm)	110
3.2.2	MSX (8, 12, 14, 21 μm)	111
3.2.3	Timmi2 (N band)	112
3.2.4	SPITZER-MIPS (24, 70 μm)	113
3.3	Infrared counterparts of dust cores	114
3.3.1	Association criteria	114
3.3.2	The core MMS1	116
3.3.3	Counterpart results	120
3.3.4	Star formation modalities and evolutionary stages	126
3.4	MIPS photometry	130
3.4.1	Color-magnitude diagrams	140
3.4.2	Comparison with IRAS sources	145
4	Mass loss phenomena in Vela-D	151
4.1	Observations	152
4.1.1	H ₂ survey (2.12 μm)	152
4.1.2	Apex data	155
4.2	Outflow parameters estimate: theory	156
4.2.1	Radiative transfer of emission lines	157
4.2.2	CO Column density	159
4.2.3	Mass, momentum and kinetic energy	161
4.3	Outflow parameters estimate: our results	162
4.4	Source-jet-outflow pictures	170

	15
5 Star Formation in the Vela-D Cloud: some answers	177
Appendices	185
A Core infrared counterparts: one by one	185
List of Figures	219
List of Tables	230
List of Publications	232
Bibliography	234

Introduction

The aim of this thesis is the characterization of the proto-stellar population of a star forming region of the Vela Giant Molecular Cloud Complex, paying particular attention on the correlation between young objects and the physical and morphological characteristics of the cloud interstellar medium. As a by-product, observational targets for new generation instrumentation have been also identified.

Giant Molecular Clouds contain over 80 % of the molecular hydrogen content of the Galaxy and are now considered responsible for most of the star formation (§ 1.1.1). These are the largest galactic structures, preferentially located within the gravitational potential wells of the spiral arms (§ 1.1.1), and are constituted by molecular gas and dust, distributed in filaments and clumpy condensations. Compared to the smaller Dark Clouds, Giant Molecular Clouds usually produce stars having a higher degree of clusterization, with a consequent higher probability to host massive stars (§ 1.1.2). Although generally more distant and more affected by contamination of unrelated galactic material, these giant structures represent the most promising sites for the research activity on star formation, because of the opportunity of investigating, through multi-wavelength and statistical approaches, *(i)* the rôle, on the star forming process, of clustering and large-scale dynamics (self-gravity, turbulence, magnetic fields, interactions with Supernova Remnants or ionized expanding shells), *(ii)* the still poorly understood mechanisms leading to the birth of high mass stars, and *(iii)* possible differences in star formation among different galaxies.

For studying the young population of a Giant Molecular Cloud, a multi-wavelength approach is needed, given the wide range of spatial scales and wavelength regimes of the emission that characterizes the various stages of the star-forming process. This approach, adopted

to perform the work presented here, consists in the correlation of the information obtained by observing the Vela cloud in an extended wavelength range.

In our case the analysed database, spanning the range from Near-Infrared to millimeter wavelengths, consists of both large maps of the cloud and dedicated observations of the most interesting regions, and has been obtained by means of both ground based and space-born facilities. In particular, we present here the first results of the on-going study of large maps acquired by the Spitzer Space Telescope, whose high sensitivity and resolution has highly improved the recent research activity on star formation.

The first step in this work has been the analysis of the maps of $^{12}\text{CO}(1-0)$ and $^{13}\text{CO}(2-1)$ line emission, tracing the molecular component, and of the millimeter continuum emission produced by the interstellar dust (Chapter 2). The main result of this analysis has been the individuation and mass estimate of the gas-dust condensations inside which collapse into new stars begins.

Thus, we have studied the details of the infrared emission arising from such condensations finding clear evidences of the on-going star formation (Chapter 3). The classification of the proto-stellar sources, based on their Spectral Energy Distributions (§ 1.3) and color indexes (§ 1.1.2), has provided indications about their evolutionary stage, allowing us to draw interesting conclusions regarding the star-forming modalities, both within each condensation and, more in general, within the cloud, enabling a comparison with other Galactic clouds.

In the last part of this work (Chapter 4), we have more deeply analysed the youngest objects of the cloud by means of the observations of mass-loss phenomena, jets and outflows, always associated with the first stages of the accreting process. To this aim, ro-vibrational emission lines of H_2 and $^{12}\text{CO}(3-2)$ have been studied.

The contribution given by this study to the present day research activity on star formation mostly concerns the debates regarding: *(i)* the spatial relation between sites of star birth and interstellar material distribution, *(ii)* the link between the mass distribution of the cloud condensations and the Initial Mass Function (§ 1.2), *(iii)* the statis-

tics of different evolutionary stages of young objects within dust and molecular cores, *(iv)* the identification of interesting sources for a future investigation by means of more powerful instrumentation (*e.g.* ALMA and Herschel).

This work has been carried out within the Infrared group of the Astronomical Observatory of Rome (INAF-OAR) under the supervision of Dr. Teresa Giannini, Prof. Dario Lorenzetti (INAF-OAR), and on the behalf of the University “Tor Vergata” of Rome (supervisor Prof. Roberto Buonanno). Part of the results of the activity presented here has taken advantage from the collaboration with Fabrizio Massi (Arcetri Astrophysical Observatory), Davide Elia and Francesco Strafella (“Università del Salento”), Brunella Nisini (INAF-OAR), Howard Smith and Massimo Marengo (Harvard Smithsonian Center for Astrophysics).

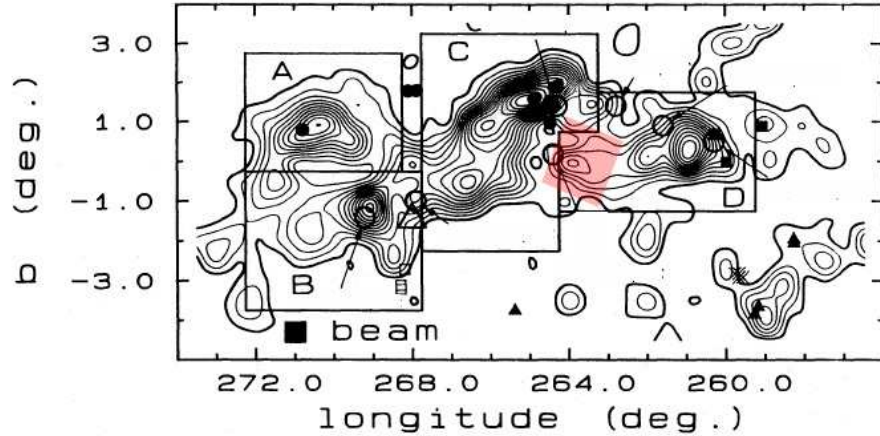


Figure 1: *The Vela Molecular Ridge according to Murphy & May (1991). The four ^{12}CO emission peaks, corresponding to clouds A, B, C and D are labeled. The region investigated in this thesis is red-shaded in the Figure.*

Vela-D

A few lines are now needed to introduce the Vela-D region (red-shaded in the following Figures), object of this discussion, and to summarize the main results of publications preceding this thesis.

The Giant Molecular Cloud Complex known as Vela Molecular Ridge, *VMR* (Murphy & May 1991), is probably one of the best regions for studying the processes involved in star formation. It is located in the galactic plane ($b = \pm 3^\circ$), outside the solar circle ($\ell \sim 260^\circ - 275^\circ$), and most of its gas is at a distance of ~ 700 pc (Liseau et al. 1992). Thus it represents the nearest giant complex hosting massive (although mostly intermediate-mass) star formation after Orion, but, unlike Orion, it is located *within* the galactic plane, where most of star formation in the Galaxy occurs.

The VMR was first mapped in the $^{12}\text{CO}(1-0)$ (§2.1.1) transition with low resolution ($\sim 30'$) by Murphy & May (1991). They subdivided it into four main regions, named A, B, C and D (Figure 1). This complex is also included in a recent review (Pettersson 2007) that describes all the main star forming features of a larger region, mainly encompassing the constellations of Vela and Puppis ($-20^\circ < b < 6^\circ$, $240^\circ < \ell < 280^\circ$) and spanning the distance range from 0.2 to 2 kpc.

A large data-base has been accumulated by our group on VMR

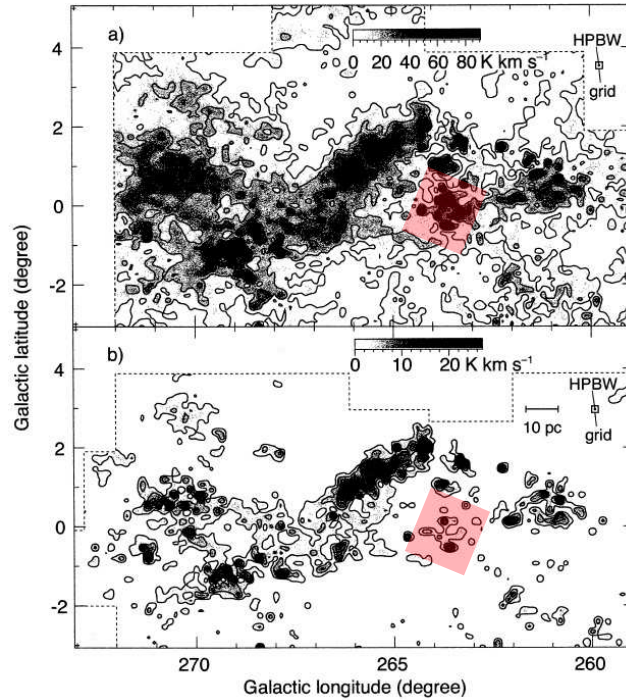


Figure 2: *The Vela Molecular Ridge according to Yamaguchi et al. (1999). $^{12}\text{CO}(1-0)$ (a) and $^{13}\text{CO}(2-1)$ (b) emission contours. Red-shaded: investigated region.*

clouds through ground-based observations from Near-Infrared to mm wavelengths. In particular, the analysis based on the IRAS Point Source Catalog (see also § 3.2.1) unveiled a remarkable concentration of red far-IR sources with bolometric luminosities $< 10^4 L_{\odot}$ (Liseau et al. 1992, Lorenzetti et al. 1993), indicated to be very young, intermediate-mass stars. Massi et al. (2000) (see also Massi et al. 2003) found that far-IR sources with $L_{bol} > 10^3 L_{\odot}$ coincide with young embedded clusters (size ~ 0.1 pc, ~ 50 -100 members). In particular, the region of the cloud D (hereinafter Vela-D) studied in this thesis hosts a large number of these clusters, revealing a high efficiency in this mode of star formation. Massi et al. (2006) found that these clusters present a stellar mass distribution that follows the canonical Initial Mass Function. At the same time, the presence in the field of IRAS sources having bolometric luminosities of only few solar luminosities, shows that the formation of a diffuse population of low mass stars is also active in this region.

In the cloud identification by Murphy & May (1991), Vela-D is located in the rightmost end of the galactic longitude interval of the

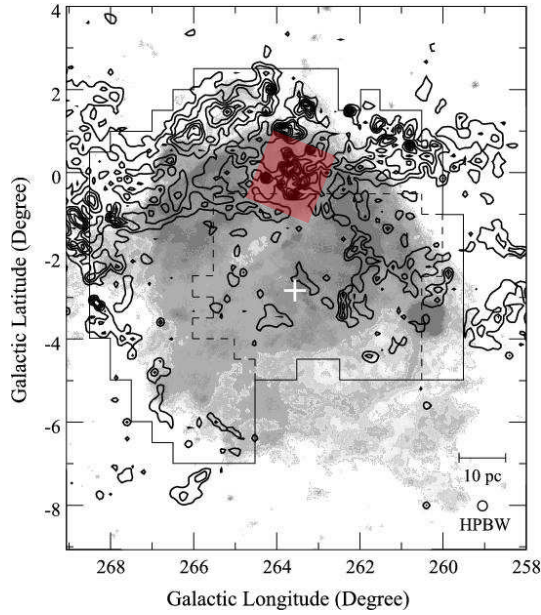


Figure 3: *The Vela Molecular Ridge according to Moriguchi et al. (2001), where $^{12}\text{CO}(1-0)$ emission contours are plotted over the soft X-ray image (gray scale), taken by the ROSAT satellite, which shows a clear evidence of the high energy emission produced by the Vela Supernova Remnant. A cross indicates the position of the Vela pulsar, result of the explosion. Red-shaded: investigated region.*

complex, and shows two main CO emission peaks (at $\ell \sim 261^\circ$ and 264°). The same characteristic is recognizable, but in greater detail, in the $^{12}\text{CO}(1-0)$ and $^{13}\text{CO}(1-0)$ maps of Yamaguchi et al. (1999) (Figure 2) and in the $^{12}\text{CO}(1-0)$ map of Moriguchi et al. (2001) (Figure 3). This last map shows also a clear spatial association of the C and D clouds with the Vela Supernova Remnant. A possible physical interaction is still under discussion (§ 1.1.4).

Lorenzetti et al. (2002b) have searched the regions around a complete sample of IRAS sources in Vela-D for protostellar jets, using near-IR imaging and spectroscopy, discovering a significant number of shock tracers (H_2 and $[\text{FeII}]$ line emission knots, § 1.3.4).

Giannini et al. (2001) and, Giannini et al. (2005) have also clarified the details of the interactions between one multiple jet and its circumstellar environment as well as the properties of the exciting sources. Such studies have highlighted the importance of having Mid- and Far-Infrared observations with suitable spatial and spectral resolution to identify correctly the young proto-stars that are driving the jets.

Chapter 1

Star Formation in the Vela-D Cloud: some questions

The beginning of Infrared (IR) astronomy, in the early 1960s with the advent of the first (single pixel) infrared detectors, and, even more, the systematic sky exploration in the IR (1985-90), with the launch of the IRAS satellite and the development of IR arrays, can be considered the starting points of the research on star formation, the astrophysical topic devoted to the comprehension of both the earliest stages of stellar evolution and the environmental conditions in which stars form. This research field, in fact, deals with astrophysical objects called *proto-stars*, not yet heated by the nuclear engine, completely embedded within dense cocoons of gas and solid aggregates that process their light and emit mainly at infrared wavelengths. So, through infrared eyes, able to go much deeper inside the clouds and to see cold objects, the sky appears populated by a new category of sources, much colder than normal stars, recognized to be very young stars.

During the following decade, theory and observations brought to a solid interpretative scheme (at least for star masses less than about eight solar masses) consisting in: *(i)* the location of the sites where star formation prevalently occurs; *(ii)* the individuation of the basic ingredients involved in the star forming processes (gravitational collapse, composition of the interstellar medium, magnetic field, turbulence, accretion disks, mass loss); and *(iii)* the characterization of each stage that precedes the birth of a new star.

The present day work of the research in this field is concerned with a new level of investigation, mainly focused on three general targets:

the comprehension of the details of the accretion processes (*e.g.* initial conditions, chemistry of the protostellar envelopes, dynamics of inflowing/outflowing material), the extension of the evolutionary scheme and concepts to high mass proto-stars, the comparison of the star forming modalities among different environments (*e.g.* global properties of the interstellar medium in star forming regions, mass distribution of the new stars, occurrence of triggers of the collapsing process, comparison with star formation within other galaxies).

In this framework, many surveys in the last few years have been devoted to the characterization of the most active star forming sites, the Molecular Clouds (MC) like Orion (*e.g.* North 2005), Taurus (*e.g.* Guedel et al. 2006), Ophiucus (*e.g.* Jorgensen et al. 2006), Perseus (*e.g.* Enoch 2006, Hatchell et al. 2007, Rebull et al. 2007). Such characterization consists of answering to many questions of fundamental importance for a deeper comprehension of the star formation process.

To catch the relevance of these questions within the framework of the present day panorama and to have an idea of the possible answers proposed until now in the literature, we give now a view of the scientific background. This is the aim of the present Chapter that deals with the questions we tried to answer in this thesis work about *our* molecular cloud, Vela-D (see the Introduction for a complete description of the region).

By reading the first Section it will be clear the non-uniqueness of environmental conditions at the origin of star formation activity, depending on spatial distribution and dynamics of the interstellar medium and on the possible occurrence of particularly energetic phenomena, such as supernova explosions and ionized shells surrounding the brightest stars. Section 1.2 deals with the mass distribution of the young stars and its link to the mass distribution of the parental cloud sub-structures. In Section 1.3 are described the main evolutionary stages of the star formation process and the clues of the presence of very young objects. The last section will address the importance of the comparison among different star forming sites.

1.1 Which are the main modalities of star formation?

1.1.1 Where does star formation preferentially occur?

Stars form in molecular clouds (MC). This is now an overwhelming evidence, at least for all present day star formation. These clouds constitute protected environments and possess all the physical conditions necessary to the collapse in a star: density and temperature values, composition of the interstellar medium, right conditions in terms of gravity, turbulence, magnetic fields and thermal pressure. The deep investigation of structure and dynamics of these entities is an unavoidable step for the knowledge of the processes at the basis of the birth of new stars.

The molecular phase of the interstellar medium (ISM) is characterized by its high density (≥ 100 particles/cm³) and low temperature (~ 10 K) compared to other phases found within the Galaxy, such as the neutral (cold and warm) and the ionized (warm and hot) ones. In such conditions, thanks also to the shielding properties of the cloud edges against high energy photons, molecules and dust grains can survive. These latter are solid agglomerates of mainly silicates and carbon covered by icy mantles, with typical size of about 0.1 microns, produced in the external layers of giant stars and their presence acts as catalyst of the molecular formation process. The molecular component of the clouds is highly dominated by the molecular hydrogen, but its emission, being the H₂ excitation temperature too high for the common cloud conditions¹, is much less intense than the main tracer of these clouds: the CO radio rotational lines (see Capters 2 and 4). Many other simple molecules are found within MCs, like ammonia, water, hydroxyl, together with more complex species, even organic ones (*e.g.* formaldehyde). Atomic and ionized gas components are also present within MCs, especially at the cloud edges, with extended and massive envelopes of atomic hydrogen, and close to the bright stars, whose ultraviolet photons produce *bubbles* of ionized and neutral hydrogen, indicated as Hii and Hi regions, respectively.

¹The dipole rotational transitions are forbidden for omo-nuclear molecules such as H₂, so that the first allowed rotational transition (0-0S(0), see Section 4.1.1), thanks also to the small moment of inertia (§ 2.1.1), has an excitation temperature of about 500 K.

Table 1.1: *Physical properties of molecular clouds (adapted from Stahler & Palla 2005).*

Cloud Type	Mass M_{\odot}	Size (pc)	Density (cm^{-3})	Temperature (K)	A_V (mag)	Examples
Giant Molecular Cloud	10^5	50	100	15	2	Orion, Vela-D
Dark Cloud Complex	10^4	10	500	10	5	Taurus-Auriga
Diffuse	50	3	500	50	1	ζ Ophiuchi
Dark Cloud individual	30	2	10^3	10	10	B1
Bok Globule	10	0.1	10^4	10	10	B335

Among molecular clouds distinctions must be done on the basis of typical masses, sizes, densities and temperatures. The usual classification scheme is reported in Table 1.1, where typical values of visual extinction (A_V) are also reported. As the mass and size values suggest, the great majority of new stars form within Giant Molecular Clouds, where resides over 80 percent of the molecular hydrogen content of the Galaxy. So, studying these giant systems, which are the largest galactic structures, is fundamental to construct a meaningful picture of star formation; picture that can be thus related to the information coming from extra-galactic observations.

Origin and evolution of GMCs are still debated topics. The key to address these points seems to reside in both their structure and placement within galactic arms, which indicates ages that cannot far exceed 10^7 years, the spiral arm crossing time. Cloud's structure is far from homogeneity and appears to be composed by sub-structures of enhanced density, called clumps, connected by filaments. Sizes and masses of the clumps can be described by power laws (see Chapter 2, Figures 2.11 and 2.23); the same power laws that describe size and mass distribution of the clouds themselves. Such universality suggests, as a first hypothesis, that giant clouds are built up by the agglomeration of many clumps, already distributed in mass according to this power law, thanks to the gravitational wells associated with Galactic arms (*bottom-up* scenario, Stahler & Palla 2005, Section 3.1.2). A second hypothesis about cloud's origin arises when considering the filamentary structures which connect the clumps (see, *e.g.* Figure 2.20). Such filaments can be well explained as a consequence of turbulent motion: high speed turbulent flows of atomic gas can reach enough density to produce molecules, especially after collision of high density regions

while crossing of Galactic arms. In this picture, molecular clouds are the *tips of the iceberg* in the general turbulent flow (Smith 2004, Section 4.2.1) of Galactic gas. Other scenarios have been proposed: gravitational instability of very large objects that fragment into smaller clouds (*top-down* hypothesis); thick *super-shells* of gas swept up by supernova winds which eventually become gravitationally bounded in the shocks with interstellar medium; streaming of material along large-scale magnetic fields; thermal instability of regions of atomic diffuse gas slightly cooler and denser than the surrounding material.

Although we cannot enter in deeper details of this debate, we must underline here its importance for understanding the initial conditions at which the collapse into a star begins. This importance is not surprising if considering that very few GMCs are not (yet) associated with young stars, so that star birth rapidly follows the formation of the clouds themselves. All the cited ingredients (gravitational instability of clumps, turbulence, magnetic field, supernova shells), in fact, are also often invoked as triggers or drivers of the star formation process.

Other important spatial features that can be often observed in the morphology of giant molecular clouds are the signposts of expanding shells produced by massive stars. These big shells are thought to be able to trigger the star formation by compressing the interstellar medium and causing the gravitational instability needed for the collapse.

In conclusion, cloud's morphology is strictly linked to the star formation activity. So the analysis of the interstellar medium (both gas and dust) distribution is an important parameter to take into account for the understanding of the initial conditions of the collapse. In particular, we can formulate a first question that address this point in the case of the investigated molecular cloud:

Where does star formation in Vela-D preferentially occur? More precisely: Is there any spatial trend in the ages and characteristics of the young population that could be linked to the filamentary and shell-like patterns well recognizable in the Vela-D maps?

1.1.2 Mainly in clusters or diffuse?

Young and very young stars are found both in *clusters*, stellar groups with a high spatial density and usually gravitationally bound, and in

more diffuse groups called *associations*, which can extend over 100 pc or more. Both clustered and diffuse star formation are observed at the same time within Giant Molecular Clouds, that present, however, a significantly higher tendency towards the first modality compared to the smaller clouds (*e.g.* Taurus), where young population is mainly diffuse.

The stellar spatial distribution necessarily reflects the clumpy, filamentary or shell-like cloud structures whose fragmentation and collapse constitutes the starting point of the star formation process. In particular, the clumpy structures described in the previous Section are observationally divided in two classes: The smaller cloud structures ($M \sim 1 - 10 M_{\odot}$, size ~ 0.1 pc, density $\sim 10^{4-5} \text{ cm}^{-3}$) whose collapse originates the birth of a new star or, more often, of a double(/triple) system, are called *cores*; *Clumps* ($M \sim 10^2 M_{\odot}$, size $\sim 0.2 - 4$ pc, density $\sim 10^{3-4} \text{ cm}^{-3}$), instead, are usually named those structures collapsing in star clusters. However, as we have previously mentioned, the mass distribution of all these condensations is characterized by a power-law shape, that does not present any characteristic scale, and there is no net physical distinction among clumps and cores. Moreover, observing a clump enough evolved to have started the fragmentation and with enough resolution, it can appear as an agglomerate of cores. Anyway, for simplicity, in the following of this work we will use the term *clump* for the condensations observed in the molecular (CO) emission and the term *core* for those emerging from the dust, continuum emission (see Cap 2), which are generally smaller, although some of them are big enough to produce entire stellar clusters.

The rôle played by multiple system dynamics in the collapse process is still not so clear, but there are some important clues supporting its relevance, maybe linked to the angular momentum transfer from the stellar envelope rotation to the orbital motions. Even apparently isolated young stars, in fact, form small groups with densities of 10-100 stars per cubic parsec (*e.g.* Gomez et al. 1993). Moreover, also on core scales, double (sometimes triple) tight systems seem to be the rule instead of exceptions. Simulations of cloud evolution (*e.g.* Bonnell et al. 2003, see Figure 1.1) reproduce quite well the *social* nature of star formation and are able to explain also the existence of a number of isolated objects. The simulation results show a scenario in which the



Figure 1.1: *Three sketches of the simulation performed by Matthew R. Bate, Ian A. Bonnell, and Volker Bromm (<http://www.ukaff.ac.uk/starcluster/>). The calculation models the collapse and fragmentation of a molecular cloud of $50 M_{\odot}$. The cloud is initially 0.4 pc in diameter, with a temperature of 10 K . The cloud collapses under its own weight and very soon stars start to form. The turbulent motions in the cloud form shock waves that slowly damp the supersonic motions. At the end of simulation, some stars and brown dwarfs (Note 10) have been ejected to large distances from the region.*

intersections of the cloud filaments rapidly evolve into clumps originating clusters. Thus, due to dynamical instability of multiple systems, some objects (still very young or even not yet collapsed) are ejected to continue their life in isolation. Being the less massive objects more subject to ejection, such mechanism would imply also a link between isolated/clustered and low-/high-mass dichotomies. Furthermore, the importance of clustering for the formation of high-mass stars has been extensively documented (*e.g.* Stahler & Palla 2005). They are, in fact, usually found close to the cluster centers². Mainly two mechanisms are usually adopted to explain the need of high stellar density to produce high-mass stars: (i) *competitive accretion*, which relies on gravitational competition for gas in a clustered environment, resulting in a few centrally located stars accreting significantly more than the rest, and *coalescence*, for which, within the center of compact clusters, the stellar density is so high to make it probable collisions resulting in the merging of two objects.

This discussion suggests that, maybe, truly isolated star formation

²To be honest, a relatively large number of O stars (about 25%) are not members of any cluster or association. However, they present exceptionally high spatial velocities, directed away from the Galactic plane, and their proper motions can often be traced back to known young stellar groups.

does not exist. Rather there are simply varying degrees of clustering, depending on the interstellar medium distribution within clouds. Thus, given the importance of clustered star formation, in the following, we will enter in some more details regarding both some cluster properties and the techniques commonly used to study these environments (and that we will extensively use in Chapter 3).

First of all, similarly to optical clusters, most of the importance of the young clusters resides in their common origin in terms of physical/chemical environment, age³ and distance. These characteristics, in fact, are fundamental for addressing the distribution in mass of the cluster stars (this point will be discussed in Section 1.2.1, where the concept of the *Initial Mass Function* will be presented). But it is not so easy to determine which stars pertain to a cluster and which are background/foreground objects. And this is particularly true for regions located along the Galactic plane like Vela-D. Different methods for determining the membership are usually adopted, depending on distance and available data: (i) statistical estimate of background/foreground sources, by using off-cloud observations, (ii) cluster member selection based on proper motions, by means of observations at different epochs, (iii) spectroscopy, by using multi-object spectrographs, (iv) multicolor photometry.

In particular we will use this last technique that permits also to have an idea on which are the youngest objects within the cluster (see Chapter 3). The most common tools used to this aim are the colour-colour and the colour-magnitude diagrams, that are usually based on observations of the cluster at the NIR J, H and K bands (centered at 1.25, 1.65 and 2.2 μm , respectively). Optical bands cannot be used because young clusters are still embedded within their original cloud cocoons, which make their emission observable only at infrared wavelengths. The extinction in this range, in fact, is much less than in the visual bands⁴, so radiation can penetrate larger columns of molecular cloud gas and dust.

As illustrated in Figure 1.2, the NIR colour-colour diagram horizon-

³Given the youth of these systems and the smaller time scales of the stellar formation compared to the evolution of mature objects, differences of 10^{4-5} years among young cluster members can be still appreciable because resulting, sometimes, in different evolutionary stages.

⁴As an example, a photon in the K band has an extinction (in magnitudes) 0.1 times than that of a photon in the V band (0.555 μm).

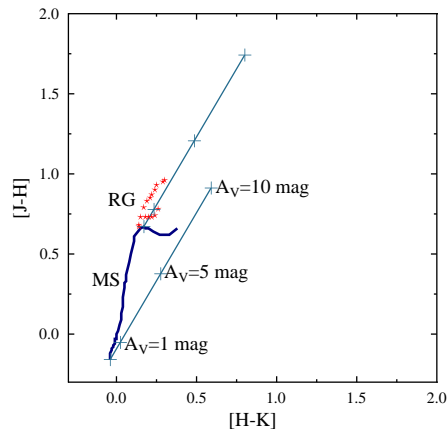


Figure 1.2: *Scheme of colour-colour diagram. Dark blue line: main-sequence stars; Red crosses: red giant stars; light blue lines: reddening lines running from two representative points, enclosing the main sequence; typical extinction values of 1, 5 and 10 magnitudes are indicated with crosses.*

tal axis is given by the difference in magnitude between H and K bands (called H-K colour, often indicated within square brackets), while on the vertical axis is reported the difference J - H (J-H colour). We can assume that all stars not belonging to the cluster are either main-sequence or red giant stars so that their colours assume a well determined ratio, depending on their mass. The loci of the main-sequence and red giant stars are indicated by the dark blue line and by the red crosses, respectively. As we have seen, the extinction depends on the observed wavelength range, so the occurrence of increasing extinction values produces a shift of the star along the diagram towards higher values of both H-K and J-H. To represent direction and values of this shift we have plotted on the diagram two reddening lines running from two representative points, enclosing the main sequence, towards the upper right side. For each line the typical extinction values of 1, 5 and 10 magnitudes are represented by crosses. Usually foreground stars are only weakly reddened because of the small amount of dust from the star to the observer. Background stars are subject, on the contrary, to the reddening due to the cloud dust (which is particularly high in proximity of the young cluster direction). The cluster members, in addition to the cloud reddening, undergo reddening phenomena which

are circumstellar rather than interstellar and due to the presence of dusty envelopes and/or disks (on a 10^{3-4} AU scale) surrounding them. The ISM infalling onto the accretion disks, in fact, makes them shine at infrared wavelengths, producing the so called *infrared excess*. Moreover, as we shall see in Section 1.3 the high luminosity produced at the photospheres by the infalling material is heavily absorbed, processed and re-emitted at longer wavelengths by the surrounding interstellar material. Such local phenomena have the effect of shifting the cluster stars, depending on the star mass, evolutionary stage and envelope characteristics, towards the right part of the diagram. In this way the cluster members (at least those presenting the higher infrared excess) can be isolated from foreground/background objects⁵.

To conclude this Section, in which we have underlined the social nature of the young stars, we formulate some questions important for the comprehension of the star formation in progress in Vela-D. As we have described in the Introduction, some papers have been already published regarding Vela-D clusters. The present work will address the correspondence between clusters and dust-molecular condensations, trying to improve, thanks also to newly acquired MIR-FIR data, the search for the location of the youngest objects. Moreover, we will try to individuate clues of diffuse star formation along the gas filaments. The questions to answer are then:

Is the present-day star formation in Vela-D mainly diffuse or located within/around clusters? What are the gas and dust characteristics in correspondence with the embedded clusters?

1.1.3 Are there any clues of evolution of these modalities?

One of the debated questions about molecular clouds concerns the possible evolution of both rate and modalities of the star forming process and their link with the cloud lifetime. New stars, in fact, especially the most massive ones, originate important feedbacks which heavily weigh on cloud dynamics, morphology, chemistry and shielding prop-

⁵Obviously, infrared excess and local reddening of young stars, given its circumstellar nature, is present also in the diffuse young population, although we have presented it in the context of the identification of the cluster members.

erties against interstellar ionization⁶ (which have been proved to be important as initial conditions of the core collapse into a star).

The *star formation rate* (SFR, the cloud mass transformed into new stars every year) quantify the efficiency of the star forming process inside a cloud and is very difficult to evaluate. Many estimates give very small values, of the order of two solar masses per year (*e.g.* Zuckerman & Evans 1974). As we shall see in Section 1.3.3, the principal mechanisms responsible for such an inefficiency of GMCs in producing stars, at least for low-mass objects, seem to be turbulence and magnetic fields. Changes in the SFR within a cloud during its lifetime are even more difficult to evaluate and require many assumptions. Recent studies are in favour of a constant rate during the cloud lifetime and some kind of self-regulation has been proposed to explain this occurrence (McKee 1989). The energy injection by newly formed stars (by means of outflowing material and radiation pressure), being the dominant source of kinetic energy for molecular clouds, is not enough to support the cloud against contraction until SFR is small. During the cloud collapse also core collapse accelerates with a resulting SFR increase. Thus it follows another cloud expansion and a consequent SFR reduction.

This can be true as long as the molecular cloud content is not destroyed by ionizing radiation and stellar winds from high mass stars. It has been evaluated (Larson 1981) that a fraction of only 4% of cloud mass collapsed into stars, distributed in mass with the typical Initial Mass Function (see Section 1.2.1), could be enough to completely ionize the rest of the cloud. Both ionization and winds operate over a period of ~ 10 Myr or less that is determined by the lifetimes of the most massive stars; this is comparable to the inferred lifetimes of molecular clouds after the onset of star formation in them. Also neutral material driven by dynamical effects, such as ionized gas pressure, winds and Supernova explosions, leaves the cloud producing large expanding shells often observed around star forming regions (*e.g.* the Barnards Loop, partially surrounding the Orion star-forming region, as described in Blaauw 1991 and Bally et al. 1991).

⁶Far UV radiation permeating the Galaxy impinges on the borders of molecular clouds, dissociating molecules. As a result, a HI shell is formed at the cloud borders which permits the molecules to survive (self-shielding). Direct photo-dissociation of H₂ from the ground state, in fact, requires a photon energy > 14.7 eV, but the Lyman continuum has already been absorbed by the external HI layer.

Changes in the star formation modalities during this cloud evolution can be expected as well as a consequence of the environment modifications. In particular, new compression fronts due to expanding Hii regions could induce fragmentation and collapse in the cluster outskirts, dispersal of inter-cluster material could stop cluster growth, coalescence of stars within crowded cluster centers, on the contrary, might produce a new generation of high mass stars, compression/dissipation of filamentary structures could enhance/lower the diffuse population formation.

Therefore, in such a complex framework, several are the unsolved problems. We will try to give some answer to the question:

Are there any clues indicating an evolution in the star formation modalities of Vela-D?

1.1.4 Can be the star formation triggered by the nearby Supernova Remnant?

Given the huge amount of emitted energy and the size of the expanding remnant, supernovae (SNe) can play a manifold and fundamental rôle in the molecular cloud life. They are able: to contribute to the compression of interstellar material causing the cloud formation (one of the possible scenarios mentioned in Section 1.1.1); to enrich the cloud material with heavy elements produced within the star and during the explosion; to inject turbulence into the cloudy environments; to trigger star formation within pre-existing clouds; to impact violently with them causing their destruction.

A supernova explosion generates a spherical shock wave that sweeps the interstellar medium, leading to the formation of a Supernova Remnant (SNR), whose interaction with a cloud may compress the gas sufficiently to drive the collapse of the cloud. The kinetic energy associated to an SN event is of the order of 10^{51} erg, the ejected mass into the ISM is $M_{ej} \sim 10 M_{\odot}$ and its terminal velocity is $\sim 10^4$ km s⁻¹. This ejected mass will expand at nearly constant velocity until it encounters a comparable mass of ambient medium. When the internal pressure of the SNR becomes comparable to the ISM pressure, it stalls, fragments and the hot gas that fills the SNR begins to mix with the ISM.

In order to trigger star formation, a remnant interacting with a cloud should, on one side, to have sufficient energy to induce cloud

collapse and, on the other side, to be evolved enough in order to not destroy it. These conditions depend on radius, density and temperature of the cloud, on ISM density and on initial SN energy (Melioli et al. 2006). Both analytical models and numerical simulations have been used to support this triggering in a number of cases (*e.g.* Ortega et al. 2004 & Melioli et al. 2006).

Several are also the controversial cases, due to the difficulty of establishing a direct causal connection between SNR and core collapse ignition. This is also the case of the Vela Molecular Ridge cloud complex (including Vela-D, see Introduction), located in the surroundings of the well known Vela pulsar⁷ and SNR. Although a causal connection between the remnant and the cloud origin has been excluded by Moriguchi et al. (2001), the study of a possible effect of the SNR on the star formation history requires a deeper investigation, especially considering that (Moriguchi et al. 2001): *(i)* comparisons among CO emission and images at other wavelengths (Hi, X-ray, optical, and radio continuum) suggest that most of the molecular gas is associated and interacting with the SNR and *(ii)* comparisons with the theoretical models of SNR expansion seem to indicate that the molecular clouds are being accelerated, and are presently evaporating.

In this work we will try to answer, by means of the analysis of the morphological large scale features (filaments and shells) observable in the available maps, to the question:

Is there any evidence supporting the hypothesis of a possible triggering of the star formation due to the nearby Vela Supernova Remnant?

⁷The Vela Pulsar (PSR B0833-45 or PSR J0835-4510) is a radio, optical, X-ray and gamma-emitting pulsar associated with Vela Supernova Remnant, in the constellation of Vela. The association of the Vela pulsar with the Vela Supernova Remnant, made by astronomers at the University of Sydney in 1968, was a direct observational proof that supernovae form neutron stars (Large et al. 1968).

1.2 Which is the mass distribution of the young population?

1.2.1 Is it possible to derive a unique Initial Mass Function for the whole cloud?

One of the basic puzzles of the star formation investigation is the origin of the *initial mass function* (IMF), the relative number of stars produced per unit mass interval. It is a central issue for star formation research because it represents a formidable constraint and benchmark for theoreticians to tuning their models.

Not directly observable, the IMF is obtained through theoretical relations from the luminosity function (number of stars produced per unit magnitude interval), which has to take into account absolute magnitude estimates and corrections for stellar life times. The first estimates of the IMF have been performed by Salpeter (1955) by considering field stars in the solar neighbourhood. Salpeter found a power-law behaviour⁸ for masses in the range 0.4-10 solar masses:

$$dN/dM \propto M^{-2.35}. \quad (1.1)$$

A most recent empirical determination of the IMF has the *canonical* form of a three-component power-law (see Figure 1.3) as proposed by Kroupa (2002):

$$dN/dM \propto \begin{cases} M^{-0.3} & 0.02 < M < 0.08M_{\odot} \\ M^{-1.3} & 0.08 < M < 0.5M_{\odot} \\ M^{-2.3} & 0.5 < M < 10M_{\odot} \end{cases} \quad (1.2)$$

For masses lower than 1 M_{\odot} , a log-normal distribution (gaussian distribution with $\log(M)$ as variable) is also often used to fit the data⁹. An interesting property of the IMF can be pointed out by roughly estimating the numbers of stars with masses exceeding 0.1, 1 and 10 solar masses, which are about 70, 12 and 0.3%, respectively (Stahler & Palla 2005). This indicates a characteristic mass of a few tenths of

⁸Sometimes IMF is also presented in the form: $dN/d\log(M)$. In this case the power law index must be increased by 1.

⁹Such distribution can be justified by considering that it would be the result of many independent processes contributing in a multiplicative way to the star formation.

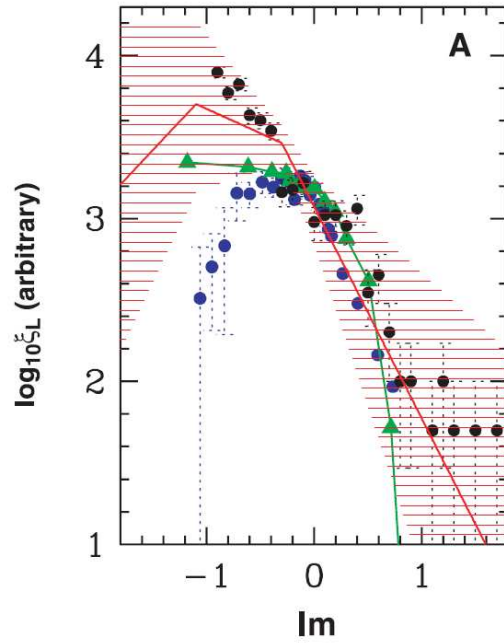


Figure 1.3: *Initial Mass function by Kroupa (2002): The measured stellar mass functions, ξ_L , as a function of logarithmic stellar mass [$lm \equiv \log_{10}(m/M_{\odot})$] in the Orion nebula cluster [ONC, solid black circles (Hillenbrand & Carpenter 2000)], the Pleiades [green triangles (Hamblly et al. 1999)] and the cluster M35 [blue solid circles (Barrado y Navascués et al. 2001)].*

M_{\odot} . Moreover, the brown dwarf¹⁰ number has been estimated to be of the same order of the star number.

Theory cannot still clearly explain all features of the empirical IMF. In particular, the main properties a complete theory should describe are (McKee & Ostriker 2007): (a) the Salpeter behaviour at high mass; (b) the turnover at $\sim 1 M_{\odot}$, (c) the upper limit in luminosity at $\sim 150 M_{\odot}$, (d) the universality of these features over a wide range of star-forming environments¹¹.

Until now we have implicitly assumed that a unique IMF could describe the mass distribution of all stellar systems throughout the Milky Way, which is, in principle, not so obvious, because it implies that star formation should result in the same distribution everywhere, independently of the variety in the environmental conditions of different regions (density, turbulence, magnetic fields, metallicity). Similar results are obtained also comparing IMF of diffuse population to IMF of stellar groups and clusters, in support of the hypothesis of a common origin within multiple systems of nearly all stars (§ 1.1.2). So the empirical result of the existence of a nearly universal IMF constitutes a powerful constraint on star formation theories. Nevertheless, thanks to the improvements in instrumentation, some clue of (maybe) significant variations in different physical conditions starts to become appreciable (*e.g.* the Taurus region presents a quite narrow and sharply peaked distribution with a deficit in brown dwarfs, see Luhman 2004).

We will try to give a small contribution to the present day debate regarding Initial Mass Function by trying to say something about the questions:

Is it possible to derive a unique Initial Mass Function for the whole cloud? Are there significant differences among IMFs of the clusters and of the diffuse population?

¹⁰Brown dwarfs are sub-stellar objects with a mass below that necessary to maintain hydrogen-burning nuclear fusion reactions in their cores. Brown dwarfs occupy the mass range between that of large gas giant planets and the lowest mass stars; this upper limit is between 75 and 80 Jupiter masses.

¹¹On the other hand, a lower limit on (sub-)stellar masses, theoretically derived (Low & Lynden-Bell 1976) still waits for an observational confirmation.

1.2.2 How the Initial Mass Function is linked to the dust core mass distribution?

Maybe, it will be easier, given the characteristics of the data analysed in this work, to answer other questions concerning the relationship between the IMF and the mass distribution of the dust and molecular cores, called CMF or core mass spectrum (see Chapter 2). Such relationship likely represents an important key to understand the origin of the stellar mass function, on the basis of the following arguments.

Large maps of molecular and dust emission have been acquired in the last decade, resulting in a large sample of cores, in several different environments, which permits to have an idea of the CMFs. Some caution, however, should be used when considering the CMF because of the possible biases and systematic effects, such as errors in the core mass estimates, incompleteness effects, sample constituted by partially collapsed or unbound, dispersing cores instead of only pre-protostellar cores (see Section 1.3.3), *i.e.* those cores which present the initial conditions for the collapse. Hence, a comparison between CMF and IMF is not always straightforward and has to take into account these effects. Nevertheless, CMFs found by using different methods, *e.g.* extinction maps to locate cores and estimate their mass, give similar results and some general CMF characteristics can be safely addressed.

- In the Salpeter regime (above one solar mass) CMFs are consistent with a power-law. Various estimates give values of the spectral index in the range: $\alpha = 0.8 \div 2.6$.
- Peak and turnover are found at about $0.2 \div 1 M_{\odot}$ (larger values are usually found for further clouds, but they are more affected by incompleteness).
- CMFs are almost rigidly (same factor for all masses) shifted towards higher masses, relative to IMF, by a factor of a few (values ranging from 3 to 8 can be found in literature, see, *e.g.* Alves et al. 2007 and Nutter & Ward-Thompson 2007).
- CMFs sometimes present shallower power-laws with respect to IMF.

- One case (Taurus cloud) has been found in which an unusual IMF (Luhman 2004) corresponds to an unusual CMF (Onishi et al. 2002).

These interesting properties of the CMF authorize some interpretations. The important mirroring of the universal IMF by the CMF suggests that the final star masses are determined already before collapse. Moreover, the rigid shift towards larger masses indicates that some process (*e.g.* stellar feedback from disk winds and outflows) reduces the star formation efficiency in a mass-independent way. The cases of shallower CMF power-laws compared with IMF are usually interpreted as an effect of a lower efficiency of more massive condensations in producing stars. Simulations of turbulent, self-gravitating flows (see, *e.g.*, Fig: 1.1) seem to reproduce the basic CMF characteristics, but unfortunately some results are still too much dependent on clump-finding algorithms, used to disentangle the cores (see discussion in Chapter 2), applied to the simulation results (McKee & Ostriker 2007). Additional complications arise, in the interpretation of the correspondence IMF-CMF, when considering that most of the stars are born in couple or in multiple systems. Therefore, there is not a trivial 1 to 1 relationship between cores and stars: The core mass will be distributed into more than one object; some stars are ejected early from multiple systems; binary systems are often destroyed within clusters (Goodwin et al. 2007).

Large statistics are needed to confirm, modify and/or clarify all the addressed points. In this context the Vela-D molecular and dust core distributions and their link with the observed young population could be helpful.

Which are the main features of the Vela-D core mass function? How the Initial Mass Function is linked to it?

1.3 What is the current stage of star formation?

Observationally, young stellar objects (YSO) can be classified according to their spectral energy distribution (SED), a plot of flux, brightness, or flux density versus frequency or wavelength. YSO SEDs usually display strong infrared excess emission due to the presence of dusty envelopes/disks around the sources (see also the description of the NIR

colour-colour diagram in Section 1.1.2). The circumstellar material is heated by the accretion process and radiation from the proto-star, and re-emits at longer wavelengths, in the infrared and submillimetre¹² spectral ranges. The spectral energy distribution, therefore, depends mostly on the properties of the envelope and can be used as an indicator of the evolutionary status of the source. Rising SEDs till long wavelengths, peaking in the FIR or sub-millimeter, are indicative of large amounts of circumstellar material and thus of very young sources. As the proto-star evolves, it frees itself of surrounding material (§ 1.3.4) and its SED changes shape, peaking at shorter and shorter wavelengths.

The main YSO classification scheme, first proposed by Lada (1987) and integrated by André et al. (1993), is based on the SED shape and is illustrated in Fig. 1.4. Four classes are defined: 0, I, II and III (André et al. 2000, see also McKee & Ostriker 2007). Objects of Class 0 and I (§ 1.3.1) are often referred to as proto-stellar objects, the others (§ 1.3.2) are said to be in the pre-main sequence phase. A further parameter often considered in classifying YSOs is the bolometric temperature, T_{bol} , *i.e.* the temperature of a blackbody whose spectrum has the same mean frequency as the observed spectral energy distribution of the object:

$$T_{bol} = 1.25 \frac{\langle \nu \rangle [GHz]}{100} [K]. \quad (1.3)$$

As the system evolves, the SED peaks at higher frequencies and T_{bol} increases, thus following the evolutionary sequence (Figure 1.4). Counts of sources at different evolutionary classes, together with an estimate for the age of one of the stages, allow one to infer lifetimes for all stages. Typical estimates for the ages are: $1 - 3 \cdot 10^4$, $1 - 2 \cdot 10^5$, 10^6 and 10^7 years, respectively (André et al. 2000).

In the following two Sub-sections we will present with more details both the observational characteristics and the theoretical interpretative scheme of the YSOs, from the beginning of the collapse to the main sequence.

1.3.1 What are the youngest objects?

- **Class 0 (main accretion phase):** Sources with a central proto-star

¹²The so called submillimeter spectral range spans the wavelength interval: 0.3-1 mm.

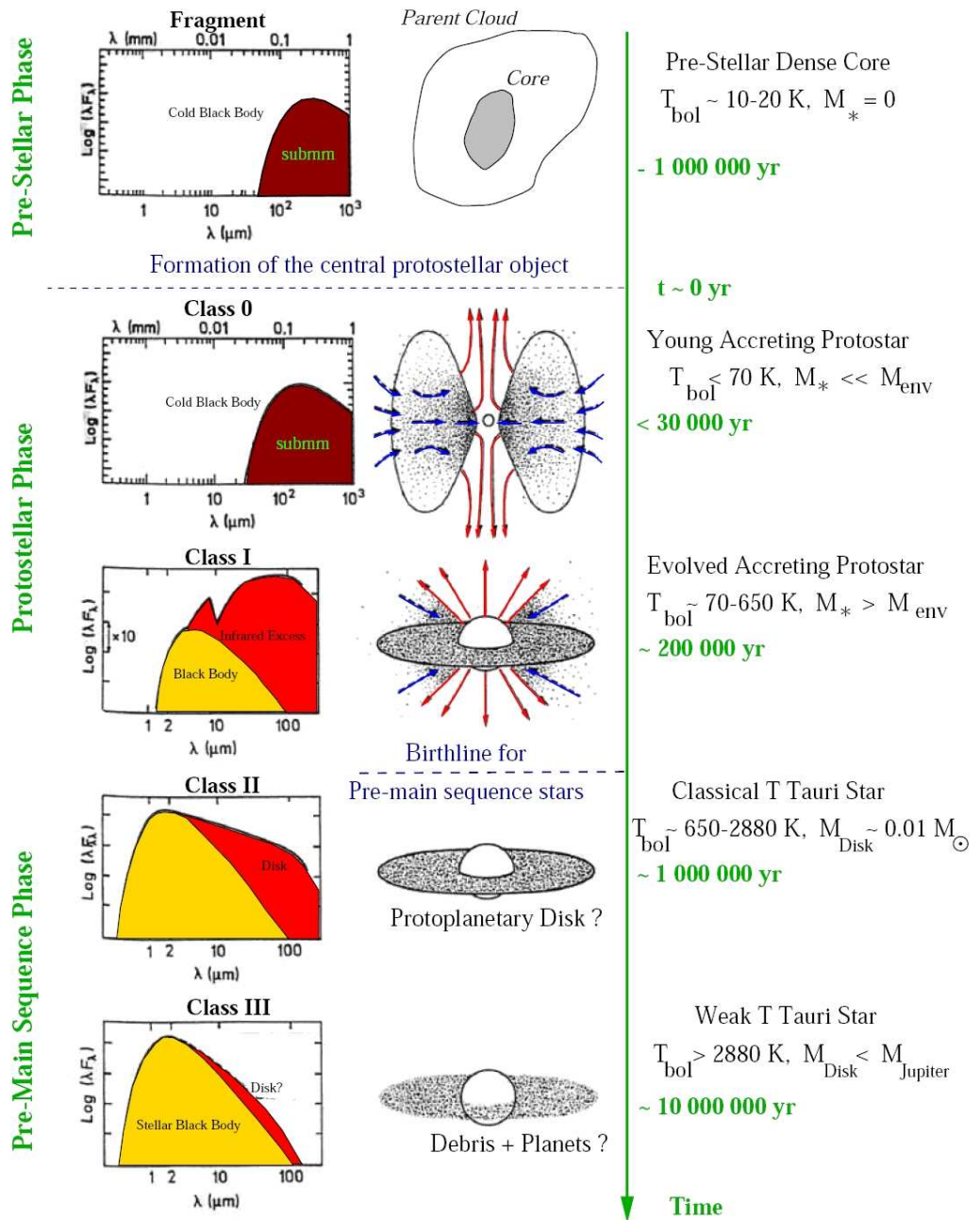


Figure 1.4: YSO classification scheme (see text).

that are extremely faint in the optical and NIR (*i.e.* undetectable at $\lambda < 10 \mu\text{m}$ with the technology of 1990s) and that have a significant submillimeter luminosity, $L_{\text{smm}}/L_{\text{bol}} > 0.5\%$. Sources with these properties have $M_{\text{envelope}} \gtrsim M_{\star}$. Proto-stars are believed to acquire a significant fraction, if not most, of their mass in this embedded phase.

Once the conditions for the collapse are met (see Section 1.3.3), accretion from the surrounding infalling gas leads to the formation of high density central cores and eventually to stars. According to the theory of low mass star formation (high mass theory still presents several unclear aspects), developed from the models originally proposed by Stahler et al. (1980), the central zones collapse more rapidly than the outer part (inside-out collapse). As a result, at the centre of the structure a core in hydrostatic equilibrium, the proto-star, is rapidly assembled, which accretes matter from the surrounding infalling envelope. In this phase, the luminosity of the object is believed to be dominated by the accretion process¹³. For typical values of $1 M_{\odot}$ and $4 R_{\odot}$ one obtains a luminosity of $50 L_{\odot}$: a proto-star is therefore much brighter than a main sequence star of equal mass.

The matter accreting onto the star from the envelope carries a given amount of angular momentum that eventually should be transferred to the central object. However, if all the angular momentum of the disk were transferred to the star, this latter should soon reach high rotational velocities which would prevent any further accretion due to the increasing centrifugal force at the stellar surface. Moreover, too high rotational velocities would actually lead to the disgregation of the star. Now, this is not observed in young sources, so that there must be a mechanism through which the excess angular momentum is removed from the system. As we shall see in Section 1.3.4, observations show that during the accretion process some of the material is ejected at high velocity away from the proto-star, in form of bipolar jets. The ejected matter, collimated and accelerated in a direction perpendicular to the

¹³Assuming a spherical geometry for the accretion, the luminosity emitted during the process is given by the conversion of gravitational energy:

$$L_{\text{acc}} = \frac{GM_{\star}\dot{M}_{\text{acc}}}{R_{\star}}, \quad (1.4)$$

where M_{\star} and R_{\star} refer to the mass and radius of the central condensation.

accretion disk, shocks (and excites) the surrounding ambient gas, also sweeping up the cloud material to form much larger molecular outflows (Richer et al. 2000).

Thus, while the envelope is progressively disrupted by the action of the jets and outflows, the star accretes matter exceeding the mass of the surrounding envelope. Observationally, the source evolves from the Class 0 to the Class I.

- **Class I (late accretion phase):** Sources with $\alpha_{IR} > 0$, where $\alpha_{IR} \equiv d\log(\lambda F_\lambda)/d\log\lambda$ (with F_λ , flux within each unit wavelength interval) is the slope of the SED over the wavelength range between $2.2 \mu\text{m}$ and $10\text{-}25 \mu\text{m}$ (see also Sections 3.3.1 and 3.3.4). Such sources are believed to be relatively evolved proto-stars with both circumstellar disks and envelopes.

Five regions can be defined in a proto-star during this phase: an hydrostatic nucleus of radius R_\star , an accretion disk ($R_\star < R < R_c$), an infalling, almost spherical, envelope in free fall towards the star ($R_c < R < R_{out}$), the outer envelope ($R_{inf} < R < R_{out}$) and the external molecular cloud ($R > R_{out}$). Typical values are 40 AU for R_c , 500 AU for R_{inf} and 15000 AU for R_{out} . Unfortunately, geometrical effects may significantly alter the shape of the SED, causing misclassification of the objects (*e.g.* White & Hillenbrand 2004): Class 0 sources whose envelope is flattened, owing to the presence of a large-scale magnetic field, or contains cavities created by protostellar jets, can appear as Class I sources.

In this work we will try to locate and classify the proto-stars by searching for signatures of outflowing activity in correspondence with dust-molecular condensations and by connecting the emitted fluxes at different wavelengths, from NIR to sub-millimeter, so to answer the questions:

What are the youngest objects? How old are they?

1.3.2 And what about the oldest ones?

Once the envelope has been dispersed, stellar radiation is no longer absorbed by the circumstellar dust and the star becomes visible at optical wavelengths.

- **Class II:** Sources with $-1.5 < \alpha_{IR} < 0$ are believed to be pre-main sequence stars with significant circumstellar disks.

Similarly to the distinction between Class 0 and Class I objects, confusion can also arise between Class I and Class II stars, depending on the inclination angle: Small or large inclination angles could make the central star either visible or obscured by the disk.

Accretion proceeds through the accretion disk but at a slower rate relative to the previous accretion phase: 10^{-8} against 10^{-5} - $10^{-6} M_{\odot} \text{ yr}^{-1}$ (*e.g.* Hartmann & Kenyon 1990). The contribution to the total luminosity due to the accretion is therefore negligible during this phase, and the object luminosity is dominated by the energy emitted by the stellar photosphere through conversion of gravitational energy¹⁴. Observed SEDs are consistent with a blackbody spectrum plus moderate IR excess emission coming from a disk.

Now that the star has become visible, it is placed in the Hertzsprung-Russel (HR) diagram along the so-called *birthline* (see Figure 1.5) that represents the locus where the stars that have entered the pre-main sequence phase first “appear” in the diagram¹⁵. The position of the birthline depends on the mass accretion rate during the protostellar phase. Assuming a value of $10^{-5} M_{\odot} \text{ yr}^{-1}$ the line intercepts the ZAMS (Zero Age Main Sequence¹⁶) for sources of $6 M_{\odot}$. Pre-main sequence stars are found in the diagram between these two lines, while their evolutionary tracks depend on their mass (see Fig. 1.2).

Stars with masses lower than $0.8 M_{\odot}$ are fully convective and move across the HR diagram along roughly vertical tracks (*Hayashi tracks*), reaching the ZAMS in positions corresponding to spectral types K and M in times of the order of 10^7 yr. More massive stars develop radiative cores and follow tracks that are basically horizontal. Such

¹⁴Pre-main sequence stars are in hydrostatic equilibrium and evolve toward the main sequence while slowly contracting on the Kelvin-Helmoltz time-scale:

$$\tau_{KH} \approx \frac{GM_{\star}^2}{L_{\star}R_{\star}} \quad (1.5)$$

The stellar luminosity is given by $L_{\star} = 4\pi R_{\star}^2 \sigma T_{\star}^4$, where T_{\star} is the photospheric temperature and σ the Stephan-Boltzmann constant.

¹⁵Since it is usually impossible to define an effective temperature for the proto-stars on the basis of their SEDs (which are dominated by strong infrared excesses), they cannot be placed in the HR diagram.

¹⁶Line on the HR diagram reached by a star when it begins hydrogen fusion.

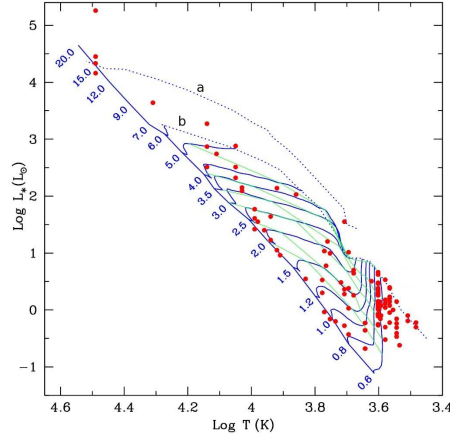


Figure 1.5: *HR diagram for a sample of pre-main sequence stars (AeBe Herbig stars and T-Tauri stars). Sources are indicated by points, while the left long, continuous line represents the ZAMS. Two birthlines are displayed (dotted lines), differing for the assumed value of the mass accretion rate: $10^{-4} M_{\odot} \text{ yr}^{-1}$ (a) and $10^{-5} M_{\odot} \text{ yr}^{-1}$ (b). The sources are found between the two lines, while following different evolutionary tracks depending on their mass (indicated in M_{\odot} along the ZAMS).*

objects, of mass around $1 M_{\odot}$, are usually called T Tauri stars, from the name of the prototype star in the Taurus star-forming region. For $M = 2M_{\odot}$ the free-fall time and the Kelvin-Helmoltz time become equal and therefore more massive stars should not display an observable pre-main sequence phase. However, at temperatures of the order 10^6 K , the energy produced by the fusion of the deuterium in the stellar core allows a partial stabilisation of the star, slowing down its contraction and consequently its “movement” toward the main sequence. As a result, stars up to $6 M_{\odot}$ (spectral types from F to late B) do show a pre-main sequence phase and are known as *Herbig AeBe* stars. For stars with masses larger than $6 M_{\odot}$ the Kelvin-Helmoltz time is so short that the hydrogen fusion is started when the main accretion phase is still running: the corresponding spectral types are O and early B.

- **Class III:** Sources with $\alpha_{IR} < -1.5$ are pre-main sequence stars that are no longer accreting significant amounts of matter.

As the evolution goes on, the amount of circumstellar matter becomes less and less significant: Class III sources are basically stars in proximity of the ZAMS with blackbody SEDs consistent with red-

dened stellar photospheres surrounded by residual debris disk inside which planet formation can take place.

The stars reach the main sequence when the temperatures at their core are high enough to permit the injection of the hydrogen fusion reactions ($T \sim 10^7$ K).

Observations in the infrared bands will permit us to derive, from the SEDs and with the help of colour-colour and colour-magnitude diagrams (see Chapter 3), the evolutionary stage of the most evolved young stellar objects. Contaminations by foreground/background (reddened, main-sequence) objects will be more difficult to disentangle and statistical approaches will be adopted too. Also the identification of Vela-D main sequence objects, even more confused among external objects, would furnish precious indications about the cloud age. Summarising, we are interested to clarify the issues:

What are the oldest objects clearly associable to the cloud? How old are they?

1.3.3 Is the star formation still in progress?

Gravitational contraction of molecular cores leads to the formation of stars. Getting a glimpse of the very beginning of the collapsing process is observationally very hard as well as theoretically fundamental.

Several *pre-stellar* (or *pre-protostellar*, e.g. Ward-Thompson et al. 1994) *core* candidates are known from literature concerning dust and molecular surveys. Maybe, only a few of them are really collapsing condensations still without a kernel in hydrostatic equilibrium (the proto-star) inside them. Many of them could be, more generically, *starless* cores, category that includes also quiescent or dispersing structures. Other are Class 0 objects whose central sources have not yet been found, how new FIR surveys (e.g. by means of the Spitzer Space Telescope, see Werner et al. 2004) have demonstrated discovering point sources missed by previous instruments (e.g. IRAS) inside pre-stellar core candidates (see Chapter 3). Multi-wavelength, high sensitivity and resolution observations permit to distinguish among these possibilities and a big effort of the astrophysical community is directed to this aim.

From the theoretical point of view, the importance of studying pre-stellar cores resides in the still relatively poor comprehension of how the various ingredients, recognized to be gravity, turbulence and magnetic field, compete and co-operate to start, slow down or stop the

collapse, with important consequences on estimates of star formation efficiency, time scales, triggering phenomena and so on.

In the classical theory, proposed by Jeans in the beginning of the twentieth century, collapse takes place when the gravitational energy of the core (E_g) exceeds its thermal energy (E_{th}), so that thermal pressure is no longer sufficient to contrast self-gravity. For a spherical homogeneous core with radius, temperature, density and numerical density R , T , ρ and n , respectively, this condition translates into the equation:

$$|E_g| = \frac{3}{5} \frac{GM^2}{R} > \frac{3}{2} \frac{MkT}{\mu m_H} = E_{th}, \quad (1.6)$$

with G gravitational constant, k Boltzmann constant, μ mean molecular weight, and m_H mass of the hydrogen atom, which gives the Jeans mass as a lower limit for the collapse:

$$M > M_J \equiv \left(\frac{3}{4\pi\rho} \right)^{1/2} \left(\frac{5kT}{2G\mu m_H} \right)^{1/2} = 6M_\odot T^{3/2} n^{-1/2}. \quad (1.7)$$

The characteristic time scale of the collapse will be the free-fall time:

$$\tau_{ff} = \left(\frac{3\pi}{32G\rho} \right)^{1/2} = 1.4 \cdot 10^6 \left(\frac{n[cm^{-3}]}{10^3} \right) [yr]. \quad (1.8)$$

The main problem of this approach is the huge star formation rate predicted: 250-300 $M_\odot \text{ yr}^{-1}$ against the $\sim 2\text{-}3 M_\odot \text{ yr}^{-1}$ inferred from observations (*e.g.* Zuckerman & Evans 1974, see also discussion in Section 1.1.3). Actually, Jeans criterion provides only a necessary and not sufficient condition to have an unavoidable collapse. Other mechanisms must therefore play a rôle during the collapse, capable of hampering and slowing down the gravitational contraction.

While rotation seems to be ineffective in halting the collapse (Goodman et al. 1993), magnetic fields and turbulence are the best candidates. Magnetic fields in molecular clouds present values usually smaller than 10 μG ; inside the cores, fields are generally more intense, with values in the range 10-50 μG (*e.g.* Heiles et al. 1993). The presence of these magnetic fields provides support against gravitational collapse. In fact, given the extremely low temperatures of the medium, the ions present in the cloud gas tend to remain coupled to the magnetic field lines, colliding with the neutrals that drift across them in a process called *ambipolar diffusion* (*e.g.* Mestel & Spitzer 1956). The friction generated by the collisions between ions and neutrals causes the collapse

to proceed at a slower rate. The ambipolar diffusion process is at the basis of the so-called standard theory of isolated star formation, according to which a core contracts in a time-scale that depends on the efficiency of the dynamical coupling between ions and neutrals. This is proportional to the degree of ionisation of the medium, χ , *i.e.* the number of ions over the number of neutral particles. The ambipolar diffusion time τ_{AD} is given by:

$$\tau_{AD} = 5 \cdot 10^{13} \chi. \quad (1.9)$$

In molecular cores $\chi = 10^{-7}$ (Caselli et al. 1998); hence, τ_{AD} is of order $5 \cdot 10^6$ yr, longer than the free-fall time τ_{ff} which is of order 10^5 yr. This theory also implies that ambipolar diffusion is less efficient within regions of higher extinction, where far ultra-violet ionizing photons permeating the Galaxy can not easily penetrate, as confirmed by observations. All regions hosting star formation, in fact, seem to possess extinction values above a threshold of $A_V \sim 2 \div 4$ mag. Nevertheless, during the last decade the standard theory has seemed to fail on certain fronts, although the debate is still ongoing. One of the mismatches is the $1/r^2$ profile predicted for the density structures in starless cores, in disagreement with observed flat profiles (Andre et al. 2000). Moreover, a high fraction of cores which contain embedded protostellar objects is observed: if cores evolved on ambipolar diffusion time-scales we would expect to find a significantly larger number of starless cores (Beichman et al. 1986).

These problems have recently led to the development of various models in which supersonic turbulence is seen as the main process controlling star formation. There is ample observational evidence that molecular clouds contain random supersonic motions: the molecular line widths indicate indeed velocity dispersions (46 km s^{-1}) that cannot be accounted for unless considering the existence of non thermal motions (*e.g.* Munoz-Tunon et al. 1995; Zuckerman & Palmer 1974). Because of the lack of a consistent theory for turbulence in compressible gas, most progress has been achieved via three dimensional computer simulations (*e.g.* Pavlovski 2004) that demonstrate how supersonic turbulence can provide global support to the clouds against gravitational collapse, increasing their lifetime by a few τ_{ff} . On the other hand, turbulence also allows local collapse through the formation of density enhancements, resulting in gravitationally unstable clumps which con-

tract and decouple from the turbulent flow. Turbulence decays quickly if there was no recurring injection of energy for driving the large scale turbulent motions and several mechanisms have been considered, that may concur in supplying the driving energy to maintain turbulence as quickly as it decays: galactic rotation and shear, protostellar outflows, expansion of Hii regions, MHD waves¹⁷ propagation and, in particular, supernova explosions (§ 1.1.4).

From this the importance of observing dust-molecular cores in a very early phase of their evolution, before a central objects could produce significant feedback on the environment (by means of internal heating and outflowing activity). In this work we will try to root out the Vela-D pre-stellar cores, if any. These would attest the very on-going star formation.

How many starless cores can be found in Vela-D? Are they genuine pre-stellar cores? Which are their characteristics?

1.3.4 What is the rôle played by mass-loss phenomena?

As we have seen in Section 1.3.1, mass loss phenomena through gas jets travelling at supersonic speed are always associated with the protostellar phases of the star formation. The analysis of the radiation emitted in the collision between these jets and the protostellar envelopes provides precious indications on both the mechanism originating the ejections and the nature/evolutionary stage of the emitting sources, which are enclosed in regions too much cold, spatially very small (~ 100 AU) and obscured to be directly observable.

Ejection of a fraction of the collapsing envelope is needed to transfer angular momentum in excess out of the accreting material, making the collapse possible onto the central object, otherwise prevented by centrifugal forces. During the first phase (Class 0 objects), jets usually possess high velocities and collimation, defined as the ratio between jet length and width, but become less and less collimated and gain more and more material from the ISM, producing large molecular lobes, the *outflows*. The gas swept up in the outflows is not gravitationally bound, given that, for typical flow velocities of 10 km s^{-1} and sizes of a

¹⁷Magneto-Hydro-Dynamical (MHD) plasma theory deals with a compressible, conducting fluid immersed in a magnetic field. The wave modes derived using this theory are called *magnetohydrodynamic* or MHD waves.

few tenth of a parsec, the required mass to bind the gas (about $10^4 M_{\odot}$) exceeds by far the clump typical mass (Wouterloot & Brand 1999). Thus, by means of this activity, the gas and dust envelopes of the proto-stars is gradually dispersed, until the accretion process stops.

Ejected material impacts the cold and slow cloud gas at supersonic speed (~ 50 - 100 km s^{-1}), deeply modifying both its composition and its physical conditions. Shock waves are produced, gas is compressed, heated and accelerated, dust grains are destroyed, molecules and atoms are dissociated and ionized. The gas de-excitation returns the accumulated thermal energy by means of atomic and molecular emission lines that allow us to observationally identify the shock surfaces.

There exist two shock types (Draine 1980). When magnetic field is high and ionization degree small ($\chi \ll 10^{-6}$), there is a *C(continuous)-shock*, without dissociation and with density and temperature increasing in a continuous way. This happens because the ionic jet components are faster than the neutral ones¹⁸ and generate a first wave front that collisionally begins heating and accelerating the ISM. Usually, temperatures are less than 3000 K, impact speeds less than 50 km s^{-1} and no dissociation of the H_2 molecules occurs. The gas cooling after the shock is dominated, in the NIR, by molecular emission, especially ro-vibrational H_2 lines, or by atomic and weakly ionized species, while in the FIR purely rotational transitions of CO, OH and H_2O are observed.

The other shock type, the *J(jump)-shock*, occurs when magnetic field is negligible or the ionization degree is greater than 10^{-6} : the ISM is not forewarned and undergoes a sudden increase of temperature (to $\sim 10^5 \text{ K}$), density and velocity (to $50 \div 100 \text{ km s}^{-1}$); H_2 is dissociated, dust grains are destroyed and their components (iron, sulfur, nitrogen, carbon and oxygen), as well as the atomic hydrogen, are ionized. The gas cooling goes through three different steps (see Figure 1.6): Collisional dissociation and ionization produce UV radiation, UV photo-ionization followed by recombination originates optical emission (*e.g.* Lyman lines), molecular formation is evidenced by IR emission.

The cartoon in Figure 1.7 can give an idea of the jets/outflows

¹⁸The perturbations of the magnetic field propagate at Alfvén speed $v_A = B/\sqrt{4\pi n}$, with B magnetic field magnitude and n density. If the medium is partially ionized, the ionic component of the perturbation travels at a speed $v_{A(ion)} = (n/n_{ion}) \cdot v_A$ that, for small values of ionic density n_i is greater than the shock propagation speed.

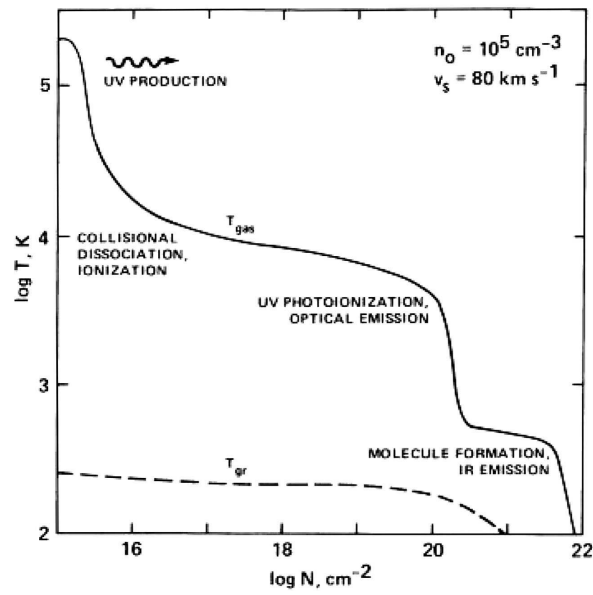


Figure 1.6: *Temperature after the J-shock crossing as a function of the hydrogen column density (density integrated along the line of sight). The gas cooling goes through three different steps (see Figure 1.6): Collisional dissociation and ionization produce UV radiation, UV photo-ionization followed by recombination originates optical emission (e.g. Lyman lines), molecular formation is evidenced by IR emission.*

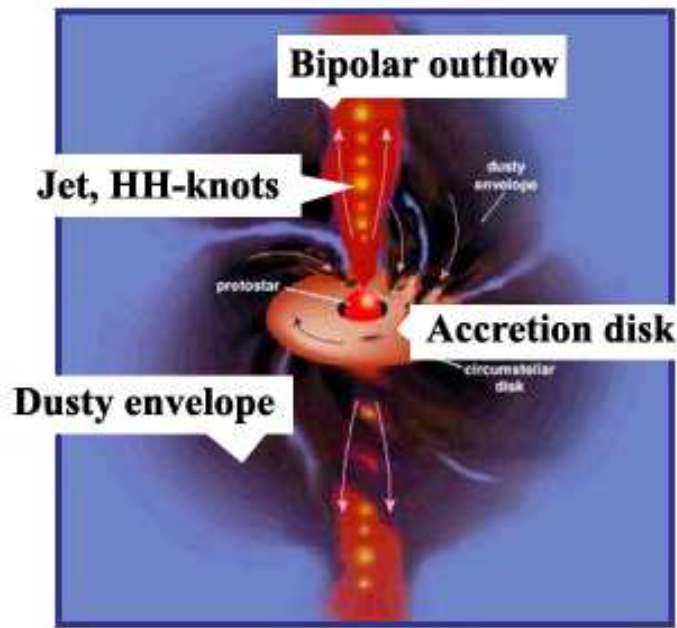


Figure 1.7: *Sketch of outflowing material from a proto-star.*

morphology. The various components possess very different speed, collimation, sizes, time scales of variability, energies and emission lines. Nevertheless, we can distinguish (Bachiller 1996):

- A molecular component (the *outflow*), evidenced by the millimeter CO emission, constituted by two big lobes at the proto-star magnetic poles with a shell-like structure enclosing a cavity. These lobes possess speeds of tens of kilometers per seconds or less and can reach sizes of up to 10 pc.
- Jets with optical (the *Herbig-Haro* objects) and IR emissions. These are small nebulosities (*knots*) escaping from the proto-stellar source at speeds of some hundreds of kilometers per second. Their spectra are rich of emission lines of hydrogen, H_2 and of forbidden lines¹⁹ ([OI], [CI], [NI], [NII], [SII], [SIII]).

¹⁹Forbidden lines are spectral lines emitted by atoms undergoing energy transitions not normally allowed by the selection rules of quantum mechanics. They have only been observed in extremely low-density gases and plasmas where the ion is left undisturbed by collisions (which could change the state of the ion). These lines (indicated by square brackets) may contribute significantly to the light observed from a nebula.

In Chapters 3 and 4 we will encounter various cases of outflowing activity, evidenced by the molecular components observed in the emission of both H₂, tracer of the shock surfaces (§ 4.1.1), and the CO (§ 4.1.2), tracer of the large scale outflows. The information obtained by this analysis will allow us to locate some of the youngest objects in the cloud, to infer their evolutionary stage, to evaluate the physical conditions of the outflowing material (by means of estimates of mass, momentum, kinetic energy carried out). More in general, we are interested in evaluating the outflow impact on the envelopes physical conditions. Thus, we can formulate our question:

What is the rôle played by mass-loss phenomena in the physics of the Vela-D protostellar cores?

Chapter 2

Gas and Dust large-scale emission

In this Chapter we present the Vela-D maps of both molecular, $^{12}\text{CO}(1-0)$ and $^{13}\text{CO}(2-1)$ radio lines¹, and dust continuum emission, at 1.2 mm, observed with the SEST telescope (ESO-La Silla, Chile). The content of this Chapter mostly consists of an organic description of the work published in two dedicated papers (Elia et al. 2007 and Massi et al. 2007) to give a coherent, global picture of the large scale cloud structure. The presented maps, in fact, allow us to trace the distribution of the interstellar medium and to find out the densest regions, those mainly involved in the star-forming process.

Molecular observations reveal, over a wide range of spatial scales (from ~ 0.1 to a few parsecs), a variety of dense structures such as arcs, filaments and clumps, that are in many cases associated with FIR point-like sources, recognized as young stellar objects and embedded star clusters (point sources will be discussed in more details in the next Chapter). Radio line data (§ 2.1.2) furnish also precious information about gas radial velocity. In our case, the velocity field analysis highlights the presence of possible expanding shells, extending over several parsecs, probably related to the star-forming activity of the cloud. Furthermore, the analysis of the line shapes in the vicinity of the FIR sources suggests the occurrence of molecular outflows (the most interesting cases will be discussed in Chapter 4).

¹The preceding numbers refer to the considered isotope ($^{12}\text{C}^{16}\text{O}$, would be more precise), while the numbers in parenthesis represent the initial and final values of the rotational quantum number J of the considered transition.

A parallel analysis has been performed on both molecular and dust maps, the so called *cloud decomposition*, consisting in the operative separation of the emitting regions into spatially defined entities, called *clumps* (for the molecular emission) and *cores* (for the dust), associated to the emission peaks (see Sections 1.1.1 and 1.1.2 for the definition of clumps and cores). The mass distribution of the obtained clumps and cores constitutes an important parameter for the characterization of the cloud morphology.

Particularly interesting from our point of view is the list of the dust cores, the densest regions of the whole cloud, inside which star formation occurs. We have found cores both clustered (maybe star cluster-forming) and isolated, which could represent young stellar objects in early evolutionary phases (see next Chapter for a detailed analysis of the core stellar population).

This Chapter consists of two parts concerning the description of data, analysis and results, respectively for the molecular and the dust maps.

2.1 Molecular emission

2.1.1 CO data

As we have seen in the first Chapter, the most important tracer of the cloud molecular component is the CO molecule, whose first rotational levels can be easily excited (by collisions with H₂ molecules) even at the low temperatures found in the quiescent cloud gas² and whose permanent dipole moment allows it to radiate copiously at radio frequencies. The ability of CO in mapping large scale molecular emission from clouds, rather than the dense cores inside them, is strictly linked to the concept of *critical density* ($n_{crit} \equiv A_{ul}/\gamma_{ul}$), the ratio between the probability per time of spontaneous decay from level u to level l and of collisional de-excitation (between the same levels). This quantity, of the order 10^3 cm^{-3} for CO(1-0), is, in fact, an estimate of the density

²The energy of the rotational levels is given by: $E_{rot} = (\hbar^2/2I)J(J+1)$, where I is the moment of inertia and J the rotational quantum number. Thanks to the greater moment of inertia with respect to the H₂ molecule, the levels are more closely spaced and the $J=1$ state is elevated above the ground state in ¹²C¹⁶O by only $4.8 \cdot 10^{-4} \text{ eV}$, corresponding to a temperature of 5.5 K.

conditions at which the considered transition reaches the maximum efficiency³.

The most abundant isotope, $^{12}\text{C}^{16}\text{O}$ (hereinafter ^{12}CO), is the easiest to detect, but also $^{13}\text{C}^{16}\text{O}$ (hereinafter ^{13}CO), $^{12}\text{C}^{18}\text{O}$ and other isotopes are usually observed. The effectiveness of various isotopes in tracing molecular emission at different physical conditions depends on the *optical thickness*, τ , of the cloud, which gives the probability for a photon to be absorbed while crossing the cloud (see Section 4.2.1 for more details). Such probability is higher for more abundant isotopes ($^{12}\text{C}^{16}\text{O}$, in this case), whose lines are more optically thick and easily saturated. This roughly means that the cloud radiates from its surface like a blackbody. On the contrary, for the optically thin lines of less abundant isotopes, every molecule along the line of sight contributes to the emission, so that the integrated line intensity is proportional to the *column density* (volume density integrated along the line of sight, § 4.2.2) of such isotope, and denser regions can be traced with more accuracy. On the other hand, the combined observation of ^{12}CO and ^{13}CO lines, assumed a given isotopic ratio, furnishes important information about the optical thickness of the cloud, which plays an important rôle in the mass estimates (*e.g.* Equations 4.20 and 4.21).

Figure 2.1 shows the typical aspect of radio line maps. One spectrum is plotted for each observed offset position (α_{off} , δ_{off}) following radio astronomical convention (*e.g.* Stahler & Palla 2005). Instead of the specific intensity I_ν , the dependent variable is a proportional quantity known as the *antenna temperature* T_A , that is defined as:

$$T_A \equiv \eta \frac{\Omega_S}{\Omega_A} T_B, \quad (2.1)$$

where the beam efficiency η accounts for such factors as the losses in the system's optics, Ω_S and Ω_A are, respectively, the solid angles subtended by the source and the telescope beam⁴ and T_B (or T_{mb} , main beam temperature) is the brightness temperature defined by (4.7). Also the independent variable is not the frequency itself, but rather the radial gas velocity along the line of sight. This is the velocity that would, through the Doppler effect, shift the line-center frequency ν_0 into ν .

³At densities higher than n_{crit} the de-excitation is mainly collisional, without emission of photons, while lower densities do not allow the upper level to be populated enough.

⁴The ratio between solid angles is known as the *beam dilution factor*.

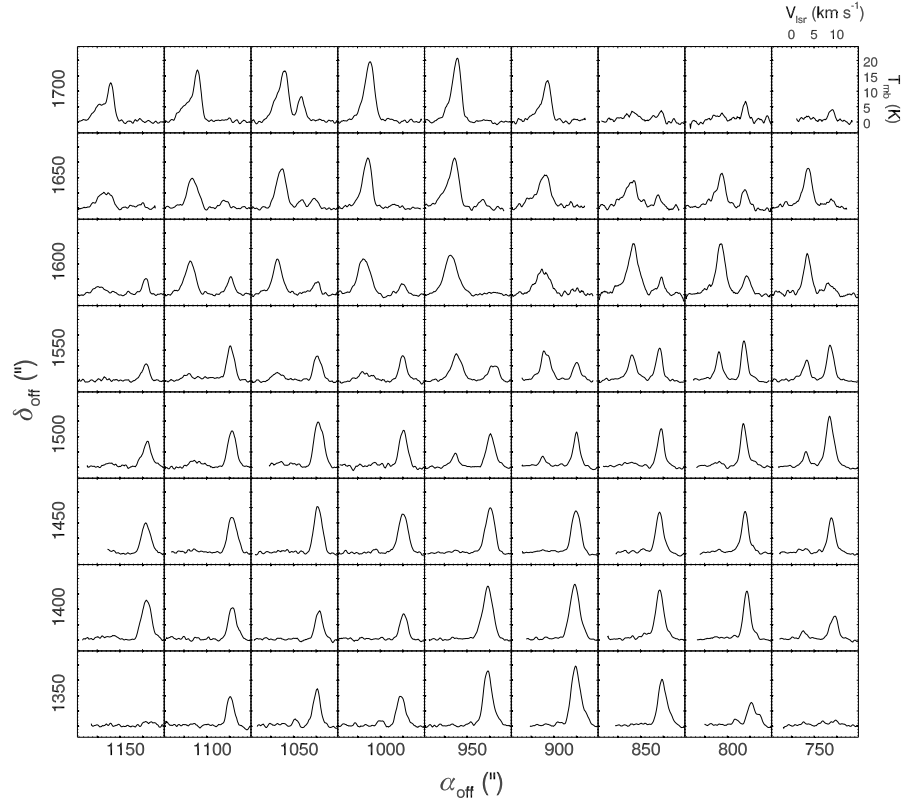


Figure 2.1: *Typical line profiles. This sample illustrates the part of the map corresponding to the offset interval $+750'' \leq \alpha_{off} \leq +1150''$, $+1350'' \leq \delta_{off} \leq +1700''$.*

Thus, V_{lsr} is given by $c(\nu - \nu_0)/\nu_0$ and a positive velocity corresponds to a red-shifted line. The subscript “*lsr*” stands for *local standard rest*, the reference system at which the cloud is at rest, on average. V_{lsr} is then the radial velocity of such system with respect to the observer.

Vela-D was mapped by our group (Elia et al. 2007) in the $^{12}\text{CO}(1-0)$ ($\nu = 115.271$ GHz) and $^{13}\text{CO}(2-1)$ ($\nu = 220.399$ GHz)⁵ lines with the 15-m Swedish-ESO telescope (SEST, see Booth et al. 1989) at La Silla, Chile, during two complementary observational campaigns, in September 1999 and January 2003, respectively⁶.

The chosen instrumental configuration allowed us to use both receivers simultaneously. For each receiver the acquired spectrum con-

⁵This line has been preferred to the $^{13}\text{CO}(1-0)$ line because it could be acquired simultaneously to the $^{12}\text{CO}(1-0)$.

⁶During the 1999 run only, the 230 GHz receiver was tuned to the frequency of $^{13}\text{CO}(2-1)$ and the corresponding mapped area is then smaller than in the $^{12}\text{CO}(1-0)$ line.

sists of 1000 frequency values (hereinafter channels). This, translated in velocity units, corresponds to a resolution of $\sim 0.12 \text{ km s}^{-1}$ at 115 GHz and $\sim 0.06 \text{ km s}^{-1}$ at 220 GHz. The half power beam widths (HPBW), *i.e.* the solid angles corresponding to the full width at half maximum of the receiver efficiencies, are $45''$ and $23''$ at 115 GHz and 220 GHz, respectively.

Due to the large size of the cloud, we adopted a grid spacing of $50''$, so that the $^{12}\text{CO}(1-0)$ is slightly under-sampled while the $^{13}\text{CO}(2-1)$ is under-sampled by a factor of two. At the estimated distance $d = 700 \text{ pc}$, this spacing corresponds to a spatial scale of 0.17 pc on the cloud. The coordinates of the (0,0) position in the maps are $\alpha(2000) = 8^{\text{h}}48^{\text{m}}40^{\text{s}}$, $\delta(2000) = -43^{\circ}46'12''$, and the pointings range from $\alpha_{\text{off}} = -2000''$ to $\alpha_{\text{off}} = +1200''$ in right ascension and from $\delta_{\text{off}} = -2000''$ to $\delta_{\text{off}} = +1950''$ in declination.

The integration time at each point was generally set to $t_{\text{int}} = 10 \text{ s}$, but there is a significant fraction of spectra observed with $t_{\text{int}} = 20 \text{ s}$. The typical rms noise affecting the data (in terms of the main beam temperature) is $\Delta T_{\text{rms}} \sim 0.7 \text{ K}$ for both lines.

Towards many pointings, the observations were repeated on different dates in order to check the data for consistency. In particular, the matching between 1999 and 2003 spectra was fully satisfactory (differences between peak temperatures are always within 10%), except for a raster of points located at south-east of the map, in the $+250'' \leq \alpha_{\text{off}} \leq +950''$, $-2000'' \leq \delta_{\text{off}} \leq -1050''$ region, which were affected by temporary instrumental problems, and then partially re-observed on subsequent dates. The reader should then be aware that in the region $+250'' \leq \alpha_{\text{off}} \leq +950''$, $-2000'' \leq \delta_{\text{off}} \leq -1700''$, these repeated pointings are not available, so this part of the map is less accurate. The pointing accuracy was checked every 2-3 hours towards nearby (in the sky) SiO masers⁷ being within $\sim 5''$.

Data reduction followed the pipeline described in [Massi et al. \(1997\)](#): first, spectra in antenna temperature were scaled by the main beam

⁷Astrophysical masers (Microwave Amplification by Stimulated Emission of Radiation), are intense line sources produced within molecular clouds thanks to population inversion of some molecules (H_2O , OH, CH_3OH , CH_2O and SiO). The particular physical conditions required to produce such population inversion (*e.g.* high density) make them important tracers of high mass star formation. In this case, these sources are simply used as calibrators, given their intense radio line emission.

efficiency factor η , in order to express them in terms of main beam temperature (Equation 2.1); then a polynomial fit of the baseline was subtracted and a folding was performed on the resulting spectra. Finally, spectra have been resampled to a velocity resolution of 0.12 km s^{-1} for the $^{12}\text{CO}(1-0)$, and 0.06 km s^{-1} for the $^{13}\text{CO}(2-1)$, respectively.

In the cases of spatial superposition of repeated observations, the corresponding spectra have been averaged (with weights depending on the integration time and the inverse of the system temperature), in order to obtain a better signal-to-noise ratio for the resulting spectrum.

2.1.2 CO maps and velocity structures

Out of the 4258 observed points, significant $^{12}\text{CO}(1-0)$ emission was detected from 3392 of them, corresponding to a detection rate of $\sim 80\%$. In Figure 2.1, a sample of reduced $^{12}\text{CO}(1-0)$ spectra, taken towards the north-western region of our Vela-D map, is shown. Despite this part of the grid is relatively small, it is representative of the velocity field complexity that characterizes this cloud. In the case of the $^{13}\text{CO}(2-1)$ line the points showing significant emission at our sensitivity level are 648 out of 2393 ($\sim 27\%$).

The bulk of the emission falls in the range $V_{lsr} = -2 \div 20 \text{ km s}^{-1}$ for the $^{12}\text{CO}(1-0)$ line and $V_{lsr} = 0 \div 14 \text{ km s}^{-1}$ for the $^{13}\text{CO}(2-1)$ line consistently with Wouterloot & Brand (1999) and Yamaguchi et al. (1999). The total intensity of the $^{12}\text{CO}(1-0)$ and $^{13}\text{CO}(2-1)$ emission, i.e. $\int T_{mb} dv$ integrated from -2 to 20 km s^{-1} , are represented in grey-scale in Figure 2.2 and Figure 2.3, respectively.

The $^{12}\text{CO}(1-0)$ map in Figure 2.2 evidences a complex clumpy and filamentary structure where intense peaks are connected by large lanes of enhanced emission relative to a diffuse component present all over the map, with the only exceptions of the South-West and East cavities void of molecular material. The analysis of the velocity components, based on the channel maps (Figures 2.5 and 2.6) and the velocity-position diagrams (Figure 2.7), helps us in separating the various emitting regions. Here we limit ourselves to sketch the main characteristics of the cloud shape (see Figure 2.4), using the locations of the bright FIR sources in the field reported in Table 2.1 as reference points; the characteristics and relevance of these sources for the star formation, as signposts of possible star-forming sites, will be extensively discussed in the next

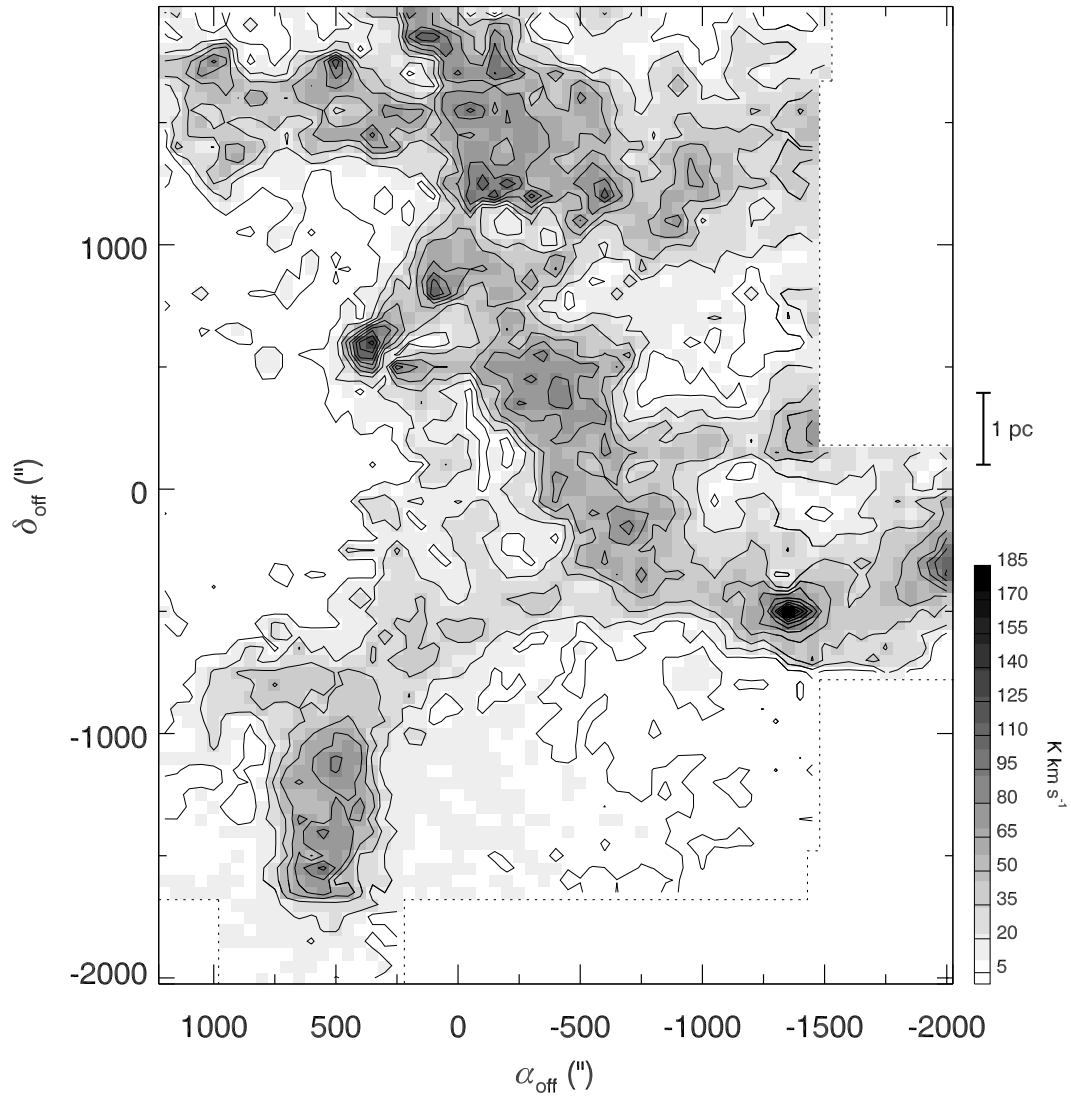


Figure 2.2: *Integrated intensity map for the $^{12}\text{CO}(1-0)$ emission in Vela-D region, in the range $-2 \div 20 \text{ km s}^{-1}$. Contour levels start from 5 K km s^{-1} and are separated by 15 K km s^{-1} . Dashed lines delimit the observed area. On the right, the spatial angular scale corresponding to the estimated distance ($d = 700 \text{ pc}$) is shown.*

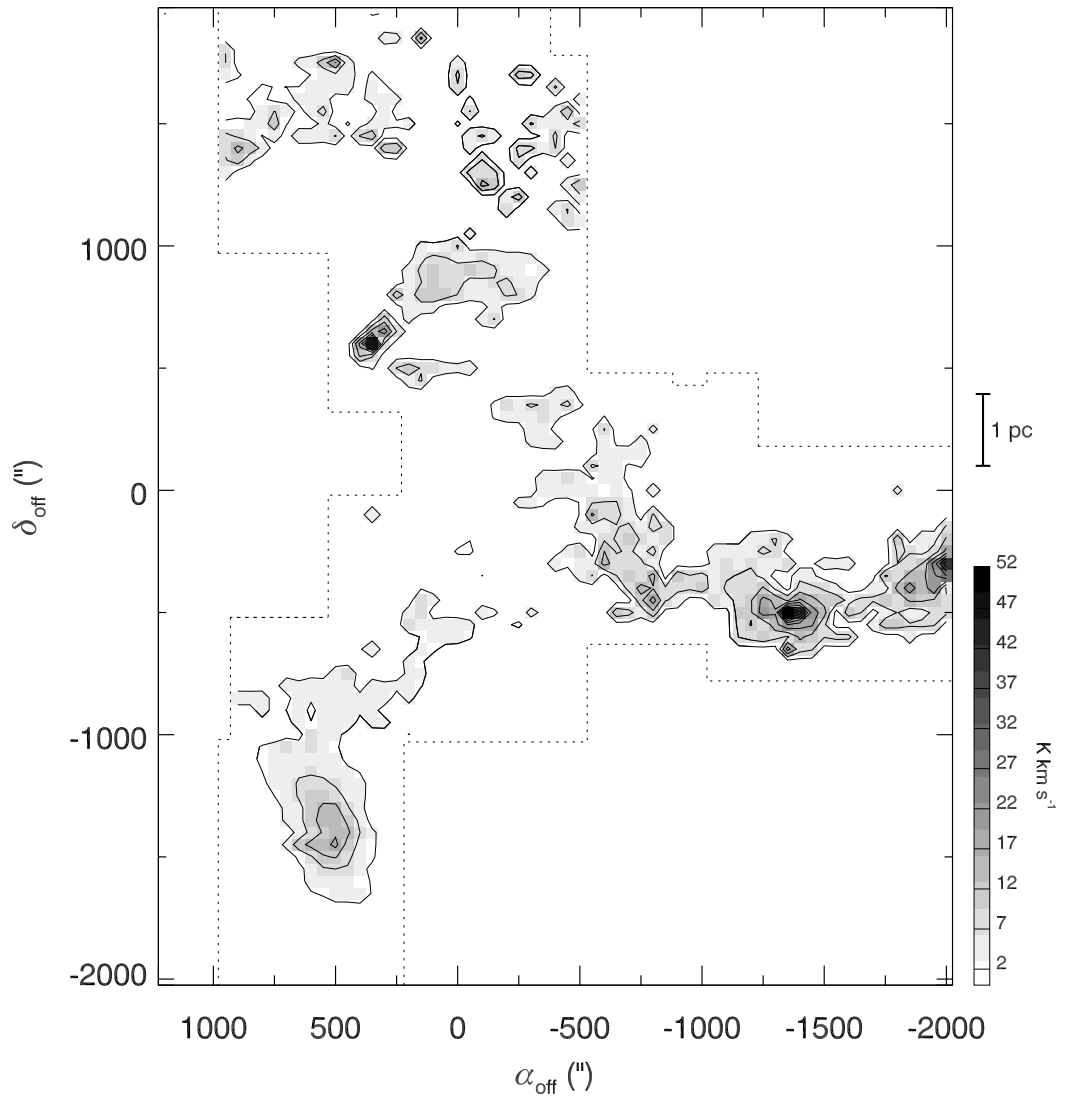


Figure 2.3: As in Figure 2.2, but for the $^{13}\text{CO}(2-1)$ emission. Contour levels start from 2 K km s^{-1} and are separated by 5 K km s^{-1} .

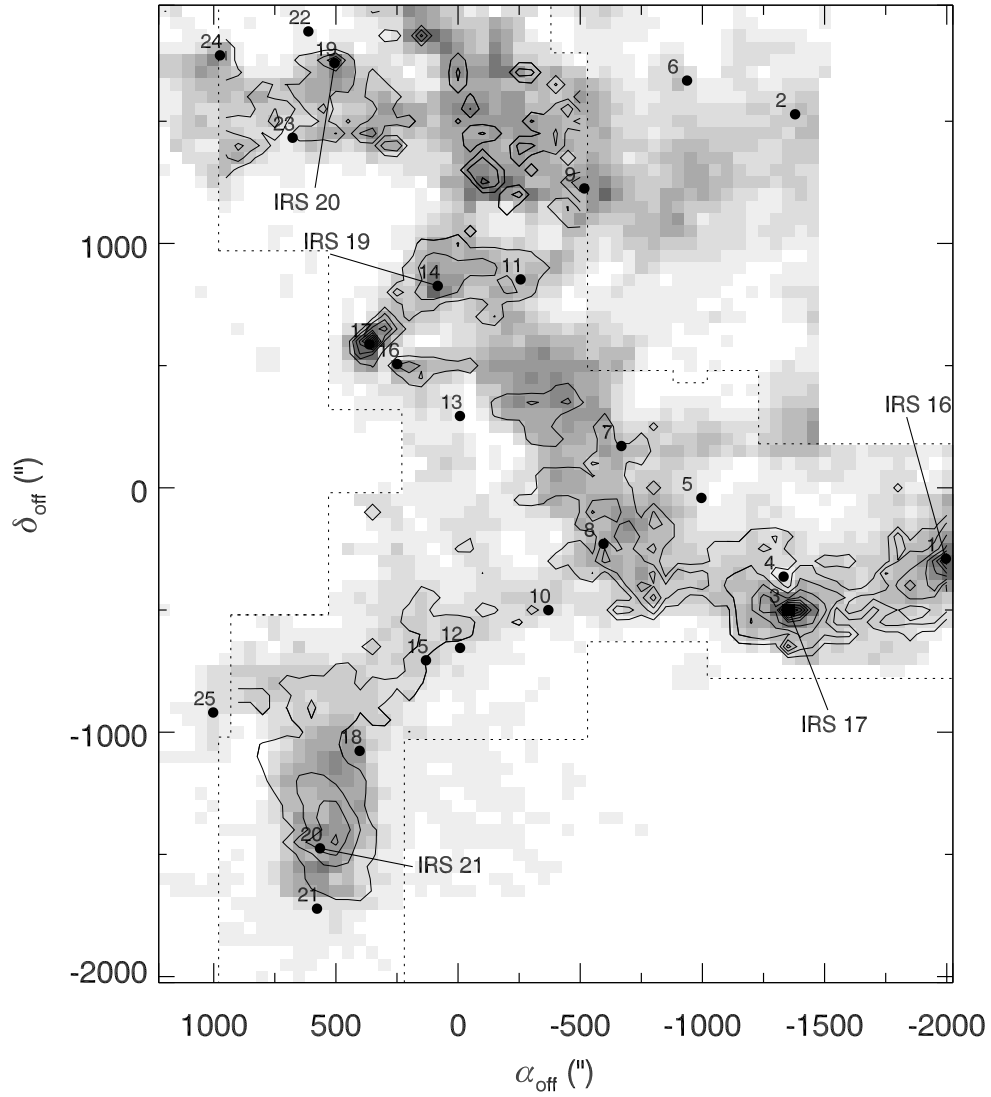


Figure 2.4: Superposition of the $^{13}\text{CO}(2-1)$ contour levels (shown in Figure 2.3) on the $^{12}\text{CO}(1-0)$ integrated intensity map (shown in Figure 2.2). The positions of the “red” ($F_{12} < F_{25} < F_{60}$) IRAS sources are also marked with filled circles.

Chapter.

- A large region in the northern part ($-1500'' \leq \alpha_{off} \leq +1200''$, $+1100'' \leq \delta_{off} \leq +1950''$) characterized by a strong, distributed emission. The coincidence between the position of IRS 20 and the most intense peak in this part of the map is evident.
- A central NE-SW region ($-2000'' \leq \alpha_{off} \leq +500''$, $-750'' \leq \delta_{off} \leq +1000''$) approximately elongated from the location of IRS 19, associated with a bright peak of integrated emission, to that of IRS 17 (the strongest peak in the whole map) and IRS 16, at the western boundary. This emitting region separate three zones, east, west, and south of it, respectively, characterized by an evident lack of emission and determining an arc-like appearance for the gas.
- An apparently compact structure in the south-eastern part of the map ($-250'' \leq \alpha_{off} \leq +1050''$, $-1800'' \leq \delta_{off} \leq -800''$), hosting IRS 21. This region contributes also to form the southern arc of molecular gas.

The distribution of $^{13}\text{CO}(2-1)$ emission closely follows that of the more intense $^{12}\text{CO}(1-0)$, as can be easily seen in Figure 2.3 and especially in Figure 2.4, in which, to highlight the correlation between the emission of the two lines, we superimpose the levels of the latter on the grey-scale map of the former. The $^{13}\text{CO}(2-1)$ (less abundant than $^{12}\text{CO}(1-0)$) traces the densest parts of the $^{12}\text{CO}(1-0)$ map, and its peaks coincide with those of the $^{12}\text{CO}(1-0)$, except for the main peak in the south-eastern region. The northern region of the map is characterized by a number of isolated peaks, some of which are also recognizable in the $^{12}\text{CO}(1-0)$ map.

Table 2.1: IRAS *PSC* sources in the observed field, with fluxes increasing from $12\ \mu\text{m}$ to $60\ \mu\text{m}$.

	<i>IRAS</i> ^{a,b} name	F_{12} (Jy)	F_{25} (Jy)	F_{60} (Jy)	F_{100} (Jy)
1	08438-4340 (IRS 16)	13.4	56	638	1580
2	08447-4309	< 0.25	< 0.4	< 4.4	36
3	08448-4343 (IRS 17)	8.7	88	327	1010
4	08448-4341	1.3	6.7	< 327	< 1010
5	08453-4335	< 0.34	0.59	< 6.4	< 49
6	08454-4307	< 0.25	0.36	< 3.3	< 39
7	08458-4332	1.1	2.7	18	53
8	08459-4338	< 0.29	0.57	6.5	38
9	08461-4314	0.69	0.79	5.9	< 49
10	08463-4343	< 0.29	0.49	7.4	< 44
11	08465-4320	< 0.25	< 1.1	< 3.5	30
12	08468-4345	0.39	< 0.87	< 4.8	< 36
13	08468-4330	< 0.3	0.43	3.4	< 32
14	08470-4321 (IRS 19)	45	130	343	407
15	08471-4346	< 0.28	< 0.5	5.4	36
16	08472-4326A	0.85	0.94	11	< 407
17	08474-4325	< 0.3	0.96	< 16	58
18	08475-4352	< 0.44	< 0.45	< 2.9	31
19	08476-4306 (IRS 20)	5.7	44	216	504
20	08477-4359 (IRS 21)	9	26	317	581
21	08478-4403	0.46	0.51	5.4	< 581
22	08478-4303	< 0.39	1.6	< 216	< 35
23	08479-4311	< 0.32	0.4	< 8.7	< 38
24	08483-4305	1.5	2.5	< 39	189
25	08484-4350	0.33	< 0.56	< 3.7	23

^aTaken from the Infrared Astronomic Satellite - Point Source Catalogue (*IRAS PSC*) described in detail in Chapter 3.

^bHereinafter for the brightest sources we will use the shorter names IRS # defined by Liseau et al. (1992).

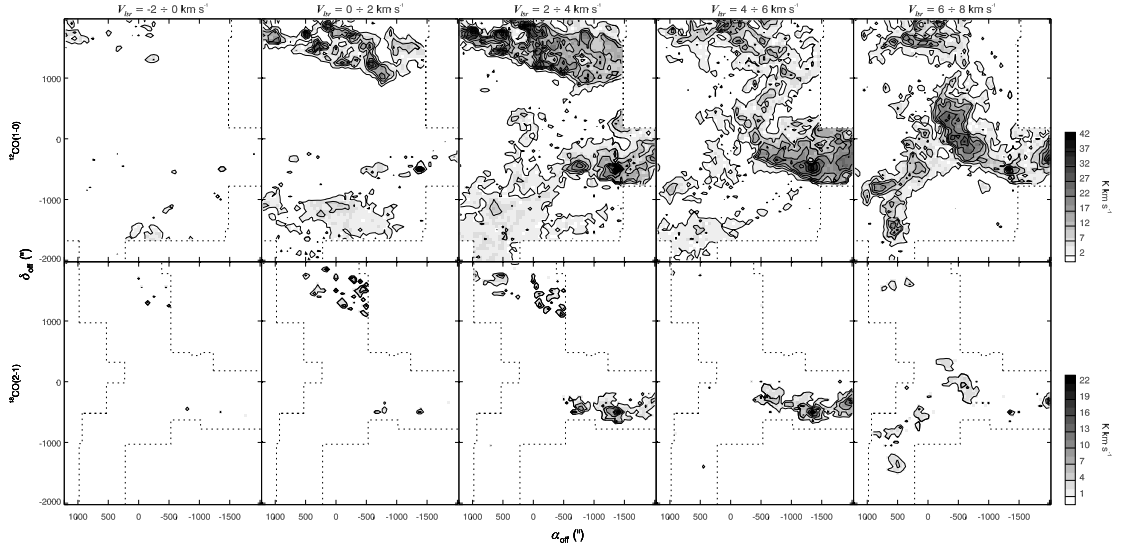


Figure 2.5: Channel maps from -2 to 8 km s^{-1} for the $^{12}\text{CO}(1-0)$ (left panels) and $^{13}\text{CO}(2-1)$ (right panels) emission in Vela-D region, in the velocity ranges indicated on the left border of each box. For $^{12}\text{CO}(1-0)$ Contour levels start from 2 K km s^{-1} and are separated by 5 K km s^{-1} , while for $^{13}\text{CO}(2-1)$ they start from 1.5 K km s^{-1} and are separated by 3 K km s^{-1} . In both cases, dashed lines delimit the observed area.

In Figure 2.4 the positions of the 25 infrared point sources of Table 2.1 are over-plotted. Five of these objects (IRS 16, IRS 17, IRS 19, IRS 20, IRS 21) have been recognized as intermediate mass young stellar objects by Liseau et al. (1992), and associated to embedded young clusters (Massi et al. 2000, 2003).

Typically, all these sources are found in the densest parts of the cloud, and in most cases their locations follow the arc-like morphology of the gas. This is suggestive of a star formation process triggered by the effects of expanding shells, driven, *e.g.*, by nearby massive young stars or supernova remnants. In Section 2.1.3 we shall explore in some detail this possibility.

In Figures 2.5 and 2.6 we present the maps, for both lines, of the integrated intensity taken in velocity intervals of 2 km s^{-1} and in steps of the same amount. These velocity channel maps clearly show how the emission detected in different locations is contributed by multiple velocity components. In Table 2.2 the characteristic velocity ranges for the main areas of the maps are summarized.

The $^{13}\text{CO}(2-1)$ channel maps, in particular, allow us to better recog-

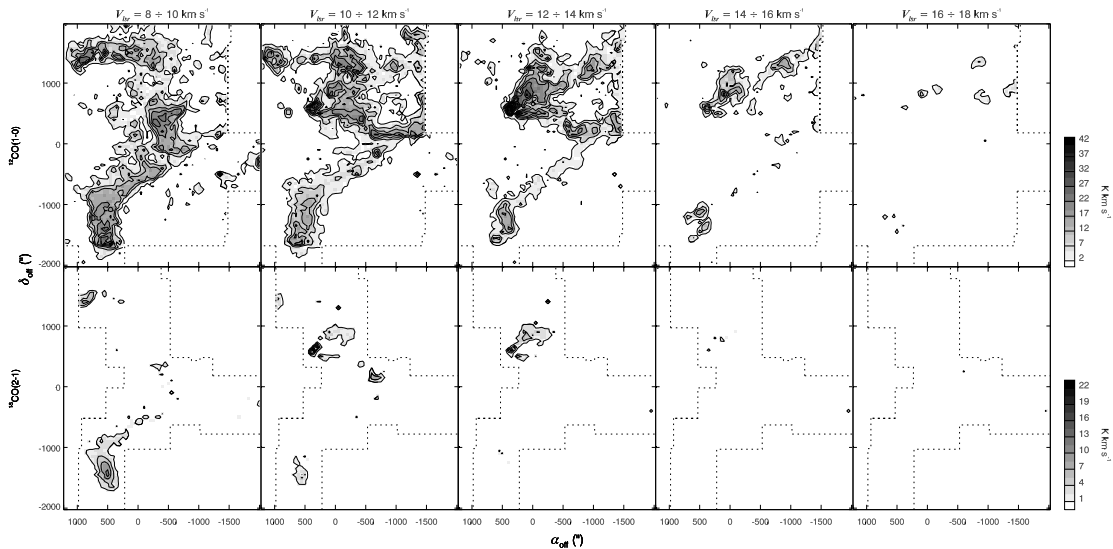


Figure 2.6: Same as in Figure 2.5, but from 8 to 18 km s^{-1} .

nize the main velocity components of the densest regions. For example, the emission from the northern part of the map appears clearly separated into two components: one in the $V_{lsr} \simeq 0 \div 4 \text{ km s}^{-1}$ range, and the other in the $V_{lsr} \simeq 6 \div 12 \text{ km s}^{-1}$ range.

Due to the large number of observed positions, as well as the geometrical regularity of the grid (in particular for the $^{12}\text{CO}(1-0)$ transition), we can extract velocity-position (hereafter vel-pos) diagrams, once an offset in α or δ is given and the observed spectra along the given strip of the map are considered. Here we present 24 declination *vs* velocity $^{12}\text{CO}(1-0)$ stripes with a fixed α_{off} spanning the range from $\alpha_{off} = +950''$ to $\alpha_{off} = -1450''$ (i.e. the location of IRS 17) in steps of $100''$ (Figure 2.7), that visualize the velocity field across the cloud. In principle the same could be done for the $^{13}\text{CO}(2-1)$ line, but at our sensitivity level the vel-pos diagrams do not add further important information so that here we omit them.

Many clump-like structures are visible in these diagrams, confirming that Vela-D possesses a high degree of inhomogeneity as will be discussed in Section 2.1.5. Several cases of strong line broadening are also detectable in correspondence with the brightest emission peaks, as, for example, at $\alpha_{off} = +50''$ or $\alpha_{off} = -1350''$, confirming the possible presence of outflows.

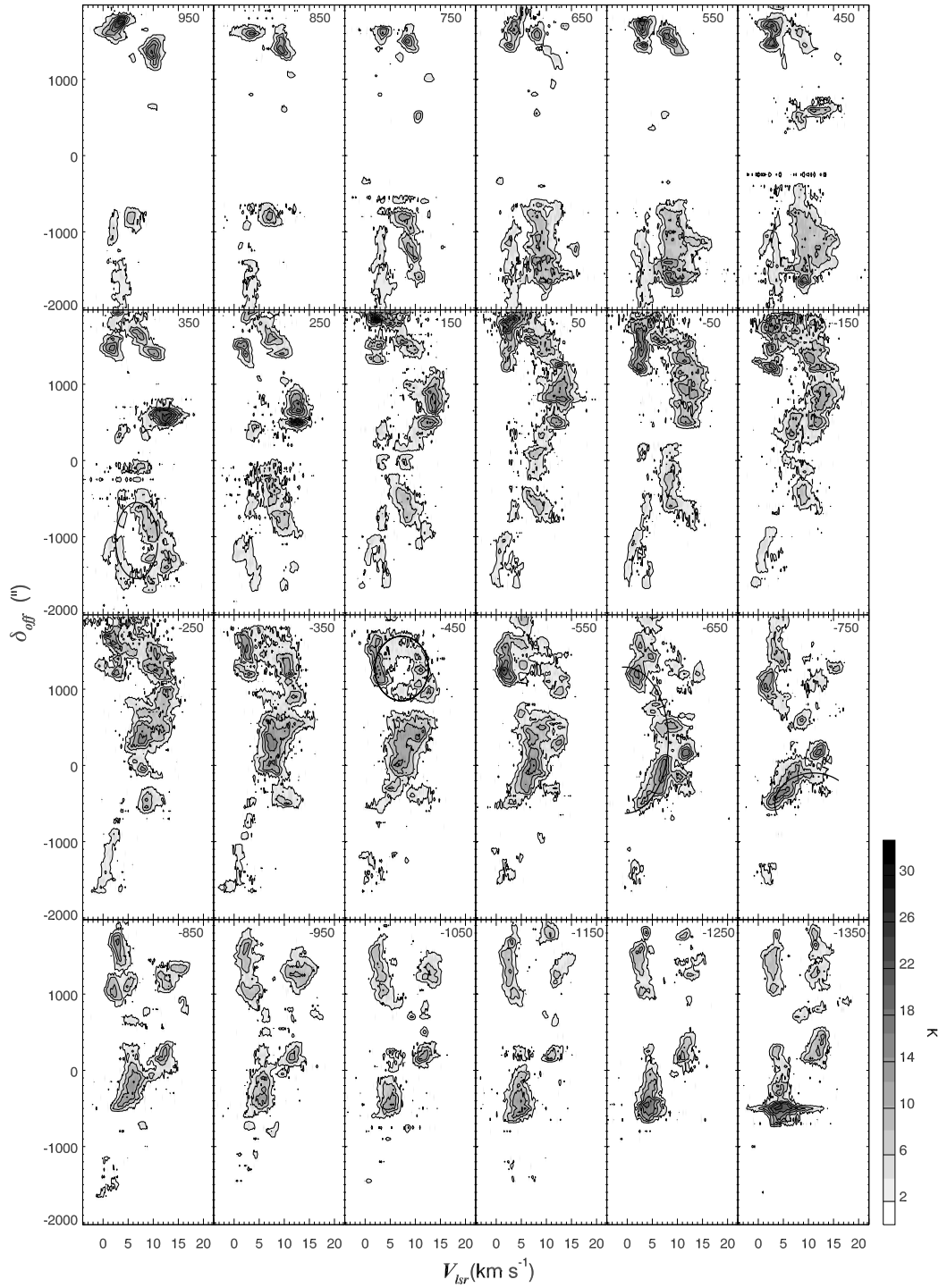


Figure 2.7: $Vel-\delta_{off}$ diagrams of the $^{12}CO(1-0)$ emission in Vela-D, for fixed values of α_{off} , indicated in each panel. Contour levels start from $T_{mb} = 2$ K and are separated by 4 K. Four arc-like structures have been recognized and marked with a solid arc of ellipse, each one in the diagram in which it is best visible.

Table 2.2: *Velocity ranges of the main emitting regions in Vela-D*

Region	$^{12}\text{CO}(1-0)$ (km s $^{-1}$)	$^{13}\text{CO}(2-1)$ (km s $^{-1}$)
North-East	$-2 \div 12$	$0 \div 4, 6 \div 12$
North-West	$0 \div 6, 10 \div 18$	$4 \div 10$
Center	$4 \div 16$	$4 \div 12$
West	$0 \div 10$	$0 \div 6$
South (diffuse component)	$0 \div 6$...
South-East	$4 \div 16$	$6 \div 12$

The appearance of arc-shaped structures in these diagrams can be explained either by the presence of two Galactic velocity components corresponding to gas located at different distances or by the action of expanding shells. In particular, this kind of structure is detectable in the regions $+750'' \leq \alpha_{off} \leq -150''$ and $-1800'' \leq \delta_{off} \leq -500''$ (southern part of the map), and $+350'' \leq \alpha_{off} \leq -750''$ and $+400'' \leq \delta_{off} \leq +1800''$ (northern part of the map).

The first hypothesis implies extremely different kinematical distances (~ 1 kpc) between the two emitting components, an occurrence indicating the presence of uncorrelated clouds along the same line of sight. The other possibility of the shell expansion, that seems more appropriate, is intuitively suggested by the arc-like shapes (in Figure 2.7 we draw ellipses to show four possible cases), and justified by simply invoking the internal motions of the cloud.

2.1.3 Searching for expanding shells and outflows

In this Section we analyze the gas distribution morphology, the velocity structures and the line shapes in order to find out signatures of large scale dynamical processes: expanding shells and molecular outflows.

The presence of arc-like features in both $\alpha - \delta$ (Figures 2.2, 2.3, 2.4) and $\text{vel} - \delta$ maps (Figure 2.7) of Vela-D region could be interpreted as a signature of possible expanding shells, a phenomenon that is often related with star-forming activity. As we have seen in Section 1.1.1, in fact, these expanding shells of ionized gas due to high energy photons emitted by bright OB stars, are often considered responsible for the

ignition of the star-forming process. In the followings we will explore this possibility by using the available literature information on the distribution of the known OB stars and Hii regions in the Vela-D field, that are shown in Figure 2.8.

Shell clues in the $\alpha - \delta$ maps - Three arc-like molecular structures are marked with dashed lines, but only in the case of the eastern arc we could guess an association with clear driving sources candidates. A possible projective correspondence can be established between the Gum 18 Hii region (Gum 1955) and this arc, that could be tentatively related to it, but not for RCW 35 (Rodgers et al. 1960). However, the centroids of the two structures do not coincide and the distance of Gum 18 is unknown. In addition, the OB stars V* OS Vel and CD-43 4690 are not far from the apparent centroid of the molecular arc, but their distances (1.7 ± 0.3 kpc in both cases, Russeil 2003) are inconsistent with that estimated for Vela-D, so that we conclude that they cannot be responsible for the arc-like morphology of the gas. Similar considerations apply to the case of the possible association between the southern arc and the location of HD 75211 ($d = 1.2$ kpc, Savage et al. 1985).

By means of simple models, describing the expansion of a Hii region and the fragmentation of the shocked dense layer surrounding it into clumps and cores, it is possible to estimate the timescales involved in the hypothesis that Hii regions drive the eastern shell. The relation between the radius R of the shell, expanding in a homogeneous and infinite medium, and its lifetime is

$$t_{dyn} = 0.559 \times \frac{R_0}{c_{ii}} \left[\left(\frac{R}{R_0} \right)^{7/4} - 1 \right] \text{ Myr} \quad (2.2)$$

(Spitzer 1978), where c_{ii} is the isothermal sound speed in the ionized region (in km s^{-1}), and R_0 is the Strömngren sphere radius (in pc), *i.e.* the size of the region where the recombination rate equals the ionization rate. Being the molecular arc $\sim 1000''$ in radius, the corresponding spatial scale is $R \simeq 3.4 \pm 1.0$ pc at the estimated distance of Vela-D, where the uncertainty is related to the distance. For a star emitting 10^{49} ionizing photons per second, we find $R_0 = 0.677 n_3^{-2/3}$ pc, where $n_3 = n_0/(1000 \text{ cm}^{-3})$ and n_0 is the ambient density. Assuming the sound speed $c_{ii} = 10 \text{ km s}^{-1}$ and varying the density in the range

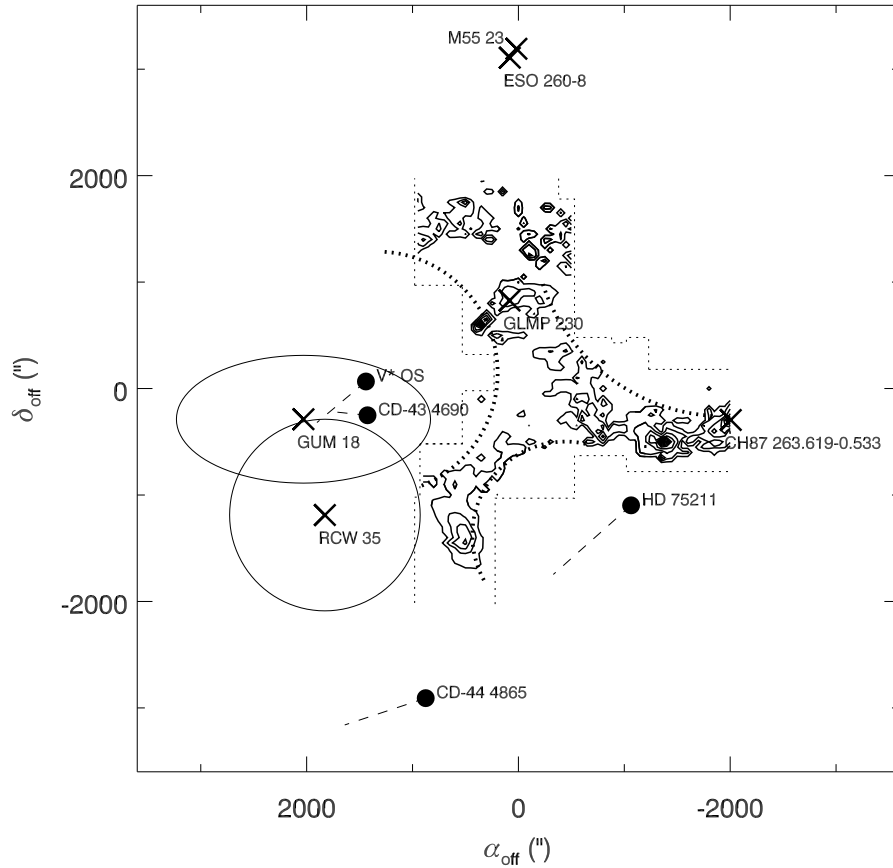


Figure 2.8: A $2^{\circ} \times 2^{\circ}$ field centered on the $(0,0)$ position of the map is shown, with the contours of the $^{13}\text{CO}(2-1)$ emission plotted as in Figure 2.3. The bold dotted circles roughly indicate three arc-like emitting regions, while the thin dashed lines mark the border of the observed zone. Crosses indicate the center of the HII regions; for two of them with significant spatial extent, Gum 18 and RCW 35, an ellipse is also drawn whose axes length is taken from literature. The remaining HII regions are compact objects and cannot be responsible for the large-scale morphology. The locations of OB-type stars (filled circles), with their proper motion track extrapolated for the last 10^5 yr, are also marked.

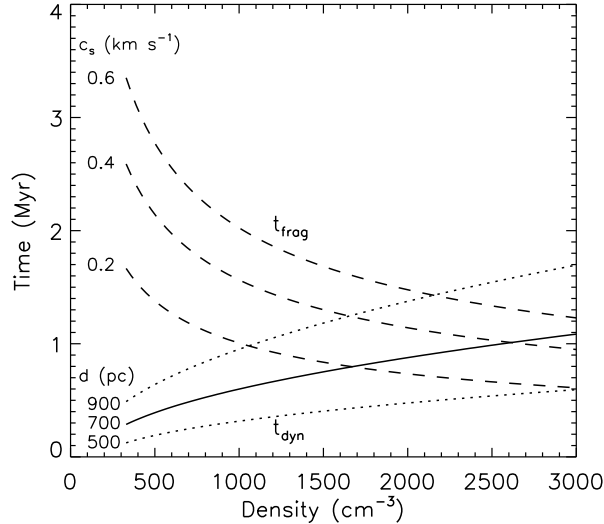


Figure 2.9: Plot of the dynamical age t_{dyn} (solid line for $d = 700$ pc, and dotted lines for $d = 500$ pc and $d = 900$ pc, respectively) for a HII region and of the time at which the fragmentation of the driven shell starts (for different values of the sound velocity c_s and a radius of ~ 3.4 pc) as a function of the density n_0 .

$n_0 = 300 \div 3000 \text{ cm}^{-3}$, we find $t_{dyn} \sim 0.2 \div 1.1$ Myr. The scaling of the age with the density is shown in Figure 2.9 for different estimates of the distance. Considering now the Whitworth et al. (1994) model describing the fragmentation of the molecular gas under the action of an expanding Hii shell, it is also possible to determine the time elapsed before the onset of this phenomenon. For the considered star this model predicts

$$t_{frag} = 1.56 c_{.2}^{7/11} n_3^{-5/11} \text{ Myr} \quad (2.3)$$

where $c_{.2} = c_s / (0.2 \text{ km s}^{-1})$, and c_s is the sound speed in the molecular gas, an important parameter of the model we chose in the range $c_s = 0.2 \div 0.6 \text{ km s}^{-1}$. Because both fragmentation and star formation appear to be already in progress, the relation between these two times has to be $t_{dyn} > t_{frag}$, and this happens when $t_{dyn} \geq 8 \times 10^5 \text{ yr}$ and $n_0 \geq 1600 \text{ cm}^{-3}$, if we consider the preferred values $d = 700 \text{ pc}$ and $c_s = 0.2 \text{ km s}^{-1}$. The effect of a different distance is also shown in Figure 2.9.

We note that these timescales are consistent with the age of the cluster formation activity in this region, estimated to be within $1 \div 6$ Myr by Massi et al. (2006). This makes possible that both arcs and the star formation activity in them are caused by the expansion

of Hii regions. However, since no clear excitation source candidates have been found in the vicinity of the arc centers, we cannot exclude different possible origins for the shells, such as, for example, stellar winds from a previous generation of young stars.

Despite another possibility is suggested by the well-known Vela Supernova Remnant (SNR), apparently interacting with the whole Vela Molecular Cloud complex on larger scales (see Figure 1 in Moriguchi et al. 2001), a correlation with the southern arc in Vela-D is far from clear. Furthermore, considering the possible connection between this molecular arc and its star formation activity, there is a clear inconsistency between the age of the young stellar objects and that estimated for the Vela SNR ($t_{\text{SNR}} \simeq 10^4$ yr, see, *e.g.*, Moriguchi et al. 2001). Two further remnants, SNR 266.3-01.2 and SNR 260.4-03.4, are too far for being responsible for the peculiar morphology of the investigated region.

In this respect, the hypothesis that the fluidodynamic evolution of the gas can be responsible for the observed filamentary condensations can not be rejected.

Shell clues in the $\text{vel}-\delta$ maps - As mentioned above, also the analysis of the cloud velocity field can provide useful information about the presence and the physical properties of possible expanding shells. For example, the shell-shaped structure highlighted in Figure 2.7 at $\alpha_{\text{off}} = +350''$ can be associated, due to its spatial location, to the southern arc identified in the $\alpha - \delta$ map. It is characterized by a peak separation $\Delta V_{\text{lsr}} \simeq 7 \text{ km s}^{-1}$, corresponding to an expansion velocity $V_{\text{exp}} \simeq 3.5 \text{ km s}^{-1}$. Adopting a spherical symmetry, we estimate a mean radius $R_{\text{sh}} \simeq 5.5 \text{ pc}$ and a corresponding dynamical age $t_{\text{dyn}} \simeq 1.5 \text{ Myr}$, a value consistent with the possible timescales calculated above for an expanding Hii region. The issue of the identification of a driving source for this shell remains open, as already discussed when we examined the corresponding arc observed in the $\alpha - \delta$ map.

Another shell-like structure is well recognizable in the northern part of the vel-pos diagrams, best visible at $\alpha_{\text{off}} = -450''$. With considerations similar to the previous case, we find $V_{\text{exp}} \simeq 4.5 \text{ km s}^{-1}$, $R_{\text{sh}} \simeq 7 \text{ pc}$ and $t_{\text{dyn}} \simeq 1.5 \text{ Myr}$. Also in this case the identification of a possible driving source is uncertain: some *IRAS* red sources are located in

the neighborhoods of the shell, but these objects might be presumably the product of a star-forming activity triggered by an expanding shell, rather than the cause of it.

In Figure 2.7 two further arc-shaped structures have been marked with solid lines, around $\alpha_{off} = -650''$ and $\alpha_{off} = -750''$, respectively. Although less evident than the cases considered above, these shapes support the hypothesis of a coupling between the arcs recognized in the integrated intensity maps (the western and the southern one, respectively) and those present in the vel-pos diagrams.

Concerning the search for outflowing activity from young objects it is necessary to remark that the grid spacing of $50''$ is quite coarse for a detailed description of the outflow morphology, and a larger integration time would have been required for each spectrum to better disentangle the outflowing emission from the noise.

Nevertheless, since several positions in the map show a clear broadening of the line profile (see, *e.g.*, the diagram at $\alpha = -1350''$ of Figure 2.7), we studied these positions in more detail because this is a typical signature of the presence of energetic mass outflows (see, *e.g.*, Bachiller 1996). We considered here the locations of the 25 *IRAS* sources shown in Figure 2.4 and quoted in Table 2.1, carrying out a systematic search for outflows in the $^{12}\text{CO}(1-0)$ line⁸ toward these objects, while a more suited search, driven by the occurrence of jet-like emissions and based on higher resolution data, will be presented in Chapter 4.

The detection method is the same as adopted by Wouterloot & Brand (1999) and described in more detail in Chapter 4: When the profile wings significantly exceed the gaussian wings, the presence of an outflow is inferred and the blue and red components are obtained by integrating the difference $T_{mb} - T_{fit}$ between the half maximum of the gaussian and the velocity where the line wing fades into the noise.

Unfortunately, the complexity of the $^{12}\text{CO}(1-0)$ spectra in this region makes sometime difficult an accurate detection of the wings by simply applying this method. In seven cases, in fact, the presence of one or more additional spectral components blended with the main

⁸ $^{13}\text{CO}(2-1)$ observations have been ignored because they are too noisy to be useful in the described analysis.

feature made impracticable a clean detection of any outflow that might be present. However, in 13 out of the remaining 18 cases, we detected a possible outflow⁹.

2.1.4 Cloud mass evaluation

The total gas mass of the cloud has been roughly evaluated by Elia et al. (2007) by adopting two different methods. The first method consists in determining the gas column density, *i.e.* the molecule density integrated along the line of sight, by means of the empirical formula

$$N(H_2) = (2.3 \pm 0.3) \cdot 10^{20} \int T_{mb}(^{12}CO) dv \quad (cm^{-2}), \quad (2.4)$$

which is based on a galactic average factor (Strong et al. 1988). The molecular mass can be derived by the relation

$$M_{gas}^{(1)} = \mu m_H \sum [d^2 \Delta\alpha \Delta\delta N(H_2)], \quad (2.5)$$

(see, e.g., Bourke et al. 1997), where $d = 700$ pc is the distance of Vela-D, $(d^2 \Delta\alpha \Delta\delta)$ is the size of the emitting area at the observed position, m_H is the mass of a hydrogen atom, and μ represents the mean molecular mass. Adopting a relative helium abundance of 25% in mass, $\mu = 2.8$ and the derived cloud mass is $M_{gas}^{(1)} = 1.5 \cdot 10^4 M_\odot$.

The second, more rigorous method, whose details will be described in Chapter 4 where we will present the observations of the molecular outflows (§ 4.2), relies on the simultaneous observation of the two lines. For this reason, it is limited to the only pointings that present a non null $^{13}CO(2-1)$ emission and the derived value of $M_{gas}^{(2)} = 1.2 \cdot 10^3 M_\odot$ can be considered only as a stringent lower limit.

While the first method is more affected by the assumptions underlying the empirical calculation, the second one suffers more effectively the under-sampling of the maps. Thus it is clear how these estimates can be regarded only as first guesses on the order of magnitude of the cloud mass. Moreover, it is important to stress the relevance of the uncertainty on the Vela-D distance estimates ($\Delta d = 200$ pc) for all the mass estimates: cloud, clumps (§2.1.5), cores (§2.2.4) and outflows (§4.2.3).

⁹The possible outflows correspond to entries 1, 3, 6, 8, 10, 12, 14, 17, 19, 20, 23, 24, 25 of Table 2.1

2.1.5 Molecular clump decomposition

To characterize the structure of Vela-D molecular emission and the distribution of its velocity components in a quantitative way we applied cloud decomposition techniques to our data, a tool typically adopted to study possible hierarchies in the molecular cloud structure¹⁰.

In particular, we adopted the 3D version of the CLUMPFIND (hereinafter CF) algorithm (Williams et al. 1994), running on a α - δ - v cube containing all the reduced spectra for each offset position. It is an automatic routine consisting in the operative separation of the emitting regions into spatially defined entities associated to the emission peaks. The algorithm works by first contouring the data at a multiple of the rms noise of the observations, then searches for peaks of emission which locate the clumps, and then follows them down to lower intensities. No a priori clump profile is assumed. Important adjustable parameters in the CF scanning procedure are the radiation temperature threshold T_{min} and the level increment ΔT , the first one being generally set slightly above the noise fluctuations. This is an important point that requires accurate tests because larger and smaller thresholds involve the loss of faint peaks and the inclusion of noise peaks, respectively. The second parameter ΔT controls the separation of close peaks, as clearly discussed in Brunt et al. (2003).

A large number of tests have been run on the ¹³CO(2-1) data cube, which is characterized by a smaller number of features and a reduced diffuse emission, two characteristics that permit a better control and verification of the reliability of the clump assignments. To obtain a convenient reduction of the noise effect and to ensure some stability to the results, the spectra were preliminarily re-sampled in velocity by a factor of 5. Exploring the input parameter space, we noted that the choice of the parameter set can produce not only systematic (as those described above), but also random effects. These are particularly evident, for example, in large clumps corresponding to a single bright line, that are sometimes decomposed in two or more clumps,

¹⁰Although completely justified from a theoretic point of view only in the case of a hierarchical structure scenario (see Section 1.1.1), this approach represents, operationally, the best way to quantitatively characterize the morphological features with a certain degree of objectiveness needed for a meaningful comparison among different clouds. Other objective approaches, based on fractal analysis, are more suited for the study of turbulent media like molecular clouds, but have not yet been proven to be more useful for the understanding of the cloud physics.

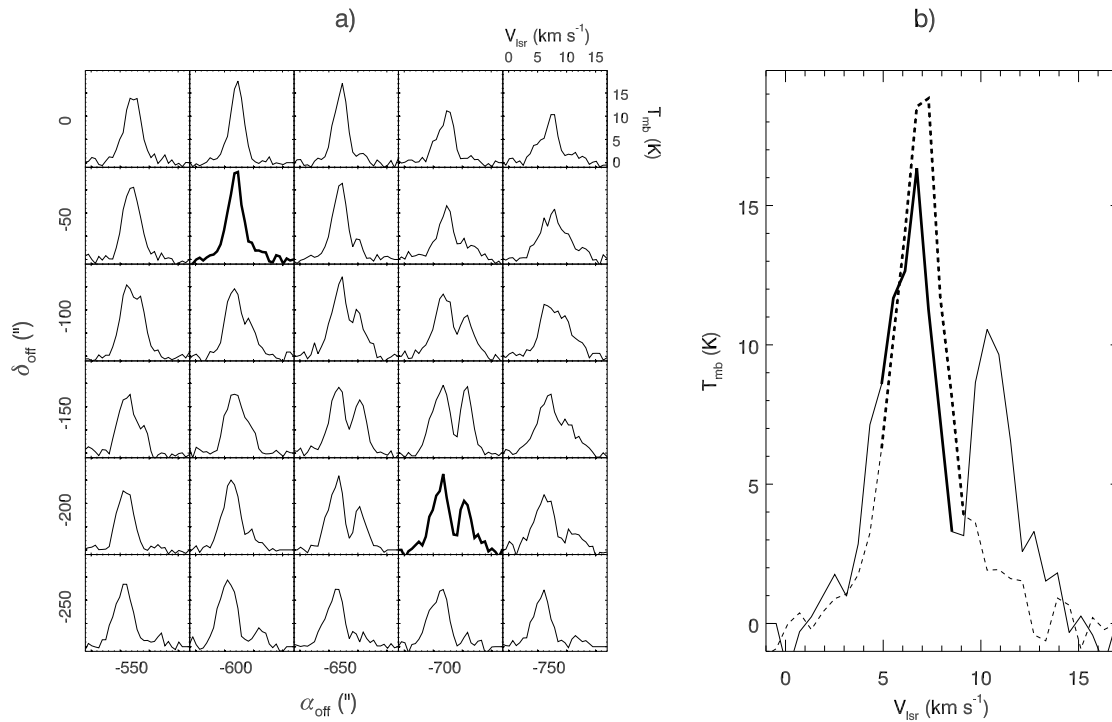


Figure 2.10: *Example of bad clump detection performed by CF. Panel a: a grid of $^{12}\text{CO}(1-0)$ spectra (resampled in resolution from 0.12 to 0.6 km s^{-1}) around two positions (marked with a thicker line) recognized by CF as centroids of different clumps, with almost coincident peak velocity ($V_{\text{lsr}} \simeq 7 \text{ km s}^{-1}$). Because these components satisfy our merging criteria (see text), we conservatively chose to consider them as a single clump. Note that a second component at $V_{\text{lsr}} \simeq 10 \text{ km s}^{-1}$ is clearly resolved in some spectra and is correctly assigned by CF to another clump. Panel b: the two thicker spectra shown in panel a are superimposed and plotted with solid and dashed line, respectively. The velocity channels erroneously assigned by CF to two different clumps are highlighted (bold line).*

an effect that is illustrated in Figure 2.10. We verified that, adopting a different set of parameters, the clump could appear as single, the price being that some other cases, previously recognized as single, now appear as separated. This experience suggests that the tuning of the parameter values is critical with respect to the number of detections. This kind of problems in cloud decomposition with CF have been extensively discussed in Brunt et al. (2003), Rosolowsky & Blitz (2005), and Rosolowsky & Leroy (2006).

In this work, the relatively low number of detected clumps suggested us a very simple approach based on the careful inspection of a large number of CF outputs. First of all, we ran CF adopting a parameter set ensuring a good detection of the features, i.e. a T_{min} value as low as possible, although above the noise limit, and a similar value also for ΔT , to minimize the effect of noise fluctuations affecting the spectra. Both values have been set to 2 K, corresponding to $\sim 3\sigma$ in our map. In this way, the cataloged emission accounts for the 66% of the total emission in the $^{13}\text{CO}(2-1)$ map. The obtained clump list has then been analyzed looking for those objects that, despite they are quite close in the α - δ - v space, clearly appear as spuriously splitted by CF. We merged together these clumps to obtain a final clump distribution as free as possible from the most apparent misinterpretations of CF. In this way, we do not claim to determine the “true” clump distribution in the cloud, but we believe that the census resulting from our clump merging method is more reliable than the simple CF output.

Our experience in analyzing the clump merging suggested a set of constraints that have been included in an automatic merging algorithm. In fact, we merged only clump pairs whose centroids satisfy all the following criteria: (i) both distances in α and δ are less or equal to 3 grid elements (corresponding to a spatial scale of ~ 0.5 pc); (ii) the difference between the central velocities is less than or equal to 3 channels (i.e. $\Delta v \leq 0.9 \text{ km s}^{-1}$, after resampling); (iii) the α - δ - v space total distance $d = \sqrt{\Delta\alpha^2 + \Delta\delta^2 + \Delta v^2}$ is less than or equal to 5 volume pixels. In this context the pairs showing a spatial discontinuity in their emission have been taken as separated.

After this procedure the number of detected $^{13}\text{CO}(2-1)$ clumps decreased from 67 to 49 clearly modifying the resulting mass spectrum, with the total detected mass remaining obviously unchanged. The list

of these clumps, along with their coordinates, velocity centroids, radii and masses is presented in Table 2.3. A similar procedure has been applied to the $^{12}\text{CO}(1-0)$ line data cube but the results are less reliable, due to the large number of blended components, as well as to the presence of a diffuse component in a large fraction of the map, that make the decomposition much more difficult and the definition itself of “clump” more uncertain.

Table 2.3: *List of the clumps detected in the $^{13}\text{CO}(2-1)$ line.*

Clump	α (J2000)	δ (J2000)	V_{LSR} (km s^{-1})	ΔV (km s^{-1})	Radius (pc)	Mass (M_{\odot})	Map limit	Dust Clump(s)	IRAS source(s) ^a
VMRD1	8 45 35	-43 52 02	5.9	2.55	0.6	83	X	MMS1,2,3	1
VMRD2	8 45 36	-43 48 42	5.3	1.80	0.4	16	X	MMS1,2,3	1
VMRD3	8 46 17	-43 56 12	4.1	1.14	0.5	17	
VMRD4	8 46 31	-43 54 32	2.9	1.09	0.7	48		MMS4	3,4
VMRD5	8 46 35	-43 54 32	5.0	1.53	0.7	70		MMS4,5,6	3,4
VMRD6	8 46 49	-43 50 22	4.7	1.06	0.4	9	
VMRD7	8 46 54	-43 54 32	4.1	1.71	0.6	38		MMS5,6	...
VMRD8	8 47 26	-43 48 42	5.6	1.11	0.4	10	
VMRD9	8 47 26	-43 52 52	2.9	1.36	0.4	17	
VMRD10	8 47 31	-43 52 52	4.1	0.93	0.4	8	
VMRD11	8 47 40	-43 43 42	11.3	0.99	0.3	11		...	7
VMRD12	8 47 45	-43 47 02	6.8	0.84	0.5	15	
VMRD13	8 47 45	-43 50 22	5.0	1.31	0.4	15		...	8
VMRD14	8 47 50	-43 47 52	5.9	0.77	0.4	8		...	8
VMRD15	8 47 54	-43 27 52	2.0	0.73	0.2	3	X
VMRD16	8 47 59	-43 39 32	10.4	0.64	0.2	2		MMS7	...
VMRD17	8 47 59	-43 25 22	2.3	0.68	0.2	3	X	...	9
VMRD18	8 47 59	-43 20 22	1.1	0.50	0.2	3	X
VMRD19	8 48 03	-43 51 12	4.7	0.76	0.2	3	
VMRD20	8 48 13	-43 47 02	7.7	1.62	0.3	3	
VMRD21	8 48 13	-43 22 52	2.3	1.07	0.4	15	
VMRD22	8 48 17	-43 17 52	1.4	1.08	0.2	5	
VMRD23	8 48 17	-43 26 12	2.3	0.88	0.2	3	
VMRD24	8 48 27	-43 41 12	6.5	1.69	0.3	5	
VMRD25	8 48 31	-43 22 02	2.0	0.85	0.2	4	
VMRD26	8 48 31	-43 25 22	2.3	0.91	0.2	6	
VMRD27	8 48 31	-43 34 32	12.5	1.18	0.4	11		...	11
VMRD28	8 48 40	-43 29 32	11.3	1.33	0.4	8		MMS8,9,12,14,15,16	14
VMRD29	8 48 40	-43 17 52	2.3	0.87	0.2	6	
VMRD30	8 48 50	-43 29 32	13.1	1.07	0.5	16		MMS8,9,12,13,14,15,16	14
VMRD31	8 48 54	-43 15 22	2.0	0.97	0.2	8	
VMRD32	8 48 59	-43 59 32	8.3	1.44	0.5	16		...	15
VMRD33	8 49 03	-43 32 52	11.9	0.86	0.2	4	
VMRD34	8 49 03	-43 37 52	11.9	1.69	0.2	10		MMS17,18	16
VMRD35	8 49 12	-43 22 02	1.4	1.27	0.3	5	
VMRD36	8 49 13	-43 36 12	11.3	1.55	0.3	32		MMS19,20,21	17
VMRD37	8 49 13	-43 36 12	12.8	0.86	0.3	9		MMS19,20,21	17
VMRD38	8 49 22	-44 00 22	8.3	1.40	0.6	19	
VMRD39	8 49 22	-43 58 42	7.4	1.07	0.4	8	
VMRD40	8 49 26	-43 22 02	3.5	0.72	0.2	3	
VMRD41	8 49 26	-43 17 02	2.6	0.90	0.3	10		MMS22,24	19
VMRD42	8 49 26	-43 17 02	1.7	0.85	0.2	3		MMS22,24	19
VMRD43	8 49 27	-44 10 22	8.9	1.57	0.7	78		MMS25,26,27	20
VMRD44	8 49 31	-43 20 22	7.7	1.16	0.3	4	
VMRD45	8 49 31	-44 07 52	9.8	1.63	0.7	141		MMS23,25,26,27	20
VMRD46	8 49 49	-43 21 12	8.3	1.01	0.3	9		...	23
VMRD47	8 49 59	-44 00 22	6.8	1.00	0.2	2	
VMRD48	8 50 03	-43 22 52	9.5	1.27	0.4	20	X
VMRD49	8 50 07	-43 16 12	4.1	0.88	0.2	4	X	MMS28	24

^aThe identification numbers are the same as in Table 2.1.

The method adopted here for evaluating the clump masses is the same introduced in Section 2.1.4, where we have computed the cloud gas mass $M_{gas}^{(2)}$ (see also Elia et al. 2007), and described in details in the Section 4.2.3, where the mass of the outflows will be estimated. The total mass assigned to the clumps amounts to $845 M_{\odot}$, corresponding to the 77% of the whole $M_{gas}^{(2)}$. It should be said, in this respect, that, while for the whole cloud this mass estimation method likely underestimates the mass, due to the impossibility of evaluating the contribution from offset positions where $^{13}\text{CO}(2-1)$ is null, in the clump mass evaluation this problem does not occur because the clumps are, *by algorithmic definition*, the emitting regions surrounding the peaks and above a given threshold, where the emission is non-null.

For clumps at the boundary of the observed zone a flag “X” is added in Table 2.3 to indicate that the quoted clump mass value actually is a lower limit. In the Table the associations with the *IRAS* PSC sources of Table 2.1 are also indicated: 22 out of 25 objects fall in the area observed in $^{13}\text{CO}(2-1)$, and the locations of 15 sources (among which are the five IRS objects of Liseau et al. 1992) can be associated with the recognized clumps.

Comparing these results with the list of 29 dust cores presented in Table 2.4, we searched for possible associations between $^{13}\text{CO}(2-1)$ and dust condensations, adopting as a criterium the correspondence between the dust core centroid and one of the map points assigned by CF to a gas clump. We found 16 cases that are reported in Table 2.3. Note that in this way the information on the velocity field, allowing to separate possible multiple components along the line of sight, can induce the association between two gas clumps and a group of dust cores (see, for example, the clumps VMRD2 and VMRD8). We note also that only the dust cores MMS10 and MMS11 are not associated to any $^{13}\text{CO}(2-1)$ clumps.

2.1.6 Clump mass spectrum and mass-size relationship

The derived mass spectrum is shown in Figure 2.11, with Poisson error bars, along with the spectrum resulting from the original CF output. For nine clumps we can only give a lower limit to the mass because they are bounded by our map limits. This effect is particularly important in the case of the large clump hosting IRS 16 (clump VMRD6 in Ta-

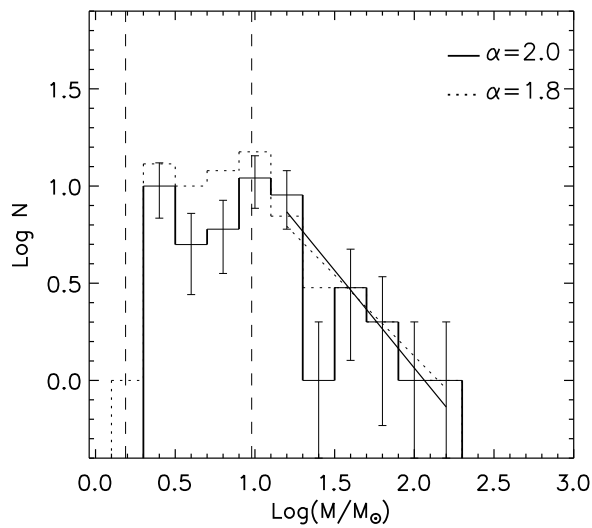


Figure 2.11: *Clump mass spectrum of Vela-D derived from $^{13}\text{CO}(2-1)$ observations using CF. The dashed vertical lines indicate the minimum mass (leftmost) and the completeness (rightmost) limits, respectively. The dotted line shows the CF mass spectrum while the solid line is obtained after the merging procedure (see text). The linear best-fit is also shown in both cases, whose slope corresponds to $\alpha - 1$, where α is the exponent of the power law $dN/dM \propto M^{-\alpha}$.*

ble 2.3). The minimum mass detectable and the completeness limits, calculated as in Simon et al. (2001) by setting a 10σ confidence level (see also Bains et al. 2006), and estimated in $0.19 M_{\odot}$ and $0.98 M_{\odot}$, respectively, are also shown.

A linear least-squares fit of the distribution of the masses above the completeness limit provides an estimate of the $dN/dM \propto M^{-\alpha}$ law exponent, which has been found to be $\alpha = 2.0 \pm 0.3$ for the “corrected” sample and $\alpha = 1.8 \pm 0.3$ for the original CF output (see Figure 2.11). In general, dealing with a relatively small sample of clumps, the spectral index can be also sensitive to the particular choice of the bin size. It was set here to be 0.2 (in logarithmic units), after verifying the stability of the resulting slope with respect to other possible choices. By varying, as in Bains et al. (2006), the bin size in the range of $\pm 10\%$ we obtain slopes that always fall within the associated error.

The spectral index found in Vela-D for the corrected clump list is compatible with those reported in the literature for molecular line observations ($1.3 \leq \alpha \leq 1.9$, see, e.g., Mac Low & Klessen 2004), and are significantly smaller than the typical slopes of the stellar IMF (e.g., $\alpha \sim 2.35$ in Salpeter 1955). This occurrence appears to be even more significant when considering that Massi et al. (2006) find a standard IMF for a sample of 6 young Vela-D clusters. Such discrepancy is likely due to the low map resolution that does not allow us to observe the fragmentation of the larger cores into sub-structures, as we shall explain in more details when the link between the core mass spectrum and the IMF will be addressed (§ 2.2.6).

The slopes obtained here, in fact, seem comparable with the power-law index $\alpha_{dust} = 1.4 - 1.9$ of the dust cores (§ 2.2.6) if we consider the quoted errors and the fact that the dust continuum observations completely include those high-mass clumps which are only partially contained in our map (in particular the massive clump hosting IRS 16). The difference found between the $^{13}\text{CO}(2-1)$ and the dust indexes could be due to opacity effects that in the case of the more massive clumps can be considerable. This corresponds to an underestimate of the larger gas masses and then to a steeper slope in the mass spectrum. For another similar case in which $\alpha_{gas} > \alpha_{dust}$, see Bains et al. (2006).

In Figure 2.12 we present also the clump mass as a function of the size. A weak linear behavior can be individuated in the bi-logarithmic

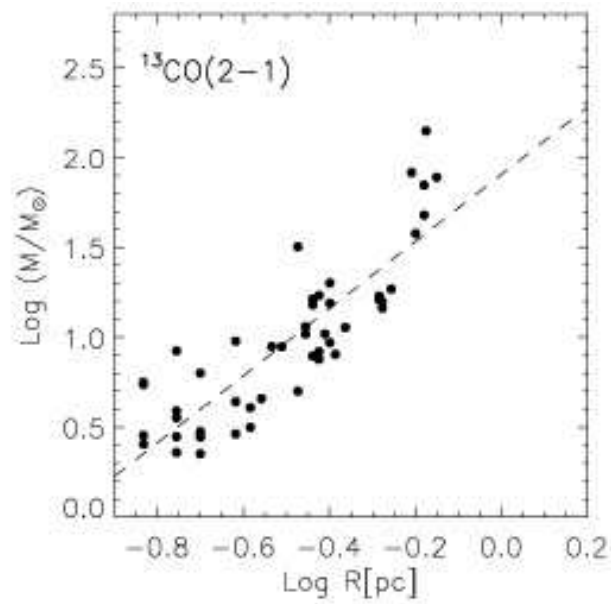


Figure 2.12: *Bi-logarithmic plot of the mass vs radius relation for the clumps resulting from the supervised clump decomposition of Vela-D, for the $^{12}\text{CO}(1-0)$ and the $^{13}\text{CO}(2-1)$ transitions, respectively. In both panels, the dashed line indicates the linear trend of the data. The slopes are $x = 2.5 \pm 0.3$ for $^{12}\text{CO}(1-0)$, and $x = 1.9 \pm 0.5$ for $^{13}\text{CO}(2-1)$.*

plot with a consequent relation $M \propto R^x$ with $x = 1.9 \pm 0.5$.

2.2 Dust emission

CO(1–0) is the best tracer of molecular gas and the most efficient transition to map large sky areas, but it fails to probe the densest molecular cores. This is due both to its large optical depth (See § 4.2.1), which often causes a saturation of the line peak, and to the fact that CO freezes onto dust grains at the highest densities, *i.e.* a not negligible fraction of CO molecules can not be detected because trapped by the grains (phenomenon known as *depletion*). However, the availability of large arrays of sub-millimeter/millimeter bolometers has recently provided a way to carry out large surveys of entire star-forming regions searching for protostellar and starless cores with high sensitivity by means of the observation of the continuum, thermal emission of the dust grains around 1 mm (see, *e.g.*, Motte et al. 1998, Motte et al. 2001; Johnstone et al. 2000; Kerton et al. 2001; Mitchell et al. 2001; Reid & Wilson 2005; Mookerjea et al. 2004; Hatchell et al. 2005).

2.2.1 Dust data

A $\sim 1^\circ \times 1^\circ$ region of Vela-D, slightly larger than that mapped in the CO lines, was observed by our group (Massi et al. 2007) in the 1.2 mm dust continuum emission in May (23–26) 2003, by using the 37-channel bolometer array SIMBA (Nyman et al. 2001) at the SEST (ESO-La Silla, Chile). At this wavelength, the HPBW (see § 2.1.1), which is $24''$, *i.e.* ~ 0.08 pc at 700 pc, matches, or is smaller than, the typical spatial size of cluster-forming cores and that of the embedded star clusters in the region (Massi et al. 2006). A total of 17 sky areas $18' \times 14'$ (azimuth \times elevation) in size were mapped in the fast scanning mode, with a scanning speed of $80'' \text{ s}^{-1}$. Each map was repeated 3 to 4 times, except for 3 marginal regions. We always performed a skydip¹¹ and pointing check every ~ 2 hrs, while the focus was checked at the beginning of each observing run and at sunset. The pointing was better than $\sim 5''$.

¹¹*Skydip* is the calibration measurement of the atmosphere by measuring the total power at equally spaced airmasses.

All data were reduced by means of the software package MOPSI¹² according to the SIMBA Observer’s Handbook (2003). The steps are summarized in Chini et al. (2003). All the available maps for each of the 17 areas were first co-added yielding 17 images that, once calibrated (see below) were mosaiced together. The final large-scale map is shown in Fig. 2.13. The r.m.s. is in the range 14–40 mJy/beam, but is ~ 20 mJy/beam (or less) over most of the map.

The flux calibration has been a tricky part of the reduction procedure, because of the lack of very suitable calibrators during the nights. Nevertheless, the combination of observations of some less reliable calibrators together with the comparison of our results with literature data of the brightest sources in the field present in literature, indicates that our flux calibration is accurate in general to within $\sim 20\%$ (see Massi et al. 2007 for more details).

2.2.2 Dust emission regions

As we have seen in the first part of this Chapter, clues about the star formation history of the cloud can be derived from the filamentary morphology of the molecular gas. In Fig. 2.20, we show the 1.2 mm continuum map overlaid with contours of the map of CO(1–0) emission integrated from 0 to 20 km s⁻¹. The dust emission appears qualitatively different from the molecular one. It is much more concentrated in small regions coincident with the molecular peaks. Most of the dust condensations are close to red IRAS sources and, among the young star clusters studied by Massi et al. (Massi et al. 2000, Massi et al. 2003, Massi et al. 2006), those that are located within the boundaries of the observed area clearly coincide with the brightest dust emission sources. All mm cores found by means of the map decomposition discussed in Section 2.2.3 and listed in Table 2.4 (named MMS \ddagger) are aligned along filaments or arcs of molecular gas; hence our choice to attribute to all cores the same distance (700 pc). The brightest of them are those associated with the red IRAS sources and embedded clusters (IRS16, 17, 19, 20 and 21, see Table 2.1).

IRS16 and IRS17 lie inside one of these arcs, in the south-western part of the map. IRS16 (see Fig. 2.14) consists of 3 massive cores

¹²MOPSI is a software package for infrared, millimetre and radio data reduction developed and regularly upgraded by R. Zylka.

located around an HII region (roughly 0.4 pc in diameter), suggesting that the expansion of the HII region may have triggered star formation there. On the other hand, IRS17 (see Fig. 2.15) is part of a filament of mm sources; it contains the most massive core (MMS4) of the whole region, which is slightly elongated in the direction of the larger-scale surrounding CO arc. Two more cores (MMS5 and MMS6, together with an unresolved one), east of it and again following the molecular gas orientation, suggest fragmentation of a larger filament. Giannini et al. (2005) showed that MMS4 can be further decomposed into two cores (mmA of $110 M_{\odot}$, and mmB of $11 M_{\odot}$) embedded in more diffuse gas ($58 M_{\odot}$). They adopted a smaller dust temperature (23 K), finding higher masses than ours.

IRS19 (see Fig. 2.16) is part of a relatively complex structure composed of filaments arranged in a roughly elliptical pattern with a major axis of ~ 2 pc. The most massive cores in the pattern (MMS12, MMS17 and MMS21) are all associated with three IRAS sources whose SED is typical of Class I sources (IRAS08470–4321/IRS19, IRAS08472–4326, and IRAS08474–4325, respectively). This structure is reflected in the CO(1–0) map (Fig. 2.20) also, suggesting a dynamical origin and a subsequent fragmentation.

IRS21 (see Fig. 2.17) is the most massive in a chain of cores, also aligned in the same direction as a surrounding filament of molecular gas (*i.e.*, north-south). IRS20 (see Fig. 2.18), as well, is part of a chain of cores aligned with a surrounding filament of molecular gas (*i.e.*, east-west). Finally, a moderately-massive isolated core lies towards the centre of the molecular cloud (see Fig. 2.19).

2.2.3 Dust core decomposition

As we did for the CO observations, the dust map has been scanned, searching for condensations, by using a two-dimensional version of the tool CLUMPFIND, described in Section 2.1.5 (Williams et al. 1994), capable of recognizing connected regions of emission with arbitrary shapes, starting from the peaks of intensity and going down to the lowest contour levels, depending on the r.m.s. of the data.

Although less parameter-dependent with respect to the three-dimensional version used for the molecular decomposition, the algorithm requires also in this case a tuning of the parameters in order to obtain a solid

output. To reduce the influence of the variations in the r.m.s. noise over the map, we divided the observed region into ten smaller sub-regions. Then, we applied CLUMPFIND to each of these areas using a local value of the r.m.s., as to properly set the two input parameters: the lowest contour level, I_{\min} , which acts as a detection threshold, and the intensity level increment, ΔI , used to separate resolved components located within the same emission region. In practice, we used $I_{\min} = 3$ r.m.s. and $\Delta I = 2$ r.m.s. in order to be conservative and to obtain a separation between substructures which seems reasonable on a visual inspection. The varying r.m.s., and the different input parameters chosen for each sub-region, do affect the sensitivity over the map, but ultimately they only change the “global” completeness limit (see Section 2.2.5). Above this completeness limit, we do not expect our source statistics to be significantly biased.

The CLUMPFIND output consists of a sample of about 50 millimeter sources for which we derived the sizes by assuming a distance of 700 pc. From the original output we selected a robust sample of 29 cores (listed in Table 2.4) which fulfil the criterion of having a size, before beam deconvolution¹³ greater than, or equal to, the SIMBA HPBW. This sample does not include those detections (although all are above 3 r.m.s.) that are revealed by CLUMPFIND, but “under-resolved” because their size is less than the SIMBA beam, *before* deconvolution (hereinafter named as umms#). We also list in Table 2.5 coordinates and peak intensity of these detections (estimates of sizes cannot be given), most of which are small components ($\leq 1M_{\odot}$) of large complex structures, but many (including isolated ones) appear in some way linked to the star formation activity, as we will see in the next two Chapters. However, we cannot exclude that some of them are artefacts of the finding algorithm and all these detections deserve dedicated observations with higher sensitivity and resolution in order to confirm them, to clarify their nature and to give reasonable estimates of their masses and sizes. In the following of this Chapter, that mainly deals with global/statistical properties of the region instead of with details of star formation, we will refer only to the sample of Table 2.4. The adopted approach is bound to affect the statistic of the faintest

¹³ The emission of a point-like source produces on the map a spot having size equal to the telescope HPBW. For the same reason the emission of extended sources appears broadened and its real dimensions can be recovered, if the source is resolved, by means of a beam deconvolution.

sources, dropping objects that would fall in the robust sample if the sensitivity were higher. But, again, we do not expect major effects *above* the completeness limit.

As we have anticipated in Section 2.1.5, we searched also for possible associations between $^{13}\text{CO}(2-1)$ and dust condensations (Table 2.3) finding that, in general, the continuum emission is able to track even denser zones than $^{13}\text{CO}(2-1)$ line. Considering the gas clumps associated to a group of dust cores, in fact, the total mass estimated from line data is larger but quite similar to the mass traced by dust continuum (see next Section), the average value of their ratio being $M_{gas}(\text{line})/M_{gas}(\text{continuum})= 1.44 \pm 0.11$.

Table 2.4: *Dust cores found by CLUMPFIND: the robust sample.*

Core designation	RA(J2000)	DEC(J2000)	Deconvolved Size (pc)	Peak Flux (mJy/beam)	Integrated Flux (Jy)	Mass (M_{\odot})
MMS1	8:45:33.4	-43:50:20.1	0.19	501	3.17	32
MMS2	8:45:34.8	-43:52:04.1	0.17	668	3.70	37
MMS3	8:45:40.1	-43:51:32.3	0.19	544	3.59	36
MMS4	8:46:34.6	-43:54:36.0	0.25	1702	8.79	88
MMS5	8:46:49.4	-43:53:08.2	0.09	155	0.28	3
MMS6	8:46:52.3	-43:52:59.9	0.24	121	0.20	2
MMS7	8:47:58.8	-43:39:47.9	0.08	180	0.43	4
MMS8	8:48:39.4	-43:31:23.9	0.02	77	0.08	0.8
MMS9	8:48:43.0	-43:31:48.0	0.08	87	0.15	1.5
MMS10	8:48:43.0	-43:37:08.0	0.03	83	0.13	1.3
MMS11	8:48:45.1	-43:37:40.1	0.06	82	0.12	1.2
MMS12	8:48:49.0	-43:32:28.0	0.13	617	1.77	18
MMS13	8:48:49.7	-43:33:15.9	0.05	69	0.04	0.4
MMS14	8:48:51.1	-43:31:08.1	0.08	117	0.12	1.8
MMS15	8:48:52.6	-43:30:28.1	0.03	91	0.12	1.2
MMS16	8:48:53.3	-43:31:00.1	0.05	163	0.23	2.3
MMS17	8:48:57.8	-43:38:28.0	0.15	156	0.76	7.6
MMS18	8:49:03.6	-43:38:12.1	0.09	105	0.28	2.8
MMS19	8:49:08.9	-43:35:48.1	0.11	126	0.38	3.8
MMS20	8:49:11.8	-43:35:24.0	0.09	126	0.19	1.9
MMS21	8:49:13.2	-43:36:28.1	0.17	345	1.76	18
MMS22	8:49:27.4	-43:17:08.2	0.09	567	1.32	13
MMS23	8:49:29.5	-44:04:36.1	0.06	71	0.14	1.4
MMS24	8:49:31.0	-43:17:08.2	0.06	421	0.76	7.6
MMS25	8:49:31.0	-44:10:44.1	0.21	258	1.70	17
MMS26	8:49:33.8	-44:10:59.9	0.20	298	1.55	15
MMS27	8:49:34.6	-44:11:56.0	0.18	710	2.85	28
MMS28	8:50:09.4	-43:16:27.8	0.06	118	0.20	2.0
MMS29	8:50:12.2	-43:17:16.1	0.10	177	0.51	5.1

Table 2.5: *Possible dust cores found by CLUMPFIND, but with size less than the SEST beam (before deconvolution).*

Core Designation	RA(J2000)	DEC(J2000)	Peak Flux (mJy/beam)	Peak Flux (\times local r.m.s.)	Integrated Flux (Jy)	Mass (M_{\odot})
umms1	8:46:25.8	-43:42:26.6	310	6	2.78	28
umms2	8:46:37.2	-43:18:34.9	86	4	0.05	0.5
umms3	8:46:37.2	-43:19:55.6	175	8	0.12	1.2
umms4	8:46:49.0	-43:20:27.1	111	5	0.09	0.9
umms5	8:46:50.4	-43:21:15.1	90	4	0.05	0.5
umms6	8:46:56.6	-43:53:07.1	97	6	0.16	1.6
umms7	8:47:28.5	-43:27:00.4	75	4	0.04	0.4
umms8	8:47:37.3	-43:43:40.1	71	4	0.03	0.3
umms9	8:47:39.5	-43:43:48.0	65	4	0.02	0.2
umms10	8:47:41.0	-43:26:28.3	84	5	0.12	1.2
umms11	8:47:42.5	-43:43:39.1	139	8	0.10	1.0
umms12	8:47:46.8	-43:25:55.4	79	5	0.03	0.3
umms13	8:47:55.7	-43:39:41.5	81	5	0.07	0.7
umms14	8:47:57.9	-43:38:59.6	110	7	0.17	1.7
umms15	8:48:02.4	-43:39:15.5	107	7	0.12	1.2
umms16	8:48:15.7	-43:47:07.8	92	5	0.06	0.6
umms17	8:48:23.0	-43:31:31.1	63	4	0.07	0.7
umms18	8:48:26.7	-43:31:39.7	66	4	0.04	0.4
umms19	8:48:33.1	-43:30:43.9	83	6	0.11	1.1
umms20	8:48:35.5	-43:30:59.8	83	6	0.07	0.7
umms21	8:48:36.8	-43:31:13.8	76	5	0.07	0.7
umms22	8:48:36.6	-43:16:51.2	84	4	0.05	0.5
umms23	8:49:24.2	-43:13:13.4	95	6	0.12	1.2
umms24	8:49:27.1	-43:12:33.5	86	6	0.07	0.7
umms25	8:49:27.8	-43:12:17.3	83	6	0.05	0.5
umms26	8:49:59.0	-43:22:55.6	91	6	0.09	0.9

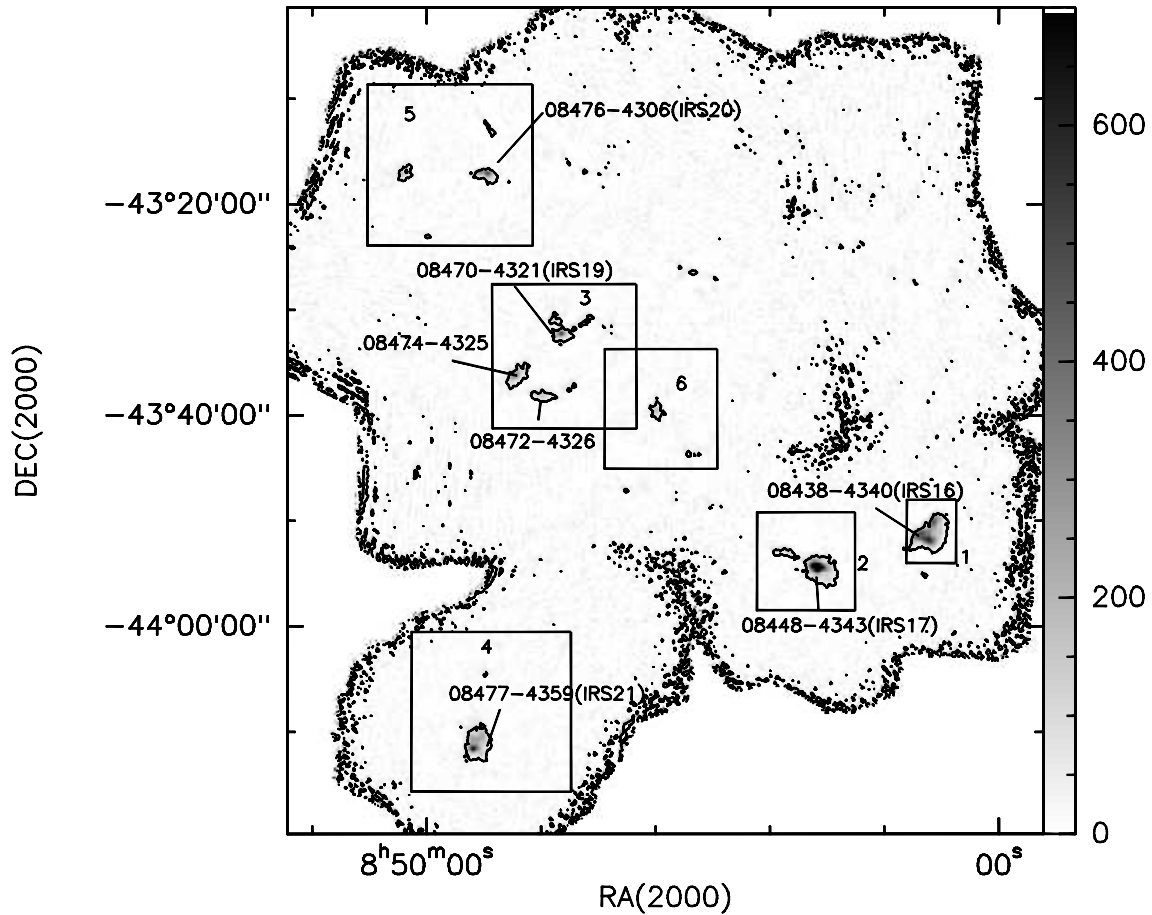


Figure 2.13: *SIMBA* 1.2-mm continuum map of cloud *D* (greyscale). The scale (in *mJy/beam*) is indicated through the bar on the right and the contour at 60 *mJy/beam* ($\sim 3\sigma$) is also drawn. The red *IRAS* sources coincident with the most intense features are labelled (along with the designation adopted by Liseau et al. (1992)). Six areas including the main mm sources are enclosed within boxes and numbered, and are shown zoomed-in in the following figures.

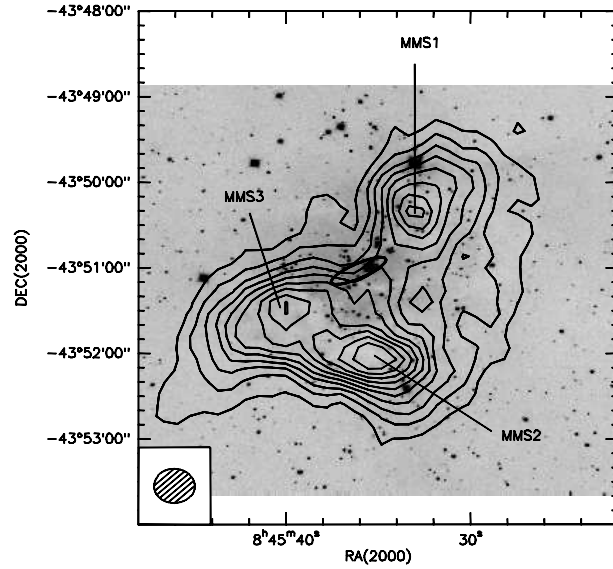


Figure 2.14: *NTT/SofI* image of IRS16 (at K_s), taken on December 2005, overlaid with a contour map of the 1.2-mm continuum emission (area 1 in Fig. 2.13). Contours are in steps of 60 mJy/beam ($\sim 3\sigma$) from 60 to 600 mJy/beam. The cores are labelled and the IRAS uncertainty ellipse is also drawn. The SEST beam is displayed in the lower left box.

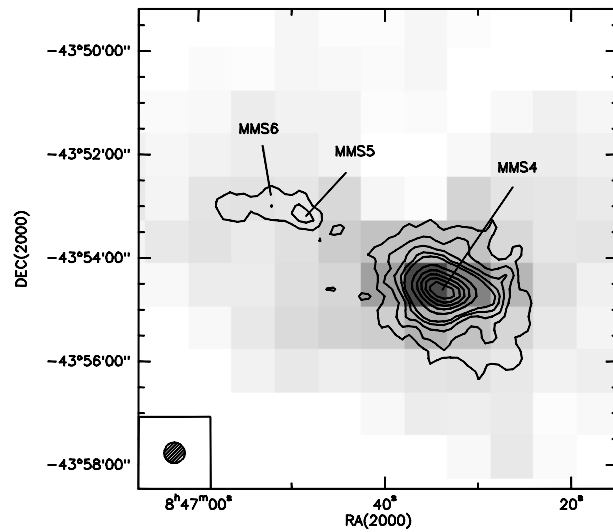


Figure 2.15: Contour map of the 1.2-mm continuum emission from the region including IRS17 (area 2 in Fig. 2.13). Contours are in steps of 60 mJy/beam ($\sim 3\sigma$) from 60 to 300 mJy/beam and in steps of 240 mJy/beam from 540 to 1500 mJy/beam. The cores are labelled and the SEST beam is drawn in the lower left box. Underlying, the $^{12}\text{CO}(1-0)$ emission integrated from 0 to 20 km s^{-1} (grayscale, from 30 to 250K km s^{-1}).

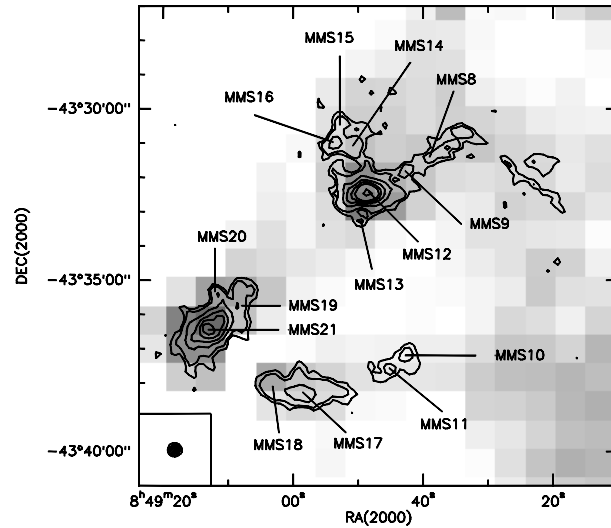


Figure 2.16: Contour map of the 1.2-mm continuum emission from the region including IRS19 (area 3 in Fig. 2.13). Contours are: 40 mJy/beam ($\sim 2\sigma$) the lowest one, then in steps of 60 mJy/beam ($\sim 3\sigma$) from 60 to 300 mJy/beam and 540 mJy/beam the highest one. The cores are labelled and the SEST beam is drawn in the lower left box. Underlying, the $^{12}\text{CO}(1-0)$ emission integrated from 0 to 20 km s^{-1} (grayscale, from 30 to 200 K km s^{-1}).

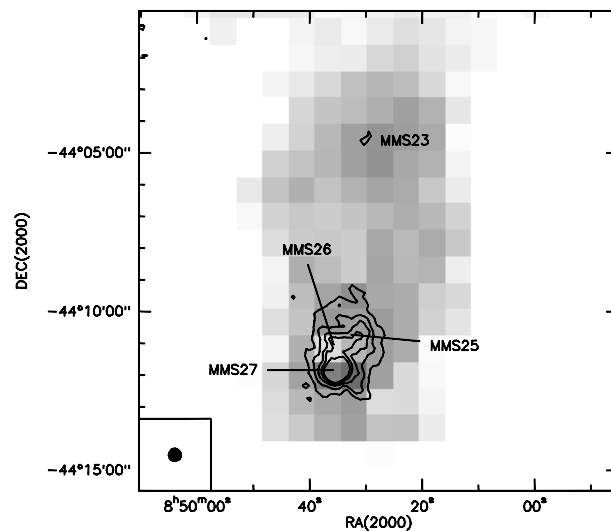


Figure 2.17: Contour map of the 1.2-mm continuum emission from the region including IRS21 (area 4 in Fig. 2.13). Contours are in steps of 60 mJy/beam ($\sim 3\sigma$) from 60 to 300 mJy/beam. The cores are labelled and the SEST beam is drawn in the lower left box. Underlying, the $^{12}\text{CO}(1-0)$ emission integrated from 0 to 20 km s^{-1} (grayscale, from 30 to 150 K km s^{-1}).

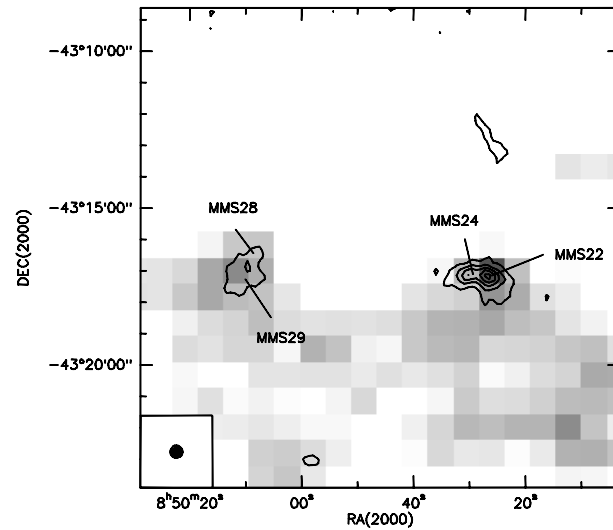


Figure 2.18: Contour map of the 1.2-mm continuum emission from the region including IRS20 (area 5 in Fig. 2.13). Contours are in steps of 120 mJy/beam ($\sim 6\sigma$) from 60 to 540 mJy/beam. The cores are labelled and the SEST beam is drawn in the lower left box. Underlying, the $^{12}\text{CO}(1-0)$ emission integrated from 0 to 20 km s $^{-1}$ (grayscale, from 30 to 150 K km s $^{-1}$).

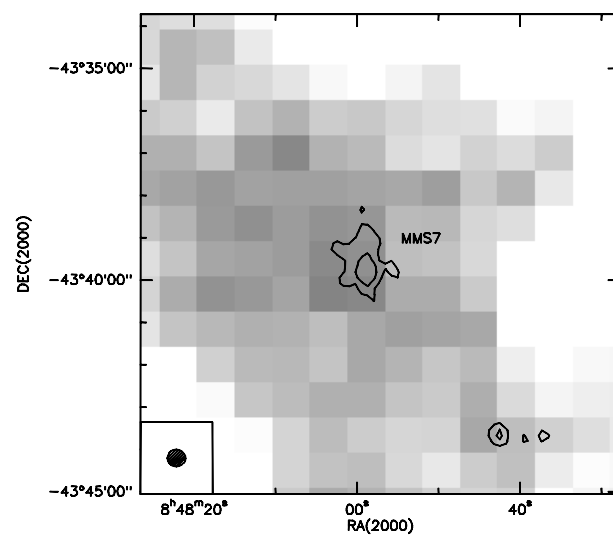


Figure 2.19: Contour map of the 1.2-mm continuum emission from the region at the centre of the mapped area (6 in Fig. 2.13). Contours are in steps of 60 mJy/beam ($\sim 3\sigma$) from 60 to 120 mJy/beam. The cores are labelled and the SEST beam is drawn in the lower left box. Underlying, the $^{12}\text{CO}(1-0)$ emission integrated from 0 to 20 km s $^{-1}$ (grayscale, from 30 to 150 K km s $^{-1}$).

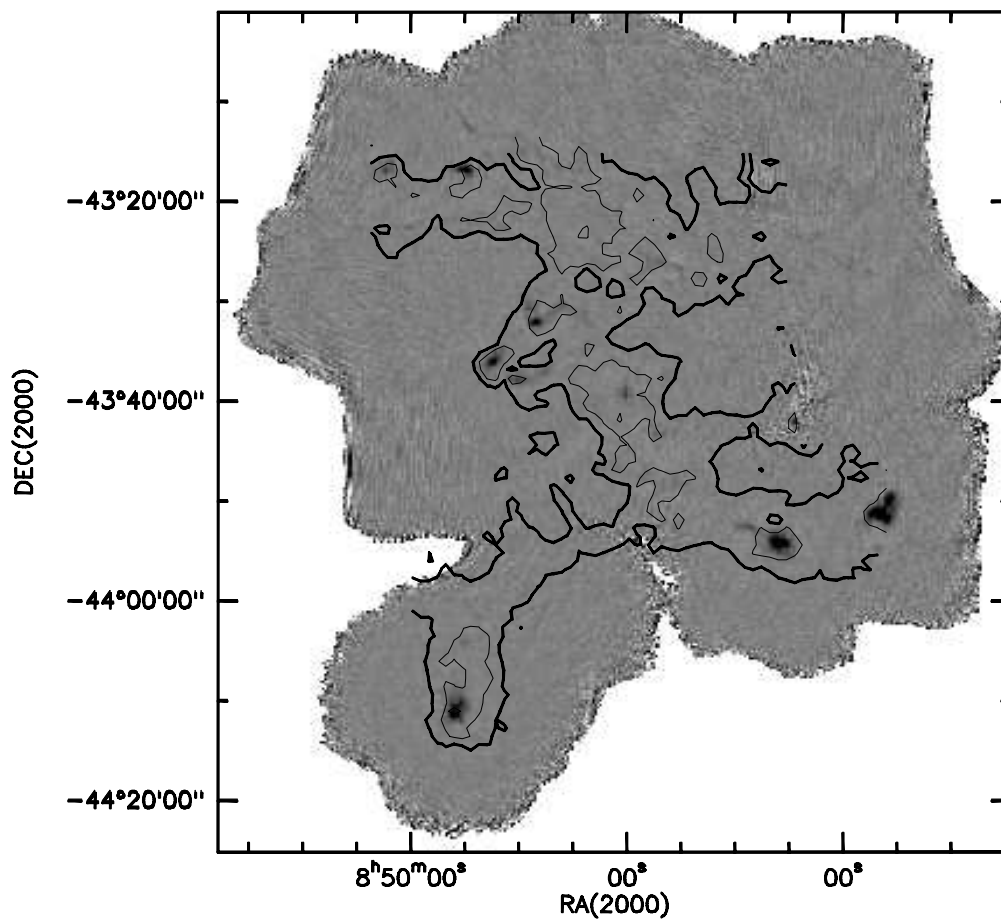


Figure 2.20: Map of $CO(1-0)$ emission from the observed area within cloud D (contours), integrated from 0 to 20 km s^{-1} , obtained with a beam of $43''$. This is overlaid with the SIMBA 1.2 mm continuum map (grayscale, beam of $24''$). The thick solid line marks the contour at 25 K km s^{-1} , whereas the light solid line marks the contour at 60 K km s^{-1} .

2.2.4 Core properties

The core masses have been determined accordingly to the expression (*e.g.* Faúndez et al. 2004):

$$M_{dust} = \frac{S_\nu d^2}{k_\nu B_\nu(T_{core})}, \quad (2.6)$$

where S_ν is the flux integrated over the pixel assigned to each core, $d=700$ pc is the distance to Vela-D, k_ν is the dust opacity (see Section 4.2.1) and $B_\nu(T_{core})$ the Planck function¹⁴ evaluated at the core estimated temperature T_{core} .

We adopted the same $k_{1.3}$ as in (Motte et al. 1998) and (Testi & Sargent 1998): $k_{1.3} = 0.5 \text{ cm}^2 \text{ g}^{-1}$ at 1.3 mm. However, values as high as $1 \text{ cm}^2 \text{ g}^{-1}$ are possible, typical of very dense regions (atomic hydrogen density, $n_H > 10^7 \text{ cm}^{-3}$; Ossenkopf & Henning 1994), such as, *e.g.*, circumstellar envelopes.

Our choice of the temperature is based on the results of other works. By fitting with a grey-body emitter having emissivity¹⁵ $\epsilon_\lambda \sim \lambda^{-1}$ the IRAS fluxes at 60 and 100 μm , Liseau et al. (1992) find temperatures in the range 30–43 K for IRS 17, 18, 19, 20 and 21. Faúndez et al. (2004) derive a typical temperature of 32 K for the cold dust component by a two-component fit to the SEDs in their sample of southern high-mass star-forming regions. Beltrán et al. (2006) find a mean dust temperature of 28 K by fitting the SED's in their sample of southern massive protostar candidates longward of 60 μm . Hence, we adopted the canonical value of 30 K for all the cores. Nevertheless, some of the cores may be colder pre-stellar cores, and decreasing the dust temperature to 15 K would increase the derived masses by a factor 2.5. Actually, an external heating could drive the temperature of pre-stellar cores towards higher values. Evidence of heating resulting from a strong external radiation field has been found for protostellar cores in Orion by Jørgensen et al. (2006). However, the presence of energetic sources in the mapped region of Vela-D should be excluded on the basis of the work presented in the next Chapter (see also Lorenzetti et al. 1993, Elia et al. 2007).

From the dust mass of each core the molecular mass can thus be

¹⁴ $B_\nu(T) = \frac{2h\nu^3}{c^2} \cdot \frac{1}{e^{\frac{h\nu}{kT}} - 1}$.

¹⁵The emissivity ϵ of a gray body is the ratio between its emission and the black body one.

evaluated by assuming a gas to dust ratio of 100.

While the possible effects on the core mass distribution of different assumptions regarding temperature and opacity will be addressed in Section 2.2.6, it is important to mention here the other possible causes of errors in deriving the masses. Massi et al. (2007) has performed a deep analysis of the contamination of the observed emission due to (i) line emission, (ii) free-free emission and (iii) synchrotron radiation concluding that the contribution of these emissions should lie under 10-20% of the measured flux for all cores (see Massi et al. 2007 for details).

The deconvolved sizes and the masses of the cores listed in Table 2.4 range from 0.03 to 0.25 pc and from 0.4 to 88 M_{\odot} respectively, while their spatial distribution exhibits a high degree of clustering. The derived sizes span the interval from the observed diameter of pre-stellar cores in cluster-forming regions to that of cluster-forming clumps (or isolated pre-stellar clumps). The achieved typical sensitivity of 20 mJy/beam translates into a point source mass sensitivity (at a 1 σ level) of $\sim 0.2M_{\odot}$, by using the above adopted temperature, opacity and distance.

2.2.5 Core mass-size relationship

The observed mass *vs* size relationship (uncorrected for beam) is plotted in Fig. 2.21. The “under-resolved” detections reported in Table 2.5 fall below the resolution limit given by the beam size (the vertical line in figure).

When assessing the sensitivity of a survey in the mm continuum in terms of core masses, one has to take into account the extent of the emitting area. Since the sensitivity limit is a flux density per solid angle, for a given total flux density an extended source is less likely to be detected than a point source. In fact, assuming constant dust opacities and temperatures, the source mass is proportional to the *total* (*i.e.*, integrated over the solid angle) flux density. Then, the *mass* sensitivity limit is given by the flux sensitivity per solid angle multiplied by the source area and so increases with increasing areas. This is illustrated in Fig. 2.21: all sources lie above a line following a $M \sim D^2$ relation (where D is the core size), which represents the actual sensitivity limit. Clearly, the data points outline a steeper dependence

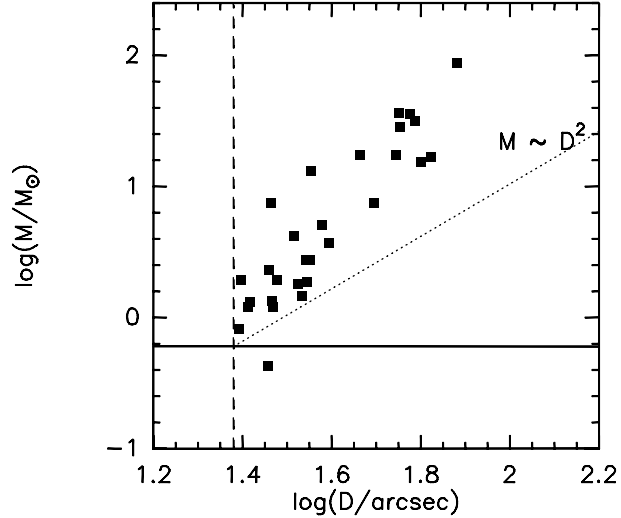


Figure 2.21: *Core mass vs size (uncorrected for beam)*. The vertical dashed line marks the SEST beam size, whereas the horizontal solid line shows the $3\text{-}\sigma$ detection limit for point sources. A dotted line has also been drawn following a D^2 relation, *i.e.*, the sensitivity limit to extended sources (see text).

of mass *vs* size; a linear fit indicates a $M \sim D^{3.7}$ relation. This appears to be intrinsic to the core population, indicating that the sample is likely to be complete at least down to $\sim 1 - 1.3 M_{\odot}$.

A more significant relation is obtained by fitting *deconvolved size* (see note 13) *vs* mass, yielding $M \sim D^{1.7}$ (see Fig. 2.22). This is flatter than found for pre-star-forming regions in the range $0.01 - 10$ pc by, *e.g.*, Heithausen et al. (1998) using CO emission ($M \sim D^{2.31}$), but steeper than found for pre-stellar cores by (Motte et al. (2001)) using sub-mm emission ($M \sim D^{1.1}$). Instead, Reid & Wilson (2005) find $M \sim D^x$ with $x \sim 1.5 - 2.1$ in the high-mass star-forming region NGC7538 from sub-mm observations, more in agreement with our result. However, note that 9 out of the 29 sources in our robust sample are smaller than the HPBW, *i.e.*, their beam-convolved size is < 1.5 HPBW. Then, the core size may become highly uncertain at the lowest end of the distribution. Moreover, as we will explain in the next Section, the actual exponent is sensitive to the fraction of warm dense gas within the sample, decreasing with increasing this fraction. When crudely accounting for this effect, the exponent lies between 1.5 and 1.

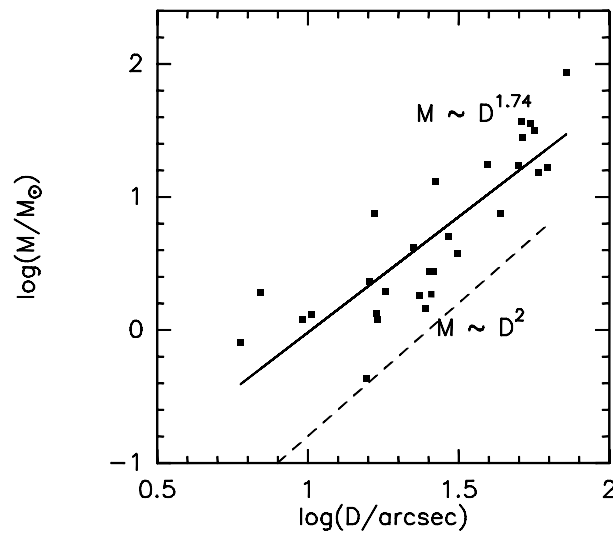


Figure 2.22: Core mass vs deconvolved size. The solid line is obtained by a fit ($M \sim D^{1.74}$), whereas the dashed line follows a D^2 relation, i.e., the sensitivity limit to extended sources (see text).

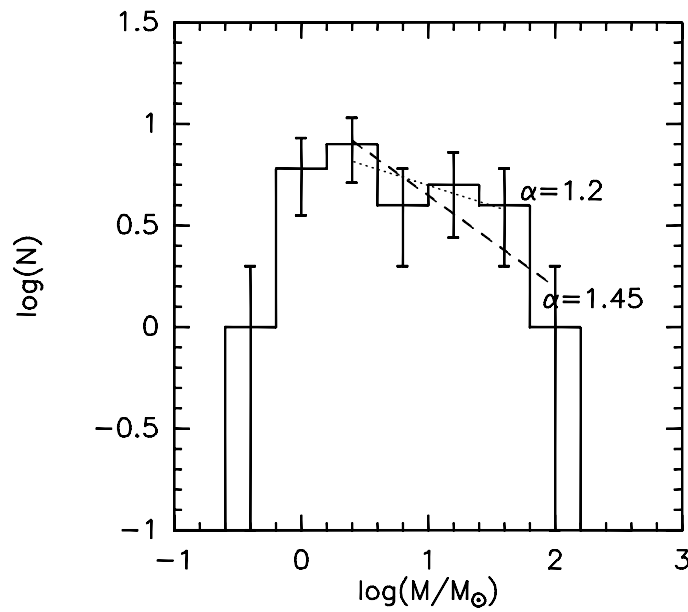


Figure 2.23: Mass spectrum of the mm cores. The error bars indicate the r.m.s. assuming a Poisson statistic. A dashed line shows a $dN/dM \sim M^{-1.45}$ relation, a dotted line shows a $dN/dM \sim M^{-1.2}$ relation. The estimated completeness limit is $\sim 1 - 1.3 M_{\odot}$ (see text).

2.2.6 Core mass spectrum

The core mass spectrum is shown in Fig. 2.23. The error bars are the r.m.s. estimated by assuming a Poisson statistic. The distribution appears quite flat and drops abruptly at $\sim 10^2 M_{\odot}$. A power-law fit to the points *above* the completeness limit indicates that the mass spectrum follows a relation $dN/dM \sim M^{-\alpha}$, with $\alpha = 1.45 \pm 0.2$ ($\chi^2 = 1.10$). This is shallower than a Salpeter-like Initial Mass Function ($\alpha \sim 2.35$, see Chapter 1), being more similar to the mass spectrum of molecular cores in pre-star-forming regions (see, *e.g.*, Heithausen et al. 1998). However, Fig. 2.23 suggests that fitting the core mass function with two power-law segments would be more adequate. In this case, we obtain $\alpha = 1.20 \pm 0.34$ ($\chi^2 = 0.42$) up to $M \sim 40 M_{\odot}$, with a significantly larger α for $M > 40 M_{\odot}$. As for (sub-)mm surveys, the derived spectral index roughly agrees with that determined by Kerton et al. (2001) for KR140 between ~ 0.7 – $100 M_{\odot}$ ($\alpha = 1.49$), and by Mookerjee et al. (2004) between 37 – $16000 M_{\odot}$ in R106 ($\alpha \sim 1.5 - 1.7$). Reid & Wilson (2005) also find a flat distribution ($\alpha = 0.9 \pm 0.1$) between $\sim 1 - 100 M_{\odot}$ in NGC7538, then steepening to $\alpha = 2.0 - 2.6$.

Before discussing the link between the mass spectrum and the IMF (see Section 1.2.1), we shortly evaluate here the spectrum dependence on the assumed dust opacity and temperature.

Dependence on dust opacity and temperature - The slope of the mass spectrum and the mass-size relationship are not sensitive to the adopted dust opacity, temperature and distance as long as *all* cores are characterized by the same *mean* opacity and temperature and lie at the same distance. Large errors may only be caused by having detected thermal dust emission coming from environments whose temperatures and/or dust opacities differ within the sample. In fact, the identified cores are likely to be a mixture of protostellar envelopes (those coinciding with the red IRAS sources), pre-protostellar cores/Class 0 sources and transient structures.

In Chapter 3 we will discuss the coincidence between mm cores and NIR/MIR/ FIR sources and the nature of the single cores. Here, just to test what would be the effect of gathering together sources with different temperatures and opacities, we have subdivided the robust sample of Table 2.4 into a subset of objects (10 out of 29) that may be associated with FIR sources (IRAS or MSX, see next Chapter) and a

subset of objects without this kind of association (the remaining 19). To the first group we have attributed a temperature of 30 K and a dust opacity $k_{1.3} = 1 \text{ cm}^2 \text{ g}^{-1}$, whereas to the second group we have attributed a temperature of 15 K and a dust opacity $k_{1.3} = 0.5 \text{ cm}^2 \text{ g}^{-1}$ (as usually found in the literature for pre-protostellar cores; *e.g.*, Motte et al. 1998, Motte et al. 2001, Nutter et al. 2006). By only adopting two different temperatures (*i.e.*, using a same dust opacity $k_{1.3} = 0.5 \text{ cm}^2 \text{ g}^{-1}$) we obtain a similar mass spectrum ($\alpha = 1.44$) but a less steep mass-size relation ($M \sim D^{1.38}$), whereas two different temperatures and two different opacities yield both a steeper mass spectrum ($\alpha = 1.89$) and a shallower mass-size relation ($M \sim D^{1.12}$).

Link with the IMF - The core mass spectrum between ~ 1 and $\sim 100 M_{\odot}$ is shallower than the stellar IMF in the same mass range, even in the worst case of a mixture of cores of different densities and temperatures.

Massi et al. (2006) find a standard stellar IMF for a sample of 6 young star clusters in the D cloud (5 of them associated with observed mm cores), hence the core mass spectrum is more reminiscent of the mass spectrum of molecular clumps, as already noted. This means that the larger cores underwent fragmentation, but this has not been observed at mm wavelengths because of low resolution. *The core mass spectrum should then be compared with the cluster mass spectrum (i.e., the mass distribution of stellar clusters) rather than the stellar IMF. Only at the lower mass end, the core mass spectrum may be dominated by the precursors of lower mass isolated stars and is likely to approximate an IMF.*

Remarkably, Lorenzetti et al. (1993), based on FIR fluxes from the IRAS Point Source Catalogue, derived a mass distribution with an index ~ 1.5 for the brightest protostars in the Class I stage associated with the Vela Molecular Ridge. As found by Massi et al. (1999), although the most luminous IRAS sources coincide with embedded young clusters, it is the most massive star of each cluster that appears to dominate the FIR emission. If so, the similarity between core mass spectrum and Class I source mass spectrum suggests that the mass of the most massive stars originated by a core is roughly proportional to the core's mass itself, at least at the high mass end. So, *the core mass spectrum would reflect the mass spectrum of the most massive stars of ev-*

ery stellar group and, probably, the cluster mass spectrum, whereas the stellar IMF would be dominated by the fragmentation undergone by the single cores.

Note that if the number of cluster members and the mass of the most massive star in a cluster both depend on the mass of the parental core, then there must also exist an observable relationship between number of cluster members and mass of the most massive star in a cluster. This would confirm that small stellar clusters cannot produce massive stars, explaining the possible lack of massive stars in the region as suggested by the results of the NIR observations by *Massi et al. (2006)*.

Chapter summary - In this Chapter we have analyzed the large scale emission of the Vela-D interstellar medium by means of tracers of both molecular and dust continuum emission. The $^{12}\text{CO}(1-0)$ line map mainly showed how the diffuse gas component presents large scale filaments and shell- or arc-like structures with a clumpy morphology. The $^{13}\text{CO}(2-1)$ emission resulted more suited for the study of such clumps, whose masses, obtained by means of the application of a decomposition algorithm, have been used to produce the mass spectrum and the mass *vs* size distribution. The dust map showed an even more concentrated morphology able to trace the densest cloud regions, locations of the most recent (proto-)stellar objects, analysed again by means of mass-size and mass spectrum tools.

The main results can be itemized as follows:

- A tight link exists between both the gas and (especially) the dust distribution and the location of the brightest point-like FIR sources known in the field.
- There is not clear evidence if the arc-like structures are produced by expanding shells, by stellar winds (both driven by nearby young massive stars) or by internal cloud turbulent motions (contributions from supernova remnants are excluded). If an expanding Hii region is considered, its dynamical age is compatible with

that estimated for the star formation activity.

- In two regions, the presence of both two velocity components and arc-shaped morphology in the vel-pos diagrams can be interpreted as a signature of expanding shells compressing the gas that can be thought as the cause of the observed cluster formation.
- The line profiles near the bright FIR sources often appear clearly broadened, suggesting the presence of outflows (13 candidates).
- The Clump mass spectrum of $^{13}\text{CO}(2-1)$ observations presents a value of the spectral index ($\alpha = 2.0 \pm 0.3$ for the “corrected” sample and $\alpha = 1.8 \pm 0.3$ for the original CLUMPFIND output) typical for interstellar molecular clouds and marginally compatible with that obtained for dust cores.
- The core mass spectrum presents a spectral index $\alpha \sim 1.45 - 1.9$ depending on the temperature and opacity distribution within the sample. Thus the spectrum appears flatter than a standard IMF in the range $\sim 1 - 100 M_{\odot}$, but agrees with the typical mass spectrum of molecular clumps.

Chapter 3

Vela-D in the Infrared

In this Chapter we describe the infrared emission of Vela-D. Two published papers (De Luca et al. 2007 and Giannini et al. 2007) contain most of the results presented here.

Thermal emission of (proto-)stellar dust envelopes dominates this spectral regime. As we have seen in Chapter 1, as far as the young objects evolve, their emission peak shifts from the far- to the near-infrared, because of the temperature increase and of the dust envelope dissipation. Ro-vibrational H_2 transitions in warm gas can be also revealed in the IR and the most commonly observed spectral line (1-0S(1) at $2.12 \mu\text{m}$, see Section 4.1.1) is used to image hot molecular gas, heated by protostellar jets impacting with their cloud. The infrared sky is only partially accessible from hearth, mainly in the atmospheric windows of the J ($1.25 \mu\text{m}$), H ($1.65 \mu\text{m}$) and K ($2.2 \mu\text{m}$) photometric bands. Thus the investigation by means of space born observations, constituted by both large surveys (IRAS, MSX missions) and dedicated observations (Spitzer Space Telescope), represents an essential part of this Chapter.

The dust cores of Table 2.4 are the starting point of the work described here. By using infrared point source catalogues (2MASS [§ 3.1.1], IRAS [§ 3.2.1], MSX [§ 3.2.2] and a NIR Vela-D catalogue by Massi et al. 1999 [§ 3.1.2]) combined with new ground based observations (J, H, K and H_2 at $2.12 \mu\text{m}$ with SofI [§ 3.1.3] and N broad band at $10.4 \mu\text{m}$ with Timmi2 [§ 3.2.3]), we characterize the dust core (proto-)stellar population and identify the counterparts of the cores, *i.e.* the sources which dominate the dust heating, according to spatial coincidence, infrared colours and spectral energy distributions. We describe in details the

population of the core MM1 (§ 3.3.2) to exemplify the adopted method and present the statistics on active *vs* inactive cores and on evolutionary stage classification, while a *case by case* analysis of each core is reported in the Appendix A.

A new, unbiased Spitzer-MIPS imaging survey of Vela-D is presented in the last part of the Chapter (§ 3.4). This latter survey revealed a total of 849 sources at 24 μm , 52 of which also have a 70 μm counterpart. Then we discuss: (i) the correlation between the Spitzer compact sources and the molecular contour levels, for finding an estimate of the possible off-cloud source contamination (§ 3.4), (ii) the protostellar population classification of the whole cloud, by means of K_s *vs* K_s -[24] and [24] *vs* [24]-[70] colour diagrams¹ (§ 3.4.1), and (iii) the improvements in our knowledge of the MIR-FIR point sources, with respect to the IRAS data, produced by Spitzer observations (§ 3.4.2).

3.1 Near-Infrared observations

3.1.1 2MASS (J, H, K bands)

The 2MASS (2 Micron All Sky Survey) project² performed, between 1997 and 2003, is a uniform scan of the entire sky in the three NIR bands J, H, and Ks (2.17 μm , slightly shifted with respect to the K band) to detect and characterize point sources brighter than about 1 mJy in each band, with Signal-to-Noise ratio (SNR) larger than 10, using a pixel size of 2.0". 2MASS used two highly-automated 1.3 m telescopes, one at Mt. Hopkins (AZ) and one at Cerro Tololo (Chile). This survey made available an unprecedented view of the Milky Way nearly free of the obscuring effects of interstellar dust and the first all-sky photometric census of galaxies brighter than $K_s=13.5$ mag, including galaxies in the 60-wide "Zone of Avoidance", where dust within the Milky Way renders optical galaxy surveys incomplete.

The main result of these observations, for our purpose, consists of a point source catalog of more than 470 million objects, containing, for each source, positions, magnitudes, astrometric and photometric

¹Here the magnitudes observed in the 24 and 70 μm filters are indicated by the symbols [24] and [70], respectively.

²<http://www.ipac.caltech.edu/2mass/releases/second/doc/explsup.html> .

uncertainties, associations with optical catalog sources and a number of flags indicating the quality of the photometry.

Given the huge number of sources within our square degree of the Galactic plane, some kind of filter was necessary searching for potential young objects. We have selected, for this work, all the catalog point sources having positive colors (*i.e.* $[J-H] > 0$ and $[H-K] > 0$). So the 2MASS sources considered, hereinafter named as 2M \ddagger following an internal numbering convention, constitute a sample of about $5 \cdot 10^4$ objects.

3.1.2 IRAC2 (J, H, K bands)

The IRAC2 (Moorwood et al. 1992) imaging data at the standard J, H and K broad band filters were obtained by our group (Massi et al. 1999) at the ESO/MPI 2.2 m telescope at La Silla (Chile). The 256×256 pixels array was used at a plate scale of 0.49 arcsec/pixel, resulting in a field of view of about 2×2 arcmin² on the sky.

A total of ≈ 1300 sources have been detected in K, ≈ 1200 in H and ≈ 800 in J, with limiting magnitudes of $K \approx 17.0$, $H \approx 18.0$ and $J \approx 18.5$ mag. In the following we will refer to these sources with the names MGL99 \ddagger . For the complete catalog see Massi et al. (1999).

3.1.3 SofI (J, H, K bands)

Broadband J , H , K_s and narrow-band images in the H_2 1-0S(1), $\lambda = 2.13 \mu\text{m}$ (see Chapter 4) were obtained on January 2006 by means of SofI³ (Lidmann et al. 2006) at the NTT ESO telescope (3.6 m diameter, located at La Silla, Chile). The total field of view is 4.9×4.9 arcmin², which corresponds to a plate scale of $0.29''/\text{pixel}$. All the observations were obtained by dithering the telescope around the pointed position and the raw imaging data were reduced by using standard procedures for bad pixel removal, flat fielding, and sky subtraction⁴. We will use

³ J and H images were obtained only for those fields containing the young clusters.

⁴Due to the extreme brightness of the NIR sky, long exposures are impossible, as they would saturate the chip, and many individual frames will normally have to be taken, and co-added to get a deep enough image. For most targets, the sky brightness is far in excess of the target brightness. This means that even tiny errors in sky subtraction can completely mess up an object. The dithering technique permits to overcome this difficulty. It consists in shifting the telescope pointing by a few arcseconds between different sets of images.

these images, in particular those in the H₂ filter, to study the spatial correspondence between NIR objects and FIR-mm emission.

3.2 Mid- and Far-Infrared observations

3.2.1 IRAS (12, 25, 60, 100 μm)

The Infrared Astronomical Satellite (IRAS, telescope diameter of 60 cm) was the first-ever space-based observatory to perform a survey of the entire sky at infrared wavelengths. The mission, a joint project of the US, UK and the Netherlands, lasted ten months (from January 25, 1983) and performed an unbiased, sensitive all sky survey at 12, 25, 60 and 100 μm . It discovered about $3 \cdot 10^5$ point-like sources (at the IRAS resolution) that constitute the IRAS Point Source Catalog, hereinafter IRAS-PSC (IRAS-PSC 1988). These objects are mainly stars with disks or envelopes of dust, wisps of warm dust called infrared cirrus, which could be found in almost every direction of space, and starburst galaxies (*i.e.* galaxies characterized by intense IR emission due to enhanced star formation).

The resolutions ranges from 0.5' at 12 μm to 2' at 100 μm , while the positional accuracy of sources detected by IRAS depends on their size, brightness and spectral energy distribution, but is usually better than 20". In the fields of view presented both in this Chapter (3.1) and in the Appendix A, the 3σ positional uncertainty will be represented by magenta ellipses⁵. Away from confused regions of the sky, the survey is complete to about 0.4, 0.5, 0.6, and 1.0 Jy at 12, 25, 60, and 100 μm , respectively.

When reducing the data, the first step is to divide the frames by a uniformly illuminated frame, the *flat field*, in order to remove differences in the sensitivity of each pixel. Then a median of all the images have to be performed. Because of the telescope shift in the pointings, the objects appear in different places in each of the individual images and hence disappear in the median which constitutes a good representation of the sky. After subtraction of this sky, all images frames have to be shifted until the stars line up and eventually they can be summed up to produce the final image. This procedure has the other advantage of removing bad pixels (*i.e.* pixels with no signal), fringing (*i.e.* interference patterns due to the detector) and many other chip defects that appear always at the same array position and disappear in the summed final image.

⁵The differences between the two axes are due to differences between the in-scan and cross-scan directions.

The IRAS-PSC contains position, flux density, uncertainty, association with known astronomical objects and various cautionary flags for each object. Particularly important are the ‘quality’ flag ($f_q = 1$ to 3), giving, for each band, the reliability of the flux measurement (where $f_q = 1$ denotes an upper limit), and an indicator, CC, which represents the correlation coefficient for each band, *i.e.* the point-like nature of the IRAS source encoded as alphabetic characters (A=100%, B=99%, ..., N=87%).

In the previous Chapter we have reported (Table 2.1), as useful signposts of possible star forming sites, all sources of the catalog falling within the Vela-D cloud and having increasing fluxes from 12 to 60 μm . Some properties of this source sample will be addressed in Section 3.3.4 starting from their colours (Figure 3.4). When addressing the core population, however, we will not consider any restriction and we will search for association between dust cores and all IRAS point sources of the original catalog. In Section 3.4.2 we will discuss the nature of the IRAS point sources by investigating the SPITZER-MIPS images.

3.2.2 MSX (8, 12, 14, 21 μm)

The Midcourse Space Experiment (MSX) mission (Price et al. 2001) was launched on April 1996 and acquired data for about ten months. This instrument had five line scanned focal plane arrays that spanned the spectral region from 4.2 to 26 μm . The point response function (see Note 17) was ~ 35 times smaller than the IRAS 12 μm detectors and the sensitivity in the MSX 8.3 μm band about four times more sensitive.

A full set of experiments mapped the Galactic Plane, the IRAS gaps, the zodiacal background, confused regions away from the Plane, deep surveys of selected fields at high galactic latitudes, large galaxies, asteroids and comets. The main result of the mission is a catalog of point sources whose fluxes are given at the wavelengths 8.3 (A), 12.1 (C), 14.7 (D) and 21.3 μm (E)⁶.

As we will see, despite the better resolution with respect to IRAS, and maybe due to the point source extraction algorithm, many sources of the MSX point source catalog (hereinafter MSX-PSC) are due, instead, to diffuse emission (like many IRAS sources, see Table 3.9).

⁶We will not use the B1 and B2 bands, whose quality is too low to be considered reliable.

Moreover, given the higher sensitivity and image quality of the A band, many objects detected in Vela-D have only upper limits at the other wavelengths (see Table 3.1). The limiting flux of our MSX source sample are: 0.1, 0.6, 0.5 and 1 Jy in bands A, C, D and E, respectively.

3.2.3 Timmi2 (N band)

Imaging in the N band at $10.4\mu\text{m}$ (N10.4 broadband filter) was carried out in January 2006 by means of Timmi2 (Saviane & Doublier 2005) at the 3.6 m ESO telescope (La Silla, Chile). The adopted plate scale is 0.3 arcsec/pxl, corresponding to a $96'' \times 72''$ field of view. The observations were obtained by chopping the signal and by nodding the telescope around the pointed position⁷. The raw data were reduced by using standard procedures for bad pixel removal and the observed field was flux calibrated by using photometric standard stars⁸ (HD29291, HD32887, HD123139). The photometric results are given in Tab. 3.1, together with the IRAS/MSX results. Although these latter refer to different effective wavelengths and different epochs, ground-based values are significantly lower than IRAS/MSX determinations. These discrepancies have been remarked on several times in the literature concerning YSO's (*e.g.* Walsh et al. 2001) and may be due to the

⁷Ground-based observing in the mid-infrared is different than observing in the near-infrared because of the very large thermal background flux that peaks near $10\mu\text{m}$. The “chopping” and “nodding” techniques have been developed for subtracting the background to high precision. The telescope’s secondary mirror is oscillated in a square-wave pattern at a frequency of several Hz. The detector alternately views two fields or “beams” on the sky called A and B. At the start of an integration, beam A is “on-source”, containing the object under observation, and beam B is “off- source”, containing blank sky. Thus we have two measurements: ($S1 = \text{source} + \text{skyA}$), and ($S2 = \text{skyB}$). Because the optical path through the telescope optics is different for the two chop positions, the background level is also slightly different ($\text{skyA} \neq \text{skyB}$) thus computing ($S1 - S2$) cancels most, but not all, of the sky emission. To completely remove the background, therefore, the telescope is “nodded” periodically ($\sim 2 - 4$ times per minute) to move the source from beam A to beam B, and the quantities ($S3 = \text{skyA}$) and ($S4 = \text{source} + \text{skyB}$) are recorded. Eventually, by computing:

$$(S1 - S2) + (S4 - S3) = ((\text{source} + \text{skyA}) - \text{skyB}) + ((\text{source} + \text{skyB}) - \text{skyA}) = 2 \cdot \text{source} ,$$

the background is properly subtracted.

⁸Photometric standard stars are objects whose photometry has been measured very carefully in various bands of photometric systems. They are used as references to calibrate flux, or magnitude, of the observed object.

higher environmental contamination suffered by the larger IRAS/MSX beams. We will use the names DGL \ddagger to refer to these objects.

3.2.4 SPITZER-MIPS (24, 70 μm)

Vela-D cloud was observed (Giannini et al. 2007) by means of MIPS, the Multiband Imaging Photometer for Spitzer (Rieke & MIPS Team 2004), on board the Spitzer Space Telescope (Werner et al. 2004). This telescope is a space-borne, cryogenically-cooled infrared observatory⁹ that covers the wavelength range between 3 and 180 μm with the aim of investigating: brown dwarfs and super-planets, debris disks around nearby stars, ultra-luminous infrared galaxies and AGN, and the early Universe, through highly red-shifted optical-ultraviolet radiation. The telescope is equipped with two (mainly) photometric (IRAC and MIPS, respectively for the Mid- and Far-IR) and one spectroscopic (IRS) instruments. In particular, the data analysed in this work consist of MIPS 24 and 70 μm emission maps.

The Vela-D observations covered ~ 1.15 (in R.A.) $\times 1.6$ (in dec.) degrees centered at α, δ (J2000) = $8^{\text{h}} 47^{\text{m}} 50^{\text{s}}$, $-43^{\circ} 42' 13''$ and $8^{\text{h}} 48^{\text{m}} 20^{\text{s}}$, $-43^{\circ} 31' 26''$ at 24 μm and 70 μm , respectively (orientation: 145° W of N).

Data were collected on 14 Jun 2006 and the mapping parameters were optimized for the 24 and 70 μm bands: as a consequence, the 160 μm map suffers from coverage gaps and saturation and will be not considered in the following.

The automatic pipeline (version S14.4.0) applied by the Spitzer Science Center to the raw data produced basic calibrated data (BCDs) constituted by small, flux calibrated frames ($5.4' \times 5.4'$ at 24 μm and $5.2' \times 2.6'$ at 70 μm) that we have used to obtain mosaiced, pointing refined images by means of the MOPEX package (provided again by the Spitzer Science Center, see Makovoz & Marleau 2005). The main instrumental artifacts have been removed from the mosaiced images by using this package. Minor problems of residual jailbars¹⁰ (expecially at 70 μm) and matching of the background level between adjacent frames

⁹Spitzer, launched on August the 25th 2003, is the final element in NASA's Great Observatories Program that includes the Hubble Space Telescope, the Compton Gamma-Ray Observatory and the Chandra X-Ray Observatory.

¹⁰Vertical pinstriping due slightly different bias level of the columns.

(at $24 \mu\text{m}$) are still visible close to the brightest objects, but they do not affect significantly the point source photometry discussed in this thesis.

The final $24 \mu\text{m}$ map global properties can be summarized as follows: pixel scale of $2.45''/\text{pixel}$, background r.m.s. of $0.3 \mu\text{Jy}/\text{arcsec}^2$, within the regions of high level of diffuse emission. The brightest sources saturate at the emission peak: for these we estimate a lower limit to the integrated flux of 4 Jy. In the $70 \mu\text{m}$ map the pixel scale is $4.0''/\text{pixel}$ and the background r.m.s. ranges between 23 and $94 \mu\text{Jy}/\text{arcsec}^2$. None of the detected sources appears saturated at this wavelength.

3.3 Infrared counterparts of dust cores

3.3.1 Association criteria

FIR-associations - Within molecular clouds the correlation between the positions of dust emission cores and FIR point-like sources represents an important method for obtaining a census of both the young stellar population and the different modalities of the star formation. To search the catalogs for sources associated with the dust cores listed in Tables 2.4 and 2.5, a working definition of the core size has to be provided first. Indeed, in that Table the core size (column 4), which results from the geometrical mean of the quantities Δx and Δy is given. These latter (see Tab. 3.2, column 2) are directly provided by the adopted search algorithm (Clumpfind), and indicate the FWHM of the linear profile of the core itself, along its x (right ascension) and y (declination) axes, respectively (Williams et al. 1994). The area covered by a dust core up to the (bidimensional) FWHM flux level can thus be roughly individuated by the ellipse centered at the peak coordinates and having axes Δx and Δy . For simplicity, we will call hereinafter this ellipse as dust FWHM-ellipse (see *e.g.* Fig. 3.1, where it is represented by the red, inner curve). Analogously, we operatively define as dust 2FWHM-ellipse that with axes $2\Delta x$ and $2\Delta y$ (red, outer ellipse in Fig. 3.1).

Searching for catalogued sources we use this FWHM value by adopting the following criterion: an IRAS or MSX point source is considered associated to the core if its positional uncertainty ellipse overlaps (or

is tangent to) the dust 2FWHM-ellipse. However, to evidence the most compelling cases, the association within one FWHM-ellipse are boldfaced in Tab. 3.1. With respect to the criterion adopted in similar works (*e.g.* Mookerjea et al. 2004, Beltrán et al. 2006), for which an IRAS/MSX source is associated to a core if it lies inside $90''/40''$, our criterion both takes into account the dust emission morphology and compensates for the large IRAS/MSX beam (§ 3.2.1, 3.2.2).

NIR-associations - Both the 2MASS catalog and the IRAC2 catalog reported in Massi et al. (1999) were searched for NIR associations, *i.e.* the sources that dominates the cores heating. Since the NIR sources positional accuracy is by far larger than the deconvolved core size, there is no need of defining a specific criterion for the association: we simply consider all the NIR sources falling within the FWHM-ellipse of each core that present a valid flux (not an upper limit) at least in a single band (J , H , K). Furthermore, we have tentatively selected the most probable NIR counterpart of the dust core according to the following criteria, suggested by the evolutionary stages described in Section 1.3.1:

1. Closeness to the peak of dust emission and to the FIR source possibly associated, if any.
2. Intrinsic excess in the two colours (J - H vs H - K) diagram (hereafter colour-colour diagram, see Section 1.1.2). This criterion makes it possible to pick up the NIR objects whose spectral energy distribution (SED) is typical of a young stellar object (YSO), and does not appear as stellar photosphere reddened by the intervening dust along the line of sight. In this context, to point out their intrinsic colour excess, we will define two loci in the colour-colour diagram (*e.g.* shaded regions in panel a of Fig. 3.2): the locus of the *red* objects (mainly T-Tauri), immediately to the right of the main sequence (reddened) stars, and the locus of the *very red* sources (mainly Class I and Herbig Ae/Be protostars), to the right of the T-Tauri (reddened) stars.
3. Largest spectral index $\alpha = d \log(\lambda F_\lambda) / d \log(\lambda)$ among those with $\alpha \geq 0$. Sources with $\alpha < 0$, in fact, are generally visible in the optical plates, thus this item cuts off at least bright visible stars.

3.3.2 The core MMS1

Here we describe a typical example of the approach adopted to detect the FIR/NIR counterparts of the *mm*-core MMS1. Similar considerations have been made for any individual *mm*-core, and all the results are provided in the Appendix A.

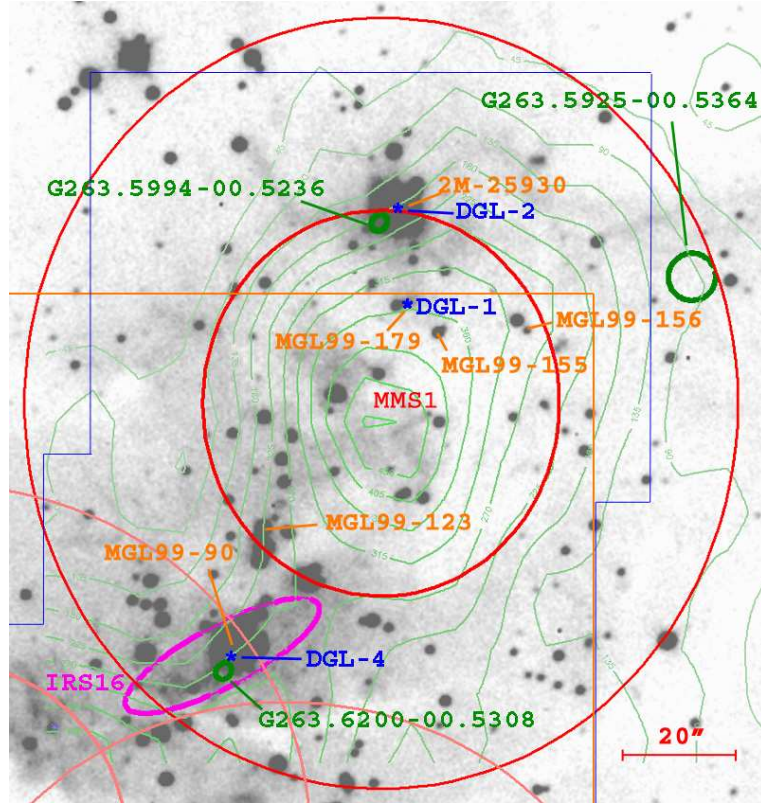


Figure 3.1: *MMS1* field of view (center $[J2000]$: $08:45:32.8, -43:50:12.3$). Grayscale image: H_2 emission; green contours: dust continuum (from 3σ , in steps of 3σ); red ellipses centered on the *mm*-peak: FWHM- and $2FWHM$ -ellipses within which the association with the IR sources has been searched for (at the bottom the ellipses pertaining to cores *MMS2-3* are also visible); magenta and green ellipses: 3σ positional uncertainties of the IRAS and MSX point sources, respectively; blue asterisks: position of the $10.4\mu\text{m}$ sources observed by *Timmi2*; 2MASS and IRAC2 NIR sources are labelled with $2M-\#$ and $MGL99-\#$, respectively; IRAC2-*Timmi2* fields of view are delimited by orange-blue lines.

As a first step, we overlay the contour map of dust emission (green contours, from $3\sigma = 3 \times 15 \text{ mJy/beam}$ in steps of 3σ) and the H_2

narrow-band (gray-scale) image (Fig. 3.1)¹¹. The red ellipses centered on the *mm*-peak represent the FWHM- and the 2FWHM-ellipses within which the association with the IR sources has been searched for (see Section 3.3.1). The magenta and green ellipses in Fig. 3.1 individuate the 3σ positional uncertainties of the IRAS and MSX point sources, respectively, while the blue asterisks signal the position of the $10.4\ \mu\text{m}$ sources observed by Timmi2 in the field of view delimited in figure by the blue line. We recall that the 2MASS and IRAC2 NIR sources are labelled 2M ‡ and MGL99 ‡ (Massi et al. 1999), respectively, while the $10.4\ \mu\text{m}$ sources are named: DGL ‡. The IRAC2 field of view does not cover the whole image and is depicted as the orange rectangle.

Both IRS16 (08438–4340, corresponding to MSX G263.6200-00.5308 and DGL 4) and G263.5925-00.5364 are located outside the FWHM-ellipse and do not appear directly associated to the core, while the association is more compelling with the sources DGL 1, DGL 2 and G263.5994-00.5236. The IRAS source coincides with a young NIR cluster and an Hii region and is located at the center of the region bordered by the cores MMS1-2-3, almost equidistant from all of them. The NIR cluster was investigated in detail by Massi et al. (2003) and we complement those data with the new *N*-band observation that points out the presence of a very diffuse emission, indicated as DGL 4, corroborating the hypothesis that the FIR source can be originated by warm circumstellar matter associated with the most luminous (in the NIR) cluster member, MGL99 90. Also the MSX source G263.5295-00.5364, that falls at the western border of the 2FWHM-ellipse, does not seem to be related to the dust peak. It has been detected at $8\ \mu\text{m}$ only and, presumably, such flux arises from diffuse emission, as an inspection of the MSX image suggests¹².

To feature the NIR stellar content close to the peak position we give in Fig. 3.2-a the colour-colour diagram of all the detected sources within the FWHM-ellipse. Here are also drawn: the locus of the main sequence, class V stars (Tokunaga 2000, dark curve), the locus of the

¹¹Instead of the J, H or K images, we prefer to use here the H_2 images, where can be observed both the colder NIR sources (not visible in the J and H bands) and the signatures of jets from the youngest objects (§ 1.3.4, 4.1.1).

¹²It lacks of any suitable NIR counterpart (unfortunately, at that position we have no IRAC2 data) although the nearest NIR significant object, MGL99 156, 27 arcseconds apart, may contribute to the measured flux.

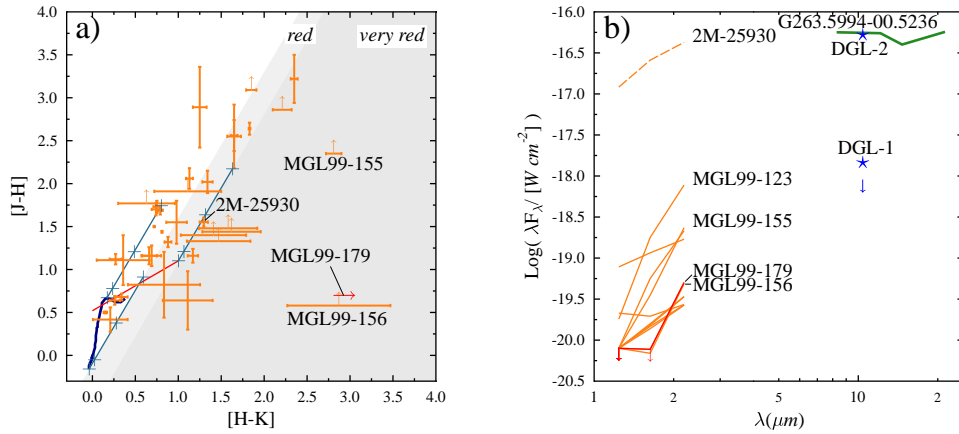


Figure 3.2: **a** - Colour-colour diagram of the sources falling within the FWHM-ellipse around MMS1. Dark curve: main sequence; red line: T-Tauri stars; blue lines: reddening lines with crosses indicating values of 0, 1, 5 and 10 mag of visual extinction. Arrows denote constraints from photometry upper limits. **b** - Spectral energy distribution of the very red sources within the FWHM-ellipse, together with the Timmi2 measured fluxes and the SED of the MSX object G263.5994-00.5236. Arrows denote again upper limits. See text for more details.

T-Tauri stars (Meyer et al. 1997, red line, see Section 1.3.2), and three reddening lines (Rieke & Lebofsky 1985, blue, see Section 1.1.2), starting from three significant points, with four crosses indicating values of 0, 1, 5 and 10 mag of visual extinction. The separation of the sources in the two regions *red* and *very red* (§ 3.3.1) is also evidenced by a different shading. The arrows on the data points denote constraints on colours derived from upper limits on the NIR photometry. This diagram allows us to select the most interesting objects: in particular, the sources labelled as MGL99 156, MGL99 179, and MGL99 155 show the highest colour excess.

We report in Fig. 3.2-b the Spectral Energy Distribution (SED) of the very red stars within the FWHM-ellipse, together with the Timmi2 measured fluxes and the SED of the MSX object G263.5994-00.5236. The arrows denote again the upper limits.

From the SEDs, we see that MGL99 179 and MGL99 156, considering the upper limits, are the sources with the steepest spectral indexes. Moreover, (see Fig. 3.1), while MGL99 179 has been identified as the counterpart of the Timmi2 source DGL 1, MGL99 156

has lack of detection in N , although its K magnitude is comparable to that of MGL99 179. This allows us to suggest that the main contributor to the millimeter flux should be the object MGL99 179 = DGL 1. However, considering the richness of very red sources in the field (Tab. 3.2), a contribution to the millimeter flux from multiple sources or from objects too embedded to be investigated with the described tools, cannot be ruled out. Moreover, the Hii region at the southern border of the core could provide an additional external heating by means of UV photons.

3.3.3 Counterpart results

All the results derived from the association to dust emission cores of sources from both FIR/NIR catalogs and our new ground-based observations are given in three different Tables organized as follows:

- Table 3.1 - Here all the dust cores (Tables 2.4, 2.5) detected in the mm map (column 1) having an association with a MIR and/or FIR object are listed. Then, for those cores associated with a FIR source, IRAS and MSX names, flux densities and distances from the peak (d) are given, along with the correlation coefficient CC for each band (§ 3.2.1). For the IRAS objects is also indicated the $1.2\ mm$ flux at the IRAS coordinates obtained by integrating the dust map within 24 arcsec (the SIMBA HPBW, see Section 2.2.1) aperture. Finally, for comparison purposes with IRAS ($12\ \mu\text{m}$) and MSX (8.28 and $12.13\ \mu\text{m}$) fluxes, the results of the Timmi2 observations (at $10.4\ \mu\text{m}$) are also reported in the last columns of this Table (again with the distances from the peak). As anticipated, the boldfaced lines correspond to FIR/MIR associations within the corresponding FWHM-ellipse, and, consequently, have to be considered as more robust cases (see Section 2.1.5 for the association dust cores-molecular clumps).
- Table 3.2 - This Table lists the NIR counterparts of all the cores. In column 2 the core size is identified through the FWHM-ellipse axes Δx and Δy (see Sect. 3.3.1). In column 3 the numbers of NIR red or very red sources that are located within the FWHM-ellipse are given. The census of the NIR population is based, whenever it is possible, on the IRAC2 images (Massi et al. 1999) that are deeper than the 2MASS frames (K band limit magnitude 18 instead of 14). Otherwise 2MASS images have been exploited. In columns 4 to 6 the location of the most probable candidate counterpart to the mm emission or to the FIR associated object is given, while the 7th column signals the morphology of the H_2 emission as detected in our ground-based observations.
- Table 3.3 - This table lists all the IRAS sources, falling within the dust map, but not associated to any core, that present at least two valid detections (not upper limits) between 12 and $60\ \mu\text{m}$ and a

flux increasing with the wavelength, namely $F_{12\mu m} < F_{25\mu m} < F_{60\mu m}$, or upper limits at 12 and 25 μm compatible with this condition. Studying the Vela-D young population, these sources have some relevance. Indeed, as Figure 2.4 shows, these red and cold sources are not randomly distributed, as the not-red sources are, but tend to be located along the gas filaments. As in Tab. 3.3, we also report the 1.2 mm flux derived at the IRAS position.

Table 3.1: Dust cores with associated FIR and/or MIR point sources.

<i>mm</i> core	IRAS associated sources ^a					MSX associated sources ^a					Timmi2 observations ^a							
	id	F_{12}	F_{25}	F_{60}	F_{100}	$F_{1.2mm}$	CC ^b	d (")	id	$F_{8.3}$	$F_{12.1}$	$F_{14.7}$	$F_{21.3}$	id	RA (J2000)	Dec (J2000)	$F_{10.4}$ (Jy)	d (")
MMS1	08438-4340 (IRS16)	13.4	56.0	638.3	1576	0.203	ECDB	49	G263.5994-00.5236 G263.6200-00.5308 G263.5925-00.5364	1.6 1.8 0.5	2.2 5.1 <0.7	2.0 6.9 <0.5	4.1 15.6 <1.6	DGL 1 DGL 2 DGL 4	8:45:33 8:45:33 8:45:36	-43:50:04 -43:49:48 -43:51:02	0.05 1.8 diffuse	17 33 ~49
MMS2	08438-4340 (IRS16)	13.4	56.0	638.3	1576	0.203	ECDB	55	G263.6338-00.5497 G263.6385-00.5217 G263.6366-00.5148 G263.6329-00.5127	0.4 0.9 0.3 0.4	<6.9 1.3 <0.9 <0.9	<5.4 0.8 <0.7 <0.9	1.6 1.4 <1.9 <2.7	DGL 3 DGL 5 DGL 4	8:45:34 8:45:38 8:45:36	-43:52:26 -43:51:14 -43:51:02	0.25 0.08 diffuse	26 26 ~55
MMS4 ^c	08448-4343 (IRS17)	8.7	88.1	326.6	1005	0.984	AABB	7	G263.7759-00.4281 G263.7733-00.4151 G263.7867-00.4437	7.5 1.2 0.3	10.1 1.3 0.8	13.8 0.5 <0.4	65.5 2.6 <1.2	MGL99 57^d MGL99 25^d MGL99 40^d	8:46:35 8:46:34 8:46:33	-43:54:31 -43:54:50 -43:54:39	8.79 0.21 0.14	7 15 17
MMS12	08470-4321 (IRS19)	44.9	130.1	342.6	406.9	0.331	AAAA	11	G263.7434+00.1161 G263.8432+00.0945 G263.8221+00.1494	30.8 0.3 0.1	52.6 <0.7 <0.9	70.3 <0.5 <0.6	93.5 <1.3 <1.9	DGL 7 DGL 8 DGL 9	8:48:49 8:49:03 8:49:12	-43:32:29 -43:37:55 -43:35:52	18.3 0.07 0.08	5 19 28
MMS18	08472-4326A	0.9	10.6	<106.9	<406.9	0.044	BABF	28	G263.8432+00.0945 G263.8221+00.1494	0.3 0.1	<0.7 <0.9	<0.5 <0.6	<1.3 <1.9	DGL 10 DGL 11 DGL 10	8:49:26 8:49:26 8:49:26	-43:17:12 -43:17:12 -43:17:21	2.01 0.02 <0.03	12 19 19
MMS20	08474-4323	1.5	1.1	<106.4	125.9	<0.005	BCAD	39	G263.8432+00.0945 G263.8221+00.1494	0.3 0.1	<0.7 <0.9	<0.5 <0.6	<1.3 <1.9	DGL 12 DGL 12	8:49:33 8:49:33	-44:10:60 -44:10:60	0.07 0.21	30 6
MMS21	08474-4325	<0.3	1.0	<16.4	57.5	0.207	DAHD	7	G263.6177+00.3652 G263.6177+00.3652	3.9 3.9	6.0 6.0	7.6 7.6	27.7 27.7	DGL 11 DGL 10	8:49:26 8:49:26	-43:17:12 -43:17:21	2.01 0.02	12 19
MMS22	08476-4306 (IRS20)	5.7	44.0	216.3	503.7	0.337	AAAB	10	G263.6177+00.3652 G263.6280+00.3847	3.9 0.3	6.0 <0.6	7.6 <0.5	27.7 <1.3	DGL 10 DGL 10	8:49:26 8:49:26	-43:17:21 -43:17:21	2.01 0.02	12 19
MMS24	08476-4306 (IRS20)	5.7	44.0	216.3	503.7	0.337	AAAB	48	G263.6177+00.3652 G263.6280+00.3847	3.9 0.3	6.0 <0.6	7.6 <0.5	27.7 <1.3	DGL 10 DGL 10	8:49:26 8:49:26	-43:17:21 -43:17:21	2.01 0.02	12 19
MMS25	08477-4359 (IRS21)	9.0	26.3	317.0	580.8	0.174	BAAA	20	G264.3225-00.1857 G264.3225-00.1857	4.7 4.7	5.0 5.0	2.3 2.3	8.0 8.0	DGL 12 DGL 12	8:49:33 8:49:33	-44:10:60 -44:10:60	0.21 0.21	30 6
MMS26	08477-4359 (IRS21)	9.0	26.3	317.0	580.8	0.174	BAAA	16	G264.3225-00.1857 G264.3225-00.1857	4.7 4.7	5.0 5.0	2.3 2.3	8.0 8.0	DGL 12 DGL 12	8:49:33 8:49:33	-44:10:60 -44:10:60	0.21 0.21	6 16
MMS27	08483-4305	1.5	2.5	<39.0	189.2	0.049	EEFD	14	G263.6909+00.4713 G263.6909+00.4713	0.1 0.1	0.6 0.6	<0.7 <0.7	<2.0 <2.0	DGL 13 not obs. not obs.	8:49:36 not obs. not obs.	-44:11:46 not obs. not obs.	0.03 not obs. not obs.	16 not obs. not obs.
MMS28	08483-4305	1.5	2.5	<39.0	189.2	0.049	EEFD	45	G263.6909+00.4713 G263.6909+00.4713	0.1 0.1	0.6 0.6	<0.7 <0.7	<2.0 <2.0	DGL 13 not obs. not obs.	8:49:36 not obs. not obs.	-44:11:46 not obs. not obs.	0.03 not obs. not obs.	16 not obs. not obs.
MMS29	08483-4305	1.5	2.5	<39.0	189.2	0.049	EEFD	45	G263.6909+00.4713 G263.6909+00.4713	0.1 0.1	0.6 0.6	<0.7 <0.7	<2.0 <2.0	DGL 13 not obs. not obs.	8:49:36 not obs. not obs.	-44:11:46 not obs. not obs.	0.03 not obs. not obs.	16 not obs. not obs.
umms1	08446-4331	<1.1	0.5	7.4	42.8	0.160	GBBB	2	G263.7651-00.1572 G263.7651-00.1572	0.2 0.2	<0.5 <0.5	0.5 0.5	<1.2 <1.2	DGL 6 not obs.	8:47:43 not obs.	-43:43:48 not obs.	0.07 <0.03	10 not obs.
umms8	08458-4332	1.1	2.7	17.8	52.7	0.017	CABA	24	G263.5672+00.4036 G263.5622+00.4185	0.1 0.2	<0.9 <0.7	<0.7 <0.5	<1.9 <1.5	DGL 6 not obs.	8:47:43 not obs.	-43:43:48 not obs.	0.07 <0.03	10 not obs.
umms9	08458-4332	1.1	2.7	17.8	52.7	0.017	CABA	29	G263.5672+00.4036 G263.5622+00.4185	0.1 0.2	<0.9 <0.7	<0.7 <0.5	<1.9 <1.5	DGL 6 not obs.	8:47:43 not obs.	-43:43:48 not obs.	0.07 <0.03	10 not obs.
umms11	umms11	<0.3	<0.3	6.6	<47.2	0.160	-JB-	19	G263.7651-00.1572 G263.7651-00.1572	0.2 0.2	<0.5 <0.7	0.5 <0.5	<1.2 <1.5	DGL 6 not obs.	8:47:43 not obs.	-43:43:48 not obs.	0.07 <0.03	10 not obs.
umms16	08464-4335	<0.3	<0.3	6.6	<47.2	0.160	-JB-	19	G263.7651-00.1572 G263.7651-00.1572	0.2 0.2	<0.5 <0.7	0.5 <0.5	<1.2 <1.5	DGL 6 not obs.	8:47:43 not obs.	-43:43:48 not obs.	0.07 <0.03	10 not obs.
umms23	umms23	<0.3	<0.3	6.6	<47.2	0.160	-JB-	19	G263.7651-00.1572 G263.7651-00.1572	0.2 0.2	<0.5 <0.7	0.5 <0.5	<1.2 <1.5	DGL 6 not obs.	8:47:43 not obs.	-43:43:48 not obs.	0.07 <0.03	10 not obs.
umms24	umms24	<0.3	<0.3	6.6	<47.2	0.160	-JB-	19	G263.7651-00.1572 G263.7651-00.1572	0.2 0.2	<0.5 <0.7	0.5 <0.5	<1.2 <1.5	DGL 6 not obs.	8:47:43 not obs.	-43:43:48 not obs.	0.07 <0.03	10 not obs.
umms25	umms25	<0.3	<0.3	6.6	<47.2	0.160	-JB-	19	G263.7651-00.1572 G263.7651-00.1572	0.2 0.2	<0.5 <0.7	0.5 <0.5	<1.2 <1.5	DGL 6 not obs.	8:47:43 not obs.	-43:43:48 not obs.	0.07 <0.03	10 not obs.

Notes to the table: the *mm* sources labeled as umms# are not resolved by the SIMBA HPBW (see text and Massi et al. 2007).

^aBold faced sources are more compelling associations (within the FWHM-ellipse of the core, see text). Distances from the peak are reported in the *d* columns.

^bPoint source correlation coefficient encoded as alphabetic characters (A=100%, B=99%, ..., N=87%) according to the IRAS Catalogs and Atlases Explanatory Supplement IRAS-PSC (1988).

^cThis core has been divided into two components by Giannini et al. (2005).

^dNames following the numbering convention used in Massi et al. (1999). A description of the Timmi2 observations of these objects is given in Giannini et al. (2005).

Table 3.2: *NIR sources and H₂ emission associated with dust cores.*

<i>mm</i> core name	FWHM Δx - Δy ($''$)	# of NIR ^a <i>red</i> / <i>very red</i> sources ^b within the FWHM-ellipse	Counterparts candidates			<i>H₂</i> emission morphology ^c
			name	RA (J2000)	Dec (J2000)	
MMS1 ^d	59-64	5 / 8 ^e	MGL99 179	08:45:32.86	-43:50:03.80	diffuse , knots
MMS2 ^d	59-55	1 / 3 ^e	MGL99 25	08:45:35.93	-43:51:45.60	diffuse , jet-like
MMS3 ^d	61-58	0 / 1 ^e	MGL99 36	08:45:39.21	-43:51:34.70	diffuse
MMS4 ^d	82-71	19 / 43 ^f	MGL99 57	08:46:34.77	-43:54:30.63	diffuse , jet-like , knots
MMS5	40-31	0 / 0				diffuse
MMS6	27-23	0 / 0				diffuse
MMS7	29-37	1 / 4				-
MMS8	24-26	0 / 1	2M 9671	08:48:39.13	-43:31:31.36	-
MMS9	32-36	0 / 0				-
MMS10	25-28	0 / 0				-
MMS11	36-24	0 / 1	2M 14732	08:48:46.54	-43:37:44.02	-
MMS12 ^d	57-37	8 / 20 ^f	MGL99 49	08:48:48.51	-43:32:29.08	diffuse , knots
MMS13	41-20	2 / 0 ^f	MGL99 2	08:48:50.04	-43:33:19.47	-
MMS14	29-38	0 / 0				-
MMS15	33-20	0 / 0				-
MMS16	23-36	0 / 0				diffuse , jet-like
MMS17	67-37	0 / 2				jet-like
MMS18 ^d	36-36	1 / 0				diffuse
MMS19	26-60	3 / 2	2M 36076	08:49:08.49	-43:35:37.79	-
MMS20 ^d	38-32	0 / 0				knots
MMS21 ^d	54-57	0 / 3	2M 29953	08:49:13.39	-43:36:29.20	knots
MMS22 ^d	35-37	9 / 13 ^f	MGL99 98	08:49:26.23	-43:17:11.11	diffuse , jet-like , knots
MMS23	39-22	0 / 0				diffuse
MMS24 ^d	35-25	0 / 3 ^f	MGL99 90	08:49:32.27	-43:17:14.43	-
MMS25 ^d	52-86	3 / 5				diffuse
MMS26 ^d	60-67	1 / 8				diffuse
MMS27 ^d	67-48	1 / 2				knots
MMS28 ^d	30-31	0 / 0				-
MMS29 ^d	40-36	1 / 1	2M 36339	08:50:11.04	-43:17:10.74	knots
umms1 ^d	<24-24	0 / 0				not observed
umms2	<24-24	0 / 0				-
umms3	<24-24	0 / 0				-
umms4	<24-24	0 / 1				-
umms5	<24-24	1 / 0				-
umms6	<24-24	1 / 0				-
umms7	<24-24	0 / 0				-
umms8 ^d	<24-24	1 / 1	2M 16128	08:47:37.87	-43:43:42.41	-
umms9 ^d	<24-24	0 / 0				-
umms10	<24-24	0 / 0				-
umms11 ^d	<24-24	0 / 2	2M 9173	08:47:42.93	-43:43:48.05	-
umms12	<24-24	0 / 0				-
umms13	<24-24	0 / 0				-
umms14	<24-24	0 / 0				-
umms15	<24-24	0 / 0				-
umms16 ^d	<24-24	0 / 0				jet-like
umms17	<24-24	0 / 0				jet-like
umms18	<24-24	0 / 0				jet-like
umms19	<24-24	1 / 0	2M 10742	08:48:33.95	-43:30:47.20	knot
umms20	<24-24	0 / 0				knot
umms21	<24-24	0 / 3	2M 16489	08:48:37.03	-43:13:53.63	-
umms22	<24-24	0 / 0				-
umms23 ^d	<24-24	0 / 1	2M 11799	08:49:24.56	-43:13:15.49	-
umms24 ^d	<24-24	0 / 0				-
umms25 ^d	<24-24	0 / 0				-
umms26	<24-24	0 / 0				-

^aWhere not specified, the reported numbers refer to 2MASS data.^bThe terms *red* and *very red* refer to different regions of the colour-colour diagram (see text and e.g. Fig. 3.2-a).^cBold-faced if inside the FWHM-ellipse.^dCores presenting a MIR or FIR association (see Tab. 3.1).^eCore only partially covered by IRAC2 observations.^fCore fully covered by IRAC2 observations.

Table 3.3: *IRAS point sources with increasing fluxes not associated with any core.*

id	F_{12}	F_{25}	F_{60}	F_{100}	$F_{1.2mm}$	CC ^a
	(Jy)					
08440-4253	<0.3	0.2	1.2	<30.5	<0.005	-BBD
08461-4314	0.7	0.8	5.9	<48.5	0.003	BCDB
08475-4255	<0.4	0.4	3.3	45.6	0.020	EDDB
08475-4311	<0.5	0.5	9.4	<37.8	0.020	DEC-
08481-4258	<0.4	1.1	7.6	<34.8	0.008	BDC-
08459-4338	<0.2	0.6	6.5	38.3	0.005	-DCB
08442-4328	<1.4	2.2	41.3	113.9	0.020	HDCA
08448-4341	1.3	6.6	<327	<1005	<0.005	DAC-
08468-4330	<0.3	0.4	3.4	<31.6	0.010	FDD-
08491-4310	0.5	0.6	7.6	38.6	<0.005	EBCC
08496-4320	0.6	0.7	7.6	<37.1	<0.005	BCBH
08463-4343	<0.3	0.5	7.4	<43.5	<0.005	NBDG
08478-4403	0.5	0.5	<5.4	<580.8	<0.005	CCJG

^aSee note *b* in Tab. 3.1.

The starting information is the sample of 29 well resolved and 26 unresolved dust cores. As discussed previously (§2.2.2) and illustrated in Figure 2.13 and in the Appendix A, some of them are not isolated, but belong to more complex structures of dust emission that present different cores (*e.g.* the one composed by MMS7, umms13-14-15, Fig. A.6); others are elongated structures formed by aligned *knots* (*e.g.* both MMS5, MMS6, umms6 of Fig. A.5 and umms23-24-25 of Fig. A.38). These multiple core structures often present associated FIR counterpart(s) that tend(s) to be located in an intermediate position between the individual cores. This is the reason why in Tab. 3.1 the same IRAS/MSX source is sometimes assigned to two different cores. Conversely, the distribution of the NIR counterparts is more clearly defined because of the increased spatial resolution at such wavelengths. In Appendix A all the observational details pertaining to each individual dust core are presented; however here we can draw some general conclusions. Firstly, all the information given in Tabs. 3.1 and 3.2 are statistically summarized in Tab. 3.4, where, among the 29 resolved

Table 3.4: *Statistics about the dust cores population.*

Cores	Associated with						
	MIR/FIR	only very red NIR object	H_2 jet	no source	NIR or FIR object	no source or H_2 only	embedded cluster
29 resolved	8	7	7	7	15	14	6
26 unresolved	4	3	3	16	7	19	2

cores (MMS) only 8 are clearly associable to a MIR/FIR source (with or without a near-IR counterpart); 7 have some MIR/FIR source in their neighbourhood, but additional evidences (*i.e.* the presence of H_2 jets) point back to an embedded object not (yet) detected; 7 additional cores seem to be associated with very red NIR objects; the 7 remaining cores do not present any sign of star formation activity at the current instrumental sensitivity. If the same approach is applied to the sample of the 26 unresolved cores (umms), we obtain 4 that are associable to a MIR/FIR source, 3 to a NIR counterpart, 3 to jet-like structures, and 16 appear as inactive sites. Substantially, both MMS and umms present a similar statistics of associated categories, although the latter sample is more widely dominated by objects that could be artifacts, caused by the searching algorithm, or sites harbouring weak IR counterparts. The total number of resolved cores associable to an IR object (irrespective of being NIR or FIR sources) is 15 (column 6 of Tab. 3.4) with respect to the 14 unassociated cores (column 7): such percentages are in full agreement with those found in other galactic surveys of star forming regions (*e.g.* Yonekura et al. 2005, Mookerjee et al. 2004, Beltrán et al. 2006).

Such categorization, however, does not necessarily reflect a property intrinsic to the cores themselves, but is likely the product of the limiting instrumental sensitivities of the considered facilities. In fact, recent results of SPITZER MIR surveys have substantially modified the percentage of active *vs* inactive cores in favour of the first ones (*e.g.* Young et al. 2004) and this is also the case of Vela-D, how we will explain in Section 3.4.

3.3.4 Star formation modalities and evolutionary stages

Different modalities of star formation are simultaneously active in Vela-D. Such a co-existence is confirmed by the presence of 8 clusters (see last column of Tab. 3.4) and by the remaining cases of isolated star formation. This twofold modality, already recognized in Orion (*e.g.* Chen & Tokunaga 1994) and now in Vela-D as well, seems to be a feature of all the regions where intermediate and high-mass stars form. Indeed, it is likely that the lacking detection of the isolated mode in far and massive star forming regions is due only to limitations on sensitivity and spatial resolution.

To investigate whether or not the different cores of Vela-D harbour protostellar objects in different evolutionary stages (see Section 1.3.1 and Greene et al. 1994) we have constructed the distribution of the spectral slope of the sources associated to the cores (see Fig. 3.3). For each source the slope α is calculated through the relationship $\alpha = \Delta \log(\lambda_i F_{\lambda_i}) / \Delta \log(\lambda_i)$, between the wavelengths λ_1 and λ_2 , corresponding to about 2 and 10 μm , respectively. A certain degree of inhomogeneity is introduced by the fact that the flux attributed to the 10 μm band corresponds to that detected by different instruments (MSX, Timmi2, IRAS) operating at different effective wavelengths (8.28, 10.4 and 12 μm , respectively). These differences affect only the details of the slope distribution, but do not alter its significance, as proved by the five sources having a multiple detection. Fig. 3.3 illustrates how the sample of the sources associated to the dust cores presents a distribution highly peaked at values $0 < \alpha < 3$, typical of Class I sources. It is worthwhile noting that the NIR contribution to the slope generally relies on 2MASS data, that provide a K band limiting magnitude of about 14 mag; deeper NIR surveys (see *e.g.* Giannini et al. 2005), could make it possible to find weaker NIR counterparts, increasing the number of sources with high α values. As a result, the presented bar graph (Fig. 3.3) could be shifted towards larger α values. As expected, the sources associated to the dust cores are essentially Class I objects, although the distribution presents a significant tail toward the less evolved objects, whose slope is greater than 3.

In Tab. 3.3 we also list all the IRAS sources lying inside the region mapped in the 1.2 mm continuum and showing a flux increasing with wavelength but not directly associated to any dust core (see

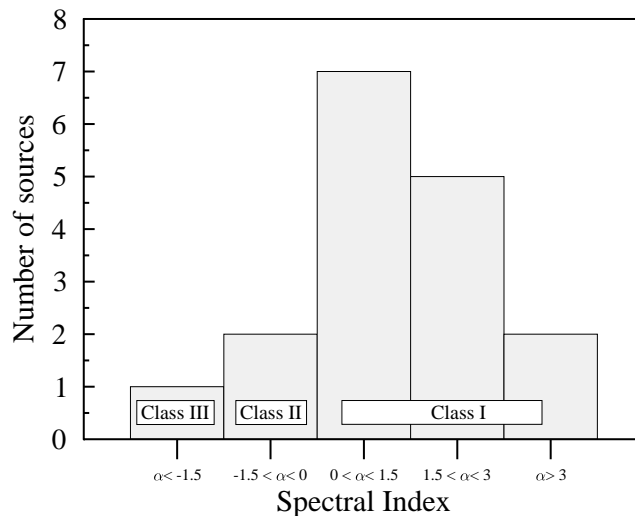


Figure 3.3: Spectral index (α_{2-10}) distribution of core counterparts. In cases of multiple estimates of the $10\mu\text{m}$ flux (Timmi2, MSX, IRAS) the value obtained with better spatial resolution was used to determine α .

Sect. 3.3.3). These sources, with only few exceptions, tend to be distributed all along both the diffuse emission detected by MSX at $8.3\mu\text{m}$ and the gas filaments.

To evaluate the intrinsic nature of all the IRAS sources in Tables 3.1 and 3.3, we present, in Fig. 3.4, an IRAS two colours diagram, [12-25] vs [25-60], with all those sources. As expected, the objects not associated to the cores have a greater number of upper limits (especially at $12\mu\text{m}$), but tend to occupy the same region of the plot where the associated sources are located. This common region pertains to sources that can be described as a two dust components system, one at 1000 K and the other in between 50 and 100 K, with variable relative contributions. The IRAS selected sources have colours definitely redder and colder than those pertaining to pre-main sequence stars (T-Tauri and Herbig Ae/Be; see, *e.g.*, Berrilli et al. 1992), apart from few cases. While the absence of IRAS sources with the colours of T-Tauri stars in our sample is probably due to an observational bias (in fact the IRAS detectability limit is $> 0.5 L_{\odot}$ in Taurus, corresponding to $> 10 L_{\odot}$ in

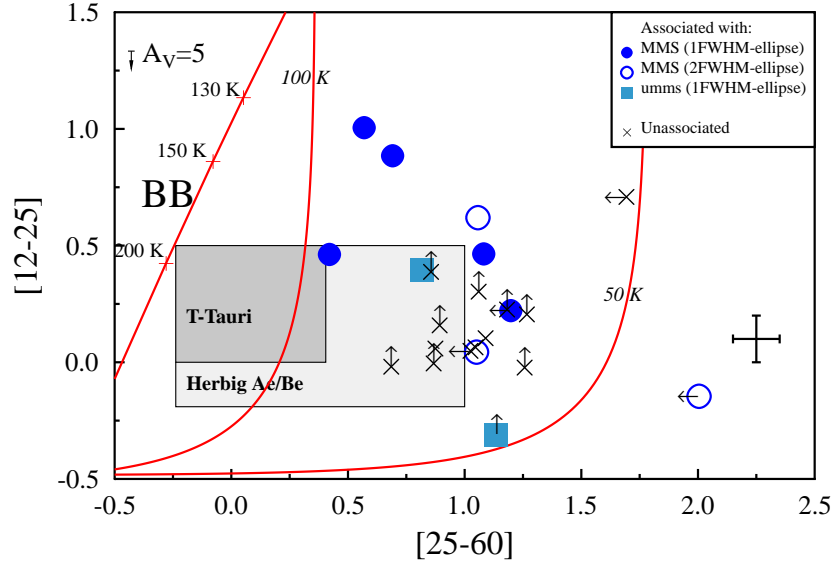


Figure 3.4: *Two colours diagram for all the IRAS sources listed in Tabs. 3.1 and 3.3. The mean error bars, the extinction vector corresponding to 5 mag of visual extinction and the locus of blackbodies (leftmost line) are indicated (see text for more details).*

Vela-D), the doubtful presence of Herbig Ae/Be appears to be an intrinsic property of Vela-D. Indeed, Herbig Ae/Be located inside dust cores having masses comparable to those belonging to the Vela-D ones have been already found at distances of 1 Kpc or less (*e.g.* Henning et al. 1998). This difference likely reflects different star formation histories, being in Vela-D a shorter time ($\approx 10^6$ yr) elapsed from the earliest collapse events Massi et al. (2000) with respect to other studied massive clouds.

We have calculated the bolometric luminosity, L_{bol} , for all the IRAS sources from 12 μm to 1.2 mm. The bar graph in Fig. 3.5 shows our result: the sources associated to the dust cores (both resolved and not) are, on average, objects of intermediate luminosity ($L_{bol} \sim 10^3 L_{\odot}$), while the unassociated FIR sources, even showing similar SEDs, tend to be lower luminosity objects ($L_{bol} \sim 10^2 L_{\odot}$). Therefore, we can firmly conclude that massive star formation ($L_{bol} > 10^4 L_{\odot}$) does not occur in Vela-D, and that our sample of Class I sources is not contaminated

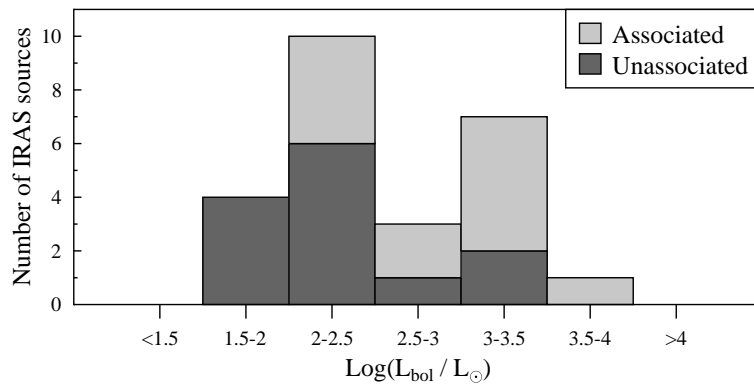


Figure 3.5: *Luminosity distribution of both associated and unassociated IRAS sources (Tabs. 3.1 and 3.3).*

by ultracompact Hii regions¹³, which would be indistinguishable based on their FIR colours alone (Wood & Churchwell 1989).

An attempt to search for Class 0 objects within our sample of IRAS sources was also been done by applying the criterion proposed by André et al. (1993) for low-mass protostars: $L_{bol}/L_{1.3mm} \lesssim 2 \times 10^4$. None of the selected IRAS sources (Tables. 3.1 and 3.3) strictly satisfies this criterion¹⁴. It should be said, however, that overestimates of the IRAS fluxes result in overestimates of the $L_{bol}/L_{1.3mm}$ ratio. Thus, leaving any quantitative approach, we point out that three sources of our sample (08446-4331, 08474-4325 and 08464-4335) show a ratio $L_{bol}/L_{1.3mm}$ one order of magnitude less than the others and thus they are likely the youngest objects in the field. This hypothesis is strongly supported by (i) the tight association of these sources with the mm cores umms1, MMS21 and umms16, respectively; (ii) by the lack of a measured flux at $12\mu m$ ¹⁵, and, but only for the last case, (iii) by the presence of H_2

¹³Ultracompact HII (UCHII) regions represent the first evolutionary stage of massive stars in which their Lyman continuum radiation escapes in the form of free-free emission at cm wavelengths. Consequently, UCHII regions connect the early 'hot core stage to later phases when the ionizing source reveals itself optically. UCHII regions possess high densities of typically 10^4 cm^{-3} and have yet to break out of their natal dust cocoons (Crowther 2005).

¹⁴Hatchell et al. (2007) reduces such limiting ratio to $L_{bol}/L_{1.3mm} \lesssim 3 \times 10^3$ and underlines how this indicator should vary with envelope mass.

¹⁵For the core MMS21 with the associated source 08474-4325 we report in Tab. 3.2 a candidate NIR counterpart, but such association is quite questionable (see Appendix A and Fig. A.18).

jet-like emission (jet2, see next Chapter) crossing the dust peak (no H_2 images are available for the core umms1).

3.4 MIPS photometry

New Spitzer-MIPS images, thanks to their better sensitivity and resolution with respect to the IRAS ones, has allowed us to improve our knowledge of the MIR emission, both diffuse and point-like, of Vela-D. In the following we will describe the new results obtained from the analysis of the Spitzer data.

Figure 3.6 shows the two-color final mosaic of Vela-D ($24\ \mu\text{m}$ in blue, $70\ \mu\text{m}$ in red), while on Figures 3.7 and 3.8, images in each of the two filters are shown separately. In these latter, the $1.2\ \text{mm}$ dust map and the $^{12}\text{CO}(1-0)$ intensity map integrated in the velocity range $-2 \div 20\ \text{km s}^{-1}$ have been superimposed for comparison.

Given the location of Vela-D, which is on the Galactic plane, it could be very useful to have an operative way to estimate the contamination of the foreground/background sources. To this purpose we define as ‘on-cloud’ all objects inside the latter $^{12}\text{CO}(1-0)$ contours. Such a definition is perforce just the first level effort of delimiting the sources belonging to the molecular cloud; indeed, it is clear from Figures 3.7 and 3.8 that the $^{12}\text{CO}(1-0)$ emission remains well above the 3σ level at the north and west borders of the gas map, and thus sources belonging to Vela-D could exist toward these directions. Considering such sources as ‘off-cloud’ will have the effect of reducing the distinctions between the ‘on’ and ‘off’ cloud populations; these sources should then be considered on a case-by-case basis. We have also considered as ‘off-cloud’ those regions where the CO peak velocity is faster than $20\ \text{km s}^{-1}$, since they are likely to be more distant and unassociated with Vela-D (see Figure 1 in Lorenzetti et al. 1993).

The point-source extraction and photometry processes were performed by using the task *DAOPHOT* of the astronomical data analysis package *IRAF*¹⁶. Given the size of the MIPS mosaic it was impossible to apply any automatic procedure for finding sources down to the sen-

¹⁶IRAF, the Image Reduction and Analysis Facility, is a general purpose software written and supported by the IRAF programming group at the National Optical Astronomy Observatories (NOAO) in Tucson, Arizona (<http://iraf.noao.edu>).

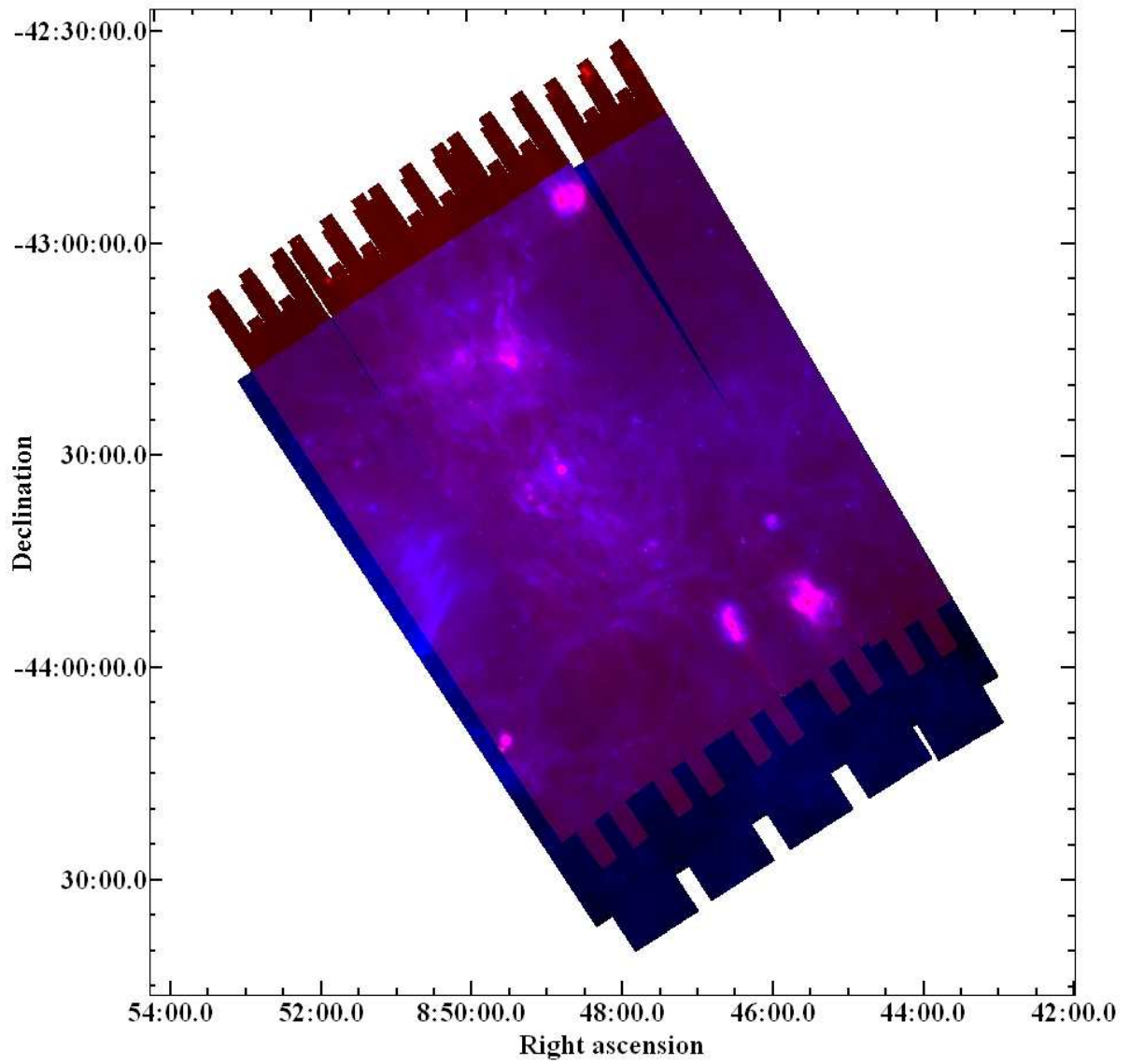


Figure 3.6: *MIPS* two-color map ($24\ \mu\text{m}$ in blue, $70\ \mu\text{m}$ in red) of Vela-D.

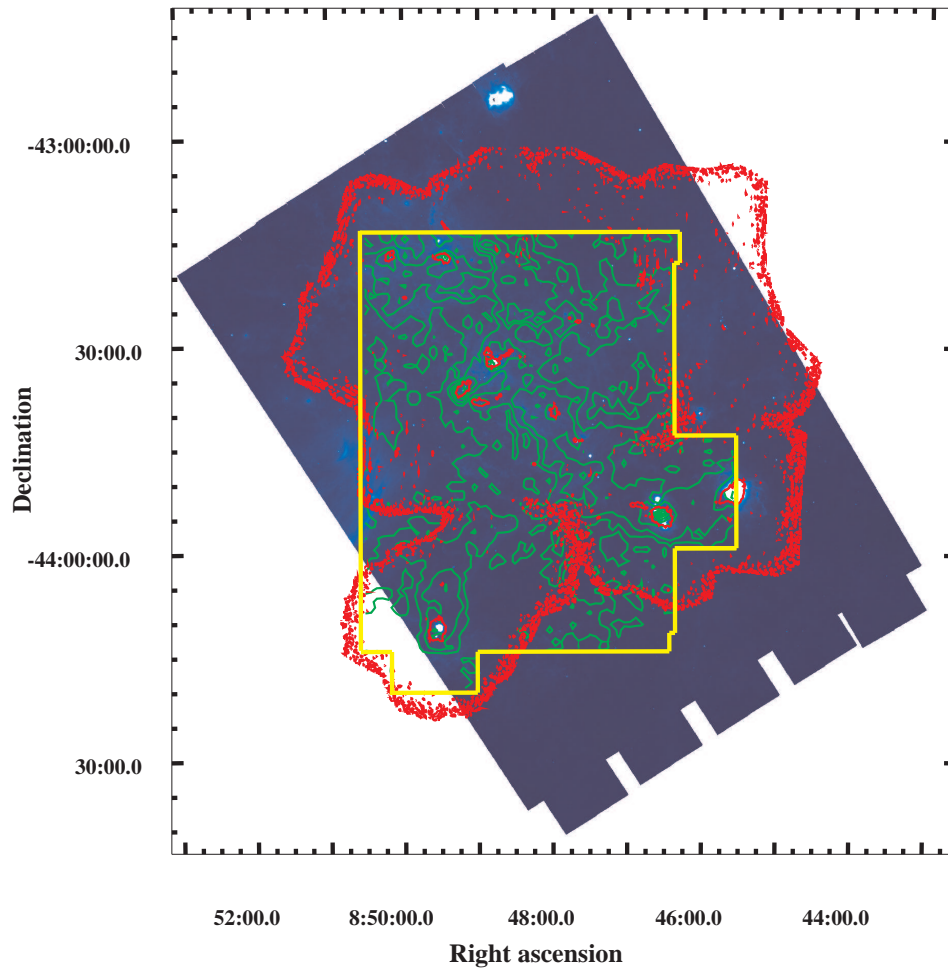


Figure 3.7: Mosaic of Vela-D map at $24 \mu\text{m}$, with superposed the $^{12}\text{CO}(1-0)$ intensity map (whose limits are depicted in yellow), where the contours (in green) are in the range $-2-20 \text{ km s}^{-1}$ (adapted by Elia et al. 2007). Also overlaid is the 1.2mm dust emission map (red contours, adapted from Massi et al. 2007). CO contour levels start from 5 K km s^{-1} and are in steps of 25 K km s^{-1} , while dust contours start from 50 mJy/beam and are in steps of 50 mJy/beam .

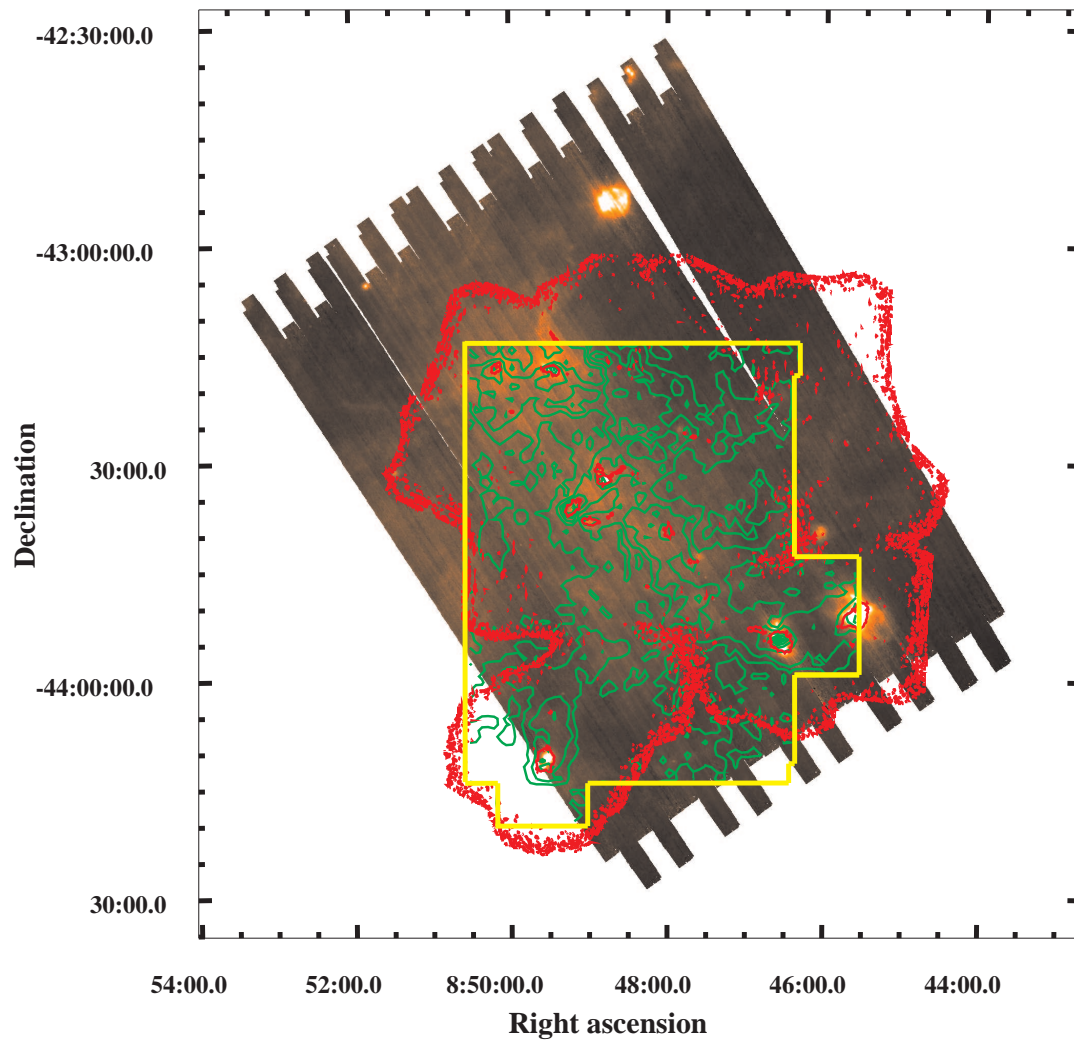


Figure 3.8: *As Figure 3.7 for the $70\ \mu\text{m}$ map.*

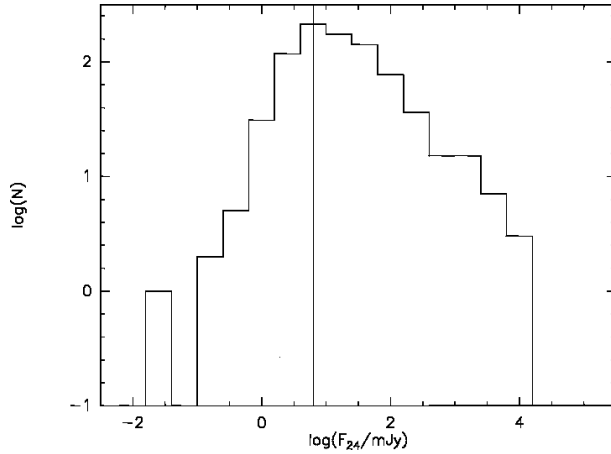


Figure 3.9: *Histogram of the sources detected at 24 μm . The completeness limit is around 5 mJy, as indicated by the vertical line.*

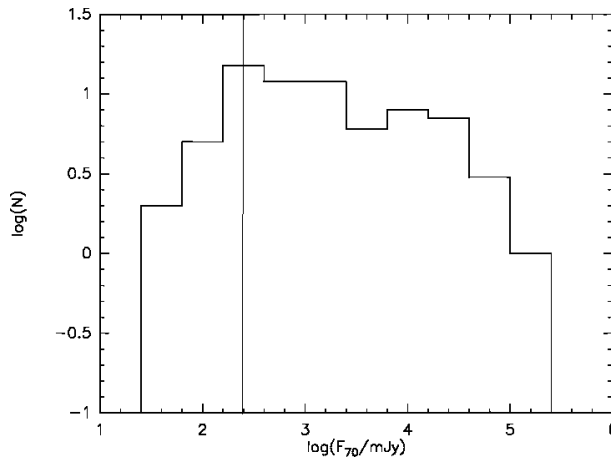


Figure 3.10: *Histogram of the sources detected at 70 μm . The completeness limit is around 250 mJy, as indicated by the vertical line.*

sitivity limits without being affected by a locally varying background level; we therefore applied a searching algorithm as deep as possible, but still compatible with an automatic procedure. The search algorithm was applied to a differential image we produced between the final mosaic and a ‘sky’ image, the latter obtained by applying to the mosaic a median filter over boxes of 5×5 pixels. A threshold of 30σ has been imposed on the sky-subtracted image, which corresponds at least to 5σ (depending on the local background) in the un-subtracted image.

The automated methods just described lead to the detection of 838 and 61 point sources at 24 μm and 70 μm , respectively. A further 12 detections have been added to the 24 μm list by applying local sky values

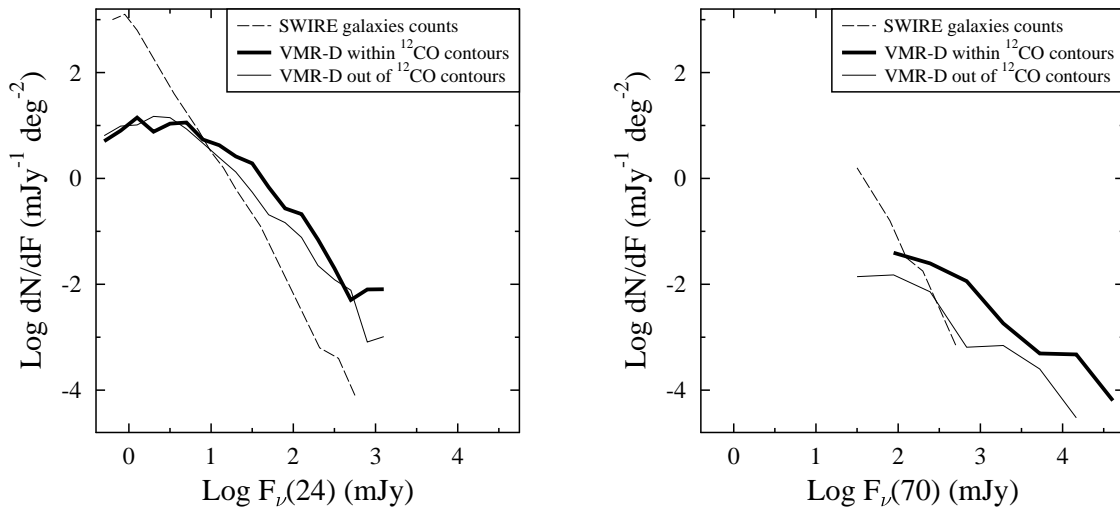


Figure 3.11: *Left panel: differential number counts at 24 μm . Thick and thin lines refer to source in Vela-D (VMR-D) within and outside the $^{12}\text{CO}(1-0)$ contours, respectively. Extragalactic background sources from the SWIRE ELAIS N1 field are shown for comparison (these latter have been taken from Figs.6 and 7 in Rebull et al. 2007). Right panel: as in left panel at 70 μm .*

in selected areas (see the discussion below). The source distribution as a function of the measured flux is depicted in Figures 3.9 and 3.10, where the completeness limits can be evaluated as the flux bin corresponding to the maximum counts before the decline at lower fluxes due to the instrumental sensitivity. We determine that our sample is complete down to 5 and 250 mJy at 24 and 70 μm , respectively.

A statistical summary of the detected sources is presented in Table 3.5. About 45% of the 24 μm sources are spatially located inside the region delimited by the $^{12}\text{CO}(1-0)$ contours ($\sim 0.61 \text{ deg}^2$), even though this latter is about one half the size of the remaining mapped area ($\sim 1.23 \text{ deg}^2$). This result gives an initial indication of how the IR source density increases by about 100% moving from outside to inside the CO contours, and the pattern becomes even more significant when considering the 70 μm sources, whose source density increase is four times.

The 24 μm counts per deg^2 are represented in Figure 3.11, left panel, where different symbols indicate those sources located respectively within and outside the CO contours. Also in this plot, where the

Table 3.5: *Statistics of MIPS point sources.*

item	overall	inside CO contours ^a	outside CO contours ^b
24 μ m	849	378	471
70 μ m	61	41	20
24 μ m & 70 μ m ^c	52	40	12
only 70 μ m	9	1	8
24 μ m & 2MASS-K _s ^d	401	180	221
24 μ m & 70 μ m & 2MASS-K _s ^d	28 ^c	23	5
24 μ m & dust peak ^e	58	55	3
70 μ m & dust peak ^e	19	19	0

^aSize=0.61 deg²

^bSize=1.23 deg²

^cCoordinates coincident within 20''

^dCoordinates coincident within 5''

^eCoordinates coincident within 24'' (SIMBA HPBW). A total of 58 (19) sources at 24 (70) μ m result associated with 22 (resolved) and 20 (under-resolved) *mm* peaks, as listed by Massi et al. (2007). Note that the area mapped in dust continuum at 1.2 mm is slightly larger than that covered with CO(1-0) observations (see Figs. 3.7, 3.8).

differential number density is shown, there is a drop for $F_\nu < 35$ mJy. For greater F_ν values the number of objects inside the gas contours (*i.e.* those more likely associated to the cloud) systematically exceeds the number of objects outside the cloud, giving reasonable support to the empirical significance of this crude classification. In addition, Figure 3.11 is a comparison between the on- and off-cloud samples and the Spitzer Wide-area Infrared Extragalactic Survey (SWIRE, Lonsdale et al. 2003) legacy program. A significant amount of contamination from the extragalactic background would be predicted (at 24 μ m) for flux densities < 10 mJy down to the completeness limit, so that ‘on’ and ‘off’ source populations at this level become indistinguishable. The counts per deg² at 70 μ m are depicted in Figure 3.11, right panel: here again the possible extragalactic contamination appears just at (or even below) the completeness limit. However, given the location of Vela-D along the Galactic plane, we expect to find a lower contamination by extragalactic objects with respect to other star forming regions (see also the discussion about Figure 3.12). In the same Figure 3.11, we also note that the 70 μ m counts confirm the on- and off-cloud distributions already found at 24 μ m.

Table 3.6: *MIPS sources in the Vela Molecular Cloud-D.*

Spitzer name	$\alpha(2000.0)$	$\delta(2000.0)$	F_{24}	ΔF_{24}	F_{70}	ΔF_{70}	CO contours	dust core
	(h m s)	(o ' ")	(mJy)	(mJy)	(mJy)	(mJy)		
SSTVMRD J084310.3-440052.7	8 43 10.3	-44 00 52.7	4.5	0.2	-	-	N	-
SSTVMRD J084332.8-440301.0	8 43 32.8	-44 03 01.0	31.6	0.2	-	-	N	-
SSTVMRD J084335.4-435539.0	8 43 35.4	-43 55 39.0	8.2	0.1	-	-	N	-
SSTVMRD J084342.4-440134.5	8 43 42.4	-44 01 34.5	2.3	0.1	-	-	N	-
SSTVMRD J084347.4-435946.3	8 43 47.4	-43 59 46.3	42.0	0.1	-	-	N	-

[The complete version of this table is in the electronic edition of the paper Giannini et al. (2007).]

The complete catalog of the detected sources is given in the electronic form of the paper by Giannini et al. (2007) (a short sample version is printed in Table 3.6). In Table 3.7 we show the list of the 70 μm detections: 52 out of 61 sources are coincident with a 24 μm source (*i.e.* the distance in both right ascension and declination is less than the 20'' PSF¹⁷ radius at 70 μm , see the summary of Table 3.5). In Table 3.7, we list the 24 μm coordinates (which are more accurate than the 70 μm ones because of the smaller PSF at 24 μm), the distance from the 70 μm coordinates, $(\Delta\alpha/\Delta\delta)_{70}$, the measured flux at 24 and 70 μm along with the relative uncertainties, a flag indicating whether or not the source is located inside the region delimited by CO emission contours, and the association with a dust core, if any. This latter is based on the distance between the 24 μm and mm coordinates, $(\Delta\alpha/\Delta\delta)_{mm}$, which must be within the SIMBA HPBW of 24''. All the dust cores associated with a 24 μm source are also associated with its 70 μm counterpart.

Nine 70 μm sources have no 24 μm counterpart. Four of these were not imaged at 24 μm because of the shift between the two maps, four appear as diffuse or with a filamentary structure at 24 μm , and one has $F_{24} < 1.2$ mJy (3σ upper limit): this source (#1 in Table 3.7) could be (if not a galaxy) a very young protostar which deserves further attention.

We also provide in Table 3.7 the association of MIPS 24/70 μm sources with dust cores. Some results of the improvement given by MIPS images on the study of the IR counterparts of the cores are presented in the next Chapter, where we locate the driving sources of jets and outflows. Here we point out some statistical aspects. As

¹⁷The Point Spread Function, PSF, describes the response on the detector to a point source due to the aberrations in the optical system, to diffraction effects and (for ground-based observations) to atmospheric turbulence.

Table 3.7: MIPS sources detected at 70 μ m.

ID	Spitzer name	α (2000.0) (h m s)	δ (2000.0) ($^{\circ}$ ' ")	$(\Delta\alpha/\Delta\delta)_{70}$ ($''/''$)	$(F\pm\Delta F)_{24}$ (mJy)	$(F\pm\Delta F)_{70}$ (mJy)	CO contours	dust core	$(\Delta\alpha/\Delta\delta)_{mm}$ ($''/''$)
1 ^d	SSTVMRD J084409.5-440018.3	08 44 09.5	-44 00 18.3	...	< 1.2	75 \pm 3	N		
2	SSTVMRD J084431.7-435005.3	08 44 31.7	-43 50 05.3	4.5/4.5	4.3 \pm 0.1	78 \pm 3	N		
3	SSTVMRD J084444.6-434214.2	08 44 44.6	-43 42 14.2	12.0/1.7	44.6 \pm 0.1	41 \pm 3	N		
4	SSTVMRD J084444.9-434927.4	08 44 44.9	-43 49 27.4	6.0/0.3	16.6 \pm 0.1	28 \pm 3	N		
5	SSTVMRD J084509.3-433802.7	08 45 09.3	-43 38 02.7	16.5/1.2	18.6 \pm 0.2	234 \pm 3	N		
6	SSTVMRD J084533.3-434952.8	08 45 33.3	-43 49 52.8	0.0/18.0	3301 \pm 4	31882 \pm 263	Y	MMS1	0.9/27.2
7 ^c	SSTVMRD J084535.5-435107.2	08 45 35.5	-43 51 07.2 ^d	...	>4000 ^b	22491 \pm 449	Y		
8 ^e	SSTVMRD J084536.7-435155.4	08 45 36.7	-43 51 55.4	0.0/ 16.5	3097 \pm 6	34414 \pm 448	Y		
9 ^e	SSTVMRD J084537.0-435134.0	08 45 37.0	-43 51 34.0	4.5/ 4.9	2740 \pm 6	34414 \pm 448	Y		
10	SSTVMRD J084541.1-435146.9	08 45 41.1	-43 51 46.9	3.0/ 2.4	1611 \pm 69	36680 \pm 331	Y	MMS3	15.3/14.9
11	SSTVMRD J084544.0-432710.7	08 45 44.0	-43 27 10.7	1.5/0.2	405.6 \pm 0.2	465 \pm 4	N		
12	SSTVMRD J084546.7-432326.0	08 45 46.7	-43 23 26.0	16.5/1.1	60.0 \pm 0.3	139 \pm 4	N		
13	SSTVMRD J084604.4-433936.5	08 46 04.4	-43 39 36.5	0.0/0.0	1041 \pm 4	4645 \pm 34	N		
14 ^e	SSTVMRD J084624.2-433415.6	08 46 24.2	-43 34 15.6	...	diffuse	217 \pm 5	N		
15 ^e	SSTVMRD J084626.4-434247.5	08 46 26.4	-43 42 47.5	18.0/ 3.2	245.6 \pm 0.8	1712 \pm 5	Y	umms1	9.4/20.9
16	SSTVMRD J084626.7-434217.3	08 46 26.7	-43 42 17.3	6.0/ 6.7	141.4 \pm 0.3	1612 \pm 7	Y	umms1	13.9/9.3
17 ^e	SSTVMRD J084627.3-434239.5	08 46 27.3	-43 42 39.5	4.5/ 4.8	234.6 \pm 0.2	1712 \pm 5	Y	umms1	22.9/12.9
18	SSTVMRD J084631.4-435605.7	08 46 31.4	-43 56 05.7	3.0/ 1.1	4366 \pm 10	16790 \pm 91	Y		
19 ^e	SSTVMRD J084631.6-435532.2	08 46 31.6	-43 55 32.2	7.5/ 7.2	367 \pm 9	14939 \pm 68	Y		
20 ^e	SSTVMRD J084633.1-435539.6	08 46 33.1	-43 55 39.6	15.0/ 0.2	349 \pm 11	14939 \pm 68	Y		
21	SSTVMRD J084634.3-432115.1	08 46 34.3	-43 21 15.1	3.0/ 0.4	18.9 \pm 0.1	211 \pm 6	Y		
22 ^f	SSTVMRD J084634.9-435437.1	08 46 34.9	-43 54 37.1 ^d	...	>4000 ^b	78368 \pm 173	Y	MMS4	5.1/1.1
23	SSTVMRD J084637.4-435217.0	08 46 37.4	-43 52 17.0	1.5/ 6.7	4292 \pm 9	9024 \pm 45	Y		
24	SSTVMRD J084637.5-435357.1	08 46 37.5	-43 53 57.1	6.0/ 0.8	4758 \pm 8	31250 \pm 180	Y		
25 ^e	SSTVMRD J084639.2-435254.1	08 46 39.2	-43 52 54.1	3.0/ 12.4	341 \pm 5	8975 \pm 110	Y		
26 ^e	SSTVMRD J084639.5-435314.1	08 46 39.5	-43 53 14.1	7.5/ 7.6	215 \pm 6	8975 \pm 110	Y		
27	SSTVMRD J084712.1-432250.6	08 47 12.1	-43 22 50.6	1.5/ 1.9	102.1 \pm 0.3	360 \pm 6	Y		
28	SSTVMRD J084714.4-431828.8	08 47 14.4	-43 18 28.8	7.5/ 1.5	314.5 \pm 0.1	127 \pm 5	Y		
29	SSTVMRD J084725.3-434900.1	08 47 25.3	-43 49 0.1	6.0/ 0.5	511.7 \pm 0.4	114 \pm 6	Y		
30	SSTVMRD J084731.2-435357.0	08 47 31.2	-43 53 57.0	4.5/ 0.7	47.7 \pm 0.1	229 \pm 4	Y		
31	SSTVMRD J084731.7-434555.7	08 47 31.7	-43 45 55.7	7.5/ 4.4	2677 \pm 2	359 \pm 10	Y		
32 ^g	SSTVMRD J084738.0-434255.3	08 47 38.0	-43 42 55.3	...	diffuse	1653 \pm 16	Y		
33	SSTVMRD J084742.8-434352.4	08 47 42.8	-43 43 52.4	13.5/ 1.7	1533.5 \pm 0.7	1629 \pm 12	Y	umms11	4.8/13.4

Table 3.7: MIPS sources detected at $70\mu\text{m}$ (continued).

ID	Spitzer name	$\alpha(2000.0)$ (h m s)	$\delta(2000.0)$ ($^{\circ}$ ' ")	$(\Delta\alpha/\Delta\delta)_{70}$ ($''/''$)	$(F\pm\Delta F)_{24}$ (mJy)	$(F\pm\Delta F)_{70}$ (mJy)	CO contours	dust core	$(\Delta\alpha/\Delta\delta)_{mm}$ ($''/''$)
34	SSTVMRD J084748.4-432536.4	08 47 48.4	-43 25 36.4	9.0/ 5.9	142 \pm 2	796 \pm 11	Y	umms12	24/19
35	SSTVMRD J084751.7-432523.4	08 47 51.7	-43 25 23.4	10.5/13.5	137 \pm 3	1114 \pm 6	Y		
36	SSTVMRD J084755.7-441119.0	08 47 55.7	-44 11 19.0	15.0/ 1.9	53.6 \pm 0.6	518 \pm 5	Y		
37	SSTVMRD J084811.3-432056.0	08 48 11.3	-43 20 56.0	15.0/ 0.6	83.4 \pm 0.3	504 \pm 6	Y		
38 ^e	SSTVMRD J084815.8-434715.8	08 48 15.8	-43 47 15.8	1.5/ 0.1	32 \pm 1	1410 \pm 7	Y	umms16	1.2/8.0
39 ^e	SSTVMRD J084816.7-434719.4	08 48 16.7	-43 47 19.4	12.0/6.4	27 \pm 1	1410 \pm 7	Y	umms16	14.7/11.6
40	SSTVMRD J084826.5-431721.2	08 48 26.5	-43 17 21.2	1.5/ 1.3	59.1 \pm 0.3	162 \pm 6	Y		
41 ^{a,g}	SSTVMRD J084828.0-423630.8	08 48 28.0	-42 36 30.8	9538 \pm 49	N		
42 ^{a,g}	SSTVMRD J084829.3-423733.2	08 48 29.3	-42 37 33.2	3279 \pm 46	N		
43 ^{a,g}	SSTVMRD J084830.6-423559.9	08 48 30.6	-42 35 59.9	12759 \pm 63	N		
44	SSTVMRD J084834.0-433051.3	08 48 34.0	-43 30 51.3	1.5/ 2.9	228 \pm 1	645 \pm 17	Y	umms19/20	13.6/7.4;22.1/8.5
45	SSTVMRD J084841.6-433149.8	08 48 41.6	-43 31 49.8	1.5/ 2.0	116 \pm 2	903 \pm 7	Y	MMS9	20.4/1.8
46	SSTVMRD J084844.2-431611.8	08 48 44.2	-43 16 11.8	6.0/ 0.3	100.0 \pm 0.2	455 \pm 10	Y		
47	SSTVMRD J084846.4-425055.6	08 48 46.4	-42 50 55.6	12.0 13.6	45 \pm 1	776 \pm 10	N		
48 ^h	SSTVMRD J084848.2-425420.2	08 48 48.2	-42 54 20.2 ^d	...	>4000 ^b	125200 \pm 270	N		
49 ⁱ	SSTVMRD J084848.7-433230.7	08 48 48.7	-43 32 30.7 ^d	...	>4000 ^b	50640 \pm 43	Y		3.9/2.7
50	SSTVMRD J084853.2-433057.1	08 48 53.2	-43 30 57.1	0.0/ 2.6	1163 \pm 2	3126 \pm 30	Y	MMS12	1.8/1.0
51	SSTVMRD J084858.8-433825.1	08 48 58.8	-43 38 25.1	10.5/ 2.0	157 \pm 2	1758 \pm 18	Y	MMS16	14.4/2.9
52	SSTVMRD J084904.3-433805.0	08 49 04.3	-43 38 05.0	3.0/ 4.9	158 \pm 4	2359 \pm 28	Y	MMS17	10.5/7.1
53	SSTVMRD J084912.2-441636.5	08 49 12.2	-44 16 36.5	4.5/ 4.4	28 \pm 1	487 \pm 10	N	MMS18	
54 ^a	SSTVMRD J084912.5-432953.3	08 49 12.5	-43 29 53.3	...	diffuse	650 \pm 10	N		
55	SSTVMRD J084913.1-433628.5	08 49 13.1	-43 36 28.5	0.0/ 0.9	685 \pm 1	2910 \pm 20	Y	MMS21	1.5/0.4
56	SSTVMRD J084914.3-430019.8	08 49 14.3	-43 00 19.8	10.5/0.1	153.5 \pm 0.6	597 \pm 9	N		
57	SSTVMRD J084915.3-433448.6	08 49 15.3	-43 34 48.6	16.5/13.3	158 \pm 2	2210 \pm 19	Y		
58	SSTVMRD J084917.0-435600.3	08 49 17.0	-43 56 00.3	3.0/ 3.5	19.5 \pm 0.4	375 \pm 6	Y		
59	SSTVMRD J084921.2-440159.5	08 49 21.2	-44 01 59.5	1.5/ 6.7	158.3 \pm 0.1	295 \pm 5	Y		
60 ^j	SSTVMRD J084926.2-431710.2	08 49 26.2	-43 17 10.2 ^d	...	>4000 ^b	38890 \pm 86	Y	MMS22	17.4/2.0
61	SSTVMRD J084928.6-440429.2	08 49 28.6	-44 04 29.2	0.0/ 0.0	1.9 \pm 0.2	339 \pm 10	Y	MMS23	13.8/6.9
62 ^k	SSTVMRD J084932.8-441050.0	08 49 32.8	-44 10 50.0 ^d	...	>4000 ^b	44306 \pm 93	Y	MMS26	15.6/9.9
63	SSTVMRD J084936.1-441200.2	08 49 36.1	-44 12 0.2	7.5/ 2.5	1420 \pm 1	13595 \pm 84	Y	MMS27	23.1/4.2
64	SSTVMRD J084959.5-432300.7	08 49 59.5	-43 23 0.7	0.0/ 0.9	97 \pm 1	1472 \pm 13	Y	umms26	6.9/5.1
65 ^a	SSTVMRD J085038.9-434948.8	08 50 38.9	-43 49 48.8	...	diffuse	356 \pm 7	N		
66	SSTVMRD J085129.7-433124.0	08 51 29.7	-43 31 24.0	16.5/ 2.2	74.1 \pm 0.2	2281 \pm 9	N		
67 ^{a,g}	SSTVMRD J085149.4-430540.2	08 51 49.4	-43 05 40.2	6656 \pm 33	N		

Notes to the table: ^a detected only at $70\mu\text{m}$; ^b saturated; ^c IRS16 in the Liseau et al. (1992) list.; ^d $70\mu\text{m}$ coordinate; ^e associated with the same $70\mu\text{m}$ source; ^f IRS17; ^g source outside the $24\mu\text{m}$ map;

^{h,i,j,k} IRS18, IRS19, IRS20, IRS21 in the Liseau et al. (1992) list, respectively.

we have seen in Section 3.3.3 (Table 3.4), 43 cores are not associated with any MIR/FIR counterpart, so that they appear to be either cold Class 0 sources/starless cores (in case of resolved cores) or possibly data artifacts (in case of under-resolved cores). Such a high fraction of starless cores as compared to protostellar cores is most likely a result of the poor sensitivity of the IRAS/MSX facilities. In order to resolve this issue we closely reexamined our maps, performing photometry on the mm peaks coordinates using local rather than global thresholds for the background level. This technique turned up 12 new objects at a flux density as low as 0.7 mJy at 24 μm , fainter than the completeness limit by more than a factor of 7. This procedure, together with automatic finding described above, when applied overall led to the association of 23 resolved and 20 under-resolved cores with 58 sources at 24 μm , 19 sources at 70 μm (in some cases we found multiple associations), thereby dramatically increasing the percentage of cores associated with an embedded protostar from 22% (Table 3.4) to 78%.

This result is in general agreement with recent MIPS findings in other GMCs that have substantially modified the percentage of active *vs* inactive cores in favor of the former (*e.g.* Young et al. 2004). We also note that the existence of a MIPS counterpart to 20 out of 26 under-resolved cores significantly reduces the possibility that these objects are simply data artifacts.

The lack, even at the MIPS sensitivity, of a FIR counterpart to five resolved dust peaks (namely MMS 6, 13, 15, 20, 24) makes these objects a very robust sample of genuine starless cores.

3.4.1 Color-magnitude diagrams

The Spitzer-MIPS wavelengths permit to obtain important information about the evolutionary stages of the young objects by means of the color-magnitude diagrams K_s vs K_s -[24] and [24] vs [24]-[70] presented in Figures 3.12 and 3.13.

K_s vs K_s -[24] - About half of the 24 μm detections have identifiable 2MASS counterparts at K_s (limiting magnitude of 15.3) within a radius of 5". These 2MASS fluxes have been used to construct the K_s *vs* K_s -[24] color-magnitude diagram (Figure 3.12), where MIPS sources inside and outside the CO contours are shown with different colors.

Also reported as hatched areas are the *loci* of the extragalactic sources in the SWIRE survey. As expected for a molecular cloud in the galactic plane, there are very few extragalactic sources seen. A remarkable number of objects fall at $K_s < 8.5$ mag and $K_s-[24] \sim 0$, which, given our completeness limit at $24 \mu\text{m}$ of 5 mJy, delimits the region of normal photospheres in Vela-D. Noticeably, in this part of the diagram, the number density (per deg^2) of the ‘off-cloud’ sources is larger than that of the ‘on-cloud’ ones (100 *vs* 69, see Table 3.9): In principle, all the un-reddened photospheres detected in Vela-D could be indeed foreground/background stars. More reasonably, we can affirm that no increase of main-sequence stars (with respect to the adjacent field) is registered in Vela-D, as expected because of the youth of the region.

The thick squares indicate the effects of an extinction of $A_V = 10$ and 50 mag, respectively, on the data. The quantitative A_V map of the overall region by Dobashi et al. (2005) does not provide values in excess to 5-10 mag (below the saturation limit of the catalog of 15 mag), while toward the dust cores A_V can increase up to ~ 20 mag (Massi et al. 2007 and Elia et al. 2007). We thus conclude that sources with $K_s-[24] > 5$ are probably reasonably young objects, and not merely extinguished objects. Indeed, it is not accidental that the large majority of these sources belong to the molecular cloud, nor that the objects with normal photospheres are outside the cloud. From an evolutionary point of view, as we have explained in Sections 1.3.1 and 3.3.4 (see also Figure 3.3), protostars can be characterized on the basis of the spectral index between 2-10 μm (Greene et al. 1994), according to which different evolutionary stages, from the accretion phase (Class I) to the beginning of the main-sequence (Class III), are manifested. Greene et al. (1994) have also found that the 2-10 μm spectral index does not change substantially when computed using fluxes up to 20 μm (by using photometry in the Q band¹⁸); this result allows one to extrapolate the 24 μm flux for different spectral indexes and accordingly to compute the expected value of the $K_s-[24]$ color. The result of this procedure is given in Rebull et al. 2007, who furthermore requested that, to select Class III sources from normal photospheres and foreground/background stars, $K_s-[24] > 2$.

The spectral classification derived for Vela-D is depicted in Fig. 3.12

¹⁸The Q band spans the 17 to 26 μm wavelength range.

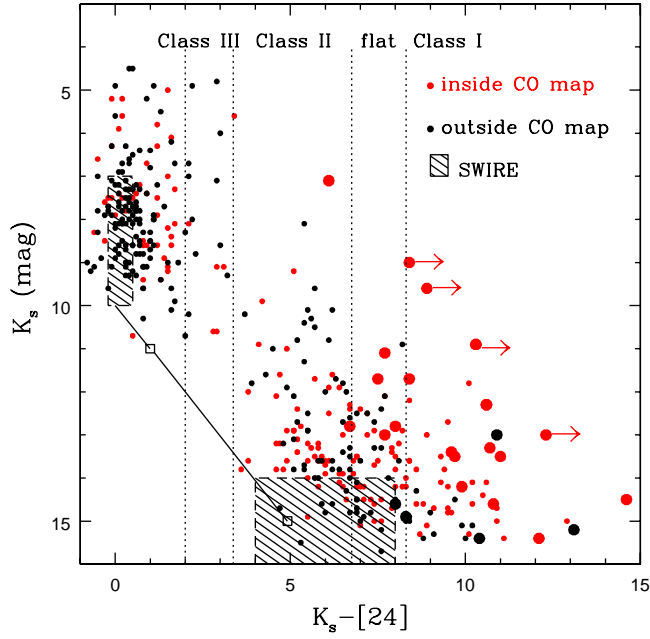


Figure 3.12: Color-magnitude diagram for the 2MASS K_s -band and the MIPS $24\ \mu\text{m}$ sources. Of the 849 $24\ \mu\text{m}$ sources in the MIPS map, 401 have a K_s detection within a radius of 5 arcsec. These are shown by red dots if located inside the CO contour map (180 sources) and by black dots if outside (221 sources). Large dots denote sources with $70\ \mu\text{m}$ detections, while arrows refer to sources saturated at $24\ \mu\text{m}$. Hatched areas are the loci of the sources in the SWIRE survey (taken from Rebull et al. 2007). The thick line indicates the effect of the extinction for different values of A_V (open squares refer to $A_V = 10$ and 50 mag).

Table 3.8: *Classification of the MIPS sources.*

item	inside CO map	outside CO map
photospheres	42(23%)	124(56%)
Class III	5 (3%)	11 (5%)
Class II	51(28%)	44 (20%)
flat spectrum	40(22%)	31 (14%)
Class I	42(23%)	11 (5%)
Class 0	6	1? ^a
Starless cores	5	0

^aThis source is observed only at 70 μ m, so that just upper limits appear in the 24-[24-70] plot.

and also reported in Table 3.8. The ratio of ‘on-cloud’ over ‘off-cloud’ objects within the same class increases with increasing K_s -[24] values; moreover, most of the younger ‘on-cloud’ objects are also detected in the 70 μ m band (large, red dots in Fig. 3.12). Noticeably, 70% of the ‘off-cloud’ objects showing the characteristics of the youngest and coldest sources (black dots at K_s -[24] \simeq 7) are located just outside the North and West borders of the CO gas map, therefore they are reasonably genuine members of Vela-D; the remaining sources (30%) with the same colours, if not belonging to Vela-D, could represent star forming regions at larger distances.

In summary, we find a definitely many more young sources associated with the cloud, but confirming that active star formation behind and/or in the close neighbourhood of our cloud is going on as well. The relative percentages of sources attributed to different evolutionary stages (see Table 3.9) can be compared with those of other well studied star forming regions. Schmeja et al. (2005), in particular, have investigated number ratios of sources in different evolutionary classes in several star forming regions (ρ Ophiuchi, Serpens, Taurus, Chamaleon I, IC348) basing on data obtained before than the Spitzer advent. They find, on average, that Class I sources are \sim 1-10%, while Class II/III sources are about 80-95% of the total. With the advent of Spitzer, these percentages have increased slightly in favor of younger protostars: by combining both IRAC and MIPS data, Reach et al. (2004) classified as Class I 11% of the sources in IC1396A and Muze-

rolle et al. (2004) 20% of the sources in NGC7129. Finally, in L1630 a ratio of 0.25 is found between Class I and Class II protostars (Muzerolle et al. 2005). A comparison of our statistics with these is not straightforward both because of the different classification adopted there and the fact that this paper uses MIPS data only. A more meaningful and direct comparison is with the works of Harvey et al. (2007) and of Rebull et al. (2007), who performed a very similar analysis as the one we do here, but on the Serpens star forming region and on the IC348 and NGC1333 clouds in Perseus. The percentage of Class I *vs* Class II objects is 6% *vs* 63% (Serpens), 6% *vs* 85% (IC348) and 7% *vs* 67% (NGC1333), thus strongly in favoring the latter. In contrast, we find percentages in Vela-D of 23% of Class I and 28% of Class II.

Two possible alternatives could explain such a difference: (i) Vela-D is significantly younger than either Perseus or Serpens. Such an hypothesis is supported by the age estimates of 1-2 Myr derived in the Perseus cloud (Palla & Stahler 2000, Rebull et al. 2007) and of 2 Myr derived in Serpens (Djupvik et al. 2006) as compared with an age of 10^5 - 10^6 yr towards the clusters of Vela-D (Massi et al. 2000); (ii) our K_s *vs* K_s -[24] diagram suffers from missing two important categories of sources. One category is represented by the ~ 450 objects detected at 24 μm , but without a K_s -2MASS counterpart (see Table 3.5). The sensitivity limits of our survey in terms of power density at a given wavelength are $\lambda F_\lambda(2\text{MASS}) \simeq \lambda F_\lambda(24\text{-MIPS}) \sim 6 \cdot 10^{-16} \text{ W m}^{-2}$. This implies that these 450 sources are objects whose SED is rising with wavelength and thus they could be additional young objects that tend even to increase the already anomalous percentage of Class I sources. The second category, however, is represented by the about $5 \cdot 10^4$ 2MASS objects not having a MIPS 24 μm counterpart. Their SEDs are allowed to decrease with increasing wavelength, therefore, although many of them could be foreground or background objects unrelated with the Vela-D population, they surely represent a potential reservoir of Class II and III objects. It should be sufficient that a very small fraction of them (~ 1 -2%) were genuine Class II/III sources to reduce significantly the relative excess of Class I in Vela-D, and then to increase the apparent age of the region. In this view the disagreement with other star forming regions could be reconciled, by considering that in those cases the lower background level implied by their loca-

tion outside the Galactic plane has permitted to reach detection limits at $24\mu\text{m}$ up to an order of magnitude fainter than in Vela, therefore allowing to trace the SED also for faint K_s sources that decline going from the near- to the far-infrared. In any case, we expect to provide a more certain answer to this issue in the next future, by means of forthcoming IRAC images covering the relevant spectral bands at more adequate sensitivity.

[24] vs [24]-[70] - In Figure 3.13 the color-magnitude diagram based on MIPS fluxes alone is shown. Here the sources detected in both bands are plotted; the large majority of them are on-cloud, although there is no clear difference between sources associated or not associated with dust cores (large dots). Remarkably, all sources (except 3) are located to the right of $[24]-[70] = 2$. This value pertains to SED's that increase with wavelength in such a way that $(\lambda F_\lambda)_{70} = 2 \times (\lambda F_\lambda)_{24}$. These red objects are much more numerous than the $70\mu\text{m}$ detections depicted in Figure 3.12, since the majority of them lack a 2MASS counterpart. Forthcoming IRAC data will help us to reconstruct their SED's more adequately, giving constraints on their luminosity and evolutionary stage. A few sources (6) lie in the locus corresponding to black-body temperatures ranging between 40 and 50 K. These are values theoretically predicted (Shu et al. 1987) for a collapsing isothermal sphere, identified as Class 0 objects. These 6 sources are all located inside the CO cloud; two of them lie within a mm core and one (#38) is also associated to a compact H_2 jet (jet2, see next Chapter, Table 4.4).

3.4.2 Comparison with IRAS sources

The similarity of the MIPS 24 and $70\mu\text{m}$ bandpasses to the 25 and $60\mu\text{m}$ filters on-board IRAS offers us the opportunity to evaluate directly the reliability of the IRAS point source catalogue (IRAS-PSC) fluxes in crowded and diffuse clouds like Vela-D, objects that are commonly found in the galactic plane. A similar study has already been performed by Rebull et al. (2007) in the Perseus molecular cloud; although in this case the geographic location makes extended emission and source confusion less critical, only 61% (at $25\mu\text{m}$) and 32% (at $60\mu\text{m}$) of the objects of the IRAS-PSC are recovered by MIPS as point-like sources, while all the others, although detected, remain confused

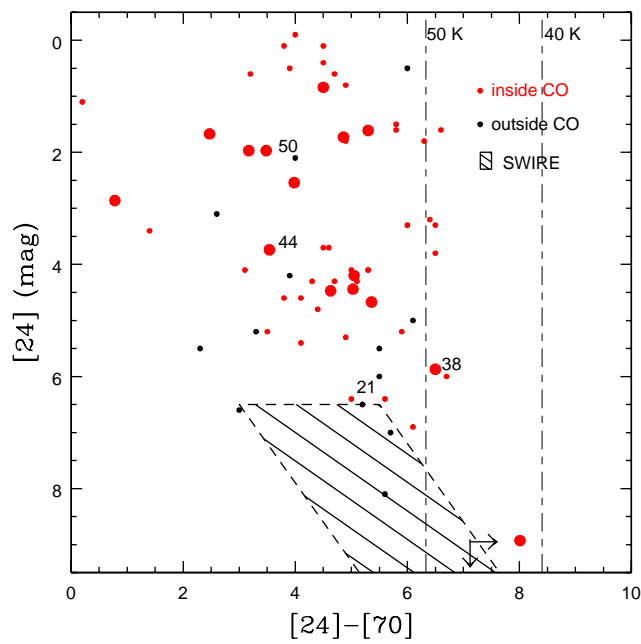


Figure 3.13: Color-magnitude diagram $[24]$ vs $[24]-[70]$, where only sources not saturated at $24\mu\text{m}$ are plotted. Red/black dots refer to sources inside/outside the CO contour map (41/12 sources). Large dots denote sources associated with a dust core, while numbered sources are the candidates exciting sources of the jets discussed in next Chapter (Table 4.4). The hatched area shows the locus of the SWIRE survey (taken from Fig.11 in Rebull et al. 2007).

by nebulosity. Higher rates of coincidence are found, at least at $25\ \mu\text{m}$, if the IRAS Faint Source Catalogue (FSC) - produced by point-source filtering the individual detector data streams - is used. Unfortunately, the FSC does not cover the galactic plane, so that we cannot confirm this result on Vela-D.

Here, a total of 57 high ($f_{qual}=3$) or moderate ($f_{qual}=2$) quality detections are listed in the IRAS-PSC catalogue at $25\ \mu\text{m}$; 46 of them (80%) are also seen by MIPS and recovered with our algorithm, while the remaining 11 IRAS objects appear as diffuse emission at $24\ \mu\text{m}$ and are thus undetected as point-sources. The matching rate for Vela-D is thus higher than in Perseus. The same trend is seen at $60\ \mu\text{m}$, where out of 48 IRAS-PSC items, the retrieval rate is of about 50%.

Table 3.9: *IRAS PSC detections not recovered by MIPS*

PSC name	MIPS $24\ \mu\text{m}$	IRAS $25\ \mu\text{m}$		MIPS $70\ \mu\text{m}$	IRAS $60\ \mu\text{m}$	
		fqual ^a	CC		fqual	CC
08441-4357	diffuse	1	null	missing	3	E
08475-4255	diffuse	3	D	diffuse	2	D
08475-4311	diffuse	3	E	diffuse	2	C
08478-4303	intense knot	3	A	diffuse	1	null
08479-4311	diffuse	3	D	diffuse	1	L
08487-4250	diffuse (map edge)	1	C	diffuse	3	B
08459-4338	diffuse	2	D	missing	3	C
08489-4241	off edge	3	C	diffuse	1	D
08457-4229	off edge	1	E	diffuse	2	D
08460-4223	off edge	2	D	intense knot (map edge)	2	C
08462-4235	diffuse (map edge)	1	J	diffuse?	3	B
08465-4230	off edge	2	B	diffuse? (map edge)	3	C
08471-4228	off edge	3	G	intense knot (map edge)	2	D
08473-4235	off edge	3	E	diffuse (map edge)	1	null
08437-4323	diffuse	1	D	missing	3	B
08468-4330	diffuse	3	D	missing	2	D
08488-4308	diffuse	2	C	diffuse	2	E
08490-4319	diffuse	1	F	missing	3	C
08491-4310	diffuse	3	B	diffuse	2	C
08491-4257	diffuse?	1	E	missing	3	B
08493-4331	diffuse	1	H	missing	3	C
08495-4306	diffuse	1	C	diffuse	3	C
08477-4329	diffuse	1	H	diffuse	3	D
08462-4400	diffuse	2	D	diffuse	1	D
08463-4343	diffuse	2	B	diffuse	3	D
08478-4403	diffuse	3	C	off edge	1	J
08478-4353	diffuse	1	I	diffuse	3	D

^aFlux density quality, encoded as 3: high quality, 2: moderate quality, 1: upper limit IRAS-PSC (1988).

In Table 3.9 we give the list of the IRAS-PSC (with any f_{qual}) not recovered by MIPS¹⁹. Along with the f_{qual} flag, we also give in Table 3.9 the IRAS correlation coefficient flag (CC, see Section 3.2.1) which provides an indication of the point-likeness confidence of the detected source. Noticeably, PSC sources retrieved by MIPS (with $f_{qual}=2,3$), show, on average, ‘CC’ flag equal to “A” or “B”: such an occurrence can thus be translated into a suitable tool to broadly distinguish between genuine point-source and diffuse emissions, if MIPS maps (and FSC detections) are unavailable.

Chapter summary - The young population of the Vela-D dust cores has been studied by means of both IR catalogues (IRAS/MSX/2MASS) and a set of new dedicated observations. The main goal of this study has been the identification of the NIR protostellar counterparts of the cores, *i.e.* the sources that dominate the core heating, which are the youngest objects of the cloud (§ 1.3.1). An example of the adopted method for finding such counterparts has been described in this Chapter while for a detailed description of all other core population we remand to the Appendix A. A significant upgrade in our knowledge of the MIR-FIR sky has been possible thanks to the Spitzer-MIPS images, whose global characteristics (photometry and source classification of the whole cloud) have been discussed in this Chapter. In the next Chapter, we will use these data for the identification of the jet driving sources (Table 4.4).

The main conclusions of this work are summarized here:

- In the majority of cases, MIR and/or FIR sources associated with dust cores do not coincide with the mm peaks, although they are located in their vicinity. In those cases of close-by cores, often the IR source is located in between them.
- The resolved mm cores (*i.e.* those larger than the instrumental beam) are more frequently associated to a NIR- or FIR-counterpart than the unresolved ones (smaller than the instrumental beam).

¹⁹The IRAS sources in the table marked as ‘off-edge’ in one MIPS bandpass are necessarily ‘on-edge’ in the other, because of the spatial shift between the two focal plane arrays.

The existence of signs of star formation activity around these latter in the form of H_2 jets and MIR/FIR new sources discovered by Spitzer, however, attests to the genuine nature of lots of them.

- The more sensitive Spitzer observations (with respect to the IRAS data) allowed us to significantly improve the statistics of active *vs* inactive cores in favour of the former²⁰. On the other hand, the list of those cores without any reliable infrared counterpart represents a robust sample of starless cores.
- The SEDs of the associated sources present a slope $\alpha = d \log(\lambda F_\lambda) / d \log(\lambda)$ between 2 and 10 μm whose distribution is strongly peaked at values typical of Class I sources ($0 < \alpha < 3$). The anomalous excess of Class I objects is confirmed by MIPS data and can be ascribed to a bias in the sensitivity limits of the 2MASS and MIPS surveys (due to the cloud distance), or to a short time elapsed since the first collapse of the cloud.
- An attempt has been done to search for Class 0 sources. Ten IRAS sources (with upper limits at 12 μm) do not present any NIR reliable counterpart, but none of them satisfies the criterion $L_{bol} / L_{1.3mm} \lesssim 2 \times 10^4$ proposed by André et al. (1993). However, considering the probable overestimates of the IRAS fluxes (and bolometric luminosities), we indicate the three objects with the lowest $L_{bol} / L_{1.3mm}$ ratios as the youngest IRAS sources of the region. Five additional Class 0 candidates have been selected among MIPS sources on the basis of their 24 and 70 μm colours.
- The sources associated to the dust cores, both resolved and unresolved, all have the same FIR colours, typical of a black-body stratification between 50 and 1000 K, with a stronger contribution of the former component. In other words, sources with FIR colours typical of pre-main sequence T-Tauri and Herbig Ae/Be stars seem to be absent, indicating Vela-D as a young ($\sim 10^6$ years) region.

²⁰IRAS-PSC detections of good quality ($f_{qual}=3,2$) are also seen by MIPS, but only when the IRAS point-likeness confidence is high (correlation coefficient, CC, equal to A or B). This result may be adopted as a broad confidence prescription for finding genuine point sources in the IRAS catalogue.

- Sources associated with unresolved cores are systematically less luminous (average $L_{bol} \simeq 1.5 \times 10^2 L_{\odot}$) than those related to the resolved ones (average $L_{bol} \simeq 1.5 \times 10^3 L_{\odot}$), providing evidence that two modalities of star formation, namely low- and intermediate-mass, are simultaneously present in Vela-D.
- About half of the $24 \mu\text{m}$ sources and two thirds of the $70 \mu\text{m}$ ones are spatially located inside a region delimited by the $^{12}\text{CO}(1-0)$ contours (0.6 deg^2). The implication is that the IR source density doubles (and is four times when considering sources at $70 \mu\text{m}$) inside the CO contours as compared to outside the molecular cloud.

Chapter 4

Mass loss phenomena in Vela-D

As mentioned in Section 1.3.4, mass-loss phenomena play a crucial rôle in the star formation process because of their ability of *(i)* removing the excess of angular momentum from the collapsing material, *(ii)* removing material out of the cocoon and *(iii)* transferring gravitational energy from small to large scales. Such phenomena are thought to be associated with all the modalities of star formation and their evolution is strictly linked to the evolutionary stages of their driving sources. The investigation over the presence and characteristics of these collimated flows, which commonly extend up to parsecs from the most embedded regions where the young protostars are located, represents a powerful approach to indirectly probe ongoing star forming activity, otherwise unaccessible.

The near infrared images in the H₂ 1-0S(1) narrow band filter (see § 1.3.4) of the dust cores and the CO maps presented in Chapters 2 and 3 revealed the occurrence in Vela-D of seven clearly identified jets (jet0 to 6, see previous Chapter), four regions of possible outflowing activity (MMS17-23-27-28/29) and three regions characterized by a complex morphology of shocking surfaces, likely due to multiple jet activity (star forming regions around IRS16-17-19). In the previous Chapter we have used the H₂ images to identify the infrared counterparts of the dust peaks and we have discussed the spatial association between jets and cores. This Chapter deals with the well identified jets and, where available, with new observations of their related outflows.

As we have seen in Section 1.3.4, molecular outflows present usually a bipolar morphology because they are cloud material swept up by jets coming from the protostar poles. So they are often found in connection

with shock regions revealed by H₂ emission, the major coolant of these regions, and a comparative study of both outflow and H₂ emission, can give important information on how energy is transferred from the jets to the circumstellar medium.

In Sections 1.1.1 and 2.1.1 we have underlined the effectiveness of CO observations in tracing molecular emission. Here we present observations collected last year of the CO emission around four jets likely originated by low-mass young objects with the aim of detecting molecular outflows and, in case, of deriving important physical parameters, such as mass, momentum and kinetic energy carried out by these outflows. Similar observations have been scheduled for the remaining discovered jets, likely produced by intermediate-mass objects.

We describe in this Chapter the performed observations (§ 4.1), the theory on which the estimate of the physical parameters is based (§ 4.2), and the results of the data analysis (§ 4.3). In the last Section (§ 4.4) we attempt to give a picture as complete as possible of the physical systems constituted by protostar, jet, outflow and core of the selected fields.

4.1 Observations

4.1.1 H₂ survey (2.12 μm)

We performed a complete survey at 2.12 μm of the dust emission regions and their surroundings with the aim of finding out signatures of shocked regions indicating the occurrence of jets. The 20 images, 4.9 by 4.9 arcmin² wide, with a resolution of 0.29 arcsec/pixel, have been acquired by means of the SofI (Lidmann et al. 2006) instrument at ESO-NTT (La-Silla, Chile) on January 2006. We used a narrow-band ($\Delta\lambda = 0.03 \mu\text{m}$) infrared filter centered on the 1-0S(1) H₂ line at 2.12 μm ¹. All the observations were obtained by dithering the telescope around the pointed position and the raw imaging data were reduced by

¹This emission line is due to the most commonly observed H₂ ro-vibrational transition. In the line identification 1-0S(1), 1-0 denotes the vibrational change from the first to the ground level, while the S indicates the change $\Delta J = +2$ in rotational state and (1) gives the value of J in the final state (the letters Q and O denote the other allowed transitions, $\Delta J = 0, -2$, respectively). Transitions with $\Delta J = \pm 1$ are forbidden because of the omo-nuclear nature of the H₂ molecule.

using standard procedures for bad pixel removal, flat fielding, and sky subtraction (see the description in Section 3.1.3 concerning the NIR images).

As we have said in the first Chapter, the H_2 molecule is by far the most abundant in the cloud gas, but it is not used to trace the molecular gas in normal conditions because of the high excitation temperature ($\simeq 500$ K) of the fundamental H_2 rotational transition (0-0S(0) at $28 \mu\text{m}$, not observable from earth because of atmospheric absorption). Within shocked regions the environmental H_2 , brought to thousands of Kelvin by the impact of the jet material ($T \sim 3000$ K, $v \lesssim 50 \text{ km s}^{-1}$), decays from the excited ro-vibrational levels emitting copiously in the NIR. So, the $2.12 \mu\text{m}$ transition, which falls within the K band atmospheric window, is particularly suited for tracing impact surfaces between the jets and the cloud (e.g. Gredel 1994). The theoretical relation $L_{\text{H}_2} \simeq 10 \cdot L_{2.12 \mu\text{m}}$ (e.g. Lorenzetti et al. 2002a) permits then to estimate the total luminosity emitted by H_2 molecules² (once the 2.12 line intensity is corrected for the extinction).

Although the total area covered by the survey is about one tenth of the entire region defined in Section 3.2.4, the jets are expected to be located within regions of dust emission, so the H_2 survey allowed us to observe likely the majority of the Vela-D jets at the reached sensitivity limit of about $10^{-15} \text{ ergs s}^{-1} \text{ cm}^{-2} \text{ arcsec}^{-2}$. As we have seen in the Chapter 3, these images reveal the presence of three regions of intense and morphologically complex emission (Figures 3.1, A.9, A.24), in correspondence with the Vela-D young clusters and of seven well identifiable jets (Figures A.1, A.33, 4.5, A.35, A.20, A.12 and Figure 1 in Giannini et al. 2005). Four of these are likely driven by low-mass stars and will be analyzed in the following Sections.

In table 4.1 we report: (i) the integrated flux³ detected at $2.12 \mu\text{m}$ of all knots constituting each jet lobe⁴, (ii) the total flux corrected for

²This is a valid approximation for a thermalized gas at about 2000 K within C-shocks (see Section 1.3.4). J-shock (dissociative), models (Hollenbach & McKee 1989) predict weaker 1-0S(1) emission (e.g. Lorenzetti et al. 2002a).

³The reported values have been obtained by integrating the flux of the continuum-subtracted H_2 images.

⁴See Giannini et al. (2005) for a detailed description of the star forming region associated to IRS17 (08448-4343), showing a complex H_2 morphology and a well identified jet more than 0.3 pc long not considered in the table.

the extinction⁵ and (iii) the corresponding total H₂ luminosity (L_{H_2}), (iv) the length and (v) the dynamical time of the jet, *i.e.* the time taken by the jet apex to reach the current distance from the source at a constant speed. To evaluate the H₂ luminosity we used the mentioned relation $L_{H_2} = 10 \cdot L_{2.12\mu m}$. Regarding the jet length we adopted again the distance estimate $d=700$ pc and an inclination angle of 45° . At last, the dynamical time of the jet can be rawly evaluated by assuming typical values for both speed and inclination angle ($v_{shock} = 50 \text{ km s}^{-1}$, $i = 45^\circ$).

We make an attempt to identify those knots as pertaining to the blue side of the jets on the basis of simple considerations on knot distributions and fluxes with respect to the hypothesized driving source. The blue shifted lobe, which emerges from the cloud towards the observer, is in fact usually more luminous than the red shifted one because less extincted.

Table 4.1: *Integrated flux and parameters of the Vela-D H₂ jets.*

jet id ^a	Lobe	F_{lobe} ($10^{-14} \text{ erg s}^{-1} \text{ cm}^{-2}$)	$F_{tot-corr}^b$ ($\text{erg s}^{-1} \text{ cm}^{-2}$)	$L_{H_2}^c$ ($10^{-2} L_\odot$)	Length ^d (pc)	$t_{dyn-jet}^e$ (10^3 yr)
jet1	blue	21.0 ± 0.1	$7.9 \cdot 10^{-13}$	12	0.30	4.3
	red	7.1 ± 0.1				
jet2	blue	8 ± 2	$4.3 \cdot 10^{-13}$	6.7	0.13	1.7
	red	7.1 ± 0.2				
jet3	blue	0.94 ± 0.01	$4.6 \cdot 10^{-14}$	0.7	0.08	1.1
	red	0.71 ± 0.01				
jet4	blue	106.7 ± 0.4	$4.9 \cdot 10^{-12}$	73	0.68	93.5
	red	65.6 ± 0.3				
jet5	blue	7.6 ± 0.2	$2.1 \cdot 10^{-13}$	3.4	0.18	5.0
jet6	blue	9.7 ± 0.1	$2.7 \cdot 10^{-13}$	3.7	0.49	15.3

^aSee Giannini et al. (2005) for the jets in the star forming region of IRS17.

^bCorrected for the extinction. $A_V=10$ mag is assumed.

^cEvaluated from: $L_{H_2}=10 \cdot L_{2.12\mu m}$.

^dAn inclination angle $i=45^\circ$ is assumed.

^eComputed for $i=45^\circ$ and $v_{shock}=50 \text{ km s}^{-1}$.

⁵The extinction law:

$$\frac{A_\lambda}{A_V} = 0.42 \cdot \left(\frac{\lambda}{\mu m} \right)^{-1.75}$$

(Draine 1980) has been used to evaluate extinction at $2.12 \mu m$ from the assumed average extinction value $A_V = 10$ mag.

4.1.2 Apex data

As we shall see in the next Sections, the line profiles of CO lines, and the ratios between lines of different isotopes, give crucial information about physical conditions of the outflowing material, such as optical thickness, mass, carried momentum and energy. Unfortunately, our $^{12}\text{CO}(1-0)$ and $^{13}\text{CO}(1-0)$ maps (presented in Chapter 2) did not give conclusive results on the presence of outflows, mainly because the spectra appear dominated by a strong contribution of the cold gas in the molecular cloud and by the presence of multiple components along the line of sight. Moreover, the poor spatial resolution of those observations, prevented us to clearly correlate the cold gas with the different parts of the jets. CO lines at higher excitation temperature (as those between the rotational levels 3 and 2) allowed us to circumvent these problems being them more effective in disentangling the molecular gas belonging to the jet from the cold gas entrained from the ambient medium and, due to the diffraction limit of the telescope, the spatial resolution reached is a factor 2.5 higher than that reached in the (1-0) transition with the same telescope.

We observed the high-J CO lines by means of APEX, the Atacama Pathfinder EXperiment. This is an ESO millimeter facility of the southern hemisphere, located at Llano Chajnantor (Chile), and is the prototype antenna of the ALMA (Atacama Large Millimeter Array) project (an impressive 64 antenna system that will see its first light on 2010 and will likely bring a new era in the star formation astronomy).

We used the APEX-2A heterodyne receiver, that works in the range 279-381 GHz with a HPBW of $18''$. In particular, we selected the 345 GHz to observe the $^{12}\text{CO}(3-2)$ rotational line, very effective in revealing large scale outflows at excitation temperatures of 10-20 K.

So the aim of these new observations is: (i) to investigate whether or not large scale outflows are associated with the jets, (ii) to evaluate the physical conditions of the outflowing material, and (iii) to compare the results with the measured fluxes in the H_2 2.12 μm line (see table 4.1).

The observations were performed in service mode from September to December 2006 and, due to time constraints, we observed only a subsample of four jets (jet1, jet2, jet4, jet5 of table 4.1), those supposed to be originated from low-mass objects, waiting for new telescope time

to complete the survey of the Vela-D jets.

The data acquired consist of small maps of $^{12}\text{CO}(3-2)$ spectra of the selected jets, centered on the supposed driving source (see § 3.3, 3.4). The maps are typically 40 arcseconds wide with a velocity channel width of 0.5 km s^{-1} .

Prior to show the results of these CO maps, a brief presentation of the theory at the basis of physical parameters estimate is in order.

4.2 Outflow parameters estimate: theory

CO rotational emission lines (see also § 2.1) are crucial as tracers of the physical conditions in molecular clouds and, in particular, the outflowing activity is detected and studied by analyzing the CO line profiles. While the velocity of the line center indicates the global radial motion of the cloud in which the proto-star is embedded with respect to the observer, the emission of the two lobes produced by the gas of the flow, pushed in opposite directions, are red- or blue-shifted in velocity (unless the outflow axes is exactly orthogonal to the line of sight). Such an additional, broad, low-level emission produces a slope change at the wings of the line (see e.g. Figure 4.1). So, due to the bipolar morphology of the outflow, the line profile will change as a function of the offset position relative to the proto-star. It should be said, however, that emission from both lobes can be present simultaneously on one spectrum if the receiver resolution is less than the angular separation of the lobes and/or if the outflow inclination is too small with respect to the line of sight⁶.

The physical parameters that can be estimated for each lobe from the CO rotational line spectra are mainly its mass, momentum and kinetic energy. These estimates start from the definition of a velocity range, on the blue or on the red side of the emission line, in which the emission is supposed to be mainly due to the gas in the outflow. It follows an evaluation of the column density pertaining to the observed lines. The calculation of the parameters is then straightforward.

⁶Sometimes, in addition to the common “standard high velocity” (HV) components, having relative velocities with respect to the cloud of up to 20 km s^{-1} , another “extremely high velocity” components (EHV) have been observed, with velocities up to 150 km s^{-1} (Wouterloot & Brand 1999). These are usually found in highly collimated flows (Smith 2004) and are common around infrared sources of moderate to high luminosity (500 to $4 \cdot 10^5 L_{\odot}$) (Choi et al. 1993).

Important assumptions are needed on outflow morphology, inclination, velocity range, rotational level populations, temperatures, relative abundances and so on. So a high degree of uncertainty is unavoidable. Nevertheless, the ranges of likelihood for mass, momentum and energy can give very useful information on the evolutionary stage of the driving source and on the dynamical behaviour of the whole core, especially if correlated to both the protostar SED and the jet emission.

4.2.1 Radiative transfer of emission lines

In order to evaluate mass, momentum and kinetic energy of the outflowing material we need an estimate of the *column density* (eq. 4.19) along the line of sight and in the velocity ranges pertaining to the lobes. Such an estimate is based on the radiative transfer theory, that describes the radiation propagation through a medium.

The molecular transition between an upper (u) and a lower (l) level gives rise to a radiation of specific intensity I_ν at the frequency ν . The intensity variation along the path ds through the cloud is linked to the emission (ϵ_ν) and absorption (k_ν) coefficients of the medium (at the transition frequency) by means of the radiative transfer equation:

$$\frac{dI_\nu}{ds} = -k_\nu \cdot I_\nu + \epsilon_\nu \quad (4.1)$$

Defining the optical thickness

$$\tau_\nu \equiv \int_0^s k_\nu(s) ds \quad (4.2)$$

and the source function

$$S_\nu \equiv \epsilon_\nu / k_\nu, \quad (4.3)$$

the transfer equation becomes⁷:

$$\frac{dI_\nu}{d\tau_\nu} = I_\nu - S_\nu. \quad (4.4)$$

In case of *Local Thermal Equilibrium* (LTE)⁸ the source function is

⁷Given the dependence of S_ν from I_ν , it follows that the transfer equation is an integro-differential equation.

⁸A thermodynamic system is said to be in thermodynamic equilibrium when it is in thermal, mechanical, and chemical equilibrium. The local state of a system at thermodynamic equilibrium is determined by the values of its intensive parameters, as pressure, temperature, etc. When these intensive parameters vary slowly with space and time one can assume thermodynamic equilibrium in some neighborhood about that point and the system is said to be in *Local Thermal Equilibrium*.

independent on the radiation intensity and takes the form of the Planck function at the system temperature:

$$S_\nu = B_\nu(T). \quad (4.5)$$

So the transfer equation solution assumes the simple form:

$$I_\nu = B_\nu(T) \cdot (1 - e^{-\tau_\nu}) + I_\nu(0) \cdot e^{-\tau_\nu}, \quad (4.6)$$

where $I_\nu(0)$ represents the background radiation.

In radio-astronomy, due to the usually verified Rayleigh-Jeans approximation ($h\nu \ll k_B T$) that simply connect temperature and black-body radiation ($T/B_\nu = c^2/2\nu^2 k_B$), it is easier to deal with brightness and excitation temperatures instead of with intensities. The brightness temperature, T_B , is defined as follows:

$$T_B \equiv \frac{c^2}{2\nu^2 k_B} \cdot [I_\nu(\tau_\nu) - I_\nu(0)], \quad (4.7)$$

while T_{ex} is defined through a generalization of the Boltzmann's law:

$$\frac{n_u}{n_l} \equiv \frac{g_u}{g_l} \exp\left(-\frac{\Delta E_{ul}}{k_B T_{ex}}\right), \quad (4.8)$$

where n_u and n_l are the effective⁹ number densities of the molecules in the upper and lower levels, respectively, g_u and g_l the degeneracies of the two levels, and ΔE_{ul} their energy separation.

Within this framework (LTE, Rayleigh-Jeans approximation) and neglecting the background radiation, which is supposed to be the Cosmic Background Radiation at 2.73 K, the transfer equation solution (4.6) translates into:

$$T_B = T_{ex} \cdot (1 - e^{-\tau_\nu}), \quad (4.9)$$

from which we can consider the two limiting cases:

$$T_B = T_{ex} \cdot \tau_\nu \quad \text{if } \tau_\nu \ll 1, \quad (4.10)$$

$$T_B = T_{ex} \quad \text{if } \tau_\nu \gg 1. \quad (4.11)$$

While in the first case (optically thin medium) the emitted photon can easily cross the cloud and reach the observer, who can thus see directly the emission region, in the second case (optically thick medium) the

⁹While Boltzmann's law deals with the number density values at thermodynamic equilibrium, with T_{ex} replaced by the kinetic temperature.

radiation is absorbed and re-emitted many times before escaping the cloud and the radiation has only memory of the physical conditions at the cloud external layer. Should be said, however, that, as far as one goes away from the peak frequency, the optical thickness decreases and, also for optically thick lines, it can happen to have optically thin wings.

4.2.2 CO Column density

The column density, needed to estimate mass, momentum and kinetic energy, is the density of particles integrated along the line of sight and can be computed from the measured brightness temperature and from the optical thickness. To derive such relation we need to describe the radiation emission and absorption through a medium in terms of microscopic processes involving level populations (n_i), level degeneracies and Einstein coefficients.

Three types of processes between two levels u and l must be considered: *spontaneous emission*, proportional to the population n_u of the upper level and to the Einstein coefficient A_{ul} of the considered transition; *stimulated emission*, proportional to n_u , to the Einstein coefficient B_{ul} of the transition and to the energy density of the radiation field; *absorption*, proportional to the lower level population n_l , to the Einstein coefficient B_{lu} and to the energy density of the radiation field. Writing down the transfer equation in terms of these quantities, the expressions of the macroscopic emission and absorption coefficients can be derived:

$$\epsilon_\nu = \frac{h\nu}{4\pi} n_u A_{ul} \varphi(\nu) \quad (4.12)$$

$$k_\nu = \frac{h\nu}{c} n_l B_{lu} \left(1 - \frac{g_l n_u}{g_u n_l}\right) \varphi(\nu), \quad (4.13)$$

where $\varphi(\nu)$ is the line profile as a function of frequency.

By using the equation (eq. 4.8), which defines the excitation temperature, and the relations occurring between the Einstein coefficients¹⁰, k_ν can be rewritten as:

$$k_\nu = \frac{c^2}{8\pi\nu^2} \frac{g_u}{g_l} n_l A_{ul} \left(1 - e^{-\frac{h\nu}{k_B T_{ex}}}\right) \varphi(\nu) \quad (4.14)$$

¹⁰Relations between Einstein coefficients: $B_{lu} = B_{ul}$, $A_{ul} = 2h \frac{\nu^3}{c^2} B_{ul}$.

and integrated along the line of sight ds , thus obtaining the optical depth as a function of the column density N_l of the level l and of the velocity width (Δv) of the observed line:

$$\tau_\nu = \frac{c^3}{8\pi\nu^3} \frac{g_u}{g_l} N_l A_{ul} \frac{1}{\Delta v} \left(1 - e^{-\frac{h\nu}{k_B T_{ex}}}\right). \quad (4.15)$$

This relation can be inverted to obtain N_l :

$$N_l = \frac{8\pi\nu^3}{c^3} \frac{g_l}{g_u} \frac{1}{A_{ul}} \frac{1}{1 - e^{-\frac{h\nu}{k_B T_{ex}}}} \int \tau_\nu dv. \quad (4.16)$$

Now we need to link the column density of a generic rotational level of the CO molecule, characterized by its rotational quantum number J , to the total CO column density (N_{CO}). By assuming the LTE population distribution, the searched relation is given by:

$$\frac{N_J}{N_{CO}} = \frac{g_J}{Z} e^{-\frac{E_J}{k_B T_{ex}}} \quad (4.17)$$

where:

- The degeneracy is $g_J = 2J + 1$;
- The energy gap E_J between the level and the ground state is given by $E_J = hBJ(J+1)$ where B is a rotational constant and the molecule is considered as a rigid rotator;
- Z is the partition function and can be approximated by¹¹:

$$Z \simeq \frac{k_B T_{ex}}{hB}. \quad (4.18)$$

The CO column density pertaining to the considered transition ($u \rightarrow l$) can be eventually linked to the observed brightness temperature by using the relations (4.16), (4.17), (4.18) and remembering the equation (4.9), valid in LTE and Rayleigh-Jeans regimes:

$$N_{CO} = \frac{8\pi\nu^3}{c^3} \frac{1}{g_u A_{ul}} \frac{k_B}{hB} \frac{e^{\left(\frac{E_l}{k_B T_{ex}}\right)}}{1 - e^{-\left(\frac{h\nu}{k_B T_{ex}}\right)}} \frac{\tau}{1 - e^{-\tau}} \int T_B dv. \quad (4.19)$$

¹¹Supposing $k_B T_{ex}$ to be greater than the energy gap between the levels ($hB \ll k_B T_{ex}$), the exact expression of the partition function

$$Z \equiv \sum_{J=0}^{\infty} g_J e^{-\frac{E_J}{k_B T_{ex}}}$$

can be approximated by the integral, giving the reported result.

In our case the observed line is the $^{12}\text{CO}(3-2)$ and the previous equation translates, for each velocity channel (i) (channel width Δv), into the following (Choi et al. 1993):

$$N_{CO_{32}}^{(i)} = \frac{1.10 \cdot 10^{15}}{D(n, T_K)} \frac{\tau_{32}}{1 - e^{-\tau_{32}}} T_B^{(i)} \Delta v. \quad (4.20)$$

Here the function D of density (n) and kinetic temperature (T_K) has been used to take into account the uncertainties both in the estimate of T_{ex} and in the assumption of LTE. LVG (Large Velocity Gradient¹²) simulations, in fact, show that such function does not vary much within reasonable intervals of n and T_K . A value of 1.5 can be assumed in calculations, which is correct within less than a factor of 2 for $10 < T_K < 200 K$ and $10^4 < n < 10^6 \text{ cm}^{-3}$ (Choi et al. 1993).

4.2.3 Mass, momentum and kinetic energy

To evaluate the mass of the outflowing material swept up by the jet, we use the estimate of the column density $N_{CO_{32}}$ in combination with a distance estimate and assumptions on species abundances. For each velocity channel we can write:

$$M^{(i)} = \mu m_H d^2 \Omega N_{CO_{32}}^{(i)} \frac{[H]}{[C]} \frac{[C]}{[CO]}, \quad (4.21)$$

where $\mu = 1.3$ is the mean atomic weight, $m_H \simeq 1.68 \cdot 10^{27} \text{ kg}$ the mass of a hydrogen atom, $d = 700 \text{ pc}$ the Vela-D distance (see §), Ω the solid angle subtended by the emission (in steradians)¹³, $[H]/[C] = 2.5 \cdot 10^3$ the hydrogen *vs.* carbon abundance (Grevesse et al. 1991) and $[C]/[CO] = 8$ the carbon *vs.* carbon monoxide abundance (Choi et al. 1993). Summation over the velocity channels in the range associated to each lobe of the outflows obviously gives us the desired mass value:

$$M = \sum_i M^{(i)}. \quad (4.22)$$

¹²Large Velocity Gradient simulations are based on the assumption of steep gradients of the gas velocity, which is usually true for shock surfaces, having velocities of tens of km s^{-1} (greater than the sound speed in the medium). In this LVG approximation, due to the Doppler shift, a photon emitted has a significant probability to be re-absorbed only locally, where the gas velocity is not much different.

¹³The solid angle subtended by a cone with angle a is given by $2\pi[1 - \cos(a)]$. $a = 9''$ corresponds to $\Omega = 5.98 \cdot 10^{-9} \text{ sr}$.

The mass per velocity channel $M^{(i)}$ is used also to evaluate momentum and kinetic energy carried by the outflow by means of the simple relations:

$$P = \sum_i M^{(i)} |V^{(i)} - V_0|, \quad (4.23)$$

$$E_K = \sum_i \frac{1}{2} M^{(i)} (V^{(i)} - V_0)^2, \quad (4.24)$$

where the velocity has to be given with respect to the protostar rest frame velocity V_0 , assumed to be the peak velocity. It should be stressed, however, that both momentum and kinetic energy of the outflow depend on its orientation with respect to the line of sight, while gas velocity measurements pertain the only radial component. The obtained values should be thus regarded only as lower limits.

Another interesting quantity that can be estimated, independently from column density, is the dynamical time of the outflows ($t_{dyn-out}$), that can be compared to the jet dynamical times ($t_{dyn-jet}$) reported in Table 4.1. In this case the dynamical time is given by the ratio between the lobe size R and the mean velocity $\langle V \rangle$ of the outflowing gas in the lobe. The observed sizes (R_{obs}) and gas velocities ($\langle V_{obs} \rangle$) are projections of the real values, respectively perpendicular ($R_{obs} = R \cdot \sin i$) and parallel ($\langle V_{obs} \rangle = \langle V \rangle \cdot \cos i$) to the line of sight. Given the lack of indications about the outflow inclination, the simplest assumption consists of considering an inclination of 45 degrees (the same assumption adopted to evaluate $t_{dyn-jet}$), in which case:

$$t_{dyn-out} = R / \langle V \rangle = R_{obs} / \langle V_{obs} \rangle. \quad (4.25)$$

At last, kinetic luminosity L_{kin} (*i.e.* the kinetic energy carried out per second by the outflow lobe) can thus be derived by simply dividing the kinetic energy (4.24) by the dynamical time (4.25).

4.3 Outflow parameters estimate: our results

Some processing from raw data has to be done before analysis. To this purpose we used the CLASS tool (Continuum and Line Analysis Single-dish Software), which is part of the GILDAS (Grenoble Image and Line Data Analysis Software) package, specifically tailored for radio data analysis. Simple IDL home-made routines have been also implemented

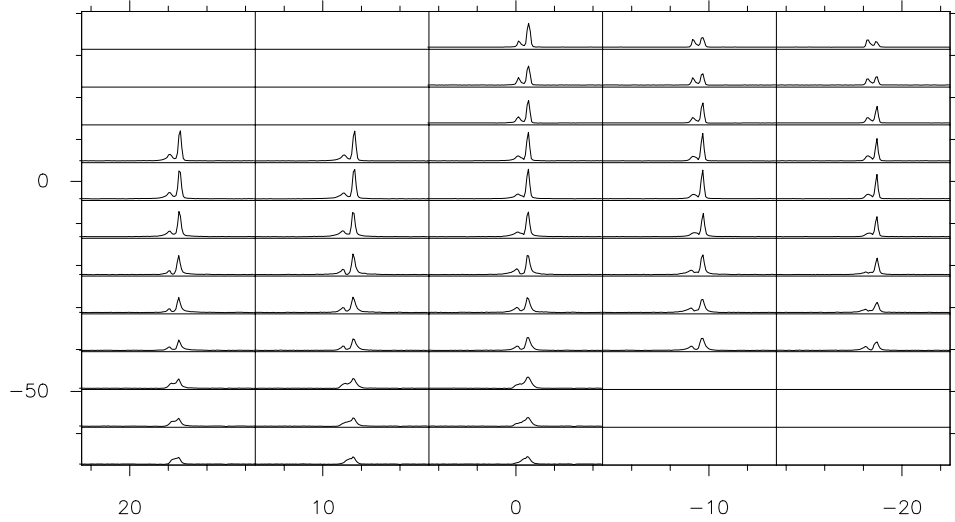
to evaluate the physical parameters and to overlay CO emission on H₂ images.

The basic reduction consists of four steps:

- As in Chapter 2, the spectra are given in terms of the *antenna temperature* T_A (Equation 2.1)¹⁴ versus gas velocity. So the first step is to divide all spectra by the beam efficiency to convert them in brightness temperatures;
- Due to spurious instrumental signals, the baselines of the spectra are not null. To remove this feature polynomial functions must be fitted and subtracted;
- We also smoothed the data to reduce noise up to a resolution in velocity of about 1 km s⁻¹, wide enough for the desired analysis;
- For each offset position multiple spectra have been acquired by the telescope. So the final step is to sum all spectra in order to rise the signal to noise ratio.

The reduced spectra (*e.g.*, Figure 4.1) have been analysed to individuate the occurrence of outflowing components by the presence of slope changes at the line wings, as described in the Section 4.2. All maps present such wing enhancement. A tricky point in the analysis is represented by the operative definition of outflows, *i.e.* the individuation of those velocity channels where emission from outflows dominates the total emission. To this aim we followed the method described in Wouterloot & Brand (1999), where, for each lobe, the *external* (with respect to the line center) velocity, v_{ext} , is the velocity at which the emission is confused with the noise (*i.e.* the first velocity at which the intensity is equal to zero), while the *internal* velocity, v_{int} is the velocity at which the outflow contribution becomes dominant with respect to the cloud one (*i.e.* where the profile slope changes). In Table 4.2 v_{ext} and v_{int} for each lobe of the outflows are reported together with the line peak velocity (V_0) needed to evaluate momentum and kinetic energy carried out by the flows.

¹⁴The beam dilution factor ($=\Omega_S/\Omega_A$) can be less than unity for observations of small sources (*e.g.* masers). In our case, given the beam size with respect to the characteristic size of our outflows, this factor can be reasonably approximated to unity.

Figure 4.1: *Spectral map of jet1.*Table 4.2: *Velocity range of each identified outflow lobe and line peak velocities.*

Velocity (km s ⁻¹)	jet1 red-lobe	jet2 red-lobe blue-lobe		jet3 red-lobe blue-lobe		jet5 blue-lobe
v_{ext}	15.7	14.5	0.3	7.8	-3.6	5.0
v_{int}	9.6	8.4	7.0	3.4	0.8	10.8
V_0	7.7	7.9		2.4		12.5

The analysis proceeds with producing the contour plots of outflowing emission obtained by integrating, for each offset position of the spectral maps, the emission in the ranges defined in Table 4.2. In Figure 4.2 we report, as an example, the contour plot of the blue-shifted lobe of the outflow associated with jet5. These contour plots are more useful, as we have seen for the case of jet1, if over-plotted on H₂ images to directly relate outflows to both the shocked material from jets and the hypothesized driving sources. All of such plots are reported in Figures 4.3 to 4.6, with red and blue colours representing, respectively the red- and blue-shifted lobes.

As can be seen from contour plots, all maps are somewhat affected

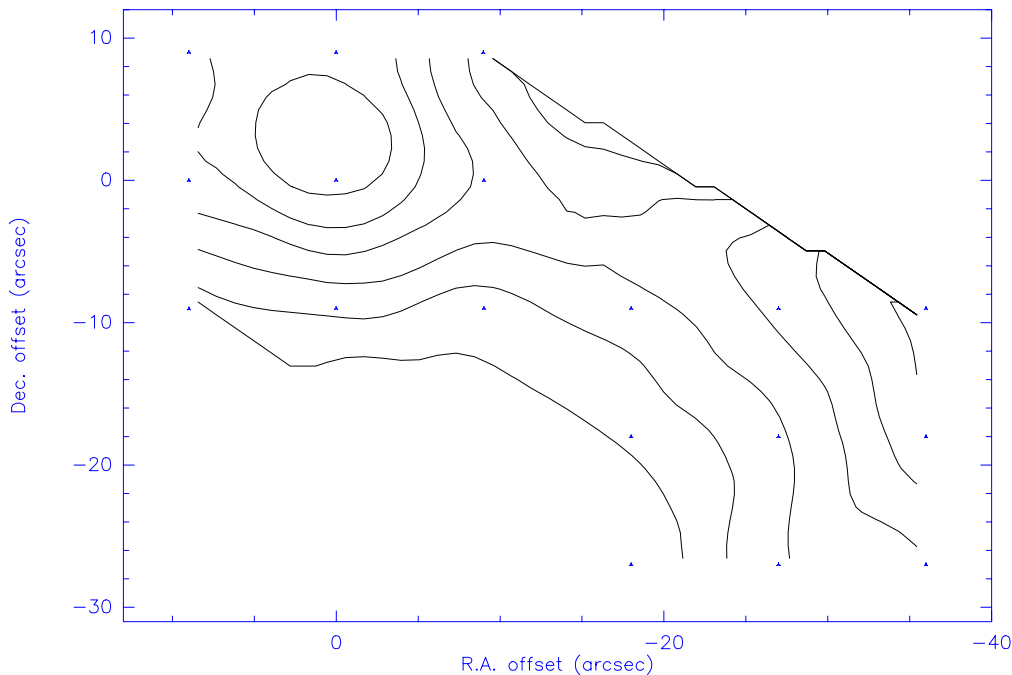


Figure 4.2: Contour plot of the blue-shifted lobe of the outflow associated with jet5. Small triangles individuate the position of all the observed offsets.

by under-mapping. Due to time constraints, in fact, we were forced to observe only small maps around the shocked regions. This is particularly evident in the case of jet3, for which our observation consists of only a 3 by 3 map¹⁵. Thus all parameters evaluated for this jet must be strictly regarded as lower limits. Our observing strategy, however, can be understood by considering our first goal for APEX observations, *i.e.* the search for the *existence* of the outflows, not so obvious at least for this very small jet, and considering also our interest in getting information, with a reasonable amount of telescope time, on all the Vela-D outflows, to have an idea as complete as possible of mass loss phenomena in the whole cloud.

As we explained in the previous Sections, the column density N_{CO} is at the basis of the outflow parameter evaluation. This quantity, defined by the equation (4.20), requires the estimate of the optical depth of the observed transition (τ_{32}), which is usually evaluated by means

¹⁵In the case of jet5, unfortunately, the individuation of the candidate driving source came later than the data acquisition, so resulting in the observation of only one outflow lobe (see next Section).

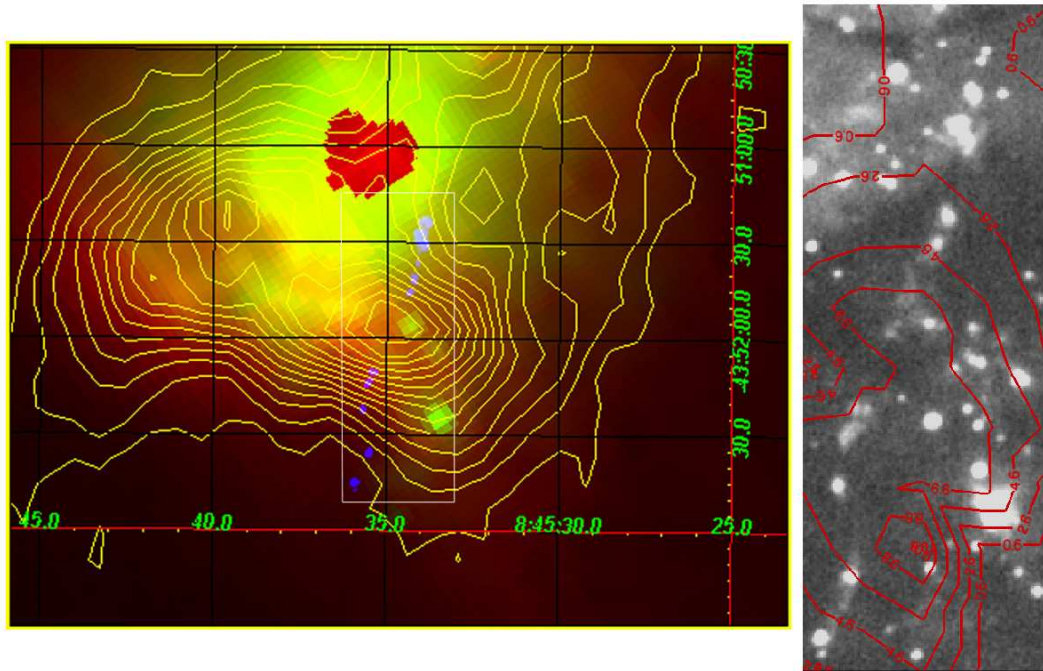


Figure 4.3: *On the left: dust contours (yellow, from a 3σ level in steps of 3σ) and H_2 knots of jet1 (blue) superposed on the MIPS two-colours image ($70\mu\text{m}$ red and $24\mu\text{m}$ green). Note the coincidence of dust peak and jet direction. The box indicates the region mapped by APEX. On the right: contour plot of the identified outflow lobe (from 3σ in steps of 3σ) superposed on the H_2 image. Just one lobe has been detected.*

of the line ratio between the intensities of the same transition for the two isotopes ^{12}CO and ^{13}CO . Because of the lack of observations in the ^{13}CO (requested in the proposal, but not performed), we will give all parameter estimates in the two cases of $\tau_{32} = 0$ and $\tau_{32} = 1$ (within parenthesis in Table 4.3), which are common values for line wings in moderately extinguished regions like those investigated¹⁶. Column densities, masses, momenta and kinetic energies have been thus computed according to the formulae reported in Choi et al. (1993) and in the previous Section. The protostar rest frame velocities (V_0) used for this calculations are reported in Table 4.2. The mean values of the velocity ranges which define each lobe in that Table have also been used to

¹⁶The consequences of using different values of τ_{32} , however, can be easily evaluated by multiplying the $\tau = 0$ value of all parameters (except $t_{\text{dyn-out}}$) by the factor $\tau_{32}/(1 - e^{-\tau_{32}})$ (see equation 4.20 and following).

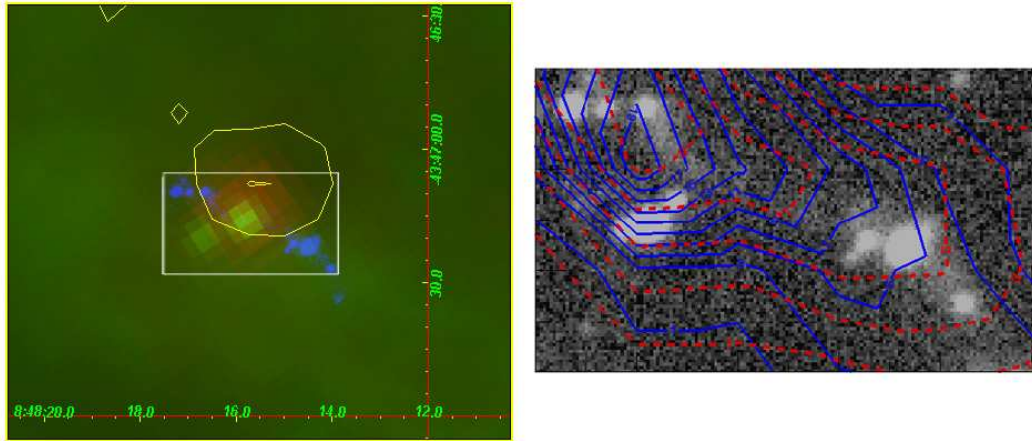


Figure 4.4: *The same as Figure 4.3 for jet 2. Peak umms16 (under-resolved at the SIMBA spatial resolution) is found near the jet center. The proposed exciting source is #38 in Table 3.7.*

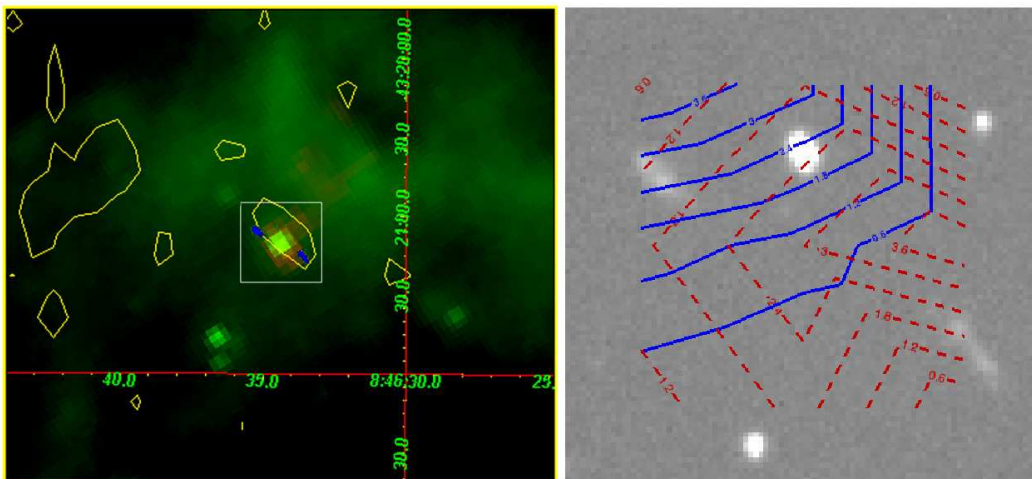


Figure 4.5: *The same as Figure 4.3 for jet 3. A MIPS source (#21) is found at the jet center, corresponding to a location of weak dust emission.*

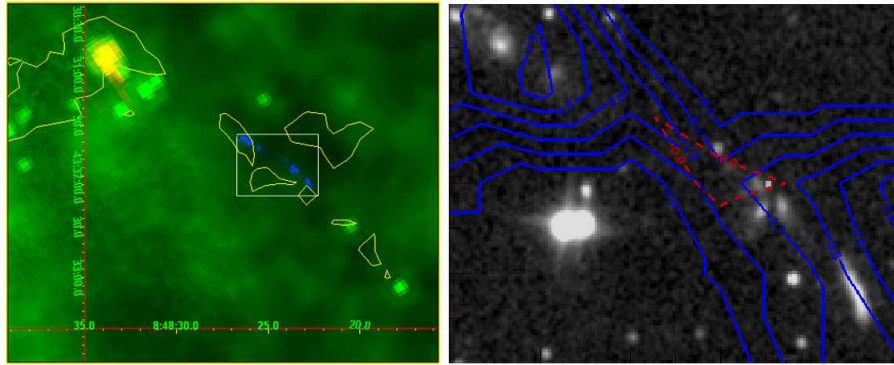


Figure 4.6: *The same as Figure 4.3 for jet 5. The driving source is likely to be the MIPS source (#44) associated with the under-resolved peak umms19. The lack of a counter jet is probably due to the driving source being located near the edge of the H_2 image.*

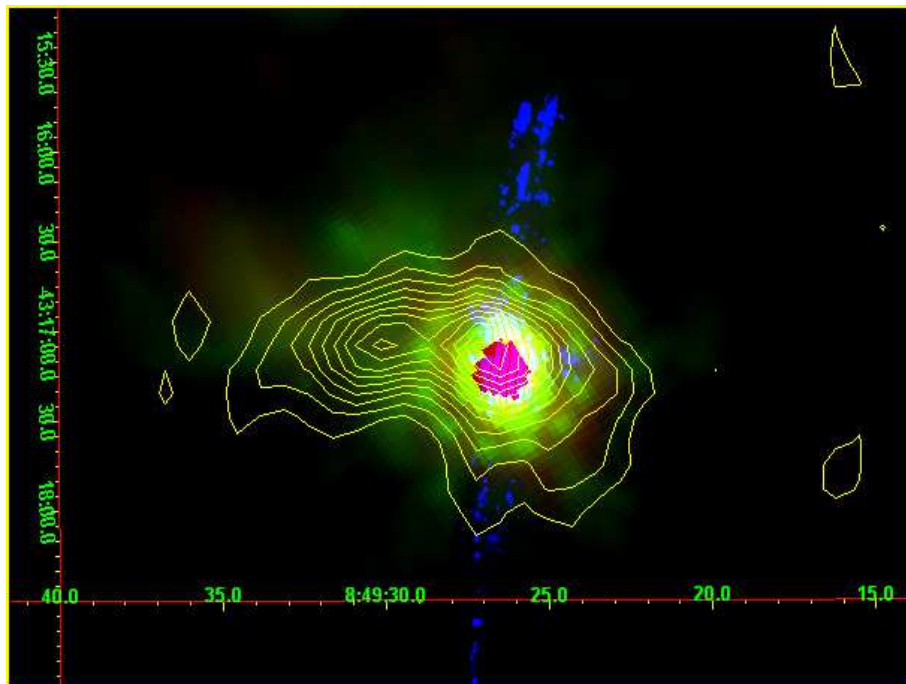


Figure 4.7: *The same as Figure 4.3 for jet 4. Dust core MMS22 crosses the jet. The candidate driving source (IRS20-MGL99#98) is indicated.*

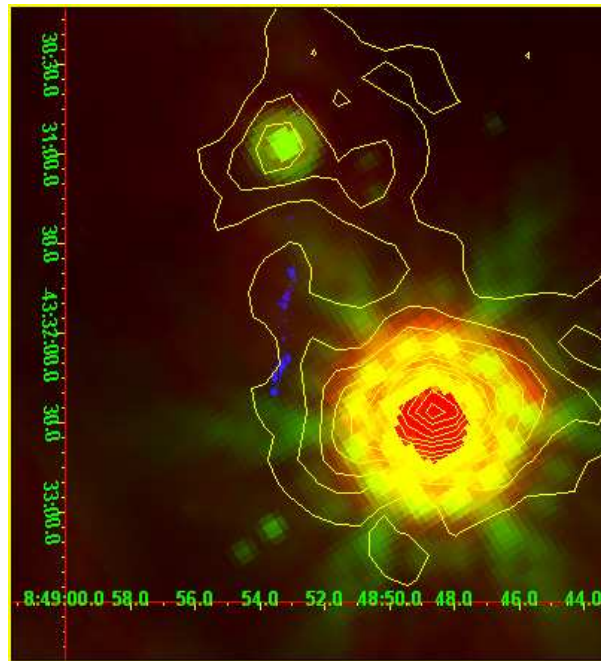


Figure 4.8: *The same as Figure 4.3 for jet 6. The candidate exciting source is the 24 and 70 μm source associated with mm peak MMS16 (#50). Just one lobe has been detected.*

evaluate the outflow dynamical time and kinetic luminosity, in the way described in Section 4.2 and by assuming an outflow inclination angle of 45 degrees with respect to the line of sight.

In Table 4.3 we report all the parameters obtained for each outflow. Given the high number of assumptions of these estimates, the errors cannot be easily evaluated. Errors of some tens percent are typical for these kind of estimates. Nevertheless, especially if in correlation with data concerning the jets and the driving sources, some conclusions can be drawn. An attempt to give a coherent scheme of each source-jet-outflow system is presented in the next section.

Table 4.3: *Outflow parameters.*

associated jet	outflow lobe	M ($M_{\tau=1}$) ^a (M_{\odot})	P ($P_{\tau=1}$) (M_{\odot} km s ⁻¹)	E_{kin} ($E_{kin,\tau=1}$) (10^{42} erg)	$t_{dyn-out}$ (10^4 yr)	L_{kin} ($L_{kin,\tau=1}$) ($10^{-3}L_{\odot}$)
jet1	red	0.17 (0.27)	0.56 (0.87)	23 (36)	8.2	2.3 (3.6)
jet2	blue	0.081 (0.13)	0.26 (0.41)	12 (19)	5.6	1.7 (2.7)
	red	0.10 (0.16)	0.20 (0.32)	6.6 (10)	9.0	0.59 (0.93)
jet3 ^b	blue	> 0.007 (0.01)	> 0.019 (0.30)	> 0.53 (0.84)	-	-
	red	> 0.034 (0.054)	> 0.083 (0.13)	> 2.5 (4.0)	-	-
jet5	blue	0.068 (0.11)	0.22 (0.35)	8.4 (13)	5.6	1.2 (1.9)

^aValues in parenthesis are computed by assuming $\tau_{32} = 1$ instead of $\tau_{32} = 0$.

^bThis outflow is heavily affected by under-mapping. The reported values must be regarded only as upper limits. For the same reason a reliable estimate of $t_{dyn-out}$ and L_{kin} cannot be given.

4.4 Source-jet-outflow pictures

The mass-loss phenomena presented in this Chapter individuate the youngest stellar objects of the whole Vela-D cloud. Interaction between the central condensation and its envelope is still particularly strong at this stages. It can be studied only by collecting information, found in the wide wavelength range from NIR to millimeter, about the driving source, its jet, the associated outflow and the parental core and by trying to connect them into a coherent picture.

As we have seen in Chapters 1 and 3 a multi-wavelength approach is also essential to find out which is the best candidate as driving source, among tens of stars found along the jet axis, on the basis of their colours and spectral indices. The youngest ones are also too much embedded within their cores and surrounding envelopes to be observable at the shorter infrared wavelengths. Near infrared images of the Vela-D jets, in fact, allowed us to identify the driving source only in the

case of jet4 and to make a guess, confirmed by MIPS and APEX observations, about jet5. MIPS has been more efficient in identifying the other very embedded sources. We recall that the MIPS completeness limits are significantly higher than the sensitivity limits, because of the highly varying background, unsuitable for an automatic search for point-like objects. So we scrutinized our maps to find out the weakest MIPS sources in selected areas and we have been able to discover new objects down to 0.7 mJy at 24 μm . We used this technique to search for the sources driving the molecular jets and we both confirmed the driving source of jet5 and discovered those of the three jets 2, 3 and 6, objects that were not detected in either near-IR (K band) or far-IR (N-band, IRAS, MSX). All the discovered driving sources are indicated in Table 4.4 and named following the MIPS catalogue described in the previous Chapter.

The first step of the analysis of these young systems is to establish in what spatial relation are found stars, jets and outflows and what is the dust content of their surroundings. To this aim we produced two kinds of figures (Figs.4.3 to 4.8; for jet0 we remand again to Giannini et al. 2005): (i) H_2 contours superposed on MIPS (24 and 70 μm) images and (ii) APEX contours superposed on the H_2 images (only for jet1-2-3-5 observed with APEX). Then we used the fluxes of the driving sources to draw both the colour-colour diagrams, presented in the previous Chapter and in Appendix A, and the SED diagram of Figure 4.9. Integrating the emission from NIR to mm-wavelengths we obtained the bolometric luminosity of each source, reported in Table 4.4.

Having collected all information, we can attempt to describe each of these systems (source-jet-outflow-core) representing the youngest stellar objects of Vela-D detected until now.

Jet 1 (Figs. 4.3) - The only jet still without a reliable counterpart is jet1. The jet center lies towards a millimeter peak (MMS2), where no infrared source is detected down to K=17 mag. In the MIPS 24 μm band, an emission peak is found, although not aligned with the jet axis. The lack of any aligned source suggests two possible alternative scenarios: (i) we are observing just one jet lobe or, more reasonably, (ii) the exciting source is too faint to be detected even by MIPS ($F(24) < 0.7$ mJy).

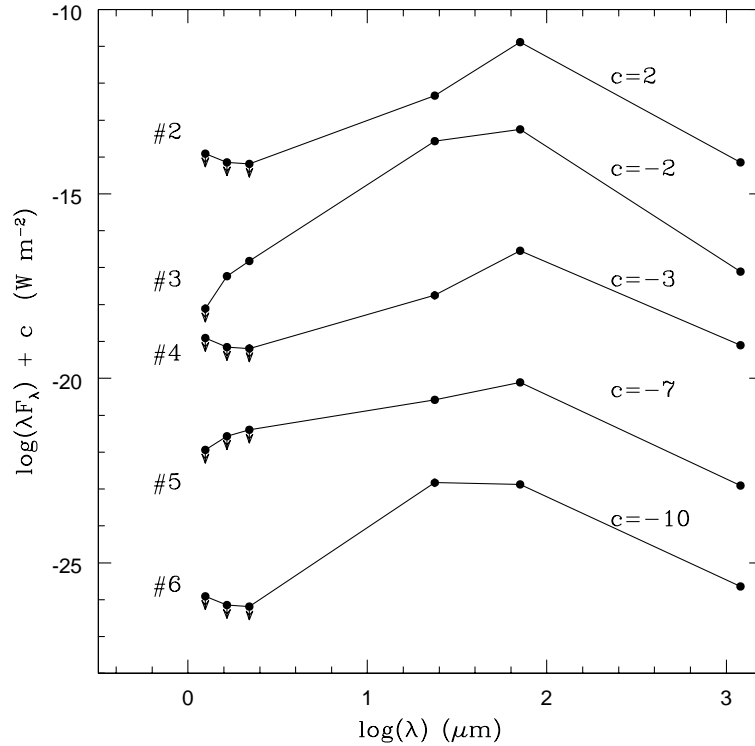


Figure 4.9: *Spectral Energy Distribution of the driving sources.*

APEX observations of the $^{12}\text{CO}(3-2)$ line shows a very complex emission (Figure 4.1), whose interpretation presents many problematic aspects, preventing us to definitely clarify the picture. It was not so easy, in fact, to separate emission coming from the outflow from that due to the cloud because of the double peaked profile, variable, in both peak intensities and velocities, with the offset position. Contour maps of the emission integrated within velocity intervals of 1 km s^{-1} and superposed on the H_2 image, however, were very helpful to individuate at least one outflow lobe. While for velocities lower than 9.6 km s^{-1} the integrated emission does not seem to form a spatially homogeneous morphology coherent with the jet structure, the emission in the range 9.6 to 15.7 km s^{-1} can be interpreted as the red-shifted lobe (Figure 4.3). The spatial coincidence of such emission with the H_2 knots previously assigned to the red-shifted part of the jet on the basis

of the knot luminosity (see Table 4.1 and Section 4.1.1) supports this interpretation, although other observations are in order to confirm it. The absence of a well identifiable blue-lobe, which is expected to lie closer to the cluster center, could be ascribed to confusion with emission independent from the jet, whose existence would be not surprising given the intense and diffuse emission centered on the cluster position in both H_2 (Figure 3.1) and Spitzer images (Figure 4.3).

The double-peaked profile is maybe due to confused emission produced by more than one very young object. This occurrence is compatible with the closeness of the Hii region surrounding the young cluster of IRS16 (Figure 3.1), which could act as a trigger of star formation (although a deeper investigation is needed to address this point). The presence of the red-shifted outflow lobe, which is mainly displaced in the south of MMS2 (Figure 4.3), is in agreement with the second proposed scenario of a driving source very embedded within the core center, which could represent a good Class 0 candidate. Nevertheless, some not neglecting red-shifted emission is present also around the H_2 knots at the north of MMS2, so the first scenario of all knots pertaining to only one lobe cannot be completely ruled out.

Jets 2 (Figs. 4.4) - This small jet corresponds to the under-resolved and isolated dust peak umms16. The exciting source, although not detected in the infrared (NIR bands, IRAS, MSX), is clearly recognizable in the MIPS images. Two sources are visible at $24\mu\text{m}$, close to the dust peak, one of which (#38 of Table 3.7) dominates the $70\mu\text{m}$ emission. Its Spectral Energy Distribution (Figure 4.9) indicates this as a very young object, compatible with a Class 0 protostar. Also the compactness of the H_2 jet implies a very short dynamical age ($t_{dyn-jet} = 1.7 \cdot 10^3 \text{ yr}$), if reasonable conditions for both shock velocity ($v_{shock} = 50 \text{ km s}^{-1}$) and inclination angle ($i = 45^\circ$) are assumed.

The outflow dynamical time appears more than one order magnitude higher ($t_{dyn-out}$ between 6 and $9 \cdot 10^4 \text{ yr}$), but still compatible with a Class 0 object. Such discrepancy between dynamical times, common to all couples jet-outflow, can be easily explained by considering the higher CO cooling times with respect to the H_2 ones, so that we could observe, in the H_2 light, only the youngest shocked regions. Should be said, however, that the high overlap of the two outflow lobes and the

small jet length suggest an inclination angle lower than the assumed value of 45° and this occurrence would even increase the discrepancy (*e.g.* by a factor of six if an angle $i = 20^\circ$ is assumed).

Jets 3 (Figs. 4.5) - Again the small jet-like H_2 knots fall very close to an isolated dust enhancement (that has not been recognized by the Clumpfind algorithm due to the small size and the low emission). The simultaneous occurrence of the knots, the MIPS $24/70\mu\text{m}$ source (#21 of Table 3.7) and the clear double-lobe outflowing CO emission, draws a picture of a young, isolated, low-mass protostar having a SED similar to the previous case (Class I/0 object). The under-mapping of the $^{12}\text{CO}(3-2)$ emission, as we have anticipated, does not allow us to give reliable estimates of the outflow parameters.

Jet 5 (Figs. 4.6) - The source was wrongly thought to lie in the middle of the region mapped in the $^{12}\text{CO}(3-2)$. The misidentification was suggested by the absence in the H_2 images of any counter-jet (maybe due to the lower intensity of red-shifted knots). A point-like $24/70\mu\text{m}$ source (#40 of Table 3.7) aligned with the jet and corresponding to the dust peak umms19 is found about 2 arcmin away towards the NE. A NIR cluster is also found at the MIPS source position. If this source is indeed driving the jet, then we are observing just one jet lobe, and this conclusion is supported by the APEX observations, clearly dominated by the blue-shifted emission.

In the following we present the remaining jets not yet observed by means of APEX.

Jet 4 (Figure 4.7) - A parsec scale jet emerges from the young near-infrared cluster centered on IRS20 (see Figure 3.7). The driving source appears to be the most massive cluster member (MGL99-98), whose colours are typical of Class I objects. It is accompanied by extended nebulosity crossed by an obscuring dust lane, but the characteristic PSF¹⁷ pattern recognizable in the $24\mu\text{m}$ image suggests that the emission at that wavelength is dominated by a point-like source.

¹⁷The Point Spread Function (PSF) is the characteristic intensity profile produced on the detector by a source not resolved by the instrument. In the case of MIPS- $24\mu\text{m}$ the PSF presents a central peak encircled by 12 smaller peaks.

Jet 6 (Figure 4.8) A chain of H₂ knots emerges from a MIPS, maybe Class I, source not visible in the near infrared bands and centered at the dust emission peak MMS16. No counter-jet is observable on the other side of the dust peak, but the mapping of the H₂ emission of the northern region is only partial.

Chapter summary - The search for outflowing activity resulted in the discovery of six very young objects, likely the youngest of the whole cloud, three of which (those associated with jet1-2-3) can be regarded as Class 0 candidates. The SofI H₂ observations revealed the outflowing activity by evidencing the shocked surfaces produced by the impact of the jet material with the surrounding interstellar medium. The jet morphology also suggested both the direction on which the driving source should lie and the dynamical ages of the jet systems, while the knot intensities allowed us to give a first guess on the position of the red- and blue-shifted lobes. The APEX ¹²CO(3-2) observations pointed out that all the mapped jets present larger scale outflows, produced by molecular, environmental gas swept up by the jets, and confirmed the positions of the blue- and red-lobes. An estimate of the main outflow parameters (such as mass, kinetic energy and momentum carried out by the outflows) has been given as well, and a comparison of the outflow dynamical times with those found for the jets revealed a significant discrepancy due to the lower cooling times of the CO emission. The MIPS observations allowed us to discover almost all the most embedded (and youngest) driving sources, whose colours permitted a first attempt of classification within the evolutionary scheme presented in the first Chapter. Observations at all wavelengths contributed to obtain the bolometric luminosities of such driving sources, confirming that all the observed objects are low- to intermediate-mass protostars.

The global view of the most recent star formation history in Vela-D that emerges from this analysis can be summarized in a few statements:

- Examples of the present day star forming activity are found for

both low- and intermediate-mass (jet0-4-6) objects.

- Protostars are found *(i)* within clusters (jet0-4-5), *(ii)* at cluster edges (jet1), and *(iii)* in isolation (jet2-3-6).
- Complex H₂ emission has been found in correspondence of the biggest Vela-D young embedded clusters (IRS16-17-19), for which a contribution could come from unresolved multiple-jets. If this is the case, the small statistics represented by the previous item could heavily change in favour of the first two cases.
- All jet driving sources are found (it seems to be true also for the uncertain cases of jet1-5) within a distance less than a few arcseconds (*i.e.* less than the SIMBA HPBM) from the dust peaks.
- Suspected triggered star formation (by the expansion of a HII region) has been found for jet1, which deserves a deeper investigation in order to explain the complex ¹²CO(3-2) behavior.

Table 4.4: *Protostellar jets associated with MIPS sources in Vela-D.*

Jet id	Exc. source id	dust peak ^a id	L _{bol} (L _☉)
1	-	MMS 2	-
2	38	umms 16	0.3
3	21	-	0.07
4	60	MMS 22	>14
5	44	umms 19/20	0.5
6	50	MMS16	2.4

^aNames from Chapter 3.

Chapter 5

Star Formation in the Vela-D Cloud: some answers

In this Chapter we summarize the main results of this thesis, whose aim is the characterization of the Vela-D Giant Molecular Cloud young population. Such a characterization consists of answering many questions of fundamental importance for a deeper comprehension of the star-forming process in general. In Chapter 1 we have described the scientific background and the present day panorama of the research activity in star formation by focusing the attention on a few questions that have driven this work. Now we will follow these questions as guidelines for drawing a picture of the Vela-D population, trying to give them an answer (if any).

Is there any spatial trend in the ages and characteristics of the young population that could be linked to the filamentary and shell-like patterns well recognizable in the Vela-D maps?

A tight link clearly exists between gas distribution and location of the youngest stellar objects. The $24\ \mu\text{m}$ source density doubles (and is four times when considering sources at $70\ \mu\text{m}$) inside the region delimited by the CO contours as compared to outside the molecular cloud and the brightest point-like FIR sources known in the field strictly follow the gas large filaments.

The correlation increases even more when considering the dust emission morphology, more concentrated than the gas in a few small

regions (in correspondence with the gas enhancements). The more massive and clustered dust condensations correspond with the young embedded clusters. MIR and/or FIR sources associated with dust cores are located close to the mm peak coordinates and the coincidence becomes more evident for the jets, signalling the presence of very young objects.

With respect to the gas morphology, there is maybe no need of invoking expanding Hii bubbles to explain the shell-like molecular patterns. This could be, more reasonably, due to voids left by filamentary structures resulting from turbulent motion, as the qualitative similarity between the MIPS- $24\ \mu\text{m}$ image (Figure 3.6, more resolved than CO maps) and the images resulting from simulations of turbulent clouds (*e.g.* Figure 1.1) seems to suggest.

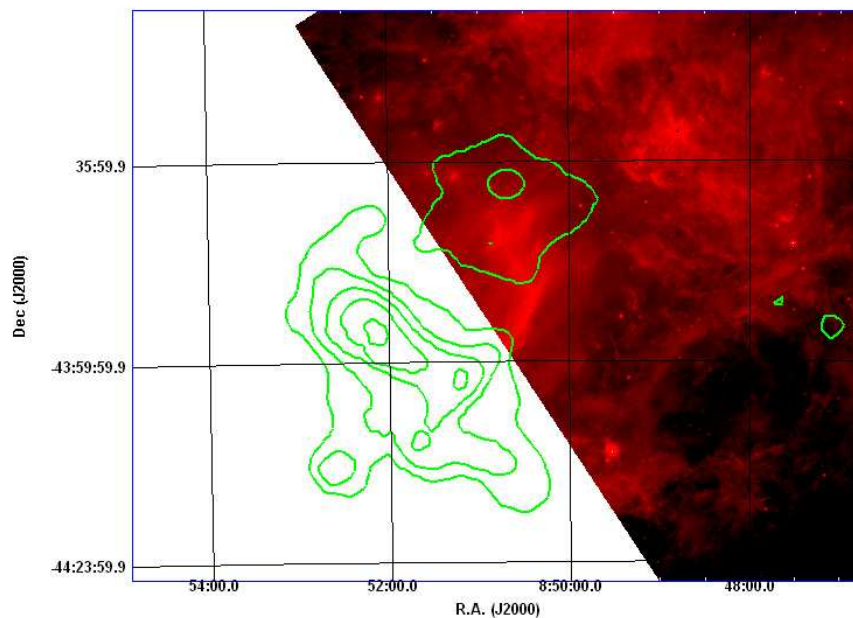


Figure 5.1: Possible interaction between Vela-D (red image: MIPS $24\ \mu\text{m}$) and the Gum 18 expanding HII region (evidenced by H α contours taken from the Southern H α Sky Survey Atlas, SHASSA, see Gaustad et al. 2001).

Double components in the vel-pos CO diagrams (Figure 2.7) and cavities in the integrated emission maps (Figures 2.8) suggested the occurrence of expanding shells triggering the star formation, but the lack of any suitable ionizing source makes this hypothesis questionable. Anyway, at least for the eastern cavity, where the lack of CO

appears more significant (Figure 2.2), an interaction of the cloud with the Hii region known as Gum 18 (Gum 1955) is very likely and is confirmed by the corresponding diffuse, intense emission detected at $24\ \mu\text{m}$ by Spitzer-MIPS (see Figure 5.1). Any attempt of explaining such a large-scale emission with physical processes inside Vela-D has failed. It could represent, instead, the H_2 evaporation front due to the expanding ionizing shell (the lack of any significant emission at $70\ \mu\text{m}$ testifies against a thermal nature of the emission). An estimate of the dynamical age of the expanding Hii region seems also compatible with the estimated age for the star formation activity. However, a deeper analysis is in order to clarify the issue.

Another case of suspected star formation triggering by the expansion of a Hii region, originated by an embedded cluster, has been found for jet1, but also this case deserves a deeper investigation in order to explain the complex $^{12}\text{CO}(3-2)$ behaviour.

Is the present-day star formation in Vela-D mainly diffuse or located within/around clusters? What are the gas and dust characteristics in correspondence with the embedded clusters?

Clues of very young protostars are found *(i)* within clusters (jet0-4-5), *(ii)* at cluster edges (jet1), and *(iii)* in isolation (jet2-3-6), indicating that both clustered and diffuse star formation is now occurring. However, complex H_2 emission has been found in correspondence of the biggest Vela-D young embedded clusters (IRS16-17-19), for which a contribution could come from unresolved, multiple jets. If this is the case, the poor statistics could heavily change in favour of the first two cases.

The cores hosting clusters are in general more massive, but their estimated mass seems to be not enough to produce any more high-mass objects.

Are there any clues indicating an evolution in the star formation modalities of Vela-D?

It is very difficult to understand if significant changes are occur-

ring, either in the cloud physical properties and in the star formation modalities.

The evaluated stellar luminosities, typical of low- to intermediate-mass stars, and the not particularly energetic outflows¹ suggest that no conspicuous energy is injected from inside the cloud and that triggering phenomena, if any (see the case of jet1), should be local, *i.e.* limited to the cluster outskirts. Nevertheless, at least in correspondence of the biggest clusters, intense and complex H₂ emission suggests that outflowing activity inside them (although not particularly energetic and massive) could be enough to progressively disperse molecular-dust material. However, there is no evidence of a particularly active star formation within cluster centers. The stellar densities seem to be not enough large to have a significant probability of close encounters resulting in merging into higher-mass objects.

Interactions with external objects could be more efficient in injecting enough energy and turbulence into the cloud medium (see the discussion about the expanding Hii regions and the Supernova Remnant) to produce significant changes in conditions and modalities of star formation, but such interactions still remain to be proven.

Is there any evidence supporting the hypothesis of a possible triggering of the star formation due to the nearby Vela Supernova Remnant?

Figure 1 in Moriguchi et al. (2001) (reported in Figure 3) shows a clear spatial association along the line of sight of Vela-D with the Vela Supernova Remnant, but a physical interaction is still under discussion.

We did not find any particular clue indicating such possibility, neither in spatial trends in stellar ages, nor in evidences of gas compression fronts. A correlation between the Remnant and the southern arc in Vela-D, in fact, is far from clear. On the contrary, there is a clear inconsistency between the age of the young stellar objects and that estimated for the Vela SNR ($t_{\text{SNR}} \simeq 10^4$ yr, see, *e.g.*, Moriguchi et al. 2001).

Possible interactions with two further remnants (SNR 266.3-01.2

¹Note that dedicated observations still unavailable of the possible outflow associated to the powerful jet4 could contradict this statement.

and

SNR 260.4-03.4) have been also considered, by they are too far for being responsible for the peculiar morphology of the investigated region.

Is it possible to derive a unique Initial Mass Function for the whole cloud? Are there significant differences among IMF's of the clusters and of the diffuse population?

Studying a sample of 6 young star clusters in Vela-D, *Massi et al. (2006)* have found a standard stellar IMF with no significant variations among the clusters. In addition to this result, the present work has evidenced, by evaluating the bolometric luminosities of the youngest sources, how the present day star-forming activity goes on in producing both low- and intermediate-mass new objects, the former mostly associated with unresolved dust cores, the latter preferentially with the resolved ones.

Unfortunately, the poor statistics regarding the diffuse population does not allow us to find out a corresponding IMF so to perform a meaningful comparison with the cluster's population.

Which are the main features of the Vela-D core mass function? How the Initial Mass Function is linked to it?

One of the central points of this work has been the molecular and dust map decomposition into spatially defined entities called clumps (for the gas) and cores (for the dust), whose mass distribution (mass spectrum) is strictly linked to the IMF (see Section 1.2.2).

The core mass spectrum presents a power-law behavior with a spectral index $\alpha \sim 1.45 - 1.9$, depending on the temperature and opacity distribution within the sample. The spectrum appears thus flatter than a standard IMF in the range $\sim 1 - 100 M_{\odot}$ (but agrees with the typical mass spectrum of molecular clumps). Such discrepancy is particularly significant, especially if we consider the mentioned result of *Massi et al. (2006)* of a standard IMF for the clusters. The simplest interpretation seems to be the bias introduced by the low spatial resolution at *mm* wavelengths that did not allow us to resolve the fragmentation oc-

curred in the large cores. The core mass spectrum, indeed, is more reminiscent of the *cluster* mass spectrum (*i.e.*, the mass distribution of stellar clusters) rather than of the stars within them.

The core mass spectrum is also similar to the Class I source mass spectrum found by Lorenzetti et al. (1993) suggesting that the mass of the most massive stars originated by a core is roughly proportional to the core mass itself, at least at the high-mass end. Note also that, if the number of cluster members and the mass of the most massive star in a cluster both depend on the mass of the parental core, then there must also exist an observable relationship between number of cluster members and mass of the most massive star in a cluster. This would confirm that small stellar clusters cannot produce massive stars, explaining the possible lack of massive stars in the region, as suggested by the estimated bolometric luminosities of the brightest objects.

What are the youngest objects? How old are they?

In Chapter 2 (and in Appendix A) we have analysed the infrared population of each dust core. This work has allowed us to establish a connection among emissions at different bands and to evaluate the evolutionary stage of the youngest proto-stellar objects of the cloud.

The spectral index of their SEDs (between 2 and 10 μm) resulted in a distribution strongly peaked at values typical of Class I sources ($0 < \alpha < 3$), whose ages are typically less than 10^6 yr. The anomalous excess of Class I objects has been also confirmed by Spitzer-MIPS data and can be ascribed to a bias in the sensitivity limits of the 2MASS and MIPS surveys (due to the cloud distance), or to a short time elapsed since the first collapse of the cloud.

An attempt has been done also to search for Class 0 sources. Ten IRAS sources (with upper limits at 12 μm) do not present any NIR reliable counterpart, but none of them satisfies the criterion $L_{bol}/L_{1.3mm} \lesssim 2 \times 10^4$ proposed by André et al. (1993). However, considering the probable overestimates of the IRAS fluxes (and bolometric luminosities), we indicate the three objects with the lowest $L_{bol}/L_{1.3mm}$ ratios as the youngest IRAS sources of the region. Five additional Class 0 candidates have been selected among Spitzer sources on the basis of their 24 and 70 μm colours.

What are the oldest objects clearly associable to the cloud? How old are they?

The IRAS sources associated to the dust cores, both resolved and unresolved, all have the same FIR colours, typical of a black-body stratification between 50 and 1000 K, with a stronger contribution of the former component. In other words, sources with FIR colours typical of pre-main sequence T-Tauri and Herbig Ae/Be stars seem to be absent, indicating Vela-D as a young ($\sim 10^6$ years) region.

Such a conclusion is supported by the colour-magnitude diagrams obtained for Spitzer sources (Figure 3.12). The region of the diagram occupied by normal photospheres (*i.e.* evolved objects), in fact, has noticeably a larger number density (per deg^2) of the ‘off-cloud’ sources relative to that of the ‘on-cloud’ ones: In principle, all the un-reddened photospheres detected in Vela-D could be indeed foreground/background stars.

How many starless cores can be found in Vela-D? Are they genuine pre-stellar cores? Which are their characteristics?

In the attempt of associating point-like sources to the dust cores described in Chapter 3 and in Appendix A and based on IRAS/MSX data for the FIR range, some of the cores remain without any reliable counterpart (the observed point sources seem to be foreground/background objects). The more sensitive Spitzer observations allowed us to significantly improve the statistics of active *vs.* inactive cores in favour of the former. On the other hand, the list of the 11 cores (5 resolved and 6 unresolved) still without any reliable infrared counterpart represents a robust sample of starless cores.

Dedicated higher resolution observations, of both molecular lines and continuum, are needed to clarify the physical nature of these condensations, so to understand if they are pre-stellar cores, dispersing structure or very embedded Class 0 objects.

This sample represents a list of suitable targets for new generation facilities under construction (*e.g.* ALMA and Hershel).

What is the rôle played by mass-loss phenomena in the physics of the Vela-D protostellar cores?

The occurrence of outflowing activity in correspondence with several dust cores is testified by both H₂ (1-0S(1) line, signalling the presence of ISM regions shocked by jets), and CO emission (¹³CO(2-1), ¹²CO(1-0) and ¹²CO(3-2) lines, tracing molecular outflows).

In particular, H₂ observations revealed seven clearly identified jets, four regions of possible outflowing activity and three regions characterized by a complex morphology of shocking surfaces, likely due to multiple jet activity. All jet driving sources are found (it seems to be true also for two uncertain cases) within a distance less than a few arcseconds from the dust peaks.

The APEX ¹²CO(3-2) observations of four jets driven by low-mass proto-stars pointed out that all the mapped jets present molecular outflows, confirming the positions of the blue- and red-lobes expected from jet luminosities. Although the maps are a bit small compared to the outflows, an estimate of the main outflow parameters (such as mass, kinetic energy and momentum carried out by the outflows) has been given as well, and a comparison of the outflow dynamical times with those found for the jets revealed a significant discrepancy due to the lower cooling times of the CO emission.

Appendix A

Core infrared counterparts: one by one

In the following we present a brief discussion of the NIR to FIR associations found for each dust core¹. Other signs of star formation activity (e.g. H_2 knots and jets or young embedded clusters) will also be evidenced. For each core (or group of cores) we will show the SofI H_2 (or 2MASS H band) gray scale image supplied with: dust emission contours, position of the most interesting sources, coverage of IRAC2 and Timmi2 fields of view and arrows indicating the occurrence of H_2 knots (see Sect. 3.3.2 for more details). Whenever needed for the analysis, the corresponding colour-colour diagrams and SED plots will be shown as well.

- MMS2 (Figs. A.1, A.2): one MSX associated object inside the FWHM-ellipse, G263.6338-00.5497, with a N band counterpart, DGL 3, having a flux ($F_{10.4\mu m} = 0.25$ Jy) smaller than that measured by MSX ($F_{8.3\mu m} = 0.4$ Jy).

Inside the FWHM-ellipse, many NIR stars (recognizable in the SofI H_2 image) have not been detected by 2MASS and are only upper limits for IRAC2 in both J and H bands. The object showing the highest colour excess (MGL99 25) and steepest spectral index (Fig. A.2) is not visible in the N band (at 30 mJy sensitivity level). We have tentatively indicated that one in Tab. 3.2 as candidate NIR counterpart. However, an intense H_2 line emis-

¹A detailed analysis of Spitzer images in correspondence with all of these cores is still ongoing. We remand to Chapter 4 for a description of the most interesting cases.

sion is present all over the core, both diffuse and in knots and, remarkably, a well collimated H_2 jet crosses the very center of the core. No reliable exciting source has been detected along the jet (see also Figure 4.3). Likely, it is heavily embedded near the peak position and contributes significantly (or mainly) to the observed dust emission.

- MMS3 (Figs. A.3, A.4): an IRAS source (IRS16) is marginally associated to the peak (see Sect. 3.3.2). Three MSX detections (one of them inside the FWHM-ellipse) fall in a region of enhanced and diffuse $8\ \mu\text{m}$ emission and don't seem to be point-like (as suggested by the MSX image and by the failed detection in N). A Timmi2 source (DGL 5, identified with MGL99 65) is instead observed in the direction of the IRAS source and NIR cluster.

A steep decrease in the number of NIR detections towards the peak suggests a high extinction level. Moreover, the majority of the IRAC2 sources within the FWHM-ellipse presents very red colours. MGL99 36, the one closest to the peak position, could be the main source associated to the millimeter core.

- MMS4: a detailed analysis of this core has already been presented in a dedicated paper (Giannini et al. 2005), which the reader is referred to.
- MMS5-6, umms6 (Fig. A.5): a dust elongated structure of connected cores pointing towards south-west in the direction of MMS4, the brightest core of the whole dust map; a dust filament which is likely undergoing fragmentation. Neither MIR-FIR associations, nor interesting NIR sources are present (although no IRAC2 data are available); signs of star formation activity are quite hidden and can only be recognized as a faint H_2 emission around MMS5 and MMS6.
- MMS7, umms13-14-15 (Fig. A.6): resolved core (MMS7) surrounded by three unresolved cores (umms13-14-15). The J , H and K_s pho-

tometry of the cluster of about 20 members around the central core will be analyzed in a forthcoming paper. Neither FIR emission nor H_2 features are present (no $10\ \mu\text{m}$ image has been collected). We just remark here the colour excess of 4 very red stars within the FWHM-ellipse of MMS7.

- MMS8-9 (Fig. A.7): these cores are part of a long tail of connected cores (extending for about 1 pc), going from the bright core MMS12 to umms19, whose dynamical behaviour is not clear (Massi et al. 2007). No FIR point sources or clues of H_2 emission have been observed. Timmi2 observations, although not covering the whole dust emission, gave negative results as well. Only one very red NIR object, 2M 9671 (no IRAC2 data available), lies within the FWHM-ellipse of MMS8.
- MMS10-11 (Fig. A.8): without any MIR-FIR counterpart, these are the only two resolved cores included in the $^{13}\text{CO}(2-1)$ map that lack of an associated CO clump (§ 2.1.5). The colour-colour diagram of the 2MASS sources (no IRAC2 data available) within the FWHM-ellipse gives only one reddened candidate (2M-14732) for MMS11.
- MMS12 (Figs. A.9, A.10): one of the brightest cores, MMS12 ($\sim 18M_\odot$) coincides with a young embedded cluster having in its center the IRAS source 08470-4321 (IRS19), the MSX G263.7434+00.1161 and the Timmi2 DGL 7 object. The new observed flux at $10\ \mu\text{m}$ ($F_{10.4\mu\text{m}} = 18.3\ \text{Jy}$) is less than a half of the IRAS/MSX measurements at 8-12 μm . We ascribe this discrepancy to the presence of a strong diffuse contribution to the flux at these wavelengths. The correspondence of these sources with the NIR object MGL99 49 has already been discussed in Massi et al. (1999) and is confirmed here.
Complex and intense H_2 emission is also present, especially at the peak position, and at the eastern part of the core; it cannot be clearly distinguished as a single jet-like structure.

- MMS13 (Fig. A.11): no MIR-FIR association and no significant H_2 emission for this core at the south of MMS12. The two possible NIR counterparts have red colours (MGL99 2, MGL99 7).
- MMS14-15-16 (Fig. A.12): neither MIR-FIR associations nor NIR red sources detected by 2MASS (no IRAC2 data). We note a faint H_2 emission aligned with both the peak MMS16 and the H_2 knot visible at the east of MMS12 (see also Fig. A.9). The existence of an embedded exciting source near the MMS16 peak position, hypothesized by De Luca et al. (2007), is confirmed by the Spitzer maps (Figure 4.8).
- MMS17 (Fig. A.13): a double H_2 knot (probably jet-like) in proximity of the peak suggests the existence of star forming activity, but no MIR-FIR objects have been detected and the 2MASS data do not point out any interesting source within the FWHM-ellipse.
- MMS18 (Figs. A.14, A.15): one IRAS source (08472-4326A) is associated within 2FWHM-ellipse, while one MSX source (G263.8432+00.0945) and one Timmi2 object (DGL 8) are inside the FWHM-ellipse. The positional uncertainties of these three objects seem to exclude their coincidence, although the IRAS and MSX fluxes (due to their beam sizes) are surely contaminated by the Timmi2 source (whose counterpart, 2M 29896, peaks in the H band) and probably by diffuse emission, visible in the H_2 filter as well.
- MMS19 (Fig. A.16): core connected to MMS20 and MMS21. Neither MIR-FIR sources associated nor H_2 emission detected. We signal two very red 2MASS objects (2M-36076, 2M 36192) within the FWHM-ellipse.
- MMS20 (Fig. A.17): one IRAS (08474-4323, corresponding to MSX G263.8221+00.1494) source turns out to be very marginally associated (positional uncertainty tangent to the 2FWHM-ellipse),

but the dust emission around its position seems to be negligible. One Timmi2 source (DGL 9) has been detected within 2FWHM-ellipse, in the middle between this core and MMS21 not signalled by IRAS/MSX (SofI images points out at least three objects, partially resolved by 2MASS in two very red sources, 2M 27831 and 2M 37241).

- MMS21 (Figs. A.18, A.19): one IRAS source, 08474-4325, whose fluxes indicate this one as one of the youngest objects of Vela-D, coincides with the peak position. The Timmi2 observation has given no results (for the source DGL 9 see MMS20 description) and no MSX sources are reported in the catalogs. Three 2MASS sources fall close to the IRAS uncertainty ellipse center, two of which (2M-29953, 2M 37193) have very red colours. The SofI H_2 image, however, points out the presence of a complex morphology, which cannot be resolved in individual sources with the SofI spatial resolution.
- MMS22 (Figs. A.20, A.21): characterized by a powerful bipolar jet (0.7 pc long, discussed in a forthcoming paper) arising from the IRAS source 08476-4306 (IRS20), located $10''$ at the west of the peak. In correspondence with the IRAS source there are a young cluster, a MSX point source (G263.6177+00.3652) and two $10\ \mu\text{m}$ objects: DGL 11 (main counterpart of the IRAS/MSX object) and DGL 10 (2σ detection, outside the FWHM-ellipse). The DGL 11 flux, $F_{10.4\mu\text{m}} = 2.01\ \text{Jy}$, is significantly smaller than those measured by MSX and IRAS: $F_{8.3\mu\text{m}} = 3.9\ \text{Jy}$, $F_{12\mu\text{m}} = 5.7\ \text{Jy}$, $F_{12.1\mu\text{m}} = 6.0\ \text{Jy}$, but the Timmi2 observation points out a diffuse emission which can have contributed to the MIR fluxes measured by IRAS and MSX. The presence of nebular NIR and H_2 emission completes the picture of this crowded region. The NIR cluster characteristics were discussed in detail by Massi et al. (1999) and the conclusions reported in that paper about the candidate NIR counterpart (MGL99 98) of IRS20 are confirmed by our Timmi2 observation. MGL99 98 is also the best candidate as exciting source of the jet, although the complexity of the jet morphology and the difficulty to discriminate between nebular and point-like

unresolved emission makes this identification questionable. We also remark one dark strip clearly visible in the H_2 image, likely due to an obscuring dust lane crossing the cluster center.

- MMS23 (Fig. A.22): isolated, small core with no IR detected sources near the peak (not observed at $10\ \mu\text{m}$). H_2 multiple knots are visible to the north of the peak together with a faint emission near the center. We cannot exclude the presence of an embedded, young, low-mass stellar object producing that emission, but more sensitive observations are required to confirm this possibility.
- MMS24 (Fig. A.23): this core is connected with the brighter MMS22 and is characterized by diffuse K emission close to a MSX source (within 2FWHM-ellipse) not detected by Timmi2. The NIR source MGL99 90, at the border of the FWHM-ellipse, shows the highest colour excess.
- MMS25-26 (Figs. A.24, A.25): this complex region is constituted by two not well resolved cores (also linked to the brighter MMS27) and, between them, in correspondence with a young NIR cluster (Massi et al. 2006), there are the IRAS source 08477-3459 (IRS21), the MSX source G264.3225-00.1857 and the Timmi2 object DGL 12 (corresponding to the NIR MGL99 27). Moreover, the $10\ \mu\text{m}$ emission observed by Timmi2 shows a diffuse emission (in the surroundings of the source MGL99 35) and, probably, another point source corresponding to MGL99 32, although an artifact in the Timmi2 image prevented us to give a reliable estimate of its flux. Also remarkable is a shell-like K emission (clearly visible also in the H_2 image) approximately centered near MGL99 63.

The colour-colour diagram (Fig. A.25) points out the existence of many red and very red sources within the FWHM-ellipse of both the cores, lots of which having upper limits in the J and H bands. The SEDs of the MIR-FIR objects and of the NIR stars with larger colour excess show significant discrepancies among the fluxes of the MIR-FIR detections. No clear evidence has been

found for NIR stars (if any) that can be most likely associated to the *mm* core².

- MMS27 (Fig. A.26): although this is one of the brightest cores of the whole dust map, no IRAS-MSX point sources have been detected. Only one faint object (DGL 13), counterpart of the NIR very red 2M 53071 (we lack of IRAC2 data for this source), can be seen at 10 μm , inside the FWHM-ellipse, together with three more very red sources.

Interesting is the case of 2M 47136, the closest one to the peak: no point-like source can be extracted from the *K* image which shows instead a very diffuse emission well observable also in the H_2 image of Fig. A.26. It is crossed by a dark horizontal strip (quite likely due to obscuring dust). A knot of H_2 emission is also visible above this strip and one more on the other side of the core, in the south-west direction, making this core of a peculiar interest for future investigations.

- MMS28-29 (Fig. A.27): inside the FWHM of MMS28 there are the IRAS 08483-4305 and MSX G263.6909+00.4713 sources and, remarkably, H_2 aligned knots are visible between the two peaks. We lack of both Timmi2 and IRAC2 observations, but the 2MASS data reveal one very red source, 2M 36339, incompatible with the position of the FIR sources, but aligned with the knots, which could be their exciting source.

In the following we present the unresolved cores not previously discussed.

- umms1 (Fig. A.28): despite the high noise level of the dust map in this position, this unresolved core is one of the most interesting cases: (*i*) it is by far the most intense core among the unresolved

²The lack of any Timmi2 detectable flux in correspondence of MGL99 50, the previously hypothesized NIR counterpart of the IRAS source (Massi et al. 1999), makes that association questionable. Observing its SED, indeed, it is quite unlikely that it could be missed, if point-like, at 10 μm .

ones, *(ii)* its coordinates coincide with an IRAS source showing fluxes increasing with wavelength and *(iii)* the ^{12}CO integrated emission map presents an increase towards this peak, although it falls immediately outside that map. Unfortunately we lack of both IRAC2 and SofI images at this position and only one 2MASS (red) object falls inside the FWHM-ellipse.

- umms2-3-4-5 (Fig. A.29): region of high noise level of the dust map. These cores are probably artifacts of the reconstruction algorithm and do not present any feature suggesting star formation activity.
- umms7-10-12 (Fig. A.30): a small cluster within 2FWHM-ellipse of umms10 (forthcoming dedicated paper) is the only noticeably feature of this field.
- umms8-9-11 (Figs. A.31, A.32): dust emission associated with an IRAS source (08458-4332, having flux increasing with λ , associated to umms8-9) and a MSX-Timmi2 object (G263.7651-00.1572-DGL 6, associated with umms11 and the 2MASS objects 2M 9173 and 2M 11131). One very red and one red NIR object (2M-116128 and 2M 18032, respectively) within the FWHM-ellipse of umms8.
- umms16 (Fig. A.33): core remarkably crossed by H_2 jet-like emission and with an IRAS source (08464-4335), although the Timmi2 observation gave no results and no red or very red NIR stars have been observed by 2MASS as possible jet exciting source. Spitzer maps reveal the presence of two weak sources, one of which (the reddest one) along the jet direction (Figure 4.4)
- umms17-18 (Fig. A.34): also this couple of cores presents an intense H_2 jet-like emission, but without any NIR-MIR interesting source.

- umms19-20 (Fig. A.35): these cores are part of a chain of connected cores (see description of MMS8-9). Spitzer reveals a small cluster dominated by a red object, driving source candidate for jet5 (Figure 4.6), which is also associated to a knot of H_2 emission visible in the FWHM-ellipse of umms19.

- umms21 (Figs. A.36): connected to the previous cores. No FIR-MIR point sources or clues of H_2 emission have been observed. One very red NIR object (2M-16489) within the FWHM-ellipse.

- umms22 (Figs. A.37): No FIR point source or clues of H_2 emission have been observed (no Timmi2 data available). Absence also of NIR red objects within the FWHM-ellipse.

- umms23-24-25 (Figs. A.38): thin, elongated dust structure with three cores coinciding with a similar shaped K emission. Two MSX sources, G263.5672+00.4036 and G263.5622+00.4185, are tightly associated to umms23 and umms24, respectively. Two very red sources fall within the FWHM of umms23, but they seem to be incompatible with the position of the MSX sources (for which we suspect a high contamination from diffuse emission).

- umms26 (Figs. A.39): a small cluster outside 2FWHM-ellipse (forthcoming paper) is the only noticeable feature of this field.

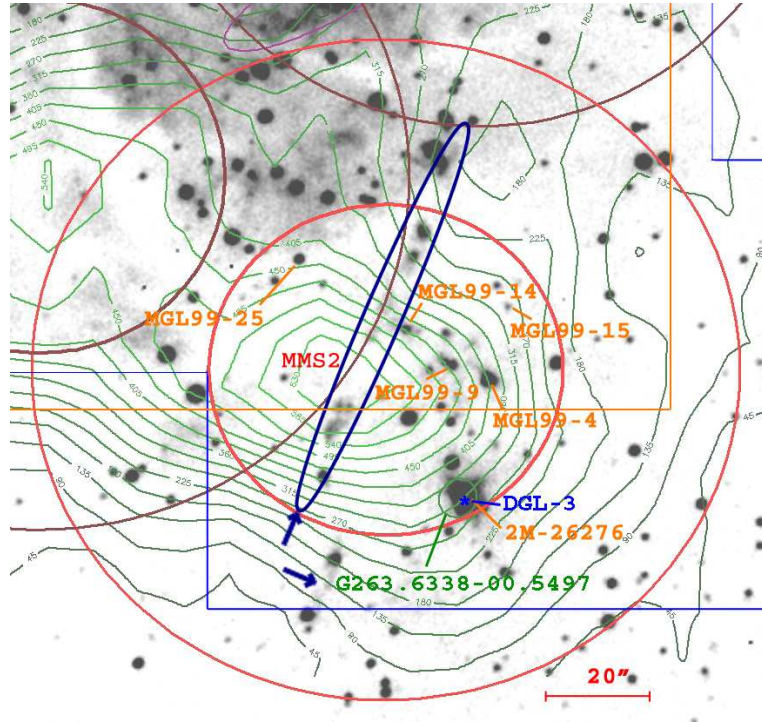


Figure A.1: MMS2 field of view (center [J2000]: 08:45:34.200, -43:51:54.40). Grayscale image: H₂ emission; green contours: dust continuum (from 3σ, in steps of 3σ); red ellipses centered on the mm-peak: FWHM- and 2FWHM-ellipses within which the association with the IR sources has been searched for (the ellipses pertaining to cores MMS1-3 are also visible); magenta and green ellipses: 3σ positional uncertainties of the IRAS and MSX point sources, respectively; blue asterisks: position of the 10.4 μm sources observed by Timmi2; 2MASS and IRAC2 NIR sources are labelled with 2M-# (following an internal numbering) and MGL99-#, respectively; IRAC2-Timmi2 fields of view are delimited by orange-blue lines. The position of the main knots of H₂ emission is highlighted by dark-blue ellipse and arrows.

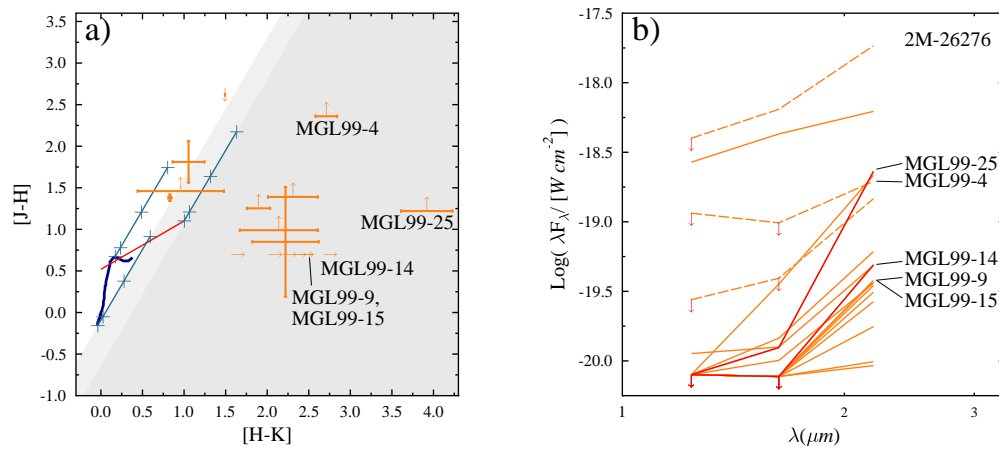


Figure A.2: a) Colour-colour diagram (see text for more details) of the NIR sources within the FWHM-ellipse of MMS2. The Spectral Energy Distributions of the very red ones are shown in panel b). To reduce confusion the wavelength range is limited to the J , H , K bands and the main objects are in red colour. Dashed lines refer to 2MASS sources and arrows denote upper limits.

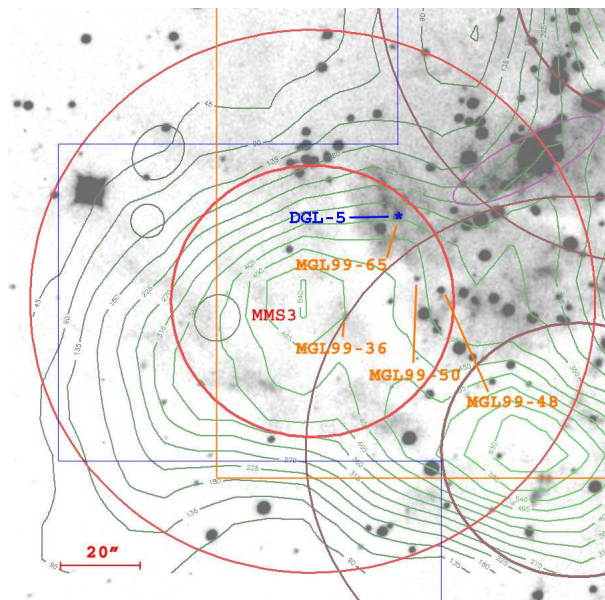


Figure A.3: MMS3 field of view (center [J2000]: 08:45:39.5, -43:51:25.0).

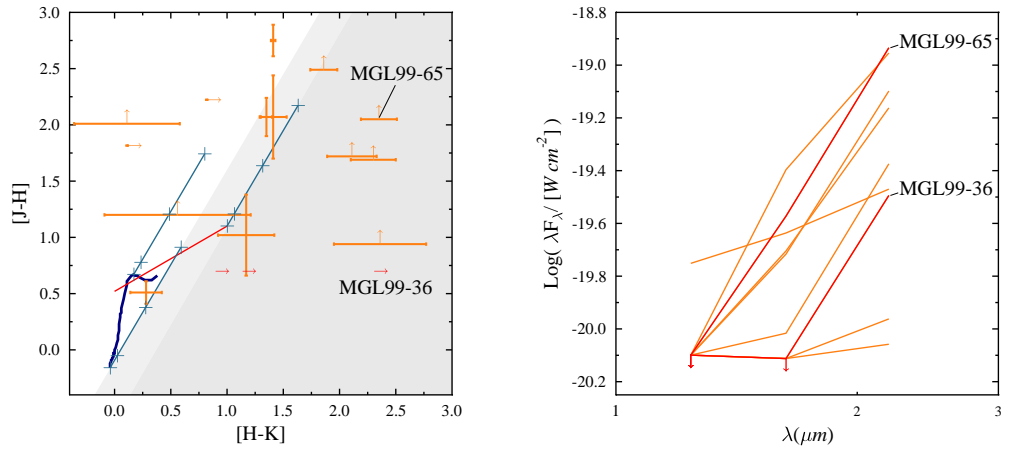


Figure A.4: *MMS3: colour-colour and SED diagrams.*

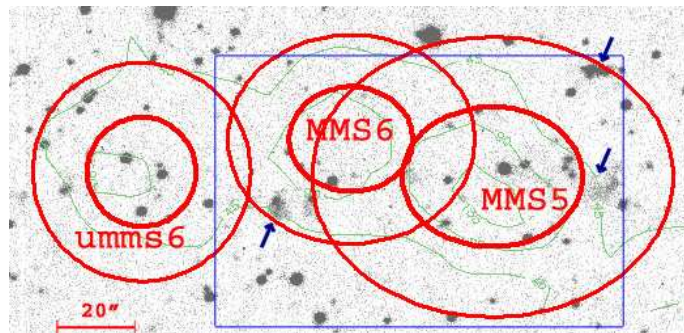


Figure A.5: *MMS5-6 and umms6 field of view (center [J2000]: 08:46:52.0, -43:53:01.3).*

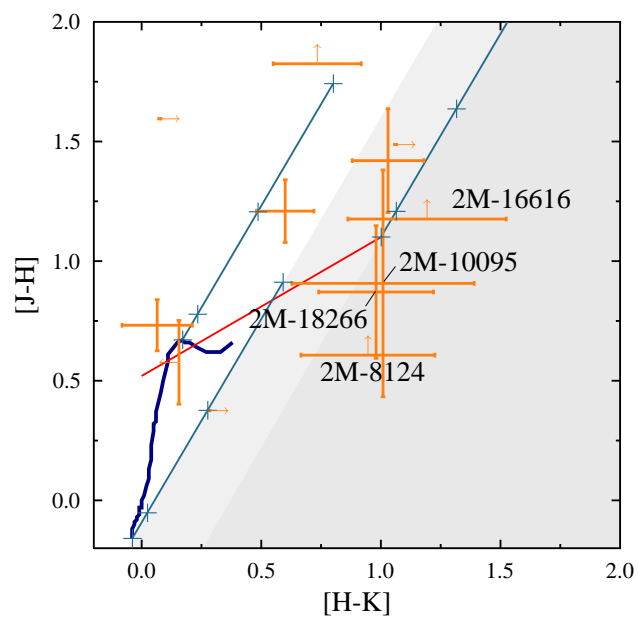
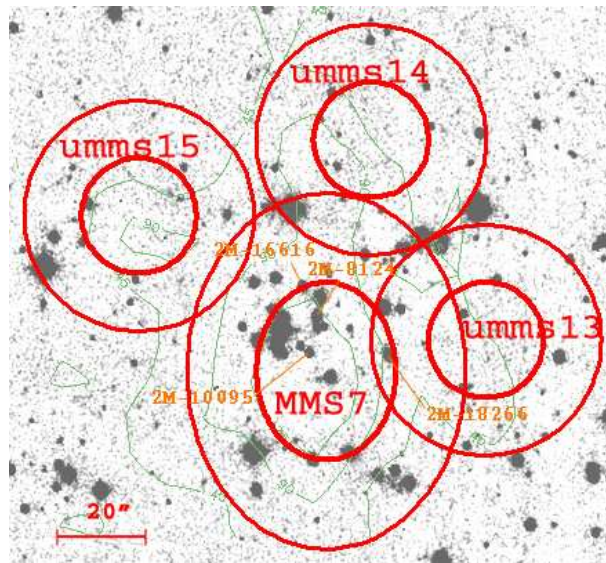


Figure A.6: *MMS7* and *umms13-14-15* field of view (center $[J2000]: 08:47:58.9, -43:39:22.9$) and colour-colour diagram.

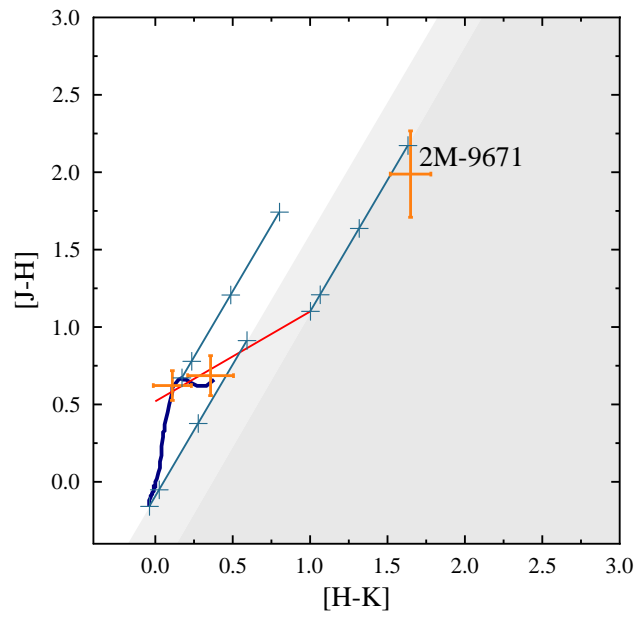
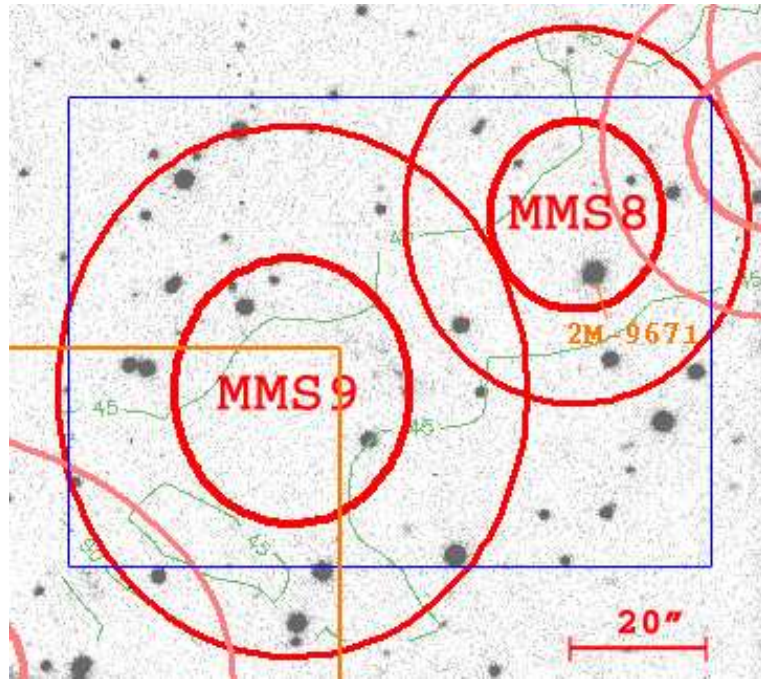


Figure A.7: *MMS8-9* field of view (center $[J2000]$: $08:48:41.3$, $-43:31:36.2$) and colour-colour diagram.

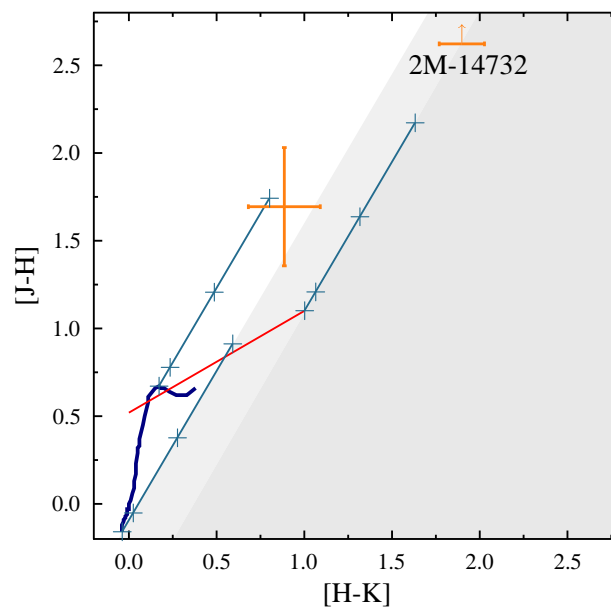
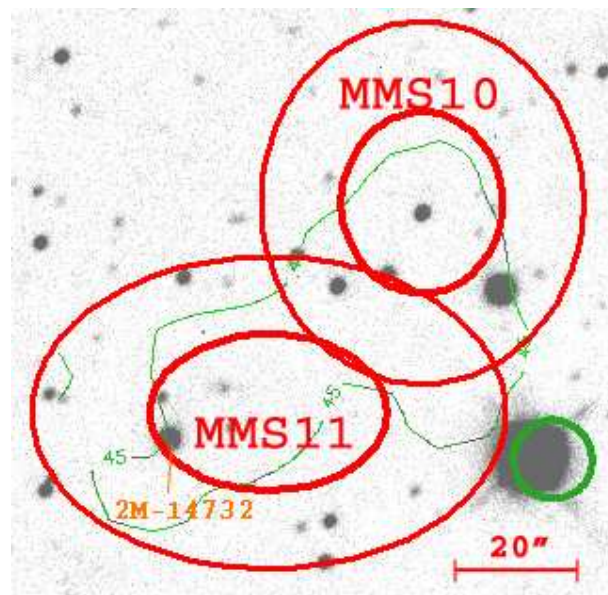


Figure A.8: *MMS10-11 field of view (center [J2000]: 08:48:44.2, -43:37:19.1) and colour-colour diagram.*

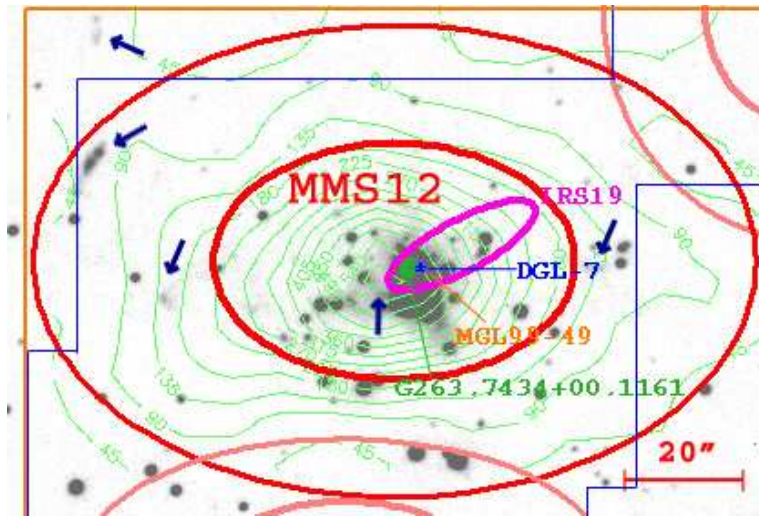


Figure A.9: *MMS12* field of view (center $[J2000]: 08:48:48.5, -43:32:20.8$).

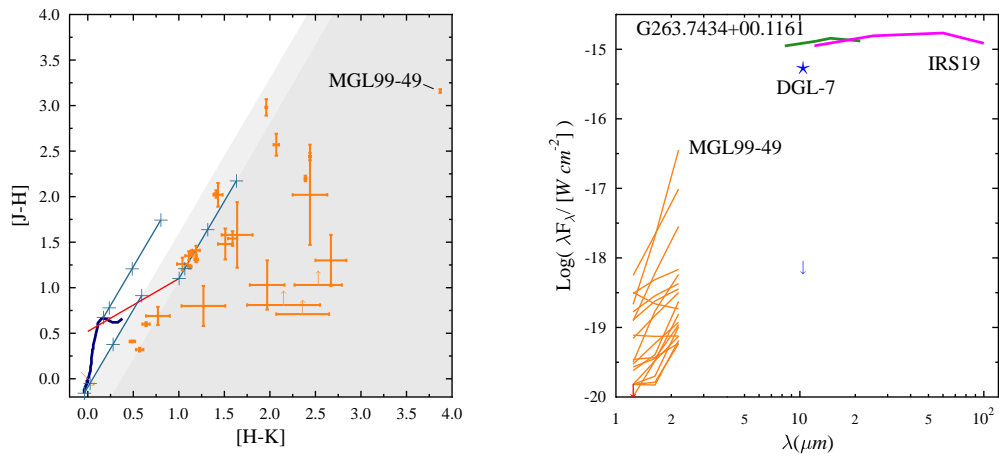


Figure A.10: *MMS12* colour-colour and SED diagrams.

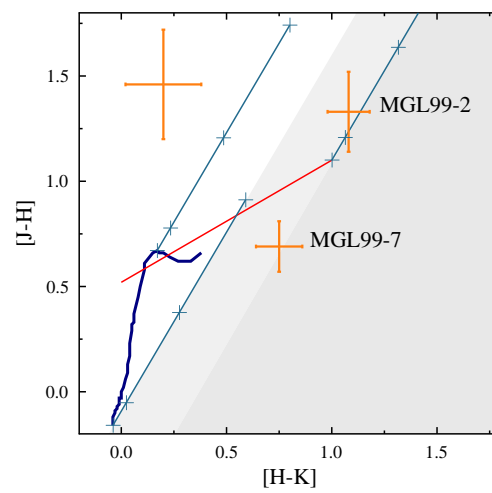
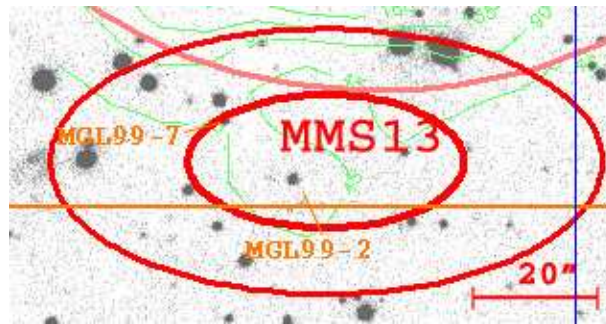


Figure A.11: *MMS13* field of view (center $[J2000]$: $08:48:49.4$, $-43:33:11.2$) and colour-colour diagram.

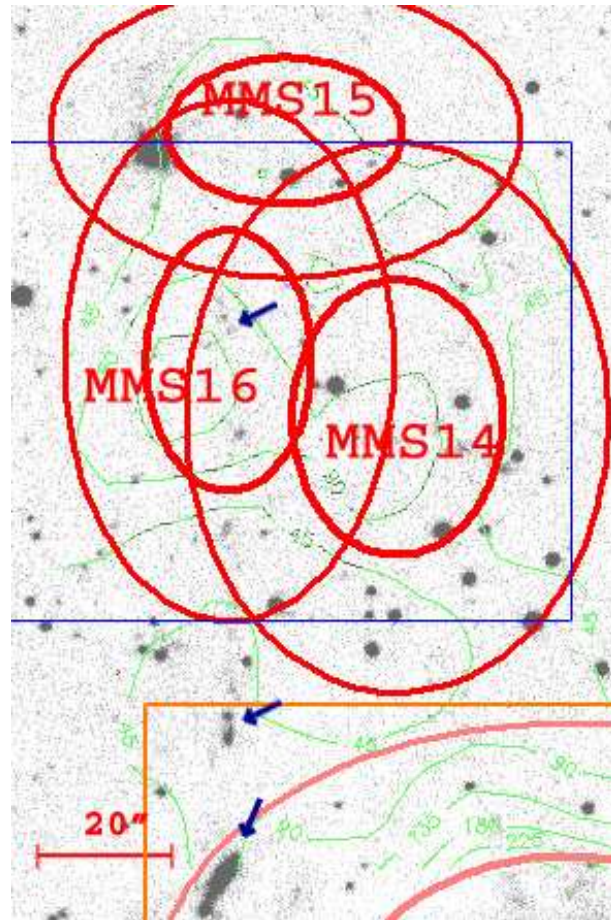


Figure A.12: *MMS14-15-16 field of view (center [J2000]: 08:48:51.6, -43:31:09.9).*

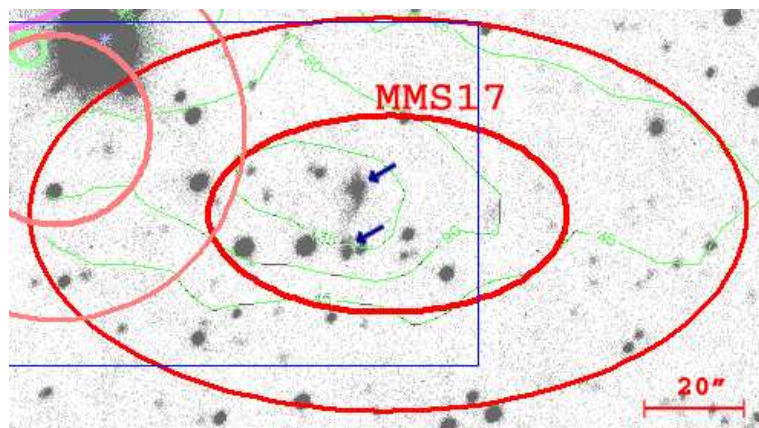


Figure A.13: *MMS17 field of view (center [J2000]: 08:48:57.2, -43:38:23.1).*

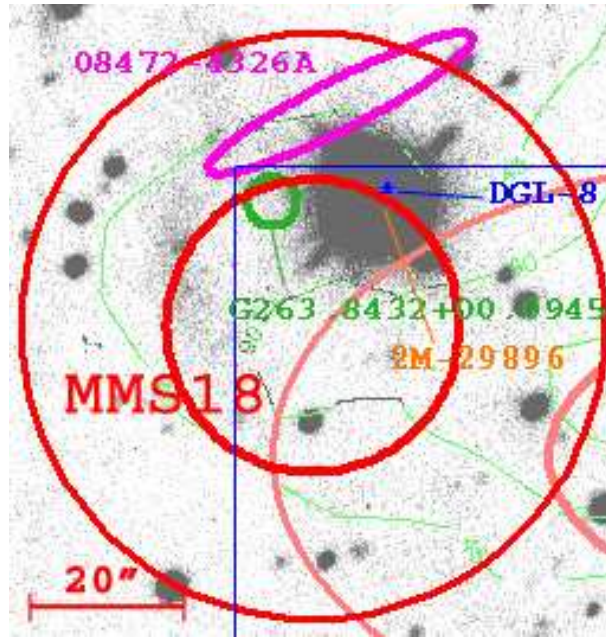


Figure A.14: *MMS18* field of view (center $[J2000]: 08:49:03.2, -43:38:05.2$).

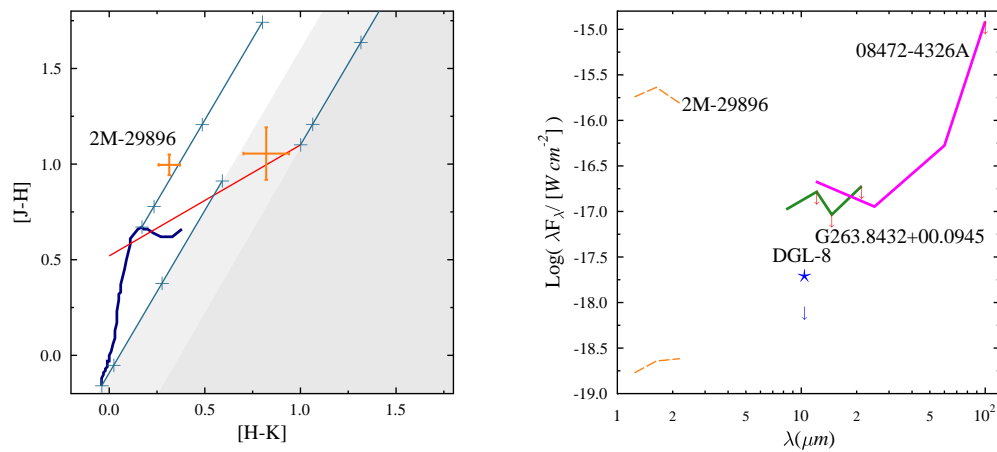


Figure A.15: *MMS18* colour-colour and *SED* diagrams.

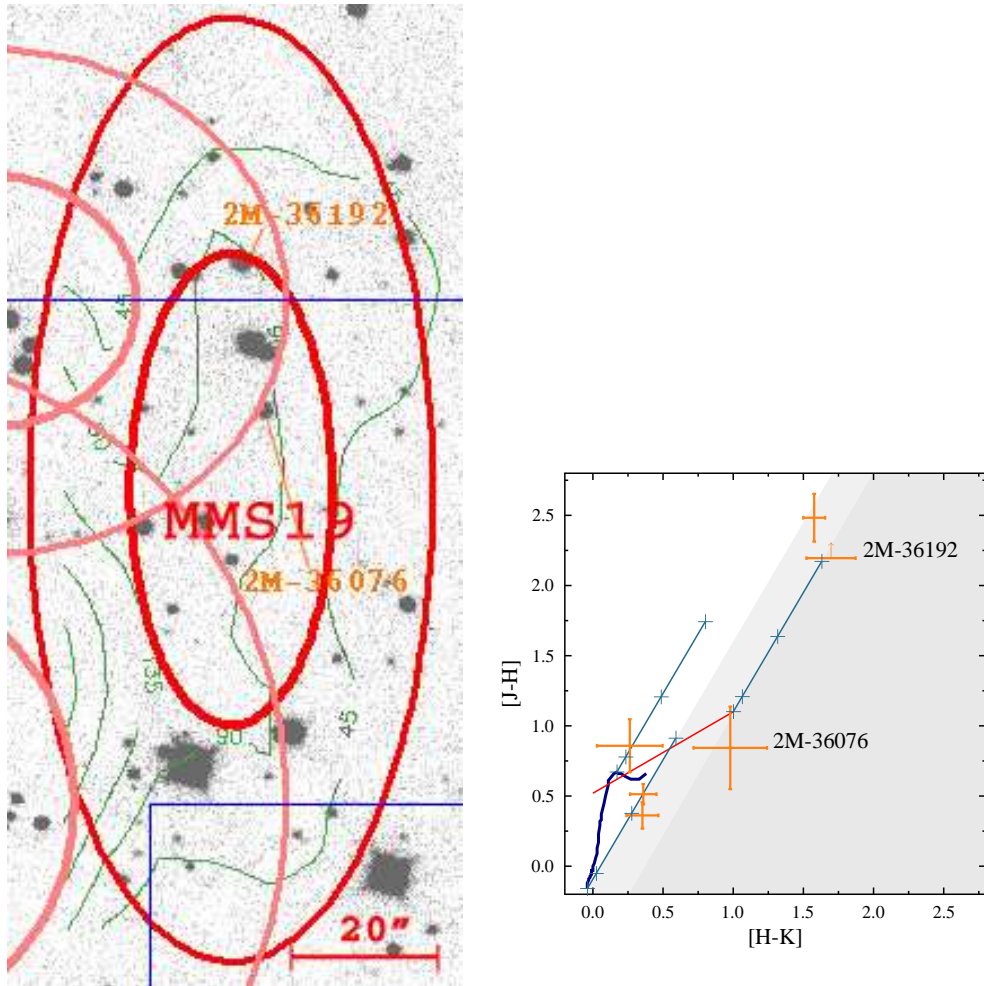


Figure A.16: *MMS19* field of view (center [J2000]: 08:49:08.5, -43:35:43.7) and colour-colour diagram.

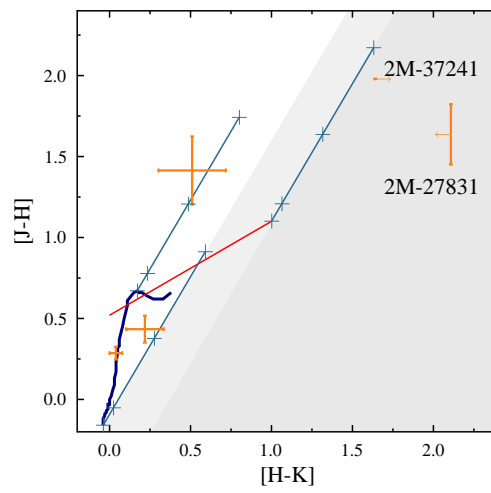
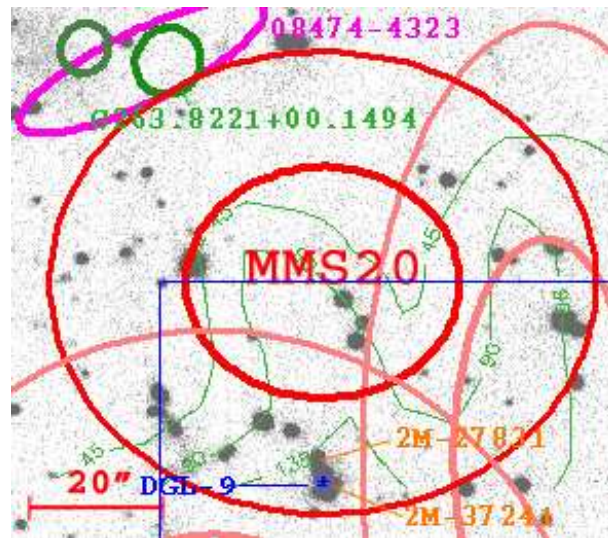


Figure A.17: *MMS20* field of view (center $[J2000]$: $08:49:11.2$, $-43:35:25.9$) and colour-colour diagram.

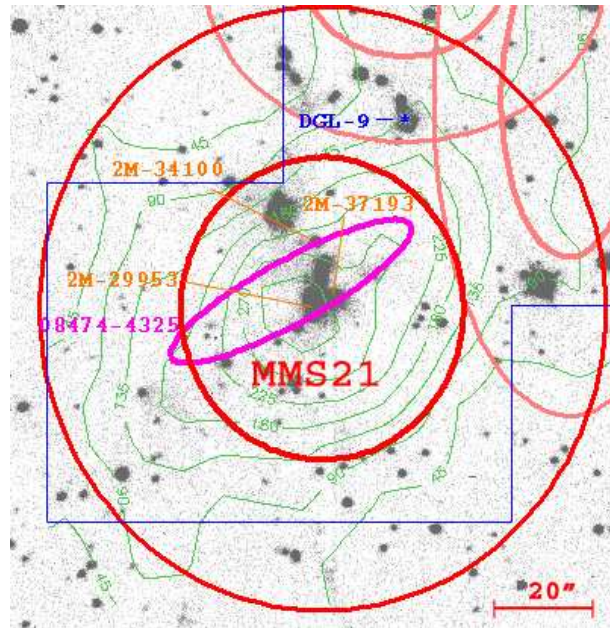


Figure A.18: *MMS21* field of view (center [J2000]: 08:49:13.0, -43:36:21.8).

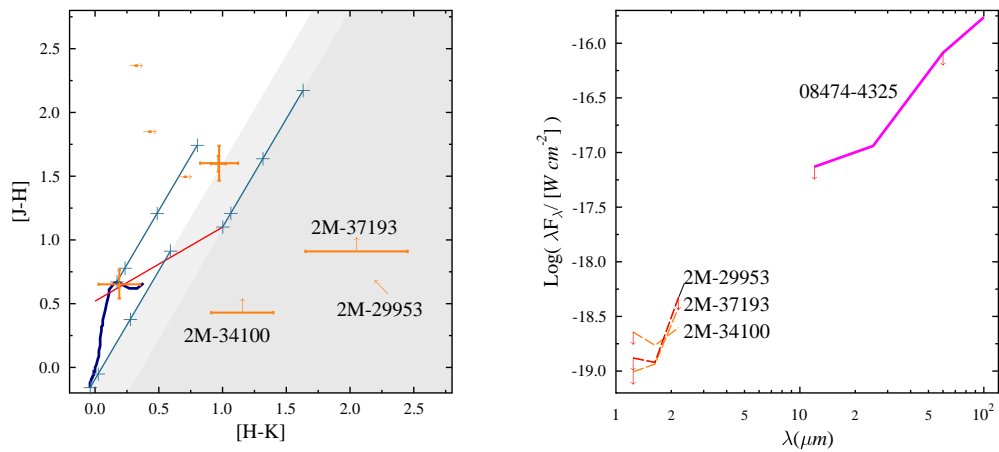


Figure A.19: *MMS21* colour-colour and SED diagrams.

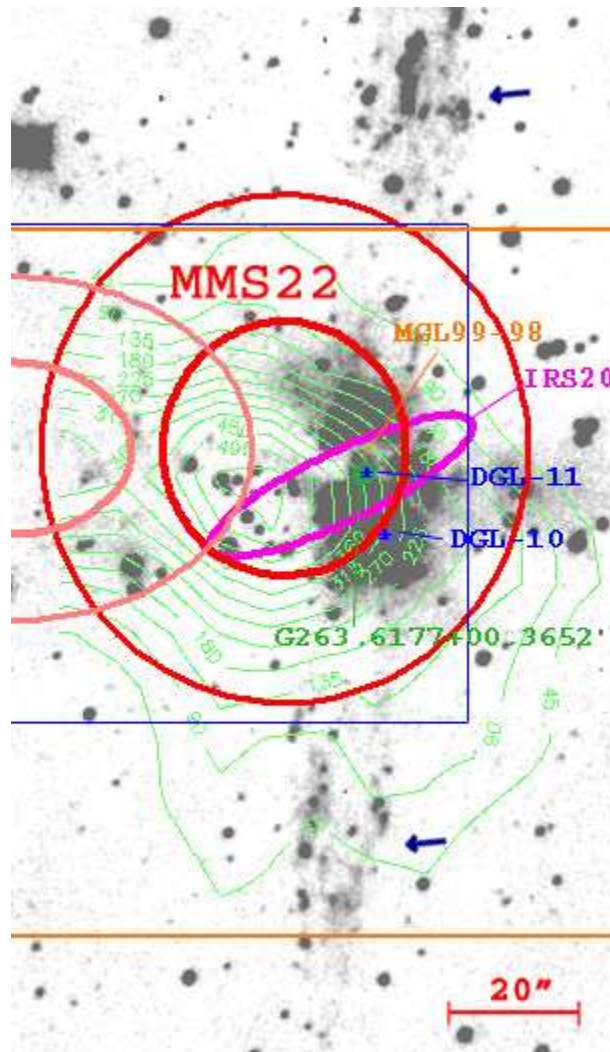


Figure A.20: *MMS22* field of view (center [J2000]: 08:49:26.0, -43:17:13.0).

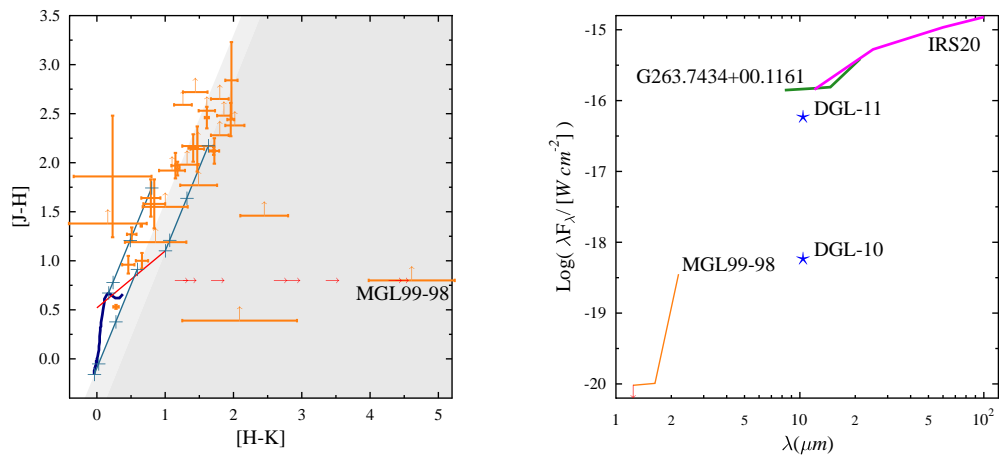


Figure A.21: *MMS22 colour-colour and SED diagrams.*

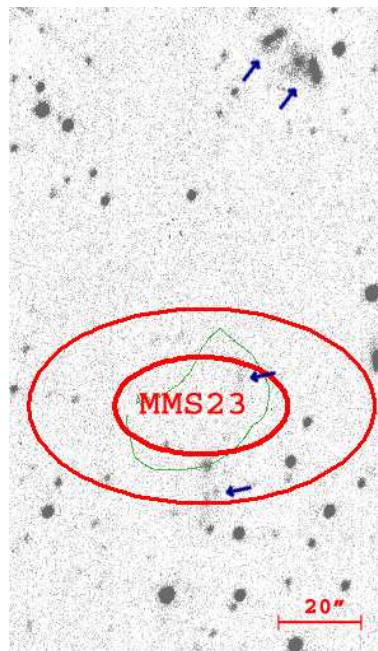


Figure A.22: *MMS23 field of view (center [J2000]: 08:49:30.2, -44:04:10.0).*

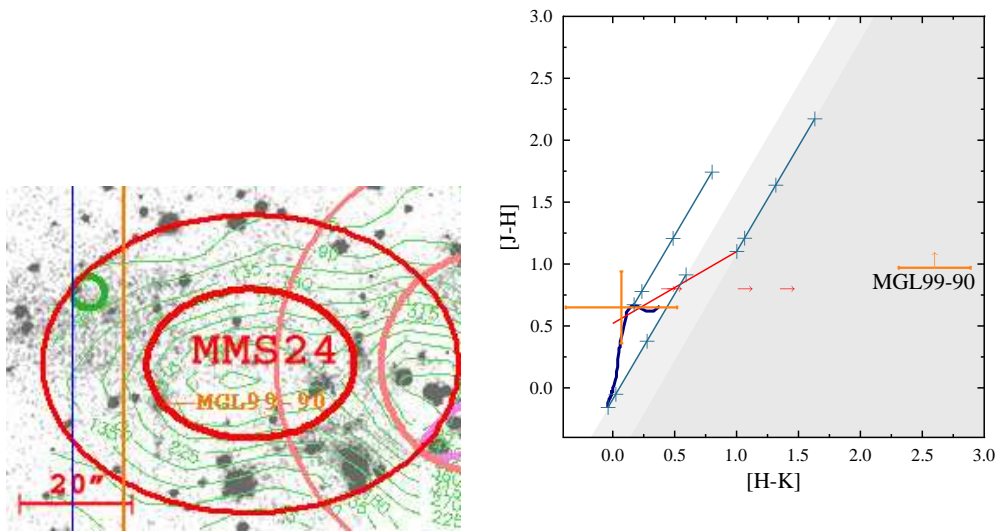


Figure A.23: *MMS24* field of view (center [J2000]: 08:49:30.1, -43:17:00.2) and colour-colour diagram.

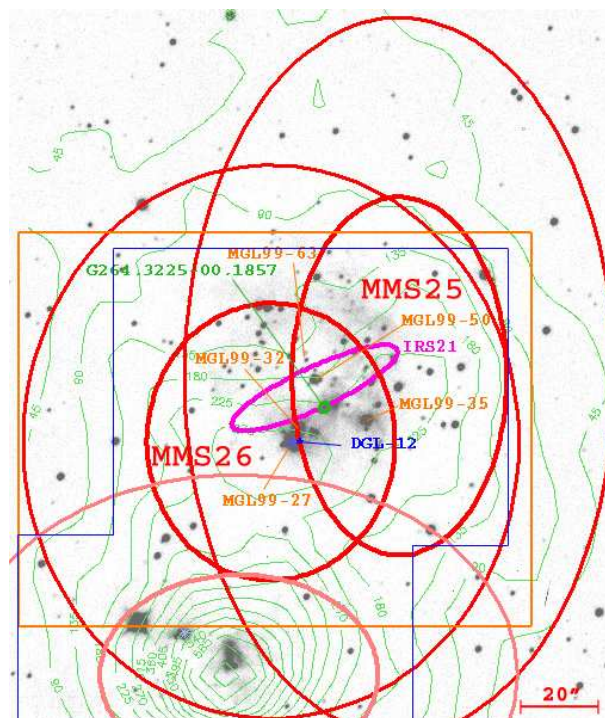


Figure A.24: *MMS25-26* field of view (center [J2000]: 08:49:33.5, -44:10:34.5).

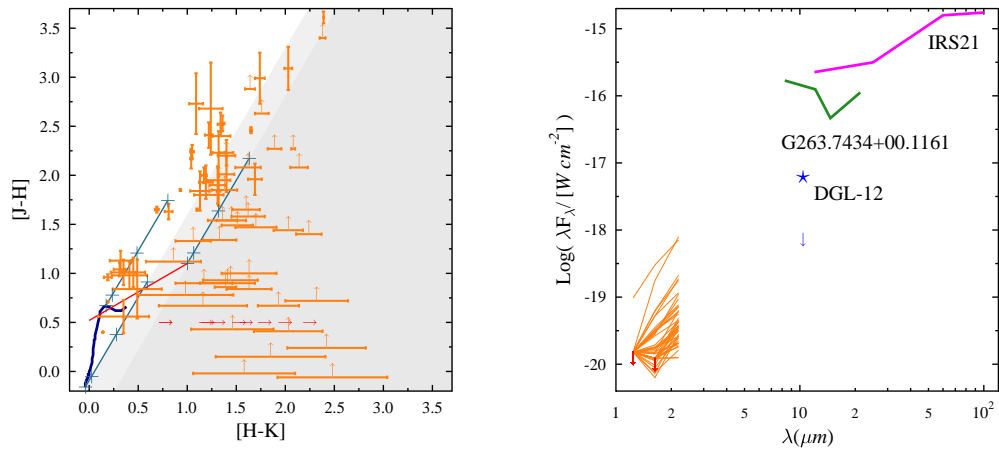


Figure A.25: *MMS25-26 colour-colour and SED diagrams.*

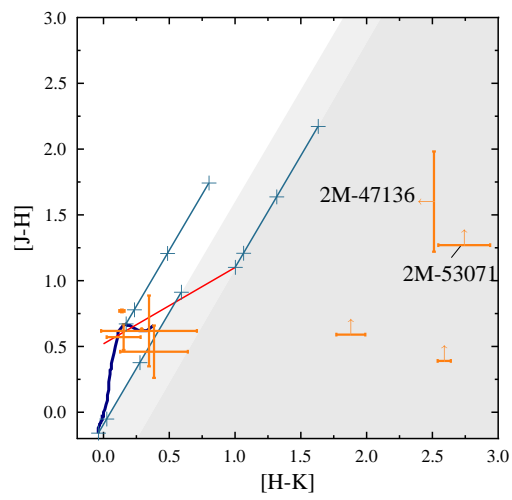
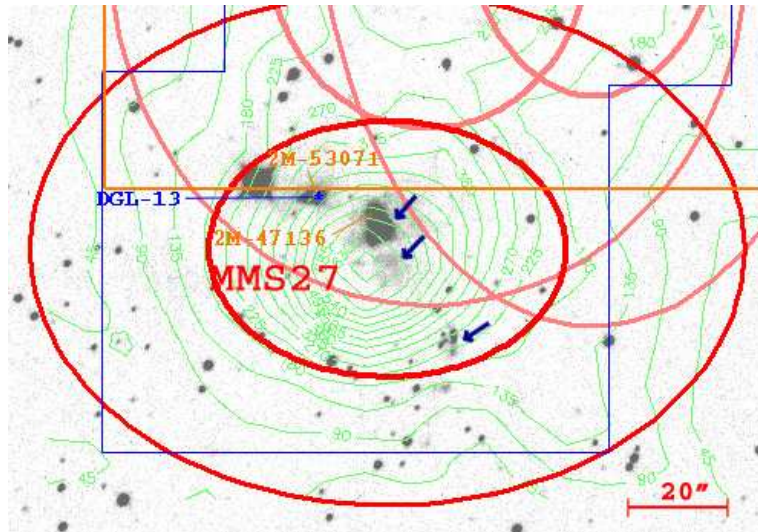


Figure A.26: *MMS27* field of view (center $[J2000]$: $08:49:35.2$, $-44:11:52.8$) and colour-colour diagram.

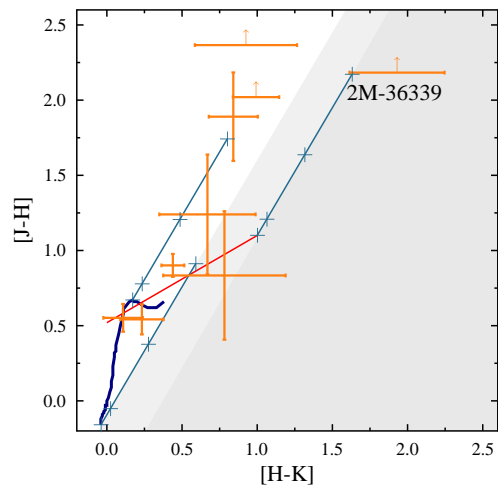
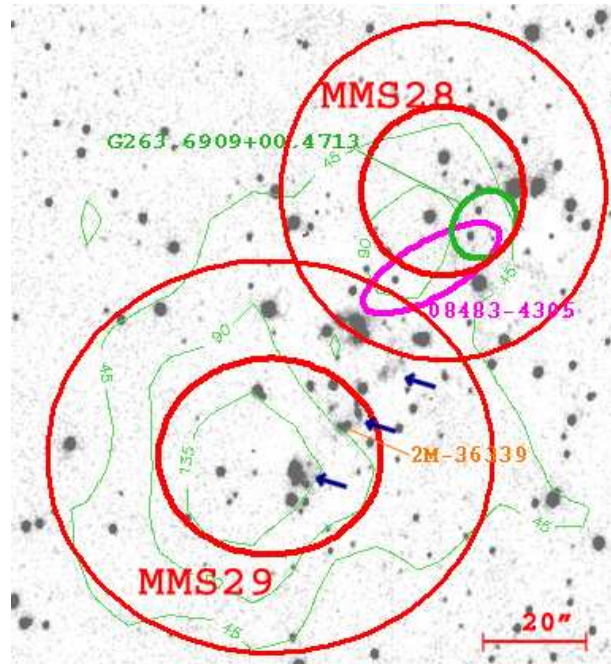


Figure A.27: *MMS28-29 field of view (center [J2000]: 08:50:10.0, -43:16:41.3) and colour-colour diagram.*



Figure A.28: *umms1* field of view (center [J2000]: 08:46:25.7, -43:42:28.3) (2MASS *H* band image).

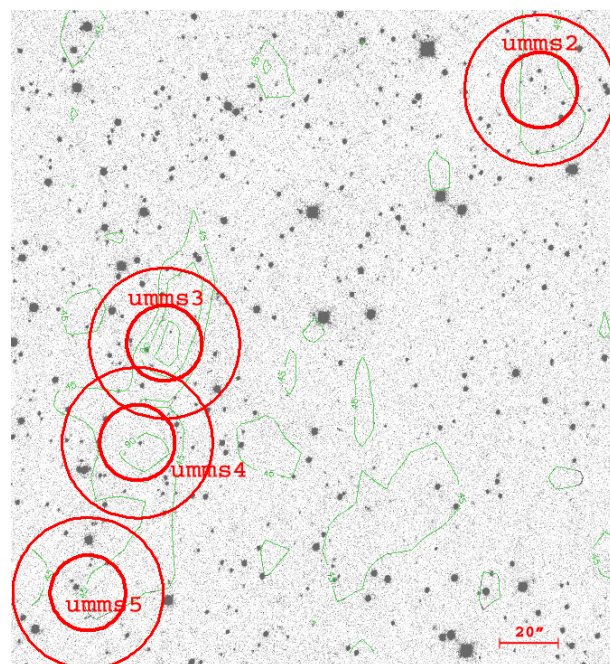


Figure A.29: *umms2-3-4-5* field of view (center [J2000]: 08:46:44.0, -43:19:48.2).

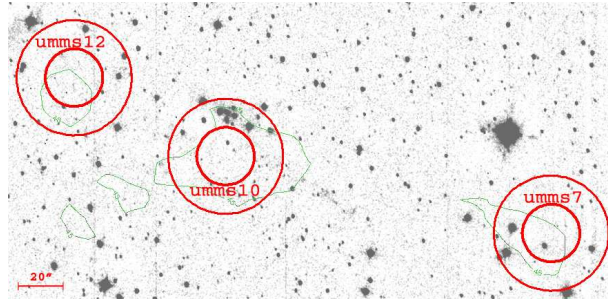


Figure A.30: *umms7-10-12* field of view (center [J2000]: 08:47:37.4, -43:26:21.7).

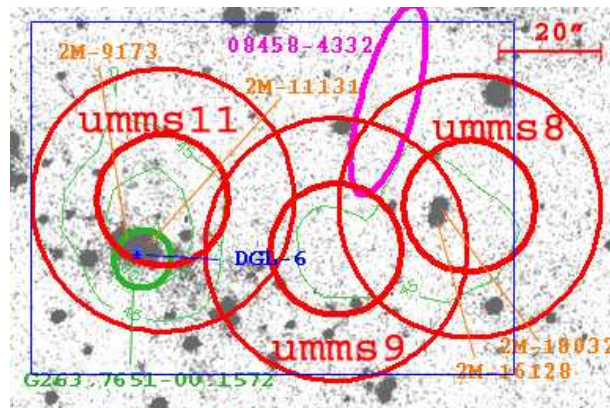


Figure A.31: *umms8-9-11* field of view (center [J2000]: 08:47:39.6, -43:43:36.1).

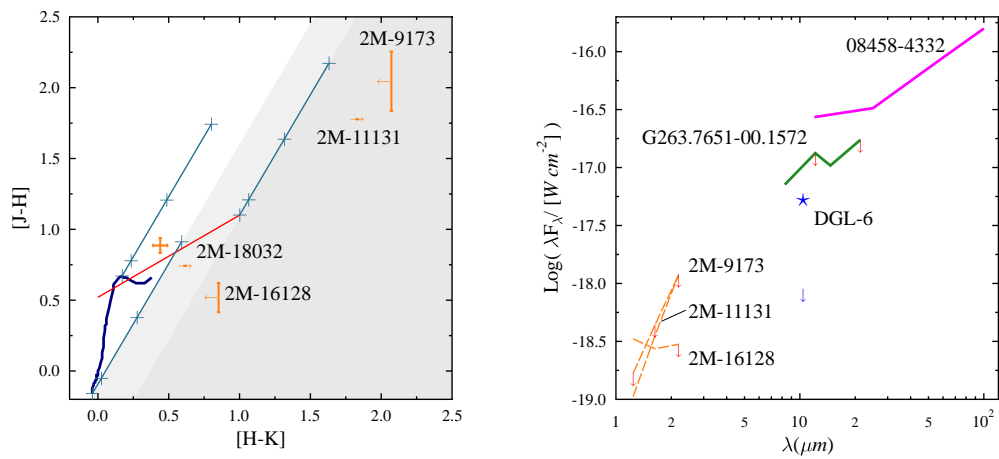


Figure A.32: *umms8-9-11* colour-colour and SED diagrams.

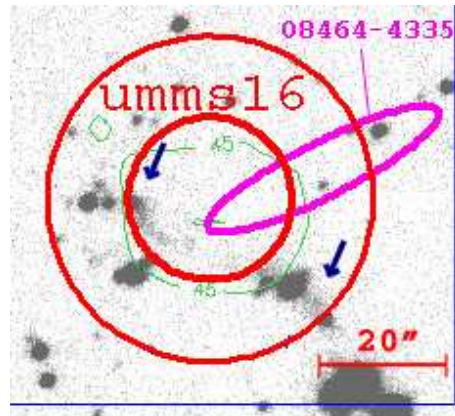


Figure A.33: *umms16* field of view (center [J2000]: 08:48:15.3, -43:47:06.5).

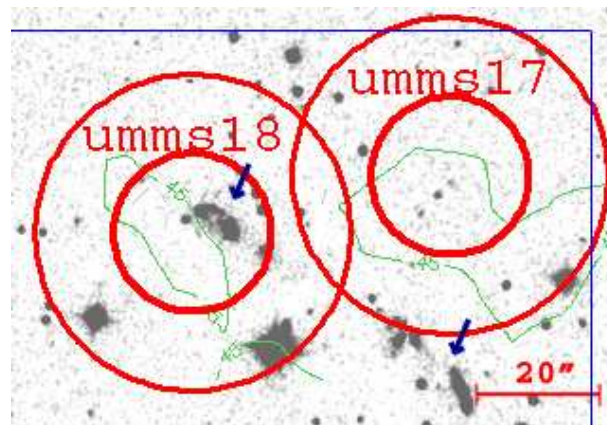


Figure A.34: *umms17-18* field of view (center [J2000]: 08:48:24.6, -43:31:36.7).

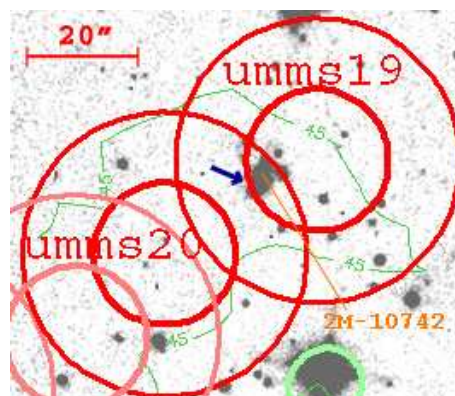


Figure A.35: *umms19-20* field of view (center [J2000]: 08:48:33.9, -43:30:46.0).

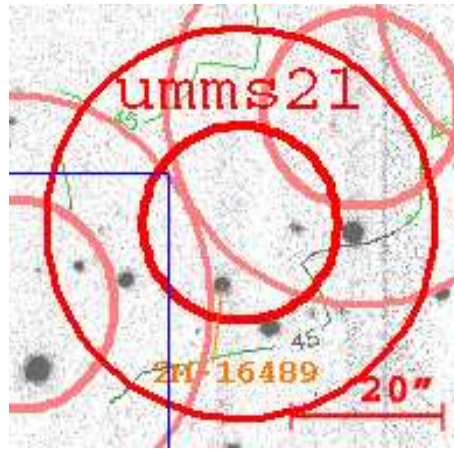


Figure A.36: *umms21* field of view (center [J2000]: 08:48:36.4, -43:31:11.5).

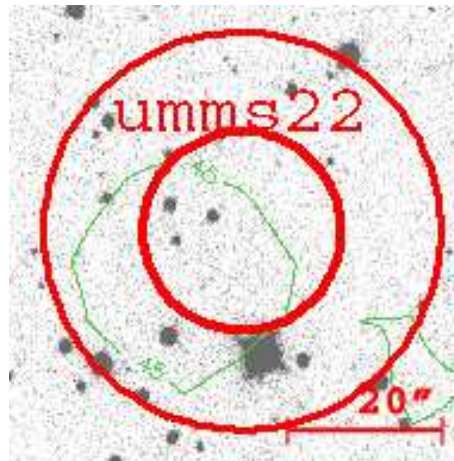


Figure A.37: *umms22* field of view (center [J2000]: 08:48:36.3, -43:16:45.9).

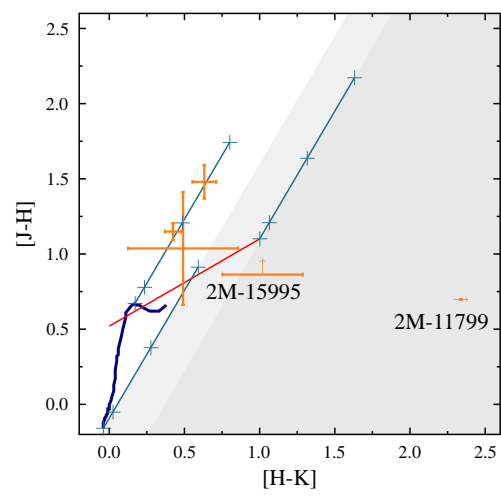
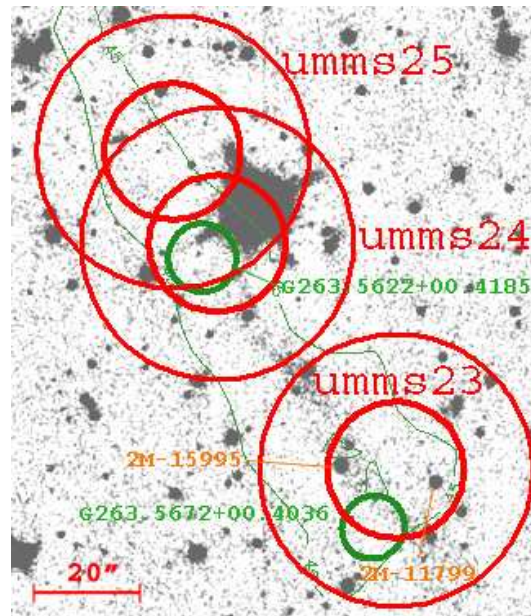


Figure A.38: *umms23-24-25* field of view (center $[J2000]$: $08:49:25.9$, $-43:12:39.2$) and colour-colour diagram.

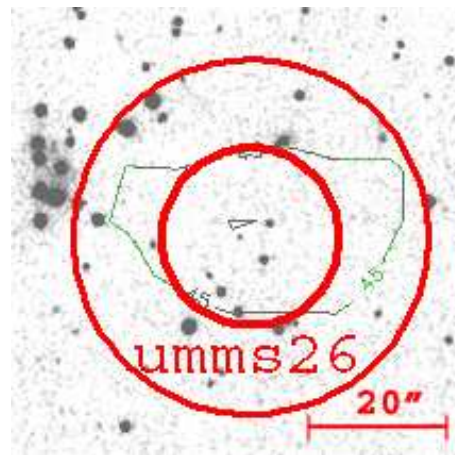


Figure A.39: *umms26* field of view (center [J2000]: 08:49:58.9, -43:22:55.1).

List of Figures

1	<i>The Vela Molecular Ridge according to Murphy & May (1991). The four ^{12}CO emission peaks, corresponding to clouds A, B, C and D are labeled. The region investigated in this thesis is red-shaded in the Figure.</i>	20
2	<i>The Vela Molecular Ridge according to Yamaguchi et al. (1999). $^{12}\text{CO}(1-0)$ (a) and $^{13}\text{CO}(2-1)$ (b) emission contours. Red-shaded: investigated region.</i>	21
3	<i>The Vela Molecular Ridge according to Moriguchi et al. (2001), where $^{12}\text{CO}(1-0)$ emission contours are plotted over the soft X-ray image (gray scale), taken by the ROSAT satellite, which shows a clear evidence of the high energy emission produced by the Vela Supernova Remnant. A cross indicates the position of the Vela pulsar, result of the explosion. Red-shaded: investigated region.</i>	22
1.1	<i>Three sketches of the simulation performed by Matthew R. Bate, Ian A. Bonnell, and Volker Bromm (http://www.ukaff.ac.uk/starcluster/). The calculation models the collapse and fragmentation of a molecular cloud of $50 M_{\odot}$. The cloud is initially 0.4 pc in diameter, with a temperature of 10 K. The cloud collapses under its own weight and very soon stars start to form. The turbulent motions in the cloud form shock waves that slowly damp the supersonic motions. At the end of simulation, some stars and brown dwarfs (Note 10) have been ejected to large distances from the region.</i>	31
1.2	<i>Scheme of colour-colour diagram. Dark blue line: main-sequence stars; Red crosses: red giant stars; light blue lines: reddening lines running from two representative points, enclosing the main sequence; typical extinction values of 1, 5 and 10 magnitudes are indicated with crosses.</i>	33

1.3	<i>Initial Mass function by Kroupa (2002): The measured stellar mass functions, ξ_L, as a function of logarithmic stellar mass [$\ln \equiv \log_{10}(m/M_{\odot})$] in the Orion nebula cluster [ONC, solid black circles (Hillenbrand & Carpenter 2000)], the Pleiades [green triangles (Hambly et al. 1999)] and the cluster M35 [blue solid circles (Barrado y Navascués et al. 2001)].</i>	39
1.4	<i>YSO classification scheme (see text).</i>	44
1.5	<i>HR diagram for a sample of pre-main sequence stars (AeBe Herbig stars and T-Tauri stars). Sources are indicated by points, while the left long, continuous line represents the ZAMS. Two birthlines are displayed (dotted lines), differing for the assumed value of the mass accretion rate: $10^{-4} M_{\odot} \text{ yr}^{-1}$ (a) and $10^{-5} M_{\odot} \text{ yr}^{-1}$ (b). The sources are found between the two lines, while following different evolutionary tracks depending on their mass (indicated in M_{\odot} along the ZAMS).</i>	48
1.6	<i>Temperature after the J-shock crossing as a function of the hydrogen column density (density integrated along the line of sight). The gas cooling goes through three different steps (see Figure 1.6): Collisional dissociation and ionization produce UV radiation, UV photoionization followed by recombination originates optical emission (e.g. Lyman lines), molecular formation is evidenced by IR emission.</i>	54
1.7	<i>Sketch of outflowing material from a proto-star.</i>	55
2.1	<i>Typical line profiles. This sample illustrates the part of the map corresponding to the offset interval $+750'' \leq \alpha_{off} \leq +1150''$, $+1350'' \leq \delta_{off} \leq +1700''$.</i>	60
2.2	<i>Integrated intensity map for the $^{12}\text{CO}(1-0)$ emission in Vela-D region, in the range $-2 \div 20 \text{ km s}^{-1}$. Contour levels start from 5 K km s^{-1} and are separated by 15 K km s^{-1}. Dashed lines delimit the observed area. On the right, the spatial angular scale corresponding to the estimated distance ($d = 700 \text{ pc}$) is shown.</i>	63
2.3	<i>As in Figure 2.2, but for the $^{13}\text{CO}(2-1)$ emission. Contour levels start from 2 K km s^{-1} and are separated by 5 K km s^{-1}.</i>	64
2.4	<i>Superposition of the $^{13}\text{CO}(2-1)$ contour levels (shown in Figure 2.3) on the $^{12}\text{CO}(1-0)$ integrated intensity map (shown in Figure 2.2). The positions of the “red” ($F_{12} < F_{25} < F_{60}$) IRAS sources are also marked with filled circles.</i>	65

- 2.5** Channel maps from -2 to 8 km s^{-1} for the $^{12}\text{CO}(1-0)$ (left panels) and $^{13}\text{CO}(2-1)$ (right panels) emission in Vela-D region, in the velocity ranges indicated on the left border of each box. For $^{12}\text{CO}(1-0)$ Contour levels start from 2 K km s^{-1} and are separated by 5 K km s^{-1} , while for $^{13}\text{CO}(2-1)$ they start from 1.5 K km s^{-1} and are separated by 3 K km s^{-1} . In both cases, dashed lines delimit the observed area. 68
- 2.6** Same as in Figure 2.5, but from 8 to 18 km s^{-1} 69
- 2.7** $\text{Vel}-\delta_{\text{off}}$ diagrams of the $^{12}\text{CO}(1-0)$ emission in Vela-D, for fixed values of α_{off} , indicated in each panel. Contour levels start from $T_{\text{mb}} = 2 \text{ K}$ and are separated by 4 K . Four arc-like structures have been recognized and marked with a solid arc of ellipse, each one in the diagram in which it is best visible. 70
- 2.8** A $2^\circ \times 2^\circ$ field centered on the $(0,0)$ position of the map is shown, with the contours of the $^{13}\text{CO}(2-1)$ emission plotted as in Figure 2.3. The bold dotted circles roughly indicate three arc-like emitting regions, while the thin dashed lines mark the border of the observed zone. Crosses indicate the center of the HII regions; for two of them with significant spatial extent, Gum 18 and RCW 35, an ellipse is also drawn whose axes length is taken from literature. The remaining HII regions are compact objects and cannot be responsible for the large-scale morphology. The locations of OB-type stars (filled circles), with their proper motion track extrapolated for the last 10^5 yr , are also marked. 73
- 2.9** Plot of the dynamical age t_{dyn} (solid line for $d = 700 \text{ pc}$, and dotted lines for $d = 500 \text{ pc}$ and $d = 900 \text{ pc}$, respectively) for a HII region and of the time at which the fragmentation of the driven shell starts (for different values of the sound velocity c_s and a radius of $\sim 3.4 \text{ pc}$) as a function of the density n_0 74

- 2.10** *Example of bad clump detection performed by CF. Panel a: a grid of $^{12}\text{CO}(1-0)$ spectra (resampled in resolution from 0.12 to 0.6 km s^{-1}) around two positions (marked with a thicker line) recognized by CF as centroids of different clumps, with almost coincident peak velocity ($V_{\text{lsr}} \simeq 7 \text{ km s}^{-1}$). Because these components satisfy our merging criteria (see text), we conservatively chose to consider them as a single clump. Note that a second component at $V_{\text{lsr}} \simeq 10 \text{ km s}^{-1}$ is clearly resolved in some spectra and is correctly assigned by CF to another clump. Panel b: the two thicker spectra shown in panel a are superimposed and plotted with solid and dashed line, respectively. The velocity channels erroneously assigned by CF to two different clumps are highlighted (bold line). 79*
- 2.11** *Clump mass spectrum of Vela-D derived from $^{13}\text{CO}(2-1)$ observations using CF. The dashed vertical lines indicate the minimum mass (leftmost) and the completeness (rightmost) limits, respectively. The dotted line shows the CF mass spectrum while the solid line is obtained after the merging procedure (see text). The linear best-fit is also shown in both cases, whose slope corresponds to $\alpha - 1$, where α is the exponent of the power law $dN/dM \propto M^{-\alpha}$ 83*
- 2.12** *Bi-logarithmic plot of the mass vs radius relation for the clumps resulting from the supervised clump decomposition of Vela-D, for the $^{12}\text{CO}(1-0)$ and the $^{13}\text{CO}(2-1)$ transitions, respectively. In both panels, the dashed line indicates the linear trend of the data. The slopes are $x = 2.5 \pm 0.3$ for $^{12}\text{CO}(1-0)$, and $x = 1.9 \pm 0.5$ for $^{13}\text{CO}(2-1)$ 85*
- 2.13** *SIMBA 1.2-mm continuum map of cloud D (greyscale). The scale (in mJy/beam) is indicated through the bar on the right and the contour at 60 mJy/beam ($\sim 3\sigma$) is also drawn. The red IRAS sources coincident with the most intense features are labelled (along with the designation adopted by Liseau et al. (1992)). Six areas including the main mm sources are enclosed within boxes and numbered, and are shown zoomed-in in the following figures. 93*
- 2.14** *NTT/SofI image of IRS16 (at K_s), taken on December 2005, overlaid with a contour map of the 1.2-mm continuum emission (area 1 in Fig. 2.13). Contours are in steps of 60 mJy/beam ($\sim 3\sigma$) from 60 to 600 mJy/beam . The cores are labelled and the IRAS uncertainty ellipse is also drawn. The SEST beam is displayed in the lower left box. 94*

- 2.15** *Contour map of the 1.2-mm continuum emission from the region including IRS17 (area 2 in Fig. 2.13). Contours are in steps of 60 mJy/beam ($\sim 3\sigma$) from 60 to 300 mJy/beam and in steps of 240 mJy/beam from 540 to 1500 mJy/beam. The cores are labelled and the SEST beam is drawn in the lower left box. Underlying, the $^{12}\text{CO}(1-0)$ emission integrated from 0 to 20 km s $^{-1}$ (grayscale, from 30 to 250K km s $^{-1}$). 94*
- 2.16** *Contour map of the 1.2-mm continuum emission from the region including IRS19 (area 3 in Fig. 2.13). Contours are: 40 mJy/beam ($\sim 2\sigma$) the lowest one, then in steps of 60 mJy/beam ($\sim 3\sigma$) from 60 to 300 mJy/beam and 540 mJy/beam the highest one. The cores are labelled and the SEST beam is drawn in the lower left box. Underlying, the $^{12}\text{CO}(1-0)$ emission integrated from 0 to 20 km s $^{-1}$ (grayscale, from 30 to 200 K km s $^{-1}$). 95*
- 2.17** *Contour map of the 1.2-mm continuum emission from the region including IRS21 (area 4 in Fig. 2.13). Contours are in steps of 60 mJy/beam ($\sim 3\sigma$) from 60 to 300 mJy/beam. The cores are labelled and the SEST beam is drawn in the lower left box. Underlying, the $^{12}\text{CO}(1-0)$ emission integrated from 0 to 20 km s $^{-1}$ (grayscale, from 30 to 150 K km s $^{-1}$). 95*
- 2.18** *Contour map of the 1.2-mm continuum emission from the region including IRS20 (area 5 in Fig. 2.13). Contours are in steps of 120 mJy/beam ($\sim 6\sigma$) from 60 to 540 mJy/beam. The cores are labelled and the SEST beam is drawn in the lower left box. Underlying, the $^{12}\text{CO}(1-0)$ emission integrated from 0 to 20 km s $^{-1}$ (grayscale, from 30 to 150 K km s $^{-1}$). 96*
- 2.19** *Contour map of the 1.2-mm continuum emission from the region at the centre of the mapped area (6 in Fig. 2.13) Contours are in steps of 60 mJy/beam ($\sim 3\sigma$) from 60 to 120 mJy/beam. The cores are labelled and the SEST beam is drawn in the lower left box. Underlying, the $^{12}\text{CO}(1-0)$ emission integrated from 0 to 20 km s $^{-1}$ (grayscale, from 30 to 150 K km s $^{-1}$). 96*

- 2.20** *Map of CO(1-0) emission from the observed area within cloud D (contours), integrated from 0 to 20 km s⁻¹, obtained with a beam of 43". This is overlaid with the SIMBA 1.2 mm continuum map (grayscale, beam of 24"). The thick solid line marks the contour at 25 K km s⁻¹, whereas the light solid line marks the contour at 60 K km s⁻¹. 97*
- 2.21** *Core mass vs size (uncorrected for beam). The vertical dashed line marks the SEST beam size, whereas the horizontal solid line shows the 3-σ detection limit for point sources. A dotted line has also been drawn following a D² relation, i.e., the sensitivity limit to extended sources (see text). 100*
- 2.22** *Core mass vs deconvolved size. The solid line is obtained by a fit ($M \sim D^{1.74}$), whereas the dashed line follows a D² relation, i.e., the sensitivity limit to extended sources (see text). 101*
- 2.23** *Mass spectrum of the mm cores. The error bars indicate the r.m.s. assuming a Poisson statistic. A dashed line shows a dN/dM ∼ M^{-1.45} relation, a dotted line shows a dN/dM ∼ M^{-1.2} relation. The estimated completeness limit is ∼ 1 – 1.3 M_⊙ (see text). 101*
- 3.1** *MMS1 field of view (center [J2000]: 08:45:32.8, -43:50:12.3). Grayscale image: H₂ emission; green contours: dust continuum (from 3σ, in steps of 3σ); red ellipses centered on the mm-peak: FWHM- and 2FWHM-ellipses within which the association with the IR sources has been searched for (at the bottom the ellipses pertaining to cores MMS2-3 are also visible); magenta and green ellipses: 3σ positional uncertainties of the IRAS and MSX point sources, respectively; blue asterisks: position of the 10.4 μm sources observed by Timmi2; 2MASS and IRAC2 NIR sources are labelled with 2M-# and MGL99-#, respectively; IRAC2-Timmi2 fields of view are delimited by orange-blue lines. 116*
- 3.2** ***a** - Colour-colour diagram of the sources falling within the FWHM-ellipse around MMS1. Dark curve: main sequence; red line: T-Tauri stars; blue lines: reddening lines with crosses indicating values of 0, 1, 5 and 10 mag of visual extinction. Arrows denote constraints from photometry upper limits. **b** - Spectral energy distribution of the very red sources within the FWHM-ellipse, together with the Timmi2 measured fluxes and the SED of the MSX object G263.5994-00.5236. Arrows denote again upper limits. See text for more details. 118*

- 3.3** *Spectral index (α_{2-10}) distribution of core counterparts. In cases of multiple estimates of the $10\ \mu\text{m}$ flux (Timmi2, MSX, IRAS) the value obtained with better spatial resolution was used to determine α 127*
- 3.4** *Two colours diagram for all the IRAS sources listed in Tabs. 3.1 and 3.3. The mean error bars, the extinction vector corresponding to 5 mag of visual extinction and the locus of blackbodies (leftmost line) are indicated (see text for more details). 128*
- 3.5** *Luminosity distribution of both associated and unassociated IRAS sources (Tabs. 3.1 and 3.3). 129*
- 3.6** *MIPS two-color map ($24\ \mu\text{m}$ in blue, $70\ \mu\text{m}$ in red) of Vela-D. . . . 131*
- 3.7** *Mosaic of Vela-D map at $24\ \mu\text{m}$, with superposed the $^{12}\text{CO}(1-0)$ intensity map (whose limits are depicted in yellow), where the contours (in green) are in the range $-2-20\ \text{km s}^{-1}$ (adapted by Elia et al. 2007). Also overlaid is the 1.2mm dust emission map (red contours, adapted from Massi et al. 2007). CO contour levels start from $5\ \text{K km s}^{-1}$ and are in steps of $25\ \text{K km s}^{-1}$, while dust contours start from $50\ \text{mJy/beam}$ and are in steps of $50\ \text{mJy/beam}$ 132*
- 3.8** *As Figure 3.7 for the $70\ \mu\text{m}$ map. 133*
- 3.9** *Histogram of the sources detected at $24\ \mu\text{m}$. The completeness limit is around $5\ \text{mJy}$, as indicated by the vertical line. 134*
- 3.10** *Histogram of the sources detected at $70\ \mu\text{m}$. The completeness limit is around $250\ \text{mJy}$, as indicated by the vertical line. 134*
- 3.11** *Left panel: differential number counts at $24\ \mu\text{m}$. Thick and thin lines refer to source in Vela-D (VMR-D) within and outside the $^{12}\text{CO}(1-0)$ contours, respectively. Extragalactic background sources from the SWIRE ELAIS N1 field are shown for comparison (these latter have been taken from Figs.6 and 7 in Rebull et al. 2007). Right panel: as in left panel at $70\ \mu\text{m}$ 135*

- 3.12** *Color-magnitude diagram for the 2MASS K_s -band and the MIPS $24\ \mu\text{m}$ sources. Of the 849 $24\ \mu\text{m}$ sources in the MIPS map, 401 have a K_s detection within a radius of 5 arcsec. These are shown by red dots if located inside the CO contour map (180 sources) and by black dots if outside (221 sources). Large dots denote sources with $70\ \mu\text{m}$ detections, while arrows refer to sources saturated at $24\ \mu\text{m}$. Hatched areas are the loci of the sources in the SWIRE survey (taken from Rebull et al. 2007). The thick line indicates the effect of the extinction for different values of A_V (open squares refer to $A_V=10$ and 50 mag). 142*
- 3.13** *Color-magnitude diagram $[24]$ vs $[24]-[70]$, where only sources not saturated at $24\ \mu\text{m}$ are plotted. Red/black dots refer to sources inside/outside the CO contour map (41/12 sources). Large dots denote sources associated with a dust core, while numbered sources are the candidates exciting sources of the jets discussed in next Chapter (Table 4.4). The hatched area shows the locus of the SWIRE survey (taken from Fig.11 in Rebull et al. 2007). 146*
- 4.1** *Spectral map of jet1. 164*
- 4.2** *Contour plot of the blue-shifted lobe of the outflow associated with jet5. Small triangles individuate the position of all the observed offsets. 165*
- 4.3** *On the left: dust contours (yellow, from a 3σ level in steps of 3σ) and H_2 knots of jet1 (blue) superposed on the MIPS two-colours image ($70\ \mu\text{m}$ red and $24\ \mu\text{m}$ green). Note the coincidence of dust peak and jet direction. The box indicates the region mapped by APEX. On the right: contour plot of the identified outflow lobe (from 3σ in steps of 3σ) superposed on the H_2 image. Just one lobe has been detected. . . 166*
- 4.4** *The same as Figure 4.3 for jet 2. Peak umms16 (under-resolved at the SIMBA spatial resolution) is found near the jet center. The proposed exciting source is #38 in Table 3.7. 167*
- 4.5** *The same as Figure 4.3 for jet 3. A MIPS source (#21) is found at the jet center, corresponding to a location of weak dust emission. . . 167*
- 4.6** *The same as Figure 4.3 for jet 5. The driving source is likely to be the MIPS source (#44) associated with the under-resolved peak umms19. The lack of a counter jet is probably due to the driving source being located near the edge of the H_2 image. 168*
- 4.7** *The same as Figure 4.3 for jet 4. Dust core MMS22 crosses the jet. The candidate driving source (IRS20-MGL99#98) is indicated. . . . 168*

4.8	<i>The same as Figure 4.3 for jet 6. The candidate exciting source is the 24 and 70 μm source associated with mm peak MMS16 (#50). Just one lobe has been detected.</i>	169
4.9	<i>Spectral Energy Distribution of the driving sources.</i>	172
5.1	<i>Possible interaction between Vela-D (red image: MIPS 24 μm) and the Gum 18 expanding HII region (evidenced by Hα contours taken from the Southern Hα Sky Survey Atlas, SHASSA, see Gaustad et al. 2001).</i>	178
A.1	<i>MMS2 field of view (center [J2000]: 08:45:34.200, -43:51:54.40). Grayscale image: H₂ emission; green contours: dust continuum (from 3σ, in steps of 3σ); red ellipses centered on the mm-peak: FWHM- and 2FWHM-ellipses within which the association with the IR sources has been searched for (the ellipses pertaining to cores MMS1-3 are also visible); magenta and green ellipses: 3σ positional uncertainties of the IRAS and MSX point sources, respectively; blue asterisks: position of the 10.4 μm sources observed by Timmi2; 2MASS and IRAC2 NIR sources are labelled with 2M-\ddagger (following an internal numbering) and MGL99-\ddagger, respectively; IRAC2-Timmi2 fields of view are delimited by orange-blue lines. The position of the main knots of H₂ emission is highlighted by dark-blue ellipse and arrows.</i>	194
A.2	<i>a) Colour-colour diagram (see text for more details) of the NIR sources within the FWHM-ellipse of MMS2. The Spectral Energy Distributions of the very red ones are shown in panel b). To reduce confusion the wavelength range is limited to the J, H, K bands and the main objects are in red colour. Dashed lines refer to 2MASS sources and arrows denote upper limits.</i>	195
A.3	<i>MMS3 field of view (center [J2000]: 08:45:39.5, -43:51:25.0).</i>	195
A.4	<i>MMS3: colour-colour and SED diagrams.</i>	196
A.5	<i>MMS5-6 and umms6 field of view (center [J2000]: 08:46:52.0, -43:53:01.3).</i>	196
A.6	<i>MMS7 and umms13-14-15 field of view (center [J2000]: 08:47:58.9, -43:39:22.9) and colour-colour diagram.</i>	197
A.7	<i>MMS8-9 field of view (center [J2000]: 08:48:41.3, -43:31:36.2) and colour-colour diagram.</i>	198
A.8	<i>MMS10-11 field of view (center [J2000]: 08:48:44.2, -43:37:19.1) and colour-colour diagram.</i>	199

A.9	<i>MMS12 field of view (center [J2000]: 08:48:48.5, -43:32:20.8).</i>	200
A.10	<i>MMS12 colour-colour and SED diagrams.</i>	200
A.11	<i>MMS13 field of view (center [J2000]: 08:48:49.4, -43:33:11.2) and colour-colour diagram.</i>	201
A.12	<i>MMS14-15-16 field of view (center [J2000]: 08:48:51.6, -43:31:09.9).</i>	202
A.13	<i>MMS17 field of view (center [J2000]: 08:48:57.2, -43:38:23.1).</i>	202
A.14	<i>MMS18 field of view (center [J2000]: 08:49:03.2, -43:38:05.2).</i>	203
A.15	<i>MMS18 colour-colour and SED diagrams.</i>	203
A.16	<i>MMS19 field of view (center [J2000]: 08:49:08.5, -43:35:43.7) and colour-colour diagram.</i>	204
A.17	<i>MMS20 field of view (center [J2000]: 08:49:11.2, -43:35:25.9) and colour-colour diagram.</i>	205
A.18	<i>MMS21 field of view (center [J2000]: 08:49:13.0, -43:36:21.8).</i>	206
A.19	<i>MMS21 colour-colour and SED diagrams.</i>	206
A.20	<i>MMS22 field of view (center [J2000]: 08:49:26.0, -43:17:13.0).</i>	207
A.21	<i>MMS22 colour-colour and SED diagrams.</i>	208
A.22	<i>MMS23 field of view (center [J2000]: 08:49:30.2, -44:04:10.0).</i>	208
A.23	<i>MMS24 field of view (center [J2000]: 08:49:30.1, -43:17:00.2) and colour-colour diagram.</i>	209
A.24	<i>MMS25-26 field of view (center [J2000]: 08:49:33.5, -44:10:34.5).</i>	209
A.25	<i>MMS25-26 colour-colour and SED diagrams.</i>	210
A.26	<i>MMS27 field of view (center [J2000]: 08:49:35.2, -44:11:52.8) and colour-colour diagram.</i>	211
A.27	<i>MMS28-29 field of view (center [J2000]: 08:50:10.0, -43:16:41.3) and colour-colour diagram.</i>	212
A.28	<i>umms1 field of view (center [J2000]: 08:46:25.7, -43:42:28.3) (2MASS H band image).</i>	213
A.29	<i>umms2-3-4-5 field of view (center [J2000]: 08:46:44.0, -43:19:48.2).</i>	213
A.30	<i>umms7-10-12 field of view (center [J2000]: 08:47:37.4, -43:26:21.7).</i>	214
A.31	<i>umms8-9-11 field of view (center [J2000]: 08:47:39.6, -43:43:36.1).</i>	214
A.32	<i>umms8-9-11 colour-colour and SED diagrams.</i>	214
A.33	<i>umms16 field of view (center [J2000]: 08:48:15.3, -43:47:06.5).</i>	215
A.34	<i>umms17-18 field of view (center [J2000]: 08:48:24.6, -43:31:36.7).</i>	215
A.35	<i>umms19-20 field of view (center [J2000]: 08:48:33.9, -43:30:46.0).</i>	215
A.36	<i>umms21 field of view (center [J2000]: 08:48:36.4, -43:31:11.5).</i>	216
A.37	<i>umms22 field of view (center [J2000]: 08:48:36.3, -43:16:45.9).</i>	216

- A.38** *umms23-24-25 field of view (center [J2000]: 08:49:25.9, -43:12:39.2)
and colour-colour diagram. 217*
- A.39** *umms26 field of view (center [J2000]: 08:49:58.9, -43:22:55.1). . . . 218*

List of Tables

1.1	<i>Physical properties of molecular clouds (adapted from Stahler & Palla 2005).</i>	28
2.1	IRAS PSC sources in the observed field, with fluxes increasing from 12 μm to 60 μm.	67
2.2	<i>Velocity ranges of the main emitting regions in Vela-D</i>	71
2.3	<i>List of the clumps detected in the $^{13}\text{CO}(2-1)$ line.</i>	81
2.4	<i>Dust cores found by CLUMPFIND: the robust sample.</i>	91
2.5	<i>Possible dust cores found by CLUMPFIND, but with size less than the SEST beam (before deconvolution).</i>	92
3.1	<i>Dust cores with associated FIR and/or MIR point sources.</i>	122
3.2	<i>NIR sources and H_2 emission associated with dust cores.</i>	123
3.3	<i>IRAS point sources with increasing fluxes not associated with any core.</i>	124
3.4	<i>Statistics about the dust cores population.</i>	125
3.5	<i>Statistics of MIPS point sources.</i>	136
3.6	<i>MIPS sources in the Vela Molecular Cloud-D.</i>	137
3.7	<i>MIPS sources detected at 70μm.</i>	138
3.7	<i>MIPS sources detected at 70μm (continued).</i>	139
3.8	<i>Classification of the MIPS sources.</i>	143
3.9	<i>IRAS PSC detections not recovered by MIPS</i>	147
4.1	<i>Integrated flux and parameters of the Vela-D H_2 jets.</i>	154
4.2	<i>Velocity range of each identified outflow lobe and line peak velocities.</i>	164
4.3	<i>Outflow parameters.</i>	170
4.4	<i>Protostellar jets associated with MIPS sources in Vela-D.</i>	176

Refereed Publications

- **Giannini, T., Lorenzetti, D., De Luca, M., et al.** *Spitzer MIPS Survey of the Young Stellar Content in the Vela Molecular Ridge-D*, **2007, ApJ 671, 470**
- **De Luca, M., Giannini, T., Lorenzetti, D.** *Near- and Far-Infrared Counterparts of Millimeter Dust Cores in the Vela Molecular Ridge Cloud D*, **2007, A&A 474, 863**
- **Lorenzetti, D., Giannini, T., Larionov, V. M., Kopatskaya, E., A., Arkharov, A., De Luca, M. and A., Di Paola** *An infrared view of the EXor variables: on the case of V1118 Ori*, **2007, ApJ 665, 1182**
- **Massi, F., De Luca, M., Elia, D., Giannini, T., Lorenzetti, D., Nisini, B.** *Star formation in the Vela Molecular Ridge. Large scale mapping of cloud D in the mm continuum*, **2007, A&A 466, 1013**
- **Elia, D., Massi, F., Strafella, F., De Luca, M., Giannini, T., Lorenzetti, D., Nisini, B., Campeggio, L. and Maiolo, B. M. T.** *Mapping molecular emission in Vela Molecular Ridge Cloud D*, **2007, ApJ 655, 316**
- **Massi, F., De Luca, M., Elia, D., Giannini, T., Lorenzetti, D., Nisini, B., Strafella, F.** *Large-scale mapping of molecular clouds: what can we learn?*, **2006, Memorie della Societ Astronomica Italiana Supplement, v.10, p.165**
- **Li Causi, G. and De Luca, M.** *Optimal subtraction of OH airglow emission: a tool for infrared fiber spectroscopy*, **2005, New Astronomy 11, 81**

Other Publications and Conference Presentations

- De Luca, M., Massi, F., Giannini, T., Lorenzetti, D., Elia *Intermediate-mass star formation in young embedded stellar clusters*, for the Massive Star Formation Meeting, 10-14 September 2007, Heidelberg
- De Luca, M., Giannini, T., Nisini, B., Lorenzetti, D., Dionatos O. *Newly detected outflows observed with APEX in the Vela star forming region*, for the JENAM 2007 Conference *Our non-stable Universe*, 20-25 August 2007, Yerevan
- Dionatos O., Nisini, B., Giannini, T., Garcia-Lopez, R., De Luca, M., Davis C., Smith, M. *Spitzer observations of the L1448-mm molecular jet*, for the Herschel winter school, April 23 - May 24 2007, Les Houches
- De Luca, M., Giannini, T., Lorenzetti, D., Elia, D., Fazio, G., Marengo, M., Massi, F., Nisini, B., Smith, H. A. *Resolving the dust emission in the Vela Molecular Cloud*, for the ALMA International Conference, 13-17 November 2006, Madrid
- Giannini, T., De Luca, M., Lorenzetti, D., Fazio, G., Marengo, M., Massi, F., Nisini, B., Smith, H. A. *Exploring southern star forming regions: H₂ jets driven by very young protostars*, for the ALMA International Conference, 13-17 November 2006, Madrid
- Elia, D., Strafella, F., Massi, F., De Luca, M., Campeggio, L. and Maiolo, B. *Structural analysis of molecular cloud maps: the case of the star forming Vela-D Cloud*, IAU Symposium 237, August 14-18, 2006, Prague
- De Luca, M., Giannini, T., Lorenzetti, D., Massi, F., Elia, D., Nisini, B. and Smith H.A. *Sailing across the southern sky: a VELA picture in the mm-light*, Protostars and Planets V, October 24-28, 2005, Big Island - Hawaii
- De Luca, M., Giannini, T., Lorenzetti, D., Massi, F., Elia, D., Nisini, B. and Smith H.A. *The Vela Molecular Clouds young population: studying protostellar targets for ALMA*, IAU Symposium 227, May 16-20, 2005, Acireale

Bibliography

- Alves, J., Lombardi, M., & Lada, C. J. 2007, *A&A*, 462, L17
- André, P., Ward-Thompson, D., & Barsony, M. 1993, *ApJ*, 406, 122
- Andre, P., Ward-Thompson, D., & Barsony, M. 2000, *Protostars and Planets IV*, 59
- Bachiller, R. 1996, *ARA&A*, 34, 111
- Bains, I., Wong, T., Cunningham, M., et al. 2006, *M.N.R.A.S.*, 367, 1609
- Bally, J., Langer, W. D., Wilson, R. W., Stark, A. A., & Pound, M. W. 1991, in *IAU Symposium No. 147: Fragmentation of molecular clouds and star formation*, p. 11 - 20, 11–20
- Barrado y Navascués, D., Stauffer, J. R., Bouvier, J., & Martín, E. L. 2001, *ApJ*, 546, 1006
- Beichman, C. A., Myers, P. C., Emerson, J. P., et al. 1986, *ApJ*, 307, 337
- Beltrán, M. T., Brand, J., Cesaroni, R., et al. 2006, *A&A*, 447, 221
- Berrilli, F., Corciulo, G., Ingrassio, G., et al. 1992, *ApJ*, 398, 254
- Blaauw, A. 1991, in *NATO ASIC Proc. 342: The Physics of Star Formation and Early Stellar Evolution*, ed. C. J. Lada & N. D. Kylafis, 125–+
- Bonnell, I. A., Bate, M. R., & Vine, S. G. 2003, *M.N.R.A.S.*, 343, 413
- Booth, R. S., Delgado, G., Hagstrom, M., et al. 1989, *A&A*, 216, 315
- Bourke, T. L., Garay, G., Lehtinen, K. K., et al. 1997, *ApJ*, 476, 781
- Brunt, C. M., Kerton, C. R., & Pomerleau, C. 2003, *ApJS*, 144, 47

- Caselli, P., Walmsley, C. M., Terzieva, R., & Herbst, E. 1998, *ApJ*, 499, 234
- Chen, H. & Tokunaga, A. T. 1994, *ApJS*, 90, 149
- Chini, R., Kämpgen, K., Reipurth, B., et al. 2003, *A&A*, 409, 235
- Choi, M., Evans, II, N. J., & Jaffe, D. T. 1993, *Revista Mexicana de Astronomia y Astrofisica*, 27, 91
- Crowther, P. A. 2005, in *IAU Symposium, Vol. 227, Massive Star Birth: A Crossroads of Astrophysics*, ed. R. Cesaroni, M. Felli, E. Churchwell, & M. Walmsley, 389–396
- De Luca, M., Giannini, T., Lorenzetti, D., et al. 2007, *A&A*, 474, 863
- Djupvik, A. A., André, P., Bontemps, S., et al. 2006, *A&A*, 458, 789
- Dobashi, K., Uehara, H., Kandori, R., et al. 2005, *pasj*, 57, 1
- Draine, B. T. 1980, *ApJ*, 241, 1021
- Elia, D., Massi, F., Strafella, F., et al. 2007, *ApJ*, 655, 316
- Enoch, M. 2006, in *Bulletin of the American Astronomical Society, Vol. 38, Bulletin of the American Astronomical Society*, 1080–+
- Faúndez, S., Bronfman, L., Garay, G., et al. 2004, *A&A*, 426, 97
- Gaustad, J. E., McCullough, P. R., Rosing, W., & Van Buren, D. 2001, *Astronomical Society of the Pacific*, 113, 1326
- Giannini, T., Lorenzetti, D., De Luca, M., et al. 2007, *ApJ*, 671, 470
- Giannini, T., Massi, F., Podio, L., et al. 2005, *A&A*, 433, 941
- Giannini, T., Nisini, B., Vitali, F., & Lorenzetti, D. 2001, *A&A*, 379, L17
- Gomez, M., Hartmann, L., Kenyon, S. J., & Hewett, R. 1993, *Astronomical Journal*, 105, 1927
- Goodman, A. A., Benson, P. J., Fuller, G. A., & Myers, P. C. 1993, *ApJ*, 406, 528

- Goodwin, S. P., Nutter, D., Kroupa, P., Ward-Thompson, D., & Whitworth, A. P. 2007, ArXiv e-prints, 711
- Gredel, R. 1994, *A&A*, 292, 580
- Greene, T. P., Wilking, B. A., Andre, P., Young, E. T., & Lada, C. J. 1994, *ApJ*, 434, 614
- Grevesse, N., Lambert, D. L., Sauval, A. J., et al. 1991, *A&A*, 242, 488
- Guedel, M., Padgett, D. L., & Dougados, C. 2006, ArXiv Astrophysics e-prints
- Gum, C. S. 1955, *memras*, 67, 155
- Hambly, N. C., Hodgkin, S. T., Cossburn, M. R., & Jameson, R. F. 1999, *M.N.R.A.S.*, 303, 835
- Hartmann, L. W. & Kenyon, S. J. 1990, *ApJ*, 349, 190
- Harvey, P. M., Rebull, L. M., Brooke, T., et al. 2007, *ApJ*, 663, 1139
- Hatchell, J., Fuller, G. A., Richer, J. S., Harries, T. J., & Ladd, E. F. 2007, *A&A*, 468, 1009
- Hatchell, J., Richer, J. S., Fuller, G. A., et al. 2005, *A&A*, 440, 151
- Heiles, C., Goodman, A. A., McKee, C. F., & Zweibel, E. G. 1993, in *Protostars and Planets III*, ed. E. H. Levy & J. I. Lunine, 279–326
- Heithausen, A., Bensch, F., Stutzki, J., Falgarone, E., & Panis, J. F. 1998, *A&A*, 331, L65
- Henning, T., Burkert, A., Launhardt, R., Leinert, C., & Stecklum, B. 1998, *A&A*, 336, 565
- Hillenbrand, L. A. & Carpenter, J. M. 2000, *ApJ*, 540, 236
- Hollenbach, D. & McKee, C. F. 1989, *ApJ*, 342, 306
- IRAS-PSC. 1988, *Infrared Astronomical Satellite (IRAS) Catalogs and Atlases*, vol. 1, Explanatory Supplement, c. beichman, et al., nasa rp-1190 (washington, dc: gpo) edn.

- Johnstone, D., Wilson, C. D., Moriarty-Schieven, G., et al. 2000, *ApJ*, 545, 327
- Jorgensen, J. K., Johnstone, D., Kirk, H., et al. 2006, in *Bulletin of the American Astronomical Society*, Vol. 38, *Bulletin of the American Astronomical Society*, 1051–+
- Jørgensen, J. K., Johnstone, D., van Dishoeck, E. F., & Doty, S. D. 2006, *A&A*, 449, 609
- Kerton, C. R., Martin, P. G., Johnstone, D., & Ballantyne, D. R. 2001, *ApJ*, 552, 601
- Kroupa, P. 2002, *Science*, 295, 82
- Lada, C. J. 1987, in *IAU Symposium*, Vol. 115, *Star Forming Regions*, ed. M. Peimbert & J. Jugaku, 1–17
- Large, M. I., Vaughan, A. E., & Mills, B. Y. 1968, *Nature*, 220, 340
- Larson, R. B. 1981, *M.N.R.A.S.*, 194, 809
- Lidmann, C., Cuby, J.-G., Vanzi, L., et al. 2006, *SOFI - User's Manual*, European Southern Observatory
- Liseau, R., Lorenzetti, D., Nisini, B., Spinoglio, L., & Moneti, A. 1992, *A&A*, 265, 577
- Lonsdale, C. J., Smith, H. E., Rowan-Robinson, M., et al. 2003, *Astronomical Society of the Pacific*, 115, 897
- Lorenzetti, D., Giannini, T., Nisini, B., et al. 2002a, *A&A*, 395, 637
- Lorenzetti, D., Giannini, T., Vitali, F., Massi, F., & Nisini, B. 2002b, *ApJ*, 564, 839
- Lorenzetti, D., Spinoglio, L., & Liseau, R. 1993, *A&A*, 275, 489
- Low, C. & Lynden-Bell, D. 1976, *M.N.R.A.S.*, 176, 367
- Luhman, K. L. 2004, *ApJ*, 617, 1216
- Mac Low, M.-M. & Klessen, R. S. 2004, *Reviews of Modern Physics*, 76, 125

- Makovoz, D. & Marleau, F. R. 2005, *Astronomical Society of the Pacific*, 117, 1113
- Massi, F., Brand, J., & Felli, M. 1997, *A&A*, 320, 972
- Massi, F., De Luca, M., Elia, D., et al. 2007, *A&A*, 466, 1013
- Massi, F., Giannini, T., Lorenzetti, D., et al. 1999, *A&AS*, 136, 471
- Massi, F., Lorenzetti, D., & Giannini, T. 2003, *A&A*, 399, 147
- Massi, F., Lorenzetti, D., Giannini, T., & Vitali, F. 2000, *A&A*, 353, 598
- Massi, F., Testi, L., & Vanzi, L. 2006, *A&A*, 448, 1007
- McKee, C. F. 1989, *ApJ*, 345, 782
- McKee, C. F. & Ostriker, E. C. 2007, *ARA&A*, 45, 565
- Melioli, C., de Gouveia Dal Pino, E. M., de La Reza, R., & Raga, A. 2006, *M.N.R.A.S.*, 373, 811
- Mestel, L. & Spitzer, Jr., L. 1956, *M.N.R.A.S.*, 116, 503
- Meyer, M. R., Calvet, N., & Hillenbrand, L. A. 1997, *Astronomical Journal*, 114, 288
- Mitchell, G. F., Johnstone, D., Moriarty-Schieven, G., Fich, M., & Tothill, N. F. H. 2001, *ApJ*, 556, 215
- Mookerjea, B., Kramer, C., Nielbock, M., & Nyman, L.-Å. 2004, *A&A*, 426, 119
- Moorwood, A., Finger, G., Biereichel, P., et al. 1992, *The Messenger*, 69, 61
- Moriguchi, Y., Yamaguchi, N., Onishi, T., Mizuno, A., & Fukui, Y. 2001, *PASJ*, 53, 1025
- Motte, F., Andre, P., & Neri, R. 1998, *A&A*, 336, 150
- Motte, F., André, P., Ward-Thompson, D., & Bontemps, S. 2001, *A&A*, 372, L41

- Munoz-Tunon, C., Gavryusev, V., & Castoneda, H. O. 1995, *Astronomical Journal*, **110**, 1630
- Murphy, D. C. & May, J. 1991, *A&A*, **247**, 202
- Muzerolle, J., Megeath, S. T., Gutermuth, R. A., et al. 2004, *ApJS*, **154**, 379
- Muzerolle, J., Young, E., Megeath, S. T., & Allen, L. 2005, in *Star Formation in the Era of Three Great Observatories*
- North, P. 2005, *Orion: Zeitschrift für Amateur-Astronomie*, **63**, 47
- Nutter, D. & Ward-Thompson, D. 2007, *M.N.R.A.S.*, **374**, 1413
- Nutter, D., Ward-Thompson, D., & André, P. 2006, *M.N.R.A.S.*, **368**, 1833
- Nyman, L.-Å., Lerner, M., Nielbock, M., et al. 2001, *The Messenger*, **106**, 40
- Onishi, T., Mizuno, A., Kawamura, A., Tachihara, K., & Fukui, Y. 2002, *ApJ*, **575**, 950
- Ortega, V. G., de la Reza, R., Jilinski, E., & Bazzanella, B. 2004, *ApJ*, **609**, 243
- Ossenkopf, V. & Henning, T. 1994, *A&A*, **291**, 943
- Palla, F. & Stahler, S. W. 2000, *ApJ*, **540**, 255
- Pavlovski, G. 2004, PhD thesis, AA(QUEEN'S UNIVERSITY OF BELFAST (UNITED KINGDOM))
- Pettersson, B. 2007, *Puppis and Vela (Handbook of Low Mass Star Forming Regions)*, in press
- Price, S. D., Egan, M. P., Carey, S. J., Mizuno, D. R., & Kuchar, T. A. 2001, *Astronomical Journal*, **121**, 2819
- Reach, W. T., Rho, J., Young, E., et al. 2004, *ApJS*, **154**, 385
- Rebull, L. M., Stapelfeldt, K. R., Evans, II, N. J., et al. 2007, *ApJS*, **171**, 447

- Reid, M. A. & Wilson, C. D. 2005, *ApJ*, 625, 891
- Richer, J. S., Shepherd, D. S., Cabrit, S., Bachiller, R., & Churchwell, E. 2000, *Protostars and Planets IV*, 867
- Rieke, G. H. & Lebofsky, M. J. 1985, *ApJ*, 288, 618
- Rieke, G. H. & MIPS Team. 2004, in *Bulletin of the American Astronomical Society*, Vol. 36, *Bulletin of the American Astronomical Society*, 700–+
- Rodgers, A. W., Campbell, C. T., & Whiteoak, J. B. 1960, *M.N.R.A.S.*, 121, 103
- Rosolowsky, E. & Blitz, L. 2005, *ApJ*, 623, 826
- Rosolowsky, E. & Leroy, A. 2006, *Astronomical Society of the Pacific*, 118, 590
- Russeil, D. 2003, *A&A*, 397, 133
- Salpeter, E. E. 1955, *ApJ*, 121, 161
- Savage, B. D., Massa, D., Meade, M., & Wesselius, P. R. 1985, *ApJS*, 59, 397
- Schmeja, S., Klessen, R. S., & Froebrich, D. 2005, *A&A*, 437, 911
- Shu, F. H., Adams, F. C., & Lizano, S. 1987, *ARA&A*, 25, 23
- Simon, R., Jackson, J. M., Clemens, D. P., Bania, T. M., & Heyer, M. H. 2001, *ApJ*, 551, 747
- Smith, M. D. 2004, *The origin of stars (The origin of stars / Michael D. Smith. London (UK): Imperial College Press, ISBN 1-86094-501-5, 2004, XIII + 248 pp.)*
- Spitzer, L. 1978, *Physical processes in the interstellar medium (New York Wiley-Interscience, 1978. 333 p.)*
- Stahler, S. W. & Palla, F. 2005, *The Formation of Stars (The Formation of Stars, by Steven W. Stahler, Francesco Palla, pp. 865. ISBN 3-527-40559-3. Wiley-VCH , January 2005.)*
- Stahler, S. W., Shu, F. H., & Taam, R. E. 1980, *ApJ*, 241, 637

- Strong, A. W., Bloemen, J. B. G. M., Dame, T. M., et al. 1988, *A&A*, 207, 1
- Testi, L. & Sargent, A. I. 1998, *apjl*, 508, L91
- Tokunaga, A. T. 2000, *Allen's Astrophysical Quantities*, A.N. Cox, Springer-Verlag 4th edition (New York), p. 143
- Walsh, A. J., Bertoldi, F., Burton, M. G., & Nikola, T. 2001, *M.N.R.A.S.*, 326, 36
- Ward-Thompson, D., Scott, P. F., Hills, R. E., & Andre, P. 1994, *M.N.R.A.S.*, 268, 276
- Werner, M. W., Roellig, T. L., Low, F. J., et al. 2004, *ApJS*, 154, 1
- White, R. J. & Hillenbrand, L. A. 2004, *ApJ*, 616, 998
- Whitworth, A. P., Bhattal, A. S., Chapman, S. J., Disney, M. J., & Turner, J. A. 1994, *M.N.R.A.S.*, 268, 291
- Williams, J. P., de Geus, E. J., & Blitz, L. 1994, *ApJ*, 428, 693
- Wood, D. O. S. & Churchwell, E. 1989, *ApJ*, 340, 265
- Wouterloot, J. G. A. & Brand, J. 1999, *A&AS*, 140, 177
- Yamaguchi, N., Mizuno, N., Saito, H., et al. 1999, *PASJ*, 51, 775
- Yonekura, Y., Asayama, S., Kimura, K., et al. 2005, *ApJ*, 634, 476
- Young, C. H., Jørgensen, J. K., Shirley, Y. L., et al. 2004, *ApJS*, 154, 396
- Zuckerman, B. & Evans, II, N. J. 1974, *apjl*, 192, L149
- Zuckerman, B. & Palmer, P. 1974, in *Bulletin of the American Astronomical Society*, Vol. 6, *Bulletin of the American Astronomical Society*, 444–+